Model Based Control of Combustion Timing and Load in HCCI Engines

by

Khashayar Ebrahimi

A thesis submitted in partial fulfillment of the requirements for the degree of

Doctor of Philosophy

Department of Mechanical Engineering
University of Alberta

Abstract

Different model based control strategies are developed for combustion timing and load control in a single cylinder Homogeneous Charge Compression Ignition (HCCI) engine. In HCCI engines, a lean homogeneous air-fuel mixture auto-ignites due to compression and the resulting combustion occurs at lower temperatures compared to spark ignition or diesel engines. The low HCCI combustion temperatures result in low Nitrogen Oxides ($\mathrm{NO_X}$) levels but high unburnt Hydrocarbons (HC) and Carbon Monoxide (CO) levels. High HCCI thermal efficiency occurs when the combustion efficiency is high and the combustion timing is appropriate. In this thesis, the effects of fueling rate and valve timing on HCCI engine performance and energy distribution are described. This analysis indicates that Variable Valve Timing (VVT) with Symmetric Negative Valve Overlap (SNVO) is an effective actuator for combustion timing control. In addition, combustion timing affects combustion efficiency which has an important role in engine energy distribution. Next, a detailed multi-zone model with fuel specific kinetics is developed for HCCI engine performance analysis that captures valve timing and fueling rate dynamics. The multi-zone physics based model has 483 states, 5 inputs and 4 outputs. PI controller gains are first tuned using the detailed multi-zone model in simulation and then the controller is implemented on a single cylinder engine. Combustion timing is used as feedback to the controller and valve timing is the main actuator. Then a Feedforward/Feedback (Fdfwd/Fdbk) strategy is developed for HCCI combustion timing control. The Fdfwd/Fdbk controller is based on a model that relates combustion timing to valve timing and it is combined with an integrator feedback to zero the steady state error. A Model Predictive Control (MPC) strategy is then developed for HCCI combustion timing and load control that takes into account actuator and output constraints. A physics based approach is used for model order reduction of the detailed multi-zone model and a discrete nonlinear control oriented model is obtained with 4 states, 2 inputs and 2 outputs. This model is linearized around one operating point and the MPC is designed based on the linearized version of the 4-state control oriented model. The MPC is then implemented on the single cylinder engine and the results are compared to the PI and Fdfwd/Fdbk controller. The MPC exhibits good tracking performance for combustion timing and load. Finally, a new control oriented model is developed for combustion timing and load control considering combustion efficiency. This model can be used for future MPC design which consider combustion efficiency constraints.

Preface

This thesis is original work by Khashayar Ebrahimi. Some parts of this research including chapters 4, 5, 6, 7 and 8 have been published as:

1. K. Ebrahimi, C.R. Koch, SNVO effects on energy distribution of a single cylinder HCCI engine, submitted to the International Journal of Engine Research, 2016.
2. K. Ebrahimi, M. Aliramezani, C.R. Koch, An HCCI Control Oriented Model that Includes Combustion Efficiency, 8th IFAC Symposium Advances in Automotive Control, AAC 2016.
3. K. Ebrahimi, C.R. Koch, Model Predictive Control for Combustion Timing and Load Control in HCCI engines, SAE Technical paper, SAE 2015-01-0822, 2015.
4. K. Ebrahimi, A. Schramm, C.R. Koch, Feedforward/Feedback Control of HCCI Combustion Timing, 2014 American Controls Conference (ACC), Portland, Oregon, USA.
5. K. Ebrahimi, A. Schramm and C.R. Koch, Effects of Asymmetric Valve Timing with Constant NVO Duration on HCCI Engine Combustion Characteristics, 2014, Combustion Institute/Canadian Section (CI/CS) Spring Technical

Meeting , pp. 6.

6. K. Ebrahimi and C. R. Koch, HCCI Combustion Timing Control with Variable Valve Timing, 2013 American Controls Conference (ACC), Washington, DC, USA.
7. K. Ebrahimi, C. R. Koch and A. Schramm, A Control Oriented Model with Variable Valve Timing for HCCI Combustion Timing Control, SAE Technical Paper, SAE 2013-01-0588, 2013.
8. K. Ebrahimi, M. Shahbakhti, and C.R. Koch, Comparison of Butanol/n-Heptane as a Blended fuel in an HCCI engines, 2011, Combustion Institute/Canadian Section (CI/CS) Spring Technical Meeting, pp. 6

Acknowledgements

First and foremost, I would like to thank my supervisor Dr. Charles Robert (Bob) Koch for his extensive support and for the unique opportunities he provided me during my Ph.D that helped me to build my skills and knowledge. Dr. Koch has been great mentor and adviser for me. His valuable advice and feedback helped me to overcome research challenges during my Ph.D and without his support none of these would have been possible.

I am also grateful to all people in the engine research lab, the great environment where I could learn and grow as a person. Many thanks to Alexander E. Schramm and Masoud Mashkournia for their contributions in collecting the experimental data. I would like to acknowledge Bernie Faulkner from the Mechanical Engineering shop for his technical support in performing the experiments. Special thanks to my examination committee for their valuable feedback on my research. Thanks to all my friends at the University of Alberta for all the good time we have had during these six years. Lastly, I want to thank my parents (Malihe and Ali) and my brothers (Khosrow and Sasan) for their love, encouragement, support and for all of the wonderful things they have done for me.

Contents

List of Tables

List of Figures

Nomenclature

AFR	Air Fuel Ratio [-]
BD	Burn Duration [CAD]
$BSFC$	Brake Specific Fuel Consumption [$\frac{g}{kW.h}$]
C_d	Discharge Coefficient [-]
C_p	Constant Pressure Specific Heat Capacity [$\frac{kJ}{kg.K}$]
C_v	Constant Volume Specific Heat Capacity [$\frac{kJ}{kg.K}$]
CO	Carbon Monoxide [%]
CO_2	Carbon Dioxide [%]
EGR	Exhaust Gas Recirculation [-]
Em_{finj}	Injected Fuel Energy [$\frac{kJ}{Cycle}$]
$FMEP$	Friction Mean Effective Pressure [bar]
$IMEP$	Indicated Mean Effective Pressure [bar]
L_{st}	Stoichiometric Air-Fuel Ratio [-]

LHV	Lower Heating Value [$\frac{MJ}{kg}$]
m	mass [kg]
m_f	fuel mass [kg]
m_{air}	air mass [kg]
$NMEP$	Net Mean Effective Pressure [bar]
NO_X	Oxides of Nitrogen [ppm]
O_2	Oxygen [%]
P	Pressure [bar]
r_c	Compression Ratio [-]
RI	Ringing Intensity [$\frac{MW}{m^3}$]
T	Temperature [K]
uHC	unburned HydroCarbon [%]
V_c	Clearance Volume [m^3]
V_d	Displaced Volume [m^3]

Greek Letters

α	Power to heat ratio
β	Power to energy loss ratio
η	Efficiency

γ	Specific heat ratio
ϕ	Equivalence Ratio
θ_{10}	Crank Angle of 10% mass fraction burned
θ_{50}	Crank Angle of 50% mass fraction burned
θ_{90}	Crank Angle of 90% mass fraction burned

Subscript

b	Brake
exh	Exhaust
f	Fuel
ind	Indicated
int	Intake

Abbreviations

ANN	Artificial Neural Network
$aTDC$	after Top Dead Center
$bTDC$	before Top Dead Center
CA	Crank Angle
CAD	Crank Angle Degree
CAS	Combustion Analysis System

CHP	Combined Heat and Power
COM	Control Oriented Model
COV	Coefficient of Variation
$DSMC$	Discrete Sliding Mode Control
EOC	End of Combustion
EPA	Environmental Protection Agency
EVC	Exhaust Valve Closing
EVO	Exhaust Valve Opening
$EVVT$	Electromagnetic Variable Valve Timing
$HCCI$	Homogeneous Charge Compression Ignition
HR	Heat Release
$HTHR$	High Temperature Heat Release
IVC	Intake Valve Closing
IVO	Intake Valve Opening
LQG	Linear Quadratic Gaussian
LQR	Linear Quadratic Regulator
LTC	Low Temperature Combustion
$LTHR$	Low Temperature Heat Release

$MIMO$	Multi-Input Multi-Output
MPC	Model Predictive Control
ON	Octane Number
PCC	Premixed Charged Compression
PI	Proportional Integral
PID	Proportional Integral Derivative
PM	Particulate Matter [ppm]
PPC	Partially Premixed Combustion
ppm	Particle Per Million
PRF	Primary Reference Fuel
PW	Pulse Width
$RCCI$	Reactivity Controlled Compression Ignition
$RMSE$	Root Mean Square Error
RPM	Revolutions Per Minute
SI	Spark Ignition
$SISO$	Single-Input Single-Output
$SNVO$	Symmetric Negative Valve Overlap
SOC	Start of Combustion

TDC Top Dead Center

Chapter 1

Introduction

Homogeneous Charge Compression Ignition (HCCI) is a promising concept for internal combustion engines to reduce $\mathrm{NO_X}$, particulate matter emissions and fuel consumption [1]. In HCCI engines, a homogeneous air fuel mixture auto-ignites due to compression, which is unlike traditional spark ignition (SI) and diesel engines where ignition is started with either a spark or fuel injection. HCCI engines can be scaled to a large variety of transportation engines and also can be applied to stationary applications such as power generation [2]. In addition, the auto-ignition characteristic of HCCI combustion means that these engines can be operated with a wide variety of fuels including bio-fuels [3, 4].

Figure 1.1 shows the relationship between combustion temperature and pollutant formations and compares HCCI technology to the convectional technologies such as SI and Diesel. In diesel engines, the combustion starts in the rich mixture (ϕ=4), and then combustion continues in diffusion mode (ϕ=1) [5, 6]. Figure 1.1 shows that these combustion modes fall in the soot and $\mathrm{NO_X}$ formation regions respectively. Spark Ignition (SI) engines have lower thermal efficiencies compared to Diesel engines due to their lower compression ratios and throttling losses and produce significant amount of $\mathrm{NO_X}$ [7]. $\mathrm{NO_X}$ formation decreases with decreasing combustion temperature, and soot formation is reduced with lean homogenous mixture as shown in Figure 1.1. Since HCCI engines typically operate at lean mixtures and low combustion temperatures, the high soot and $\mathrm{NO_X}$ formation zones are avoided. HCCI has the advantage of the high thermal efficiency similar to Diesel as the engine compression ratio can be high with un-throttled operation [8]. HCCI operating range is limited by misfire at low loads and knock at high loads [1]. The major HCCI engine emissions are CO and unburnt HC [1]. To reduce these emissions, different actuators and strategies, are used such as Variable Valve Timing (VVT) [9], oxidation catalyst [10], EGR and fuel Octane number [11, 12]. In addition, HCCI combustion timing is difficult to control since there is no direct initiator of combustion. Combustion timing in HCCI engines is highly sensitive to trapped mixture temperature, pressure and composition at Intake Valve Closing (IVC) [13]. Several techniques have been developed and implemented for combustion timing control in HCCI engines including variable compression ratio [14], intake air heat-

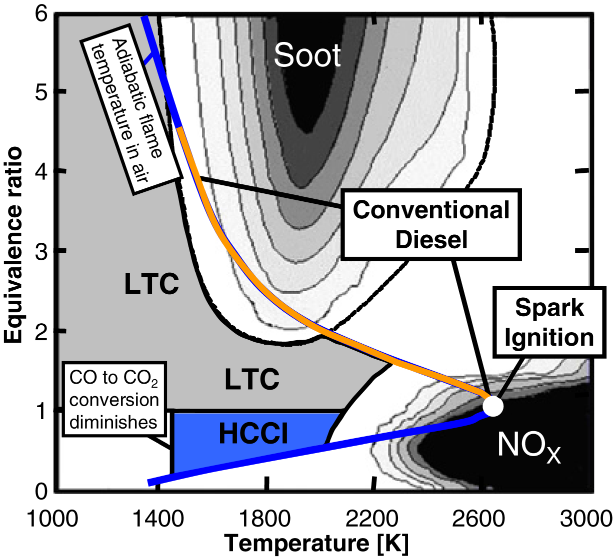

Figure 1.1: LTC, HCCI, Diesel and SI regions [8]

ing [15], dual fuels [16, 17], pilot injection [18–20], Variable Valve Timing (VVT) [21, 22], water injection [23] and Exhaust Gas Recirculation (EGR) [24]. Among these strategies, VVT shows potential since it reduces residual gas heat loss and achieves fast cycle-by-cycle control response [25]. VVT changes the amount of trapped residual gas and the effective compression ratio cycle by cycle both of which have a strong effect on HCCI combustion timing. Intake air heating is not a practical control of HCCI combustion timing as energy is required to heat the air and the heater response time is slow compared to an engine cycle. Exhaust Gas Recirculation (EGR) is usually not fast enough for cycle-by-cycle combustion timing control. Controlling the combustion timing by varying the auto-ignition properties of the fuel using dual-fuels is also effective but at least two fuels are needed [26–29]. HCCI with dual-fuels has wider operating range with acceptable pressure rise rate and ringing intensity that helps to obtain very high indicated efficiencies [27]. Variable compression ratio can also be used to control the combustion timing but requires a complex mechanical mechanism [14, 30]. Pilot injection is another interesting technique for combustion timing control, however this technique increases CO and HC emissions and decreases fuel efficiency [29, 31–33]. Water injection slows down the combustion rate and retards the combustion timing, however, it increases the unburnt HC and CO emissions [34].

Three different VVT strategies that have been used for HCCI engines are Symmetric Negative Valve Overlap (SNVO), Positive Valve Overlap (PVO) and Exhaust Re-breathing technique as shown in Figures 1.2, 1.3 and 1.4. PVO has lower pumping and less heat transfer losses compared to SNVO [35] and is used to extend high load limits of the HCCI. Two different re-breathing techniques are examined in

[36] including late exhaust valve closing and a second exhaust valve opening event during the induction. Higher thermal efficiencies are reported with re-breathing techniques compared to PVO and SNVO. In [37], higher net indicated efficiencies achieved with re-breathing technique compared to SNVO. The combustion stability of the re-breathing and SNVO are compared in [37] and it is found that the combustion is more stable if part of the fuel is injected during SNVO. The re-breathing technique is reported as a good strategy for extending the lower load limit of the HCCI [38].

In this work SNVO strategy is used for cycle-by-cycle combustion timing control using port fuel injection [25]. In SNVO, the Exhaust Valves Close (EVC) timing is set to a crank angle before the piston reaches Top Dead Center (TDC) in the exhaust stroke and the Intake Valves Open (IVO) timing is set to the same amount, or symmetric, after TDC (see Figure 1.2). With symmetric changes of EVC and IVO timing around TDC, the re-compression work can be partially regained as expansion work and the pumping work is minimized with this strategy. The effects of symmetric NVO on HCCI combustion have been investigated in [9, 39–43]. Measured pressure traces of HCCI engine for different NVO durations are shown in Figure 3.1. NVO has significant effect on HCCI combustion timing, rate of pressure rise and maximum in-cylinder pressure as shown in this figure.

A variety of controllers with various levels of complexities have been developed for HCCI combustion timing and load control. HCCI combustion timing control is essential to improve the fuel consumption and emissions [44] that affects engine energy distribution [43]. Some of the controllers are based on models obtained from system identification [21, 45–49] while others are based on physical mod-

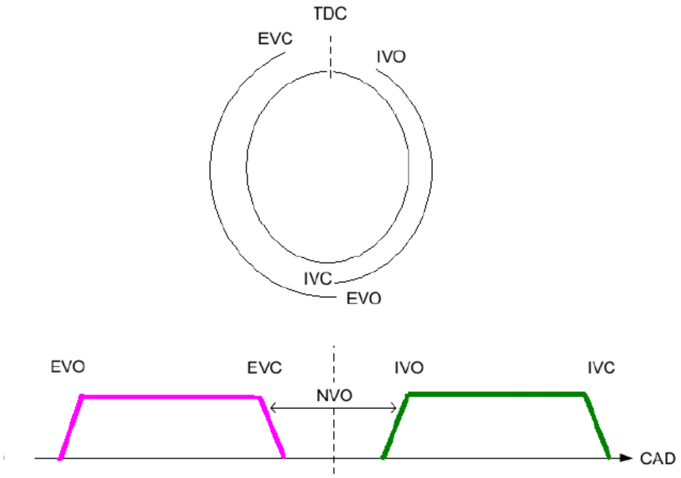

Figure 1.2: Symmetric negative valve overlap strategy [25]

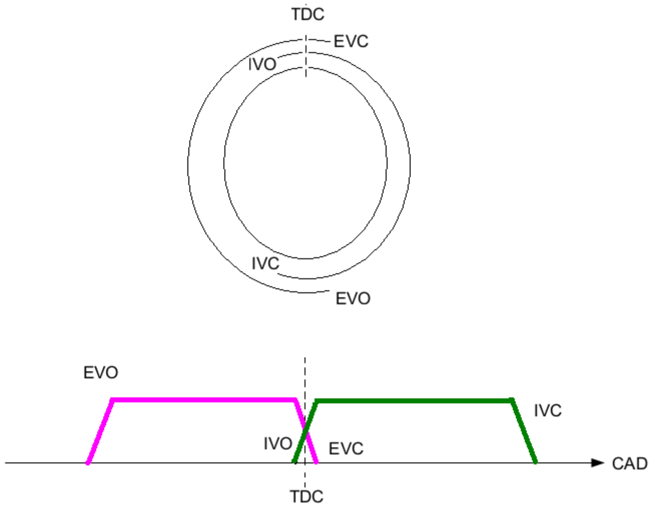

Figure 1.3: Positive valve overlap strategy

els [18, 42, 50, 51]. Physical models are classified according to the number of spatial dimensions in the cylinder, e.g. zero-dimensional [52–55] or computational fluid dynamics (three dimensional) models [56–59]. Zero dimensional models provide no spatial resolution. Most of the zero-dimensional models are based on detailed chemical kinetics and are not suitable for control analysis since the chemical kinetics are complex and time consuming. Computational fluid dynamics models

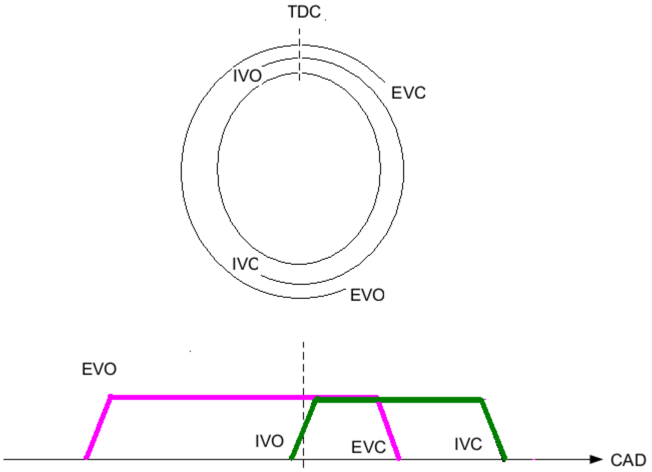

Figure 1.4: Exhaust re-breathing technique

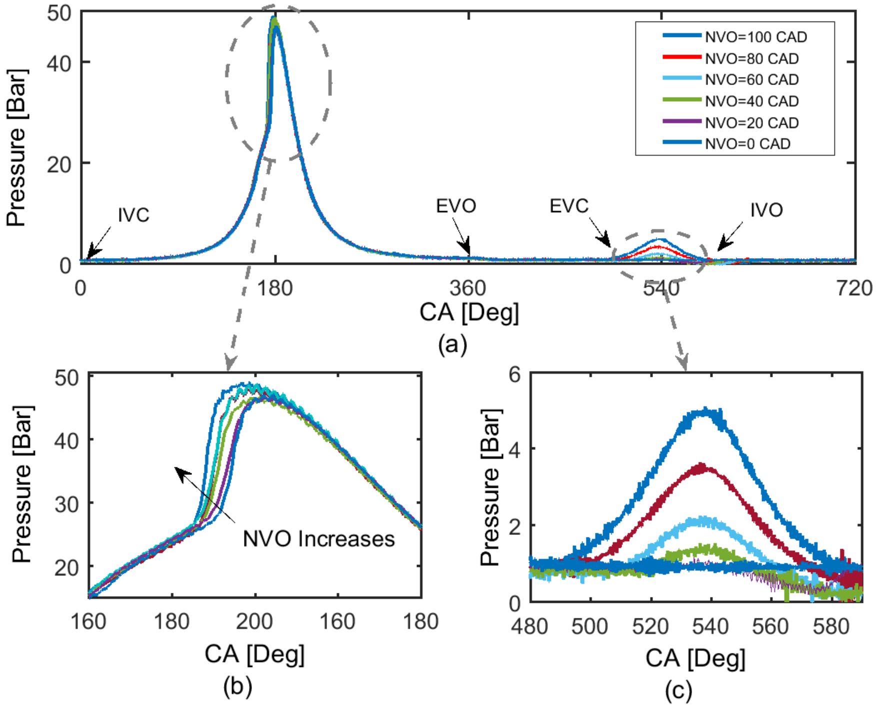

Figure 1.5: Measured HCCI engine cylinder pressure traces [Em_{finj}=0.49 $\frac{\text{kJ}}{\text{Cycle}}$, Ω=815 RPM]

are even more complex and usually produce only a single engine cycle of data. For control analysis, a model that is capable of quickly simulating many engine cycles is required. A short summary of the existing HCCI control oriented model is provided next.

1.1 HCCI Modeling

Many HCCI engine models for control purposes have been developed [18, 60–63, 42, 64, 65]. In these models, the combustion mechanism is greatly simplified to decrease the computaion time. In [60], a real time physics based model is developed for in-cylinder Air/Fuel ratio and trapped residual gas mass fraction estimation where air and residual gas mass fraction at the beginning of compression are determined based on signals from an air flow meter and in-cylinder pressure transducer. A physical based control oriented model is detailed in [61] for a propane HCCI engine. An integral Arrhenius rate expression is used to capture the importance of species concentrations and temperature on the ignition process. A discrete time control oriented speed dependent HCCI model is developed in [66] for combustion timing control considering volumetric efficiency, heat transfer during combustion and intake and exhaust mass flow dynamics. The effect of engine speed on chemical kinetics and the reaction time is captured using the Arrhenius integral and the model is validated against the steady state and transient experimental data that shows good accuracy. A nonlinear control oriented model is developed in [63] for HCCI with exhaust re-compression. The fueling rate and valve timing are the model inputs while combustion timing and load are the model outputs. Start of combustion is tabled as a function of IVC temperature and oxygen concentration offline using Arrhenius integral and the burn duration is modeled as linear function of start of combustion. In [67], a mean value model is developed for combustion timing control in an HCCI engine equipped with variable valve timing. The re-breathing technique is used as the variable valve timing strategy. The model has three continuous manifold states (the mass composition and pressures in the intake and exhaust manifolds), three discrete cylinder states (cycle-averaged cylinder flows and residual gas temperature leaving cylinder), and one sensor lag (the delay between cylinder intake and exhaust processes). A simple Arrhenius integral model is used to estimate the start of combustion and algebraic equations are used for the heat release rate calculation. In [62], a physics based model is detailed for a gasoline HCCI engine considering variable valve timing. The model integrates the SENKIN code of the CHEMKIN library [68] to the AVL BOOST [69] engine cycle simulation code and parametric studies of the combustion process in a single cylinder HCCI engine are described. A simple non-linear control oriented physics based model is developed in [70] for a gasoline HCCI engine equipped with variable valve timing. The gas exchange is based on in-cylinder dynamics and it is assumed that the manifold pressure is constant during gas exchange. Combustion is modeled in a semi empirical fashion. In [71], a system identification approach is used on a dual-fuel HCCI engine for combustion timing control. The model inputs are IVC timing, fuel octane number, injected fuel energy and engine speed. A control oriented model is detailed that simulates the engine cycle from the intake to the exhaust stroke and the model includes the thermal coupling dynamics caused by the residual gases from one cycle to the next cycle in [72]. The gas exchange process, engine output work and combustion are predicted using semi-empirical correlations. A grey-box model is developed in [73] for predicting HCCI engine performance. The model consists of a combination of physical models and three feed-forward artificial neural networks to estimate six major HCCI combustion indexes including combustion timing, load, exhaust gas temperature, unburned HC, CO, and $\mathrm{NO_X}$ emissions. In [74], a black-box model is developed for HCCI exhaust gas temperature. The model is developed based on experimental data from a single cylinder engine [74] using artificial neural network. Effects of fuel equivalence ratio, combustion temperature, intake manifold temperature, and engine speed on exhaust gas temperature is detailed. A physics-based model is developed in [75] for cycle-by-cycle modeling of HCCI exhaust gas temperature. The model inputs are engine speed, fuel equivalence ratio, EGR, mass of injected fuel, exhaust manifold pressure, intake manifold temperature and pressure. The model shows good accuracy against steady-state and transient experimental data with step changes in fueling rate.

Model based controllers are attractive since they provide component-based structure [44]. The model can be easily modified to reflect changes in the engine structure. In system identification, the modeling process must be repeated for even small changes on the engine structure. The model based controllers suffer from plant/-model mismatch that often makes their functionality limited to the operating range that the model is accurate. Only a few of the model based controllers have been implemented [18, 22, 46, 48, 51, 63, 65, 76]. A short summary of some HCCI combustion timing and load control is given next to provide context for the control strategies developed in this work.

1.2 HCCI Control

Different approaches and control strategies have been developed for HCCI combustion timing and load control. In [77], closed-loop control of the combustion timing and load is performed in an HCCI engine using a gain-scheduled experimentally tuned PID controller. For combustion timing control, the fuel Octane Number (ON) is adjusted by changing the mixing ratio of n-heptane and iso-octane while the total fueling rate is the main actuator for load control [77]. The combustion timing and IMEP are used as feedback to the controller and are calculated in real-time based on the measured cylinder pressure. A PID controller is developed to vary the ratio of the hot to cold intake air entering a variable compression ratio engine in [78] for combustion timing control while the fueling rate is used for load control. Engine speed effect is examined and it is found that fuel type and its low temperature reaction properties has a large influence on the controller closed-loop response. Compression ratio is varied to control combustion timing in a variable compression ratio HCCI engine with a PID controller in [76]. The controller shows acceptable performance with disturbances in fueling rate, engine speed and intake charge temperature. A PID control strategy for combustion timing control in a single cylinder research engine is described in [79]. Combustion timing is used as feedback to the controller and valve timing is used for combustion timing control. NVO duration and IVC timing are used as valve timing strategies. NVO is used to adjust IVC temperature by trapping the residual gas and IVC is used to adjust effective compression ratio for load cntrol [79]. Extremum seeking is used to tune PID controller gains in [80] for HCCI combustion timing control by minimizing the fuel consumption. Combustion timing control is done by intake charge heating and the engine is equipped with thermal-management system that allows the intake temperature of each cylinder to be quickly adjusted. The extremum seeking does not require a system model and can handle cost functions without local optima [44, 81].

An Iterative Learning Controller (ILC) is developed in [17] for dual-fuel HCCI engine combustion timing and load control. The amount of n-heptane and iso-octane injected into the intake manifold is used as the main actuator. The controller is designed based on a model obtained from system identification. The controller performance is compared to PI controller and it is found that ILC can track the desired trajectories with less RMS error after three iterations.

A feedforward controller is developed in [82] based on a physical mean value model to control combustion duration. Combustion duration is controlled by changing the mixing ratios of the cold and hot fresh charge in the intake manifold [82]. In [83], a layered closed loop control for an HCCI engine equipped with variable valve timing is implemented by combining classical PID and a feed-forward control strategy to realize effective control of load and combustion timing. NVO duration is adjusted for load control while IVC timing is used to control combustion timing. A feedforward-feedback controller is developed in [63] for HCCI combustion timing and load control. The controller is based on a four-state linear model with temperature, oxygen and fuel concentration at 60 CAD before TDC and in-cylinder volume at IVC as the states. Fueling rate is used for load control while IVC and EVC timings are the main actuators for combustion timing control.

A LQG controller is detailed and implemented on a multi-cylinder engine for cycle by cycle combustion timing control based on a system identification model in [47]. A subspace-based method called Multivariable Output-Error State Space Model, MOESP is used for system identification and the model order is defined based on the singular values of the Hankel matrix. Two fuels with different octane numbers are used to control the combustion timing. Feedback linearization is used to synthesize a nonlinear controller for HCCI combustion timing and peak pressure control in [51]. The model inputs are the molar ratio of re-inducted products to fresh reactants and IVC timing. The molar ratio of re-inducted products to fresh reactants is controlled by IVO and EVC timings at constant IVC. IVC timing is used as the second actuator for maximum in-cylinder pressure control. The controller is implemented on a single cylinder HCCI engine. In [65], a two-input two-output H_2 controller is designed based on a physics based two-state model for combustion timing and peak in-cylinder pressure control. The actuators are EVC and IVC timings and the controller is implemented on a HCCI engine. Cylinder to cylinder cross talk in a multi-cylinder HCCI engine is modeled in [84] and a LQG controller is used to control combustion timing for each cylinder. In [85], closed loop control for HCCI combustion timing and load control is developed using Local Linear Model Tree (LOLIMOT) adaptive neural network [86] and the actuators are split fuel injection and EVC timing. In [50], a Discrete Sliding Mode Controller (DSMC) coupled with a Kalman filter is designed to control combustion timing by adjusting the ratio of two Primary Reference Fuels (PRFs) while a feed-forward controller is used for load control [87]. The controller is designed based on a five-state model. The model states are combustion timing, temperature and pressure at start of combustion, residual gas mass fraction and temperature of the trapped residual gases after EVC. The model developed in [87] is used for combustion timing and load control in [88] with fuel Octane Number (ON) and fuel equivalence ratio as main actuators. The desired combustion timing trajectory is calculated from experimental desired load trajectory and an integral state feedback controller is used for combustion timing control while a feedforward controller is used for load control. In [89], exergy based optimal control is developed for HCCI combustion timing control in simulation. An algorithm is used to define desired combustion timing based on the required IMEP and the engine operating conditions. Fuel ON is used to control HCCI combustion timing by manipulating the ratio of two PRFs using an integral state feedback controller detailed in [90].

In [21], Model Predictive Control (MPC) is designed and implemented for the first time on HCCI. The modeling is based on system identification and the model has four inputs and three outputs. The model inputs are fueling rate, ethanol fraction, engine speed and inlet temperature. Combustion timing, load and rate of cylinder pressure rise are selected as model outputs. The fuel octane number is used as the main actuator and the ratio of n-hepatane to ethanol is changed for cycle by cycle combustion timing control. IMEP is controlled using the amount of injected fuel. Constraints are applied on the actuators and rate of pressure rise and the controller shows robust performance in tracking the combustion timing and load. In [46], MPC is developed based on system identification with IVC timing, intake manifold temperature, engine speed and injected fuel energy as the inputs. Combustion timing and IMEP are controlled using IVC timing and fueling rate as main actuators considering constraints on rate of pressure rise. In [49], MPC, LQG and PID controllers developed based on identified models and are implemented in a six-cylinder heavy duty engine for cycle by cycle control of combustion timing. Two different actuators are used for combustion timing control including variable valve timing and dual fuel. IVC timing is varied as the valve timing strategy as it changes the effective compression ratio. It is found that the variable valve timing has more direct control of combustion timing than the dual-fuel. Two different sensors are used for pressure measurement in this work: pressure transducer and ion current sensor. The measured pressure is used to calculate combustion timing and load for the controllers' feedback. The controllers show good performance with both sensors and ion current feedback is found to work well in a range of λ of $[2, 2.7]$. The MPC shows better performance in combustion timing and load control compared to the other controllers.

A model predictive control based on a second order physics based model is developed in [91] for combustion timing control. The controller outputs are IVC timing and inlet temperature while the feedback is combustion timing and load. A fast thermal management system is designed and used to modulate intake charge temperature. A weight is introduced on IVC timing to achieve a mid-ranging effect as both IVC timing and inlet temperature are redundant. The controller is implemented in a multi-cylinder engine and the results indicate that the controller is robust and has fast closed loop response. In [92], MPC is detailed and tested in simulation for maximum in-cylinder pressure and combustion timing control with EVC and IVC timings as main actuators. The controller is based on a four-state physics based model with in-cylinder volumes at IVC and SOC, residual mole fraction and maximum in-cylinder pressure as the states. MPC is designed in [18] based on a five-state physical model for combustion timing and output work control with valve timing and split fuel injection as main actuators. The physical model used in [18] is the model developed in [63] with split injection combustion threshold as new state. The controller is implemented on a single cylinder of a multi-cylinder HCCI engine. The MPC developed in [18] is implemented in a multi-cylinder HCCI engine for combustion timing and load control using the same actuators used in

[18] with shared cam phaser [93]. An output disturbance estimator is added to the controller that compensates the non-modeled cylinder to cylinder cross talk. The MPC framework used in this work allows for the implementation of HCCI utilizing actuators currently in production. Nonlinear MPC is detailed in [94] for HCCI combustion timing and load control in simulation. A nonlinear system identification is performed using an extreme learning machine for model development. The MPC optimization is then formulated as a convex problem for which a fast quadratic programming method is used to optimize cost function. The main actuators used in this work are EVC timing, fueling rate and fuel injection timing.

1.3 Thesis Overview and Contribution

1.3.1 Overview

In this study, three different strategies are used for HCCI combustion timing and load control. First, a Detailed Physical Model (DPM) is developed for HCCI engine thermodynamic performance analysis. The model has simple structure and can predict combustion timing, pressure evolution and work output for n-heptane fuel with good accuracy. Then, a PI controller is developed for combustion timing control using the DPM to tune the controller gains and the controller is implemented in a single cylinder HCCI engine. A feedforward/feedback controller is then developed to improve the PI controller performance. The controller is based on a model that relates combustion timing to the valve timing in feedforward and combustion timing is used as feedback to zero the steady state error using a constant gain integrator. The controller is implemented on the engine and the results are compared to the PI controller. Finally, MPC with Laguerre function [95] is designed and implemented for combustion timing and load control. MPC is useful for HCCI control predominantly because of its ability to handle constraints explicitly. To construct MPC, a nonlinear control oriented model for cycle by cycle combustion timing and load control is developed. The developed control oriented model is based on model order reduction from the DPM [64]. The nonlinear model is then linearized around one operating point and engine experimental validation results show that it has sufficient accuracy for combustion timing and output work prediction. Then VVT with SNVO strategy is used for HCCI combustion timing control while the fueling rate is predominantly used for output work control. The crank angle of fifty percent fuel mass fraction burned, θ_{50}, is used as the cycle by cycle measurement of combustion timing. MPC with Laguerre function is very useful as it simplifies the traditional MPC algorithm used in [18, 21, 92, 93] and reduces the computation time [95]. The controller is then implemented on the single cylinder engine and the results are compared to the PI and feedforward/feedback controllers. Engine energy distribution analysis is performed considering effects of VVT and fueling rate. The analysis indicates that combustion efficiency has important effects on engine energy distribution. A new control oriented model is then developed based on the measured experimental data as the DPM predicts higher values for combustion efficiency. The model includes effects of combustion efficiency on the output work and combustion timing. MPC can be designed based on the new model considering constraints on combustion efficiency.

1.3.2 Contributions

The contributions of this thesis include

- Detailed analysis of NVO and fueling rate effects on HCCI combustion characteristics and HCCI energy distribution
    - Effects of NVO duration on combustion timing, rate of pressure rise, combustion duration and ringing (knock) are investigated experimentally for several injected fuel energies
    - Effects of NVO duration on engine energy distribution, coolant and exhaust exergy, CHP first and second law efficiency are experimentally detailed for several injected fuel energies
    - Power to energy losses ratio is defined for energy distribution analysis in HCCI engine.
- Developed and validated a physics based multi-zone model (DPM) for HCCI open cycle simulation considering fuel chemistry
    - The model captures the effects of system inputs (valve timing and fueling rates) on the system outputs (exhaust gas temperature, maximum rates of pressure rise, combustion timing, in-cylinder pressure, peak in-cylinder pressure and work output).
    - The model captures the cycle-to-cycle coupling through exhaust gas temperature and composition.
    - The model captures combustion timing via kinetics using Cantera [96] and known reaction mechanism of n-heptane [97, 98].
    - The model runtime with 483 states, 5 inputs and 4 outputs is about 156 sec per engine cycle on a 2.66 GHz Intel PC that makes it amenable to

  use it as a virtual setup for control development and implementation.
  - The model can be easily adapted to a new fuel if the kinetic mechanism is known

- Developed and validated control oriented model using DPM for cycle by cycle control of HCCI combustion timing and load
  - The model captures the effects of control inputs including variable valve timing and fuel injection quantity on the HCCI combustion timing and load
  - The model has two inputs (NVO duration and fueling rate), two outputs (combustion timing and IMEP) and five states (IVC temperature, residual gas fraction, fuel equivalence ratio, injected fuel energy and combustion timing)
  - The model captures cycle-to-cycle coupling through exhaust gas temperature and composition
  - The model can be used easily for the development of the model-based control strategies
  - The model is validated against the DPM and the experimental measurements

- Several control strategies are developed and implemented in experiment
  - PI controller gains are tuned using DPM and implemented for combustion timing control with variable valve timing as the main actuator

  - Feedforward/Feedback controller is developed and implemented based on a model that relates combustion timing to the valve timing in feedforward and combustion timing is used as feedback to zero the steady-state error using a constant gain integrator (the integrator gain is tuned using the DPM).
  - MPC with Laguerre function is developed based on the linearized control oriented model and the controller is implemented for combustion timing and load control. The actuators are NVO duration and injected fuel energies while the feedback are the combustion timing and IMEP.
- Developed and validated control oriented model using experimental data for cycle by cycle control of HCCI combustion timing and load control
  - Following the detailed HCCI engine energy distribution analysis, insights gained from the combustion efficiency role on engine performance and the new control oriented model is developed considering combustion efficiency
  - A physics based control oriented modeling approach is detailed for the case that fuel reaction mechanism is not available.
  - The model captures the effects of varying the quantity of fuel injection as well as the NVO duration on the combustion timing and output work.
  - The model can be used easily for the development and implementation of the MPC considering constraints on combustion efficiency (emission).

1.3.3 Thesis Outline

The remainder of thesis is organized as follows:

Chapter 2 provides information about the experimental setup (single cylinder engine, EVVT mechanism, and the computer software and hardware used for engine control and data acquisition).

Chapter 3 provides detailed analysis of NVO duration and fueling rate effects on HCCI combustion characteristics (combustion timing, rate of pressure rise, IMEP, ringing (knock) and emission). It is found that combustion timing has important effect on HCCI combustion characteristics and emission. The results show that NVO can be used as an effective actuator for combustion timing and emission control.

Chapter 4 provides HCCI engine energy distribution analysis considering NVO duration and fueling rate effects. It is found that NVO can be used as an effective actuator for CHP first and second law efficiency improvement specifically at low loads. Power to energy losses ratio is defined for energy distribution analysis in HCCI engines that includes fraction of the fuel energy lost due to incomplete combustion. Finally it is shown that higher power to energy losses ratios are obtained at higher combustion efficiencies where combustion timings are near TDC.

Chapter 5 formulates a physics based multi-zone model of a residual-affected HCCI engine. HCCI is a complex physical process and the simple model presented in this chapter can capture the HCCI combustion aspects including pressure evolution, combustion timing, output work, maximum rate of pressure rise and exhaust gas temperature. Cantera [96] is used for HCCI combustion modeling using the n-heptane reaction mechanism from [98]. The DPM can be used as virtual setup for the formulation of control strategies using different actuators (VVT, Fueling rate, and Dual Fuel) and outputs (maximum rate of pressure rise, output work, combustion timing, maximum in-cylinder pressure, and burn duration).

Chapter 6 PI controller gains are tuned using the DPM developed in chapter 5. The PI controller is then implemented in a single cylinder research engine. The actuator is VVT with symmetric NVO strategy and the feedback signal is the combustion timing. A feedforward/feedback controller is then developed to improve PI controller performance. The controller is based on a control oriented model that relates combustion timing to the valve timing in feedforward. The model is parameterized using the DPM developed in chapter 5. Similar to the PI controller, VVT is used as the main actuator and combustion timing is used as feedback to the controller. The DPM is then used to tune the integrator gain of the controller. The controller is then implemented and the results indicate that the feedforward/feedback controller performance has improved tracking of the desired combustion timing and performs well in maintaining a desirable engine combustion timing during load and engine speed disturbances.

Chapter 7 outlines a control approach that allows the control of combustion timing and IMEP through modulation of trapped residual gas and fueling rate. MPC with Laguerre function [95] is developed based on a linearized version of the nonlinear control oriented model developed in this chapter. The nonlinear control oriented model has two inputs (NVO duration and fueling rate), two outputs (combustion timing and IMEP) and four states (IVC temperature, residual gas fraction, fuel equivalence ratio, and combustion timing). The model is parameterized using experimental data and the DPM. A long control horizon can be realized through the exponential nature of the Laguerre functions, hence optimization is performed without using a large number of parameters that simplifies the optimization problem and reduces the execution time. The controller is implemented in a single cylinder engine with hard input constraints while the output constraints are soft. The MPC performance is then compared to the PI and feedforward/feedback controller developed in previous chapter and better performance is achieved.

Chapter 8 The analysis performed in chapter 4 indicates that combustion efficiency has important role in HCCI engine energy distribution. A new physics based control oriented model is detailed for combustion timing and output work control considering combustion efficiency. The model has two inputs (NVO duration and fueling rate) , two outputs (combustion timing and output work) and 4 states (IVC temperature, fuel equivalence ratio, combustion efficiency and combustion timing). The model is parameterized using measured data and the detailed modeling approach is useful when the fuel reaction mechanism is not available. Steady state and transient validation of the model are provided against the measurements and the DPM. The model can be used for MPC design considering constraints on HCCI combustion efficiency (emission).

Chapter 9 summarizes the results and conclusions of this research and briefly outlines possible future work.

Chapter 2

Experimental Setup

Experiments are conducted on a single cylinder Ricardo Hydra Mark III engine equipped with a custom Electromagnetic Variable Valve Timing (EVVT) system [99, 100]. The engine compression ratio is fixed at 13.9 although it can be adjusted using the cylinder jug. The EVVT systems allow independent opening and closing of the intake and exhaust valves. Each valve has a high speed motion controller that is triggered at the desired crank angle by the engine controller. A schematic of the test setup is shown in Figure 2.1 and photographs of the test cell are shown in Figures. 2.2 and 2.3. The engine specifications are listed in Table 2.1. Air enters the system through a laminar flow meter and then passes through the electronically controlled throttle. It then passes through a roots-type supercharger (Eaton Automotive MP45) which is driven by a variable speed electric motor. In this study intake manifold is not boosted and so the supercharger is not used. The air then goes through an intake air heater and is heated to 80 °C. Two separate port fuel injection systems with 3-bar fuel pressure are available with fuel injection timing set to inject on closed intake valves and both injectors are aimed directly at the back of the intake valves. This could allow cycle-by-cycle combustion timing control by modulating fuel Octane Number. However, this experiment only n-heptane is used as fuel. Fuel flow rate is measured only on the n-heptane side using a Coriolis meter (Pierburg PLU4000) and pulse width calibration is used for calibration [71, 100, 9]. The calibration details are available in [71]. On the exhaust side, the external Exhaust Gas Recirculation (EGR) loop is controlled by an EGR valve. External EGR is not used in this study since the flexible valve timing allows internal EGR. Exhaust gas is then passed through the emissions bench sample extraction and five gas analyzers [71] for emission measurement.

Parameter	Values
Bore × Stroke [mm]	97 × 88.9
Compression Ratio	13.9
Displacement [L]	0.653
Intake Valve Diameter [mm]	36
Exhaust Valve Diameter [mm]	24
Connecting Rod length [mm]	159

Table 2.1: Engine Specifications

2.1 dSPACE MicroAutoBox

A dSPACE MicroAutoBox is used for the engine control using ControlDesk V3.3P1 software. It consists of a dSPACE model ds1401 computer connected to custom power electronics. The controller is designed using MATLAB Real-time Workshop and is used to set the valve timing, fueling rate, and spark timing (not used in this study). The dSPACE ControlDesk computer runs these tasks at a rate of 1000Hz, and calculates the next cycles fuel injector pulse width during the current cycle's intake stroke. The MicroAutobox computer receives a crank angle position signal from a hall sensor and a 36-1 toothed wheel on the crank shaft. The dSPACE ControlDesk interpret the signal for appropriate valve timing as the engine has been

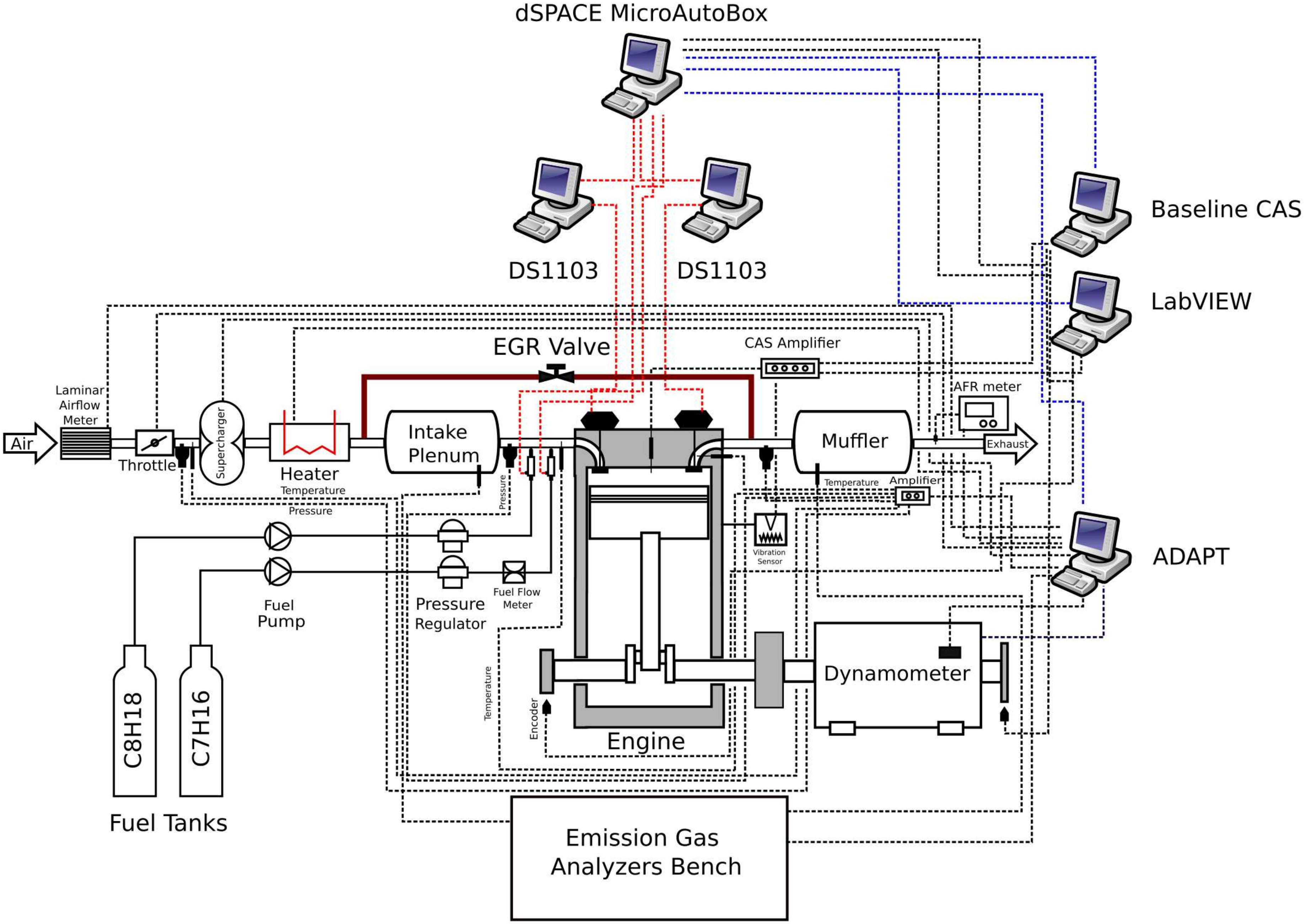

Figure 2.1: Single cylinder engine experimental setup including electromagnetic valve

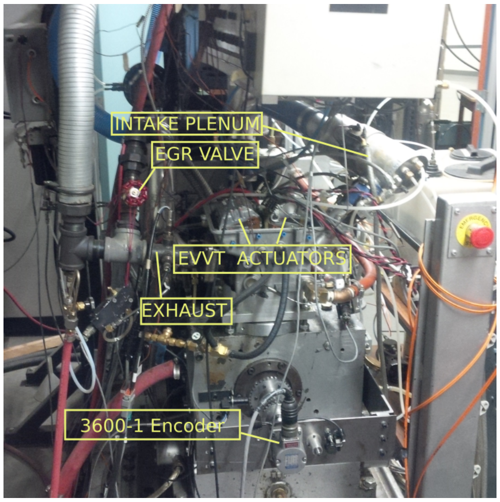

Figure 2.2: Photograph of single cylinder research engine equipped with Electromagnetic VVT

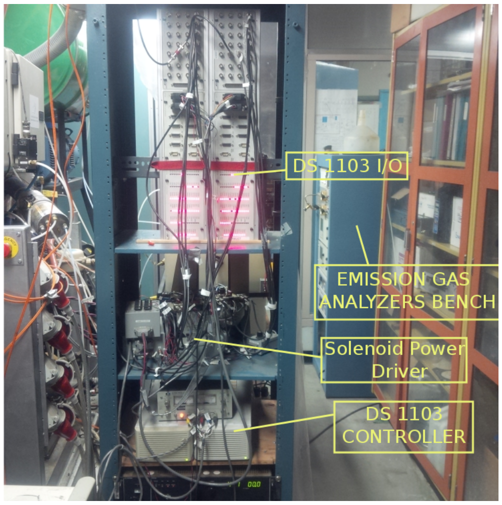

Figure 2.3: Photograph of the electromagnetic valve controllers, power electronics and power supplies

equipped with electromagnetic valves. To find combustion TDC, a cam signal is generated using a 2:1 gear reduction from a hall sensor. The dSPACE ControlDesk computer receives intake and exhaust manifold pressure and temperature data from ADAPT computer and combustion metrics from CAS computer at a rate of 100Hz used for controller design and implementation. All data from this system is logged on a per-cycle basis. Combustion timing and IMEP signals are fed from the CAS system into the dSPACE ControlDesk via A/D converter. The combustion timing and IMEP are calculated based on measured pressure trace. The dSPACE ControlDesk sets the valve timing and fueling rate according to the controller and feeds those as triggers to the ds1103 valve computers and fuel injectors. The ds1103 valve motion control program is written in C language [101], that measures the coil voltages, currents, flux linkage signals, pressure signal and executes the control algorithm at 50kHz while lower priority tasks such as communication with host is executed at 10kHz [101, 100]. The valve controllers maintain the commanded valve timing angle as they are triggered by the engine dSPACE MicroAutoBox controller. The engine has been designed as a free running engine to avoid piston valve contact for any commanded valve timing.

2.2 Electromagnetic valves

Intake and Exhaust valves are fully electromagnetic variable valve timing system developed by Daimler AG [102]. A schematic of the valve is shown in Figure 2.4 and a model of the valve is depicted in Figure 2.5. The valves consist of a hinged armature moved by opener and closer electromagnetic coils. Each valve have been equipped with a spring to keep the valve in middle position when the power is off. Two dSPACE ds1103 processors are used to control intake and exhaust timings independently on a cycle-by-cycle basis.

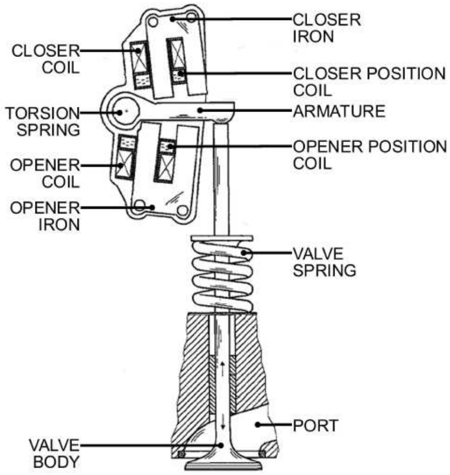

Figure 2.4: Schematic of the EVVT [102]

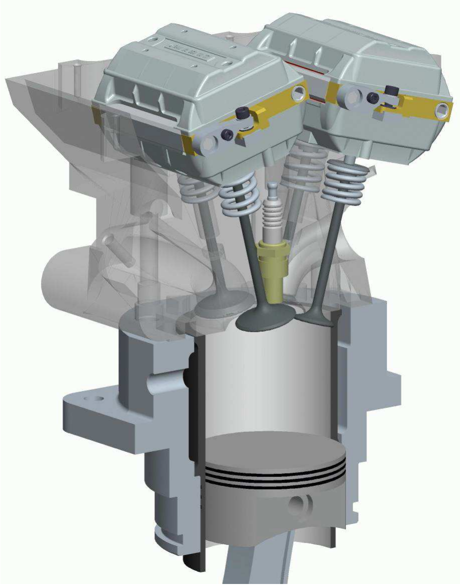

Figure 2.5: 3D model of the EVVT, each unit has 2 valves [101]

2.3 A&D ADAPT Data Acquisition System

The A&D Technologies Adapt system is used for the dynamometer control and data acquisition at a sampling rate of 10Hz from all the temperature and pressure sensors except the in-cylinder pressure. The dynamometer is an active type consisting of a 37 kW DC motor with a Eurotherm Drive 590+ drive controller in speed control mode. To measure the torque, an Interface Inc. SSMA-A-J-200N load cell mounted on the dynamometer is used. The Adapt computer is also used to control throttle body angle, supercharger, intake temperature, oil temperature, and coolant temperatures. The temperatures are measured with J and K type thermocouples, while the intake and exhaust manifold pressures are measured by Valedyne P305D pressure transducers. The oil and coolant temperatures are regulated by PI controllers using a liquid to water heat exchanger. The Adapt also collects data from the emissions bench which measures five exhaust gases. The emission gas analyzer bench measures the amounts of CO, $\mathrm{CO_2}$, $\mathrm{O_2}$, $\mathrm{NO_x}$ and unburnt hydrocarbons (HC) and the measurements are collected using ADAPT computer via an D/A link. The stream can be switched between the exhaust and the intake side for EGR measurement. Only, the exhaust side is measured for this study as no EGR is used. The emission gas analyzer information is available in [71].

2.4 A&D CAS Baseline System

The A&D Baseline CAS system is used for in-cylinder pressure as well as vibration sensor measurement. The pressure transducer is a water cooled Kistler 6061B piezoelectric sensor mounted in the cylinder head. The transducer is connected to a charge amplifier to amplify the signal before being sent to the CAS system. At every engine cycle the sensor voltage is pegged to the intake runner pressure at intake valve closing timing. The CAS system is triggered to measure based on a crank angle signal. A BEI Industries model XH25D-SS-3600-T2-ABZC-7272-SM18 encoder with 3600 pulses per revolution is used which results in cylinder pressure being collected every 0.1 CAD. The CAS computer calculates many combustion metrics such as θ_{50}, start of combustion, maximum rate of pressure rise, peak pressure, NMEP and IMEP. The CAS computer sends IMEP and combustion timing as feedback in real-time to dSPACE MicroAutoBox computer for engine control.

2.5 National Instruments

The National Instruments (NI) PCIe-6341 data acquisition card is used in conjunction with LabVIEW v9.0 graphical program for in-cylinder pressure measurement. The pressure trace and vibration sensor are recorded on a 0.1 CAD basis from 89.90 CAD bTDC of combustion to 90.1 CAD aTDC. The measured in-cylinder pressure with LabVIEW is scaled and calibrated using CAS in-cylinder pressure measurements. The LabVIEW computer was added as it has enough memory to record pressure traces up to 3000 cycles that is useful for cyclic variability analysis [103]. The program also monitors and records the vibration sensor data. Engine vibration is measured with a Bosch Model 261-230-120 vibration sensor which is mounted next to the cylinder jug [104].

Chapter 3

HCCI Combustion Analysis

Emission standards are becoming more stringent worldwide. EPA-420-F-051 requires that CO_2 (fuel efficiency) of the cars and trucks be improved to 163 g/mi (54.5 mpg) by 2025 [105]. Engine and automobile manufacturers are working on new technologies to achieve this. These technologies include hybrid and electric vehicles, fuel cells, alternative fuels (bio-fuels and natural gas), new combustion technologies such as Homogeneous Charge Compression Ignition (HCCI) and Reactivity Controlled Compression Ignition (RCCI) [106–108]. Among these technologies, HCCI/RCCI engines are of interest for fuel efficiency improvement in the next 15 years [108]. HCCI engines work with lean mixture and they produce low NO_X and particulate matter emissions. Spark Ignition and Diesel engines can run on HCCI mode with little to no modification and HCCI engines can operate with wide variety of fuels including bio-fuel [104, 109]. These characteristics make HCCI engines an attractive option for improving fuel economy and reducing emissions of the automobiles.

The objective of this chapter is to examine the effects of Variable Valve Timing (VVT) with Symmetric Negative Valve Overlap (SNVO) strategy on HCCI engine performance using Electromagnetic Variable Valve Timing (EVVT) as the actuator

[9, 100]. The effects of VVT on HCCI combustion timing, burn duration, thermal, combustion efficiency and emissions are detailed. Ringing intensity from cylinder pressure is calculated for each operating point to define the safe and high efficient engine operating range. It is found that with a proper valve timing, the exhaust emission is reduced, and the engine efficiency can be improved. This analysis indicates that VVT with SNVO strategy is an effective actuator for HCCI engine control.

3.1 Background

Although HCCI shows promise to improve engine fuel efficiency and reduce exhaust gas emission, it is necessary to understand the factors affecting thermal efficiency in HCCI to further improve HCCI engine fuel efficiency. Thermodynamically, thermal efficiency is a function of compression ratio, r_c, and the ratio of specific heats, k for an ideal Otto cycle as

$$\eta_{th} = 1 - \frac{1}{{r_c}^{k-1}} \tag{3.1}$$

To improve thermal efficiency, both ratio of specific heats and compression ratio can be increased. Combustion timing is found as the important factor affecting thermal efficiency [110]. Crank angle of 50% mass fraction burned, θ_{50} is used as combustion timing index in this study. Combustion timing directly changes the compression and expansion work. The expansion work is reduced by retarding θ_{50} after Top Dead Center (TDC) and the thermal efficiency is reduced as a consequence. Also θ_{50} before TDC, has negative effects on thermal efficiency since it increases the compression work. The possibility of ringing (knock) is high with advanced combustion timing is another issue. For higher thermal efficiencies, θ_{50} is required to occur about 6-8 CAD after TDC [111–113]. Another important factor that influences thermal efficiency is k, and this parameter depends on the mixture composition and temperature [7]. Combustion timing affects combustion efficiency [110] and consequently mixture composition and cycle temperature [112, 114]. Specific heat ratio, k decreases with higher cycle temperatures, and with higher trapped residual gas and fuel equivalence ratio. Lean mixtures with lower temperatures and less trapped residual gas tend to increase k and improve the thermodynamic efficiency [7, 112].

Combustion efficiency is improved by advanced θ_{50} and thermal efficiency is improved if θ_{50} is not advanced before TDC. At higher combustion efficiencies, the combustion is more complete and more CO is converted to CO_2 [7]. Combustion efficiency can be improved by trapping more residual gas inside the cylinder since it gives the unburned HC and CO remaining from the previous cycle a second chance to react [64]. Combustion timing affects the rate of heat transfer to the cylinder walls and engine thermal efficiency can be improved by reducing the heat transfer rate to the cylinder walls [115]. Cycle temperatures are increased by advancing the θ_{50} and it increases the rate of heat transfer. Heat transfer to the cylinder walls is mainly by convection in HCCI engines and compared to the conventional SI and Diesel engines, heat transfer in HCCI engines are lower due to low in-cylinder turbulence level and cycle temperatures [116].

In summary, combustion timing is a key parameter that directly or indirectly affects thermal efficiency in HCCI engines. To study the effects of θ_{50} on HCCI engine performance, NVO duration is changed at constant fueling rates. Exhaust emissions must also be considered. Effective strategies to further reduce CO and unburned HC emission in HCCI engines are required to meet the new emission regulations defined by EPA [117]. In this work it will be shown that that emissions can be reduced by combustion timing control using VVT with a Symmetric NVO strategy.

3.1.1 HCCI Engine – Thermal Efficiency

There have been several studies regarding how to improve HCCI thermal efficiency with combustion timing control. In [114], a Partial Fuel Stratification (PFS) method is used to reduce the rate of heat release and the maximum rate of pressure rise to improve thermal efficiency. In PFS strategy, 80% or more of the fuel is premixed and the rest of the fuel is directly injected into the combustion chamber in the latter part of the compression stroke. With PFS method, thermal efficiency is improved by advancing θ_{50} while keeping Ringing Intensity (RI) low. Primary Reference Fuel (PRF) with 2-ethylhexyl nitrate (EHN) and di-tert-butyl peroxide (DTBP) additives is used at boosted intake pressure in a Cummins B-series six-cylinder diesel engine working in HCCI mode. The study indicates that by optimizing fuel additive concentrations, boosting intake pressure and PFS strategy, engine efficiency is improved. The effects of fuel additives on emission shows that $\mathrm{NO_X}$ emission increases when EHN is used as fuel additive, however, the reported emission level is below the US2010 standard for most operating conditions studied in [114]. In [113], ethanol is used as fuel additive to gasoline in order to increase thermal efficiency in a single cylinder HCCI engine with a compression-ratio of 14:1 and boosted intake pressure. The study indicates that combustion timing is the key parameter that affects the engine thermal efficiency. The thermal efficiency is improved by advancing combustion timing, however, it is reduced when ringing happens at advanced combustion timings. The measurements in [113] show that PFS strategy with 10% ethanol as fuel additive at boosted intake pressures has significant effect on improving engine thermal efficiency. Using 10% ethanol in gasoline increases the high-load limit of boosted HCCI and the measured $\mathrm{NO_X}$ and soot emissions are well below US-2010 standards. In [118], it is found that HCCI engine thermal efficiency is improved by advancing the combustion timing to TDC at low loads. Intake temperature is increased as one strategy to advance combustion timing and consequently improving thermal efficiency. The other techniques used in this study are late fuel injection to stratify the mixture and use of throttler to reduce air flow rate and increase fuel equivalence ratio. In [119], intake pressure is boosted to increase the IMEP of a HCCI engine. This study indicates that under boosted conditions, the combustion timing can be retarded substantially for ringing control with good combustion stability. The effects of PFS on a boosted HCCI engine thermal efficiency are investigated in [32]. With PFS, rate of pressure rise is controlled by advancing combustion timing and advanced combustion timing improves the thermal efficiency.

In [120], effects of intake pressure, equivalence ratio, combustion timing and exhaust back pressure on a multi-cylinder HCCI engine performance and emissions are detailed. The study indicates that engine efficiency and output power are improved by advancing combustion timing at higher fuel equivalence ratios, however, output power and engine efficiency deteriorate for very advanced combustion timings due to higher heat loss and ringing. It is found that combustion timing has important effect on CO, unburned HC and $\mathrm{NO_X}$ emissions and the combustion efficiency deteriorates with retarding combustion timing. Engine power output and thermal efficiency are improved by boosting intake pressure with delayed combustion timing. $\mathrm{NO_X}$ and unburned HC emissions are reduced by boosted intake pressure however CO emission increases and a loss of combustion timing controllability is observed at ambient intake temperature. Exhaust back-pressure is used as a technique to lower intake temperature required for combustion timing control and this strategy shows little effect on engine output power, efficiency, ringing and CO emission. The study indicates that with higher exhaust back-pressure, $\mathrm{NO_X}$ and Unburned HC emissions are decreased. In [121], exhaust heat recovery system with wet ethanol (20% water) without intake air heating is used in a HCCI engine. The study indicates that the best operating conditions are obtained with exhaust heat recovery at high intake pressures and high equivalence ratios with delayed combustion timing. Since removing water from wet ethanol is not economical the study demonstrates that HCCI engine shows good performance with wet ethanol equipped with exhaust heat recovery system. In [122], delayed combustion timing at high fuel equivalence ratios, fuel stratification, double fuel injections and spark-assisted combustion are introduced as the main techniques that can be used to improve HCCI engine performance characteristics. The use of HCCI engines in advanced hybrid electric power-train is discussed and the analysis indicates that HCCI combined with electric power-train over the EPA urban and highway drive cycles enables significant fuel savings compared to SI and SI-electric hybrids. Diesel fueled HCCI is compared to n-butanol fueled HCCI in [123] and it is shown that the low reactivity of n-butanol gives better combustion timing controllabilty with high thermal efficiency. The higher load limit of HCCI is extended using n-butanol while the $\mathrm{NO_X}$ and soot emissions are kept ultra-low. Effects of EGR and intake manifold pressure on combustion timing, rate of pressure rise and emissions are detailed. It is shown that the engine emission is very sensitive to the intake manifold pressure at low to medium loads. N-butanol fueled HCCI does not need EGR for $\mathrm{NO_X}$ reduction in low to medium loads while EGR and boosted intake pressure are required to modulate combustion timing, lower the rate of pressure rise and improve the thermal efficiency at high loads.

Since these studies indicate that combustion timing has strong effect on HCCI engine performance and thermal efficiency, VVT with SNVO strategy is used for combustion timing control in this work. The effects of VVT with SNVO strategy on combustion timing and thermal efficiency are detailed with the evaluation of combustion efficiency and ringing intensity. For this analysis, SNVO duration is changed at constant fueling rate.

3.1.2 HCCI Engine – Combustion Timing

Crank angle of 50% fuel mass fraction burned, θ_{50} is used as combustion timing index in this study. Combustion timing is calculated based on the net heat release. The net heat release is calculated by integrating rate of heat release during combustion. The rate of heat release is calculated using a single zone model [7] as

$$\frac{dQ_{HR}}{d\theta} = \frac{1}{k-1} V \frac{dP}{d\theta} + \frac{k}{k-1} P \frac{dV}{d\theta} + \frac{dQ_{HT}}{d\theta} \tag{3.2}$$

where k is the specific heat ratio and P and V are the in-cylinder pressure and volume respectively. The gas to wall heat transfer, Q_{HT} is calculated using modified Woschni heat transfer model [124]. The net heat release is calculated as

$$Q_{HR} = \int_{\theta_1}^{\theta_{99}} \left(\frac{dQ_{HR}}{d\theta} \right) d\theta \tag{3.3}$$

where θ_1 and θ_{99} are defined as the crank angles for 1%, and 99% mass fraction burned respectively (HCCI combustion indexes are detailed in Appendix A).

The single zone model is first validated against the model developed for predicting combustion timing in [125]. The method developed in [125] is based on the in-cylinder pressure measurement and is a very accurate graphical method. Figure 3.1 shows pressure versus volume in log-log scale for the operating point listed in Table 3.2 with a constant injected fuel energy of $\mathrm{Em}_{\mathrm{finj}} = 0.42\frac{\mathrm{kJ}}{\mathrm{Cycle}}$. The compression and expansion lines are extended to the TDC cylinder volume, p_1 and p_3 as shown in Figure 3.2.

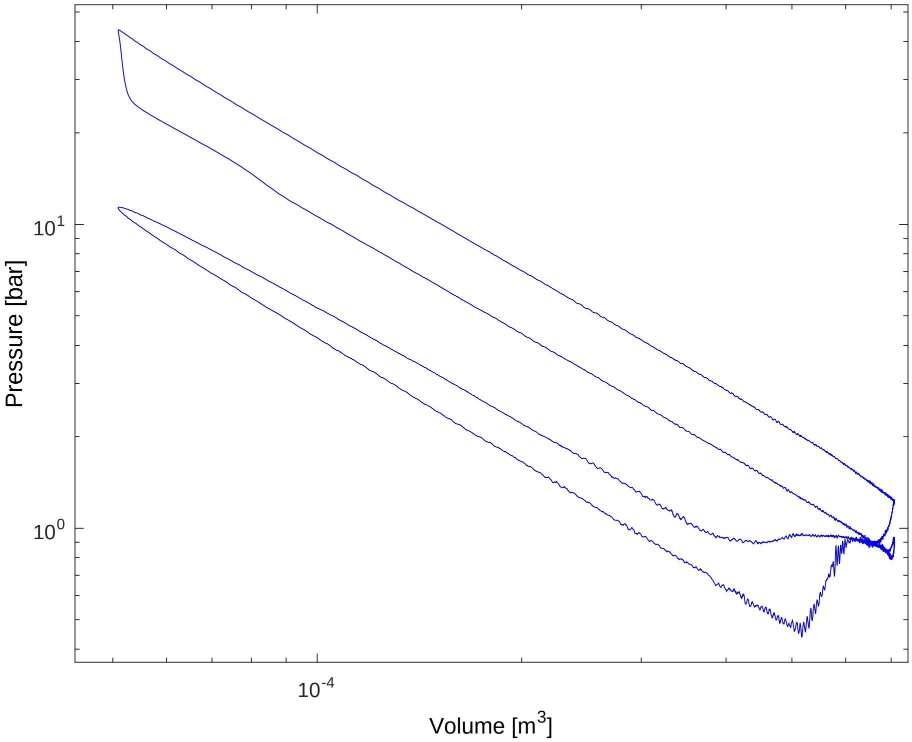

Figure 3.1: Pressure versus in-cylinder volume in log-log scale for the operating point listed in Table 3.2

Polytropic compression and expansion are shown as straight lines in Figure 3.1.

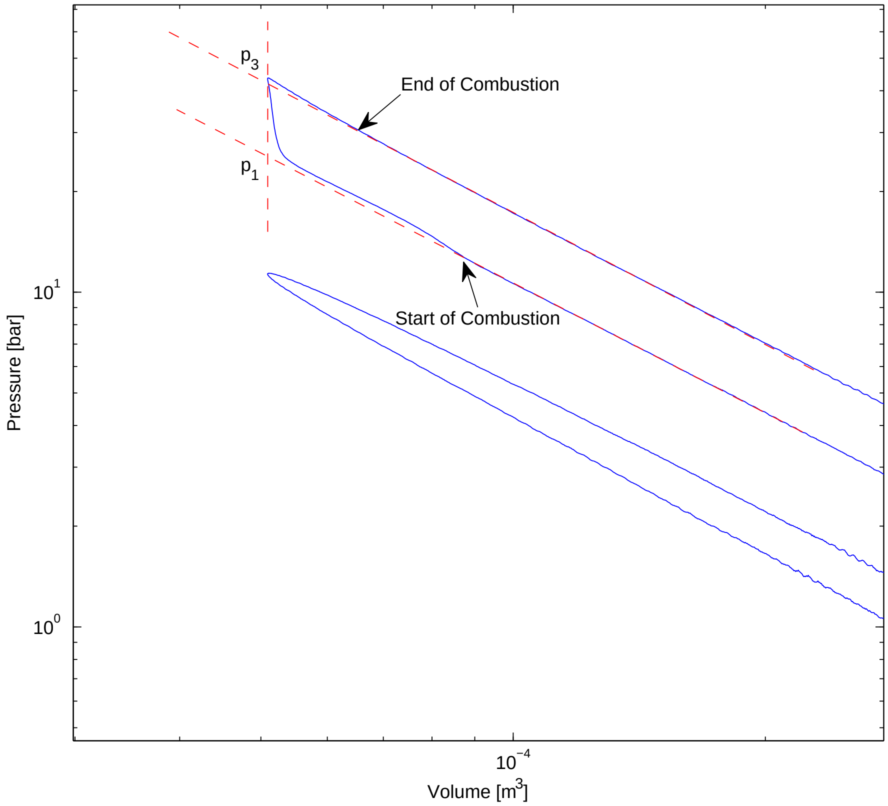

Figure 3.2: Zoom of pressure versus in-cylinder volume in log-log scale for the operating point listed in Table 3.2

At the end of compression stroke, the line begins to rise slowly due to start of Low Temperature Reactions (LTR) (see Figure 3.2). This point is considered as the start of combustion. The blue line is the actual pressure and the red dashed line shows the theoretical HCCI cycle. The HCCI cycle pressure is defined [126] as

$$p_2(\theta) = p(\theta)\left(\frac{V(\theta)}{V_c}\right)^{n(\theta)} \tag{3.4}$$

where $p(\theta)$, $V(\theta)$ and V_c are the measured in-cylinder pressure, in-cylinder volume and clearance volume respectively. To calculate the HCCI cycle pressure values in eqn. 3.4, the polytropic coefficient $n(\theta)$ is required. Before TDC, the poly-tropic coefficient is determined based on the compression line slope and after TDC the poly-tropic coefficient is determined based on the expansion line. The fuel mass fraction burned is calculated as

$$MFB(\theta) = \frac{p_2(\theta) - p_1}{p_3 - p_1} \tag{3.5}$$

The mass fraction burned for the pressure trace in Figure 3.1 is shown in Figure 3.3. Figure 3.3 compares the normalized mass fraction burned calculated from the single zone model and the graphical method developed in [125] for the operating point listed in Table 3.2. To check the single zone model against the graphical model for θ_{50} all measured operating points are shown in Figure 3.4. The operating points examined in this study are listed in Table 3.1. The maximum difference between the single zone model and the graphical method in predicting combustion timing is 0.8 crank angle degree. This indicates that single zone model is accurate enough for predicting combustion timing (θ_{50}) and the heat transfer model is sufficient.

Parameter	Values
Engine Speed [rpm]	725 - 825
T_{Intake} [$^{\circ}C$]	80
P_{Intake}[kPa]	88 - 90
Injected Fuel Energy	0.356 - 0.495
$T_{Coolant}$ [$^{\circ}C$]	50
Oil temperature [$^{\circ}C$]	50
ON [PRF]	0
EVC [bTDC]	-360° - -270°
IVO [bTDC]	270° - 360°
EVO [bTDC]	-180°
IVC [bTDC]	180°

Table 3.1: Engine Operating Conditions

$T_{coolant}$ [$^{\circ}C$]	50
T_{oil} [$^{\circ}C$]	50
T_{int} [$^{\circ}C$]	80
ω [RPM]	820
Injected Fuel Energy [kJ]	0.42
ON [-]	0
EVC [bTDC]	-320°
IVO [bTDC]	320°
EVO [bTDC]	-180°
IVC [bTDC]	180°

Table 3.2: Engine Operating Condition

$T_{coolant}$ [$^{\circ}C$]	50
T_{oil} [$^{\circ}C$]	50
T_{int} [$^{\circ}C$]	80
ω [RPM]	809
Injected Fuel Energy [kJ]	0.49
ON [-]	0
EVC [bTDC]	-360°
IVO [bTDC]	360°
EVO [bTDC]	-180°
IVC [bTDC]	180°

Table 3.3: Engine Operating Conditions

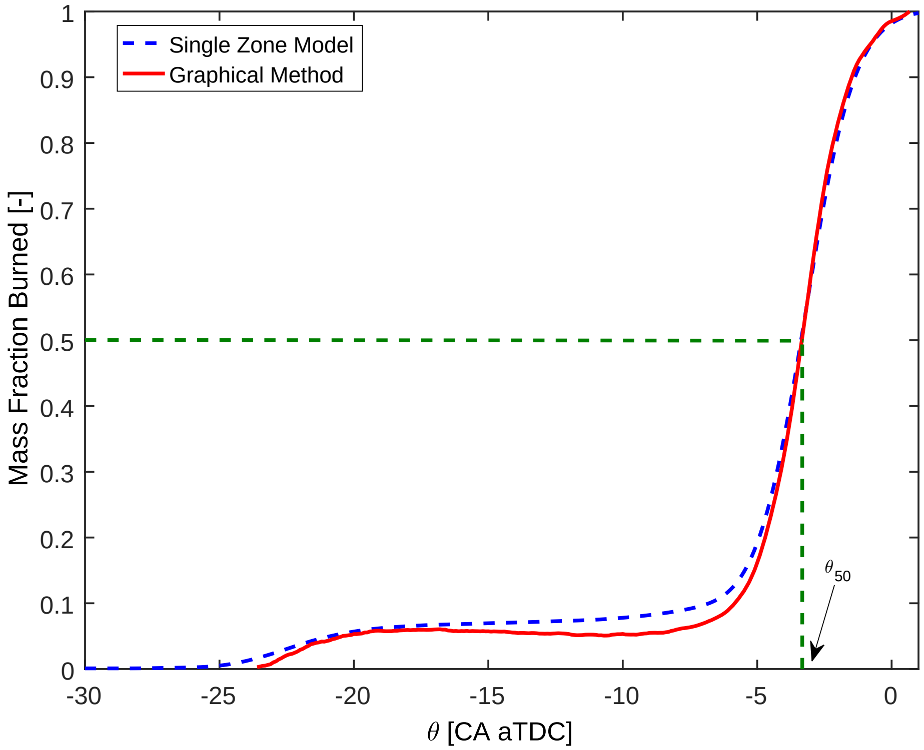

Figure 3.3: Mass fraction burned - comparison between the single zone model and the graphical method for the operating point summarized in Table 3.2

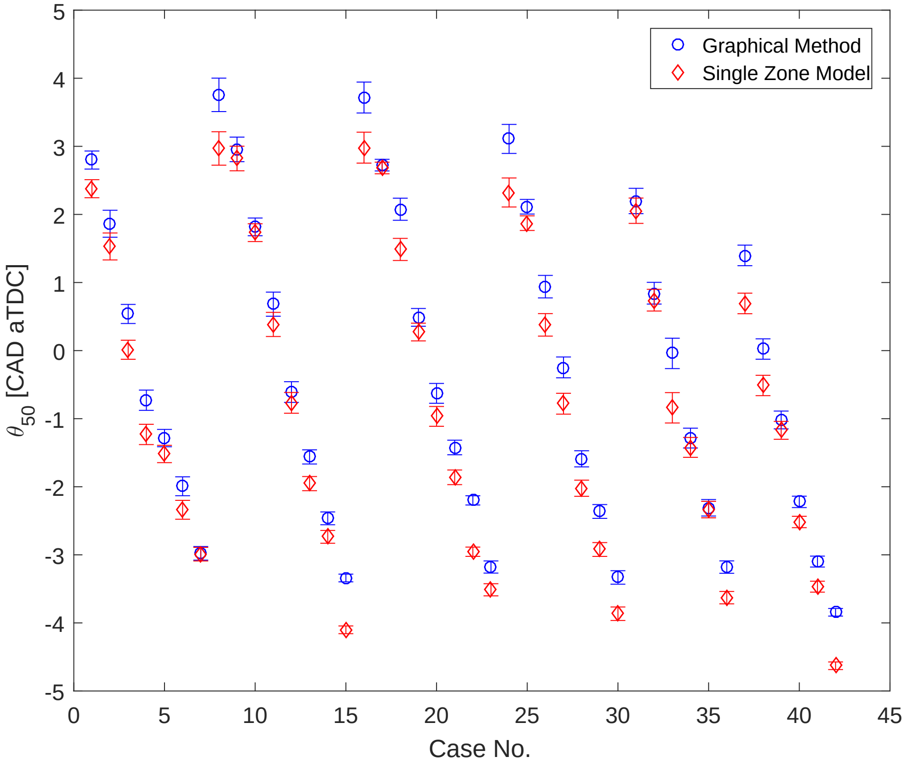

Figure 3.4: Combustion timing - comparison between the single zone model and the graphical method (operating conditions listed in Table 3.1)

3.1.3 HCCI Combustion – Ringing (Knock)

The maximum load of HCCI engine is often limited by ringing [12]. Ringing is different from SI engine knock that is caused by end-gas auto-ignition in front of the flame front (see Figure 3.5). When knock happens in SI engines, pressure pulses are generated and these high pressure pulses can cause damage to the engine that are quite often in the audible frequency range [7]. In HCCI, combustion starts with the random multi-point auto-ignition in the combustion chamber (see Figure 3.6) [1]. Ringing in HCCI occurs as a result of excessive pressure rise and heat release rates [127]. The HCCI ringing is induced by the significant difference of High Temperature Oxidation (HTO) and Low Temperature Oxidation (LTO) regions and their interactions [128]. Unbalanced pressures in the cylinder from the uneven combustion initiation results in oscillating pressure waves. As the fueling rate is increased, the potential for spatial variations in the trapped mixture grows, leading to higher pressure oscillations similar to the knock in SI engines [128–130]. Ringing increases the heat loss to the cylinder walls since it breaks the thermal boundary layer [131] and reduces the thermal efficiency and could damage the engine that should be avoided.

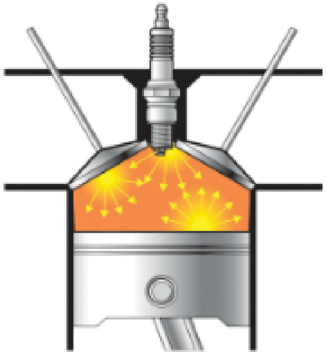

Figure 3.5: SI Knock [132]

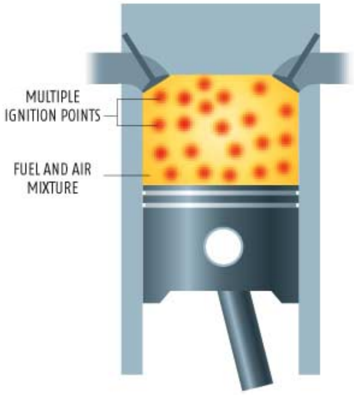

Figure 3.6: HCCI combustion [133]

The ringing intensity correlation developed in [134] is used for HCCI ringing analysis. The model first is compared against the previously developed ringing index developed in [129]. The ringing intensity correlation used in this analysis is detailed in [134] and is calculated as

$$RI = \frac{1}{2\gamma}\frac{\left(\beta\left(\frac{dP}{dt}\right)_{max}\right)^2}{P_{max}}\left(\gamma R T_{max}\right)^{\frac{1}{2}} \tag{3.6}$$

where P_{max} [MPa], T_{max} [K] and $\left(\frac{dP}{dt}\right)_{max}$ [$\frac{\mathrm{MPa}}{\mathrm{S}}$] are the maximum cycle pressure, temperature and the maximum rate of pressure rise respectively. All parameters in eqn. 3.6 can be directly measured or calculated except β. The β relates the pressure pulsation amplitude to the maximum rate of pressure rise and is tuned from the experimental data. The factor β is set to 0.05 ms for this study. The Ringing Intensity RI in eqn. 3.6 has units of $\frac{\mathrm{MW}}{\mathrm{m}^2}$ which is an index developed based on the acoustic energy of the resonating pressure wave [112].

The ringing index developed in [129] is based on the Root Mean Square (RMS) of the measured pressure. The RMS of the pressure is calculated as

$$P_{RMS} = \left(\frac{1}{N} \left[\hat{P} . \hat{P} \right] \right)^{\frac{1}{2}} \tag{3.7}$$

where $\hat{P}$ is the filtered pressure trace. A 10th order Chebyshev Type II bandpass filter with a pass band of 3-10 kHz is used to filter the pressure trace and the N is the number of collected pressure points. Figure 3.7 shows HCCI engine pressure trace with ringing (the pressure oscillations after TDC) for the operating condition listed in Table 3.3. The RMS of the pressure signal spectrum is shown in Figure 3.8 and the first large peak of the RMS occurs near 6.5 kHz. This frequency is defined as the first oscillation frequency in [129]. The ringing index is defined as [129]

$$K_{RMS} = \left(\frac{\Sigma_L^H P_{RMS}}{H - L} \right)^{\frac{1}{2}} \tag{3.8}$$

where L and H are beams corresponding to 3 and 10 kHz respectively.

The ringing intensity values explained in eqn. 3.6 are compared to the the ringing index in eqn. 3.8 and the results are shown in Figure 3.9. Both ringing intensity indexes increase with increasing maximum rate of pressure rise.

3.2 SNVO Effects on HCCI Combustion

Effects of NVO duration on HCCI combustion at constant injected fuel energies are investigated first. A table listing the experimental points is given in Appendix

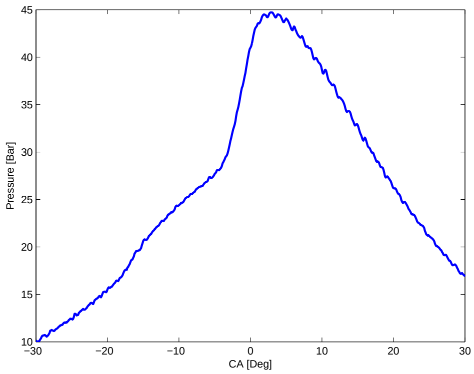

Figure 3.7: Pressure trace for HCCI with ringing for the operating point listed in Table 3.3

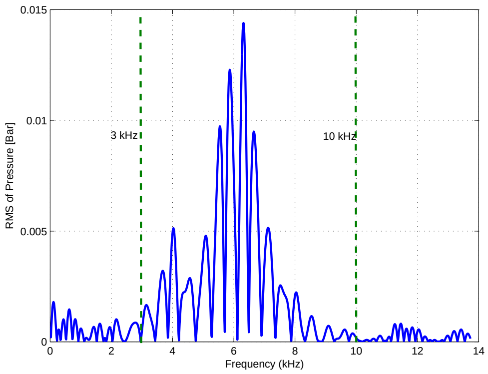

Figure 3.8: P_{RMS} for pressure trace with ringing for the operating point listed in Table 3.3

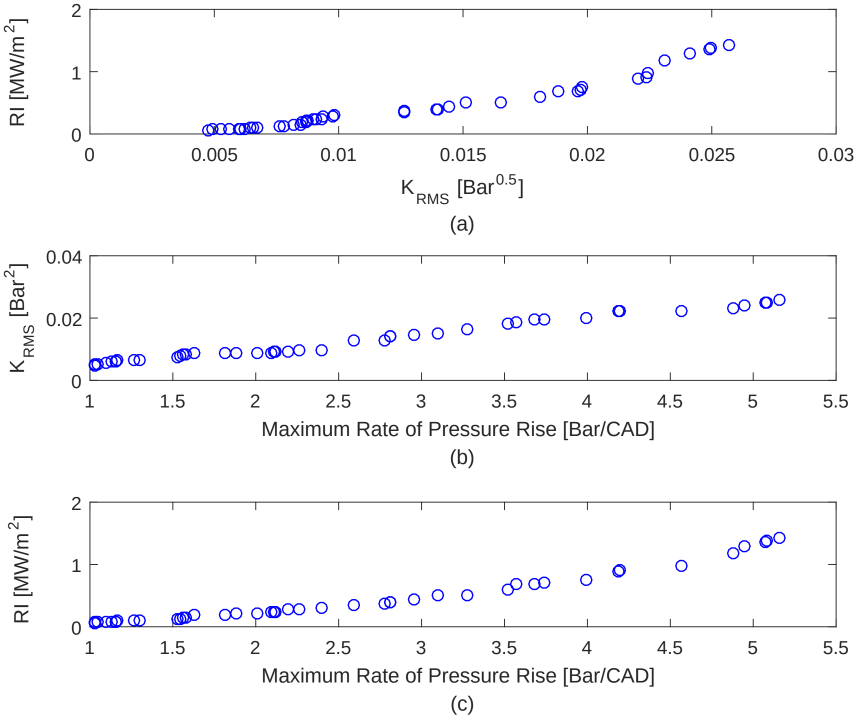

Figure 3.9: (a) Ringing Intensity versus K_{RMS}, (b) K_{RMS} versus Maximum Rate of Pressure Rise and (c) Ringing Intensity versus Maximum Rate of Pressure Rise for the operating points summarized in Table 3.1

B. Figure 3.10(a) shows effects of NVO duration on combustion timing at constant injected fuel energies. The combustion timing is advanced by increasing the

NVO duration. More residual gas is trapped by increasing the NVO duration and the trapped charge temperature at IVC is increased (see Figure 3.10(b)). The IVC temperature, T_{IVC} is calculated [13, 135] as

$$T_{IVC} = x_r T_{res} + (1 - x_r) T_{int} \tag{3.9}$$

where T_{res}, T_{int} and x_r are residual gas temperature, intake charge temperature and residual gas fraction respectively. It is assumed that the specific heat values of the intake charge, residual gas and the trapped charge at the beginning of compression are almost equal [135]. Residual gas fraction, x_r is calculated [135] as

$$x_r = \frac{m_{res}}{m_{res} + m_{int}} \tag{3.10}$$

where m_{int} and m_{res} are inducted fresh charge mass and trapped residual gas mass from the previous cycle respectively. The m_{int} and m_{res} are calculated using ideal gas law [42, 135, 136] as

$$m_{int} = \frac{\eta_v P_{int} \left(V_{IVC} - V_{EVC}\right)}{R T_{IVC}} \tag{3.11}$$

$$m_{res} = \frac{P_{exh} V_{EVC}}{R T_{res}} \tag{3.12}$$

where P_{int}, P_{exh}, V_{IVC}, V_{EVC} and R are the intake manifold pressure, exhaust manifold pressure, in-cylinder volume at EVC and IVC and specific gas constant respectively. The volumetric efficiency, η_v is calculated based on the method explained in [137]. HCCI combustion is highly sensitive to the IVC temperature, and combustion timing is advanced with an increase in the IVC temperature [1, 13, 64, 138].

Figure 3.11(a) shows equivalence ratio based on total charge mass versus NVO duration at constant injected fuel energies. This equivalence ratio is referred as the charge-mass equivalence ratio [112] and is calculated as

$$\phi = \frac{\left(\frac{F}{C}\right)}{\left(\frac{F}{A}\right)_{stoich}} \tag{3.13}$$

where $\frac{\mathrm{F}}{\mathrm{C}}$ is the ratio of the trapped fuel mass to the total trapped charge, and the $\left(\frac{\mathrm{F}}{\mathrm{A}}\right)_{\mathrm{stoich}}$ is the fuel-air stoichiometric ratio. This definition helps to understand the effects of valve timing on the amount of fuel trapped inside the cylinder. As shown in Figure 3.11(a), the charge-mass equivalence ratio is reduced when NVO duration increased and it means that less fuel is trapped at higher NVO durations. Figure 3.11(b) shows λ measured from the wide band oxygen sensor versus NVO duration at constant injected fuel energies. The measured λ is based on oxygen concentration in the exhaust. At higher NVOs, λ is reduced as shown in Figure 3.11(b). The reason is the air mass flow rate is reduced at higher NVOs while fueling rate remains constant.

Figure 3.12 shows that burn duration is reduced by advanced combustion timing at higher NVO durations and for the operating points that combustion timing occurs after TDC, the burn duration is longer. The effect of burn duration on ringing intensity at constant fueling rates is shown in Figure 3.13. Ringing intensity increases when burn duration is reduced at constant fueling rates. The reason is that by reducing the burn duration, more energy is released at short period of time and it increases the ringing intensity. Figure 3.14(a) shows effects of NVO duration on maximum rate of pressure rise. As shown in this figure, maximum rate of pressure rise is increased by increasing NVO duration. This is attributed to the advanced combustion timing at higher NVO durations and since combustion timing occurs before TDC for most of the measured points the rate of pressure rise increases.

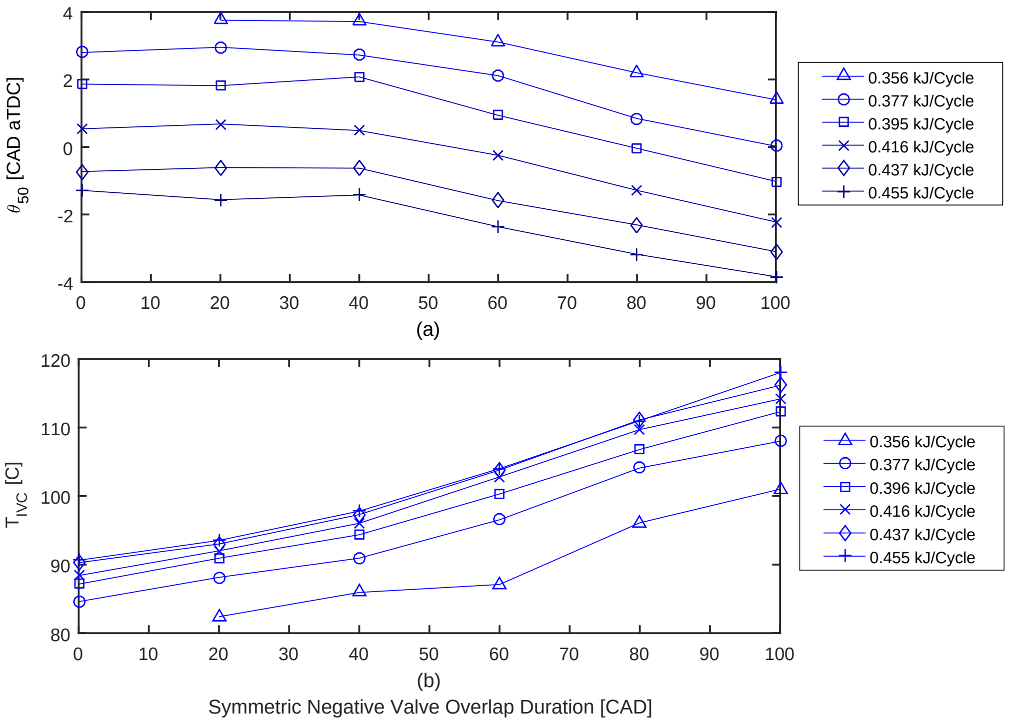

Figure 3.10: Effects of NVO on (a) Combustion timing and (b) IVC temperature at constant injected fuel energies

Figure 3.14(b) confirms this and it shows that the ringing intensity calculated from eqn. 3.6 is increased at higher NVO durations.

Figure 3.15 shows effects of valve timing on in-cylinder temperature, pressure and rate of heat release for constant injected fuel energy of 0.455 $[\frac{\mathrm{kJ}}{\mathrm{Cycle}}]$. As shown in Figure 3.15(c), the rate of heat release has two stages. The early heat release starts around 20 Deg CA bTDC and is due to Low Temperature Reactions (LTR) and the main combustion occurs around 8 Deg CA bTDC and it is due to the High Temperature Reactions (HTR) [1]. Both LTR and HTR are advanced at higher NVOs and since combustion occurs before TDC the maximum rate of pressure rise is increased as well as the maximum in-cylinder pressure. The rate of pressure rise

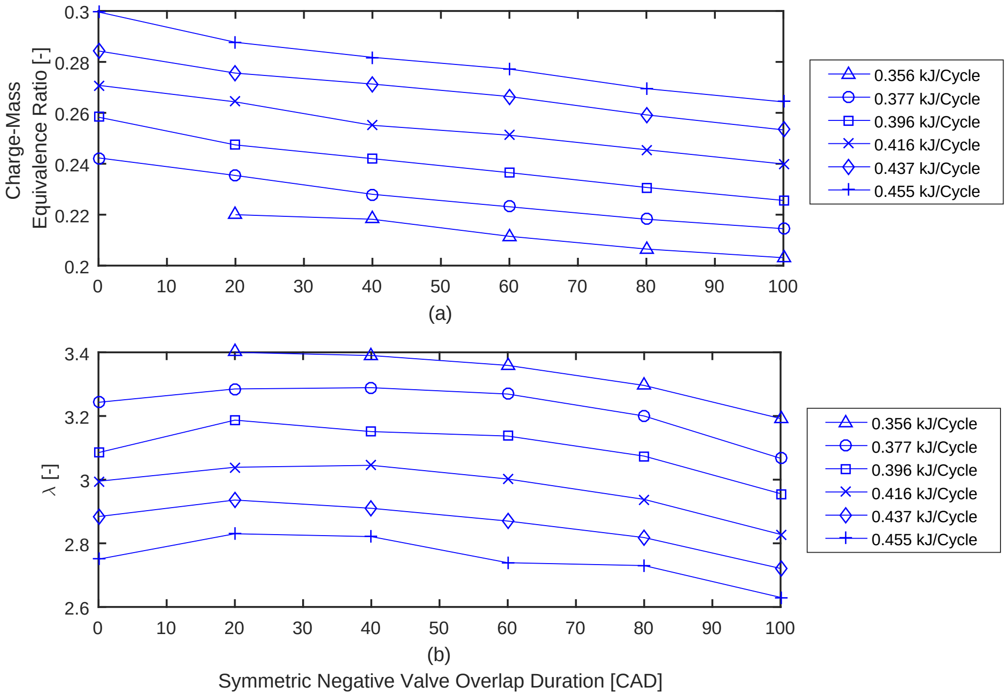

Figure 3.11: Effects of NVO on (a) Charge-mass fuel equivalence ratio and (b) measured λ at constant injected fuel energies

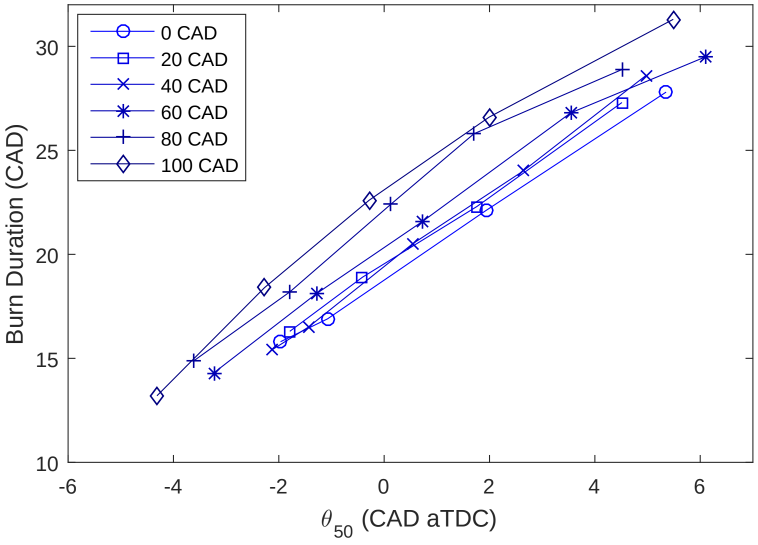

Figure 3.12: Burn duration versus combustion timing at constant NVO durations

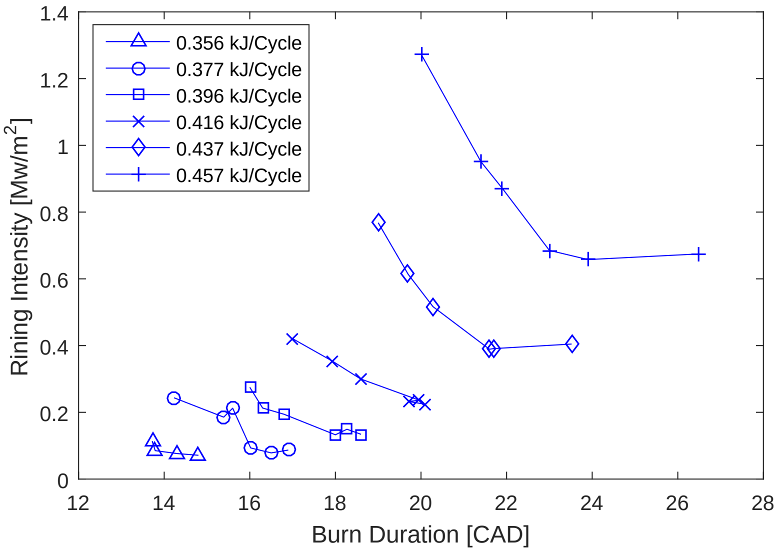

Figure 3.13: Effects of burn duration on ringing intensity at constant injected fuel energies

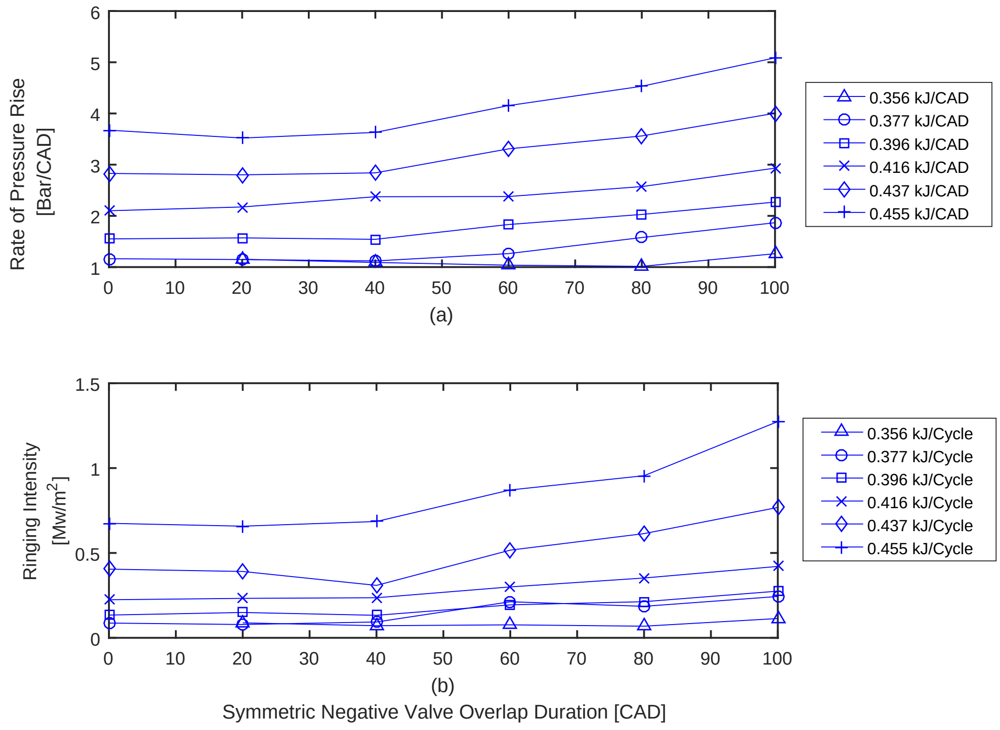

Figure 3.14: Effects of NVO on (a) maximum rate of pressure rise and (b) ringing intensity at constant injected fuel energies

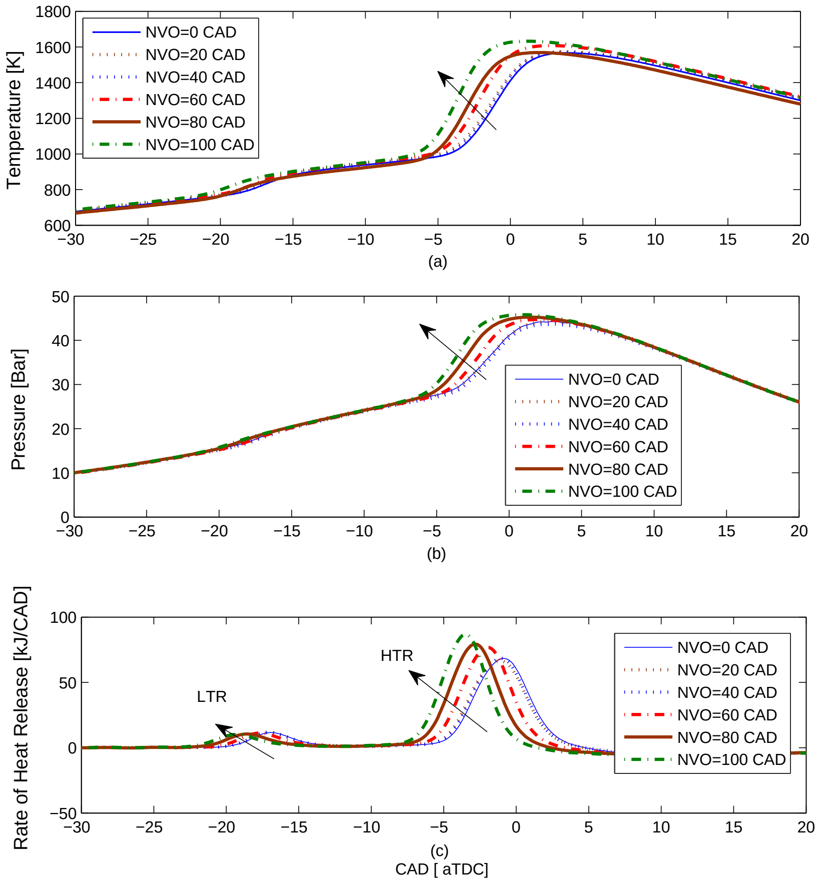

Figure 3.15: Effects of NVO duration on (a) temperature, (b) pressure and (c) rate of heat release (calculated from eqn. 3.2) at constant injected fuel energy ($\mathrm{Em}_{\mathrm{finj}}$=0.4560 [kJ/Cycle])

is reduced by an increase in NVO duration if the dilution effect becomes dominant and combustion timing happens after TDC [139]. An increase in NVO duration does not significantly affect the LTR duration, but does reduce the HTR duration and consequently the total burn duration as shown in Figure 3.12 and Figure 3.15(c).

The effects of NVO duration on the engine brake thermal efficiency at constant injected fuel energies is investigated next. The brake thermal efficiency calculation is explained in chapter 4 section 4.2. As shown in Figure 3.16(a), brake thermal efficiency improves significantly at low injected fuel energies when NVO duration is increased. It means that for low loads, running on higher NVOs is preferred. At high injected fuel energies, brake thermal efficiency is not sensitive to NVO duration. Figure 3.16(b) shows effects of combustion timing on brake thermal efficiency. Brake thermal efficiency is a strong function of compression ratio and in-cylinder gas properties. Combustion timing changes the effective expansion ratio and consequently the brake thermal efficiency. By retarding the combustion timing after TDC, brake thermal efficiency is deteriorated as the expansion ratio is decreased. The optimum brake thermal efficiency is obtained when combustion timing advances to TDC [112]. The reason is burn duration in HCCI is short and when combustion timing occurs near TDC then the engine cycle is very closed to ideal Otto cycle. These results are consistent with [113], as indicates there is little potential benefit for advancing θ_{50} to TDC without ringing, since the piston motion per crank angle degree is small near TDC, and heat transfer losses increases.

Figure 3.17(a) shows effects of NVO duration on combustion efficiency at constant injected fuel energies. Combustion efficiency calculation is detailed in chapter 4 section 4.2. Combustion efficiency improves considerably by increase in NVO durations for low injected fuel energies. For high injected fuel energies, combustion efficiency is not affected by the NVO duration. Combustion timing is advanced at higher NVO durations and it gives enough time for combustion to proceed. Combustion efficiency is deteriorated when combustion timing happens after TDC. With late combustion timing, in-cylinder gas temperature is reduced during expansion which terminates reactions earlier. Figure 3.17(b) shows thermal efficiency versus combustion efficiency at constant NVO durations. As shown in this figure, thermal efficiency is linearly correlated with combustion efficiency at constant NVO. Ther-

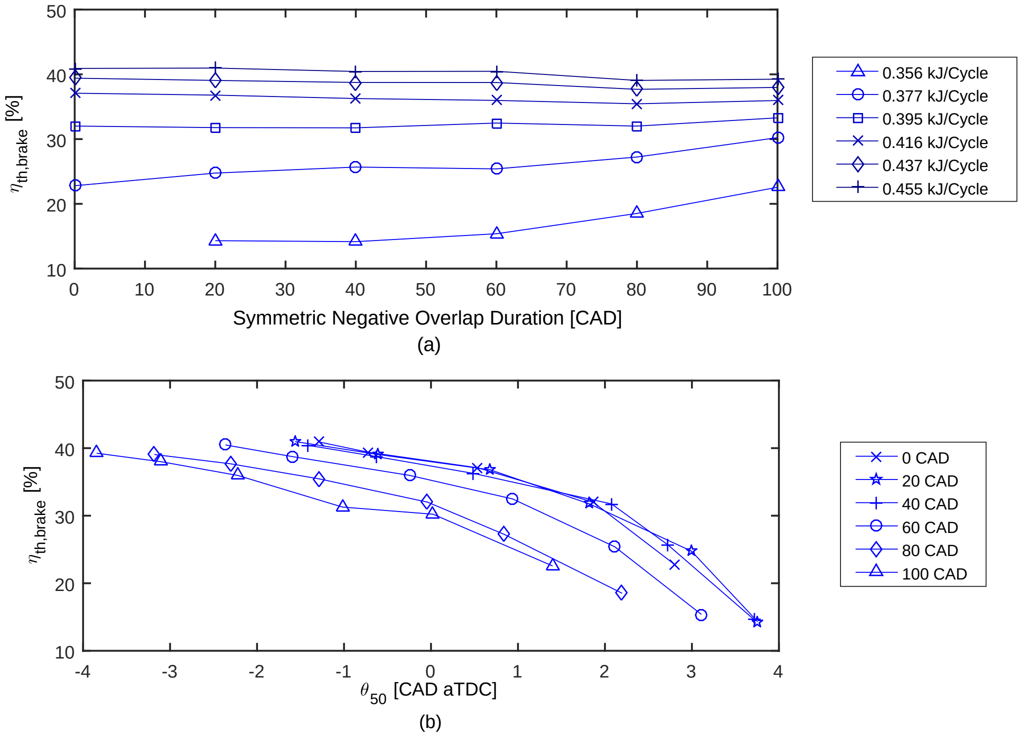

Figure 3.16: (a) Effects of NVO duration on thermal efficiency at constant injected fuel energies (b) Thermal efficiency versus combustion timing at constant NVO durations

mal efficiency is slightly reduced for combustion efficiencies higher than 80%. The reason is combustion timing to occur before TDC (for these operating points) that increase the compression work and consequently reduces the thermal efficiency. Figure 3.18(a) shows effects of valve timing on IMEP at constant injected fuel energies. As shown in this figure, IMEP is improved at higher NVOs specifically at low loads. The reason is combustion efficiency is improved at higher NVOs (see Figure 3.17(a)) and more energy is released during combustion.

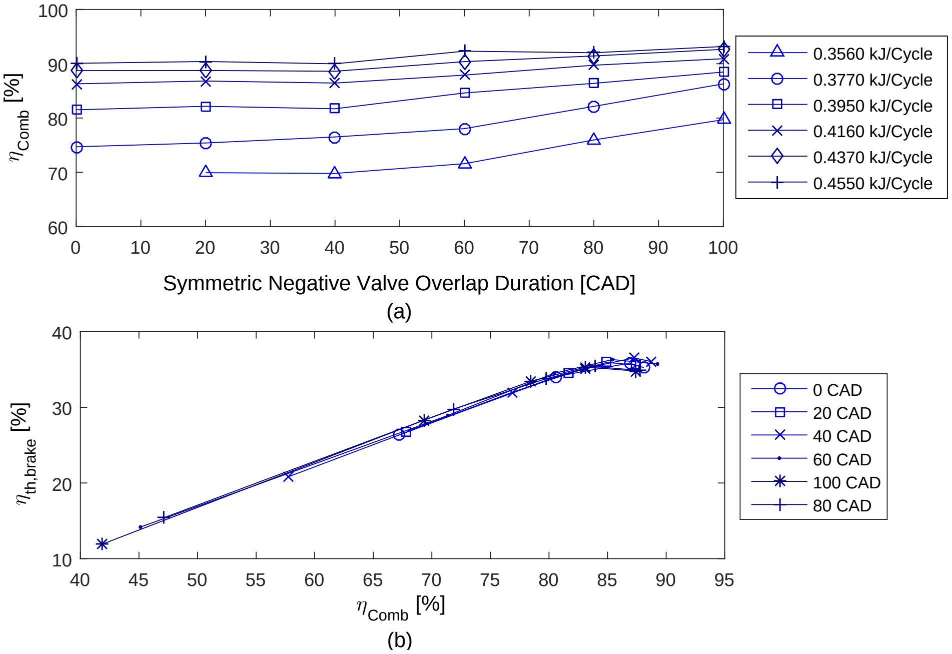

(a)

(b)

Figure 3.17: (a) Effects of NVO duration on combustion efficiency at constant injected fuel energies (b) Thermal efficiency versus combustion efficiency at constant NVO durations

3.3 SNVO Effects on HCCI Emission

Exhaust emissions are another factor that must be considered for HCCI engine control. The major HCCI engine emissions are CO and unburned HC [1] and these emissions can be controlled using different actuators, strategies and components such as an oxidation catalyst [10], EGR and fuel Octane number [11]. Effects of NVO duration on HCCI engine emission are explained in this study. NVO effects on engine emission are studied for three different injected fuel energies. 16 points are measured for emission analysis and the experimental conditions are summarized in Table 3.4. A detailed list of operating points are given in Appendix C. Figure 3.19 shows effects of NVO duration on CO, CO_2 and unburned HC emissions. A decrease in CO emission is observed in Figure 3.19 when NVO duration is increased

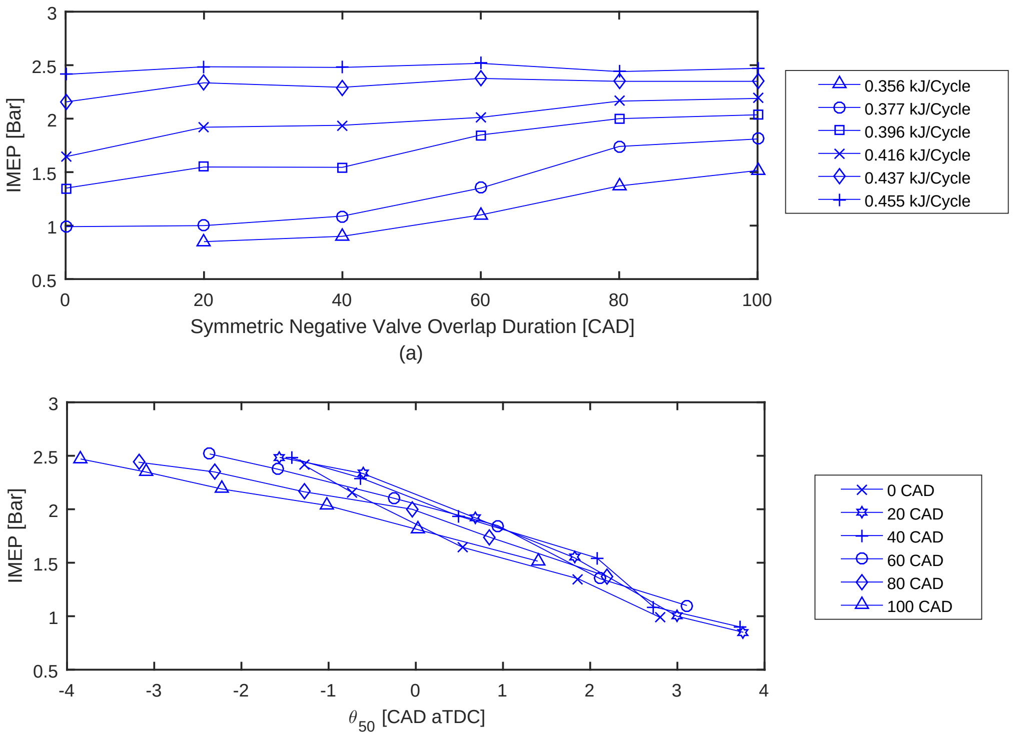

(a)

(b)

Figure 3.18: (a) Effects of NVO duration on IMEP at constant injected fuel energies (b) IMEP versus combustion timing at constant NVO durations

at constant injected fuel energies. CO is reduced as combustion efficiency is improved by increasing NVO duration. Enhanced combustion efficiency promotes the oxidation of CO to $\mathrm{CO_2}$ as shown in Figure 3.19. Due to low combustion temperature, $\mathrm{NO_X}$ emissions are low, near the instrument resolution of 10 ppm so is not reported.

3.4 Discussion

Combustion timing plays important role on HCCI combustion characteristics, engine ringing and emission. The technology drawbacks for HCCI are the requirement for combustion timing control, the high CO and unburned hydrocarbon emissions and the narrow load-speed operating range. To overcome these issues, tech-

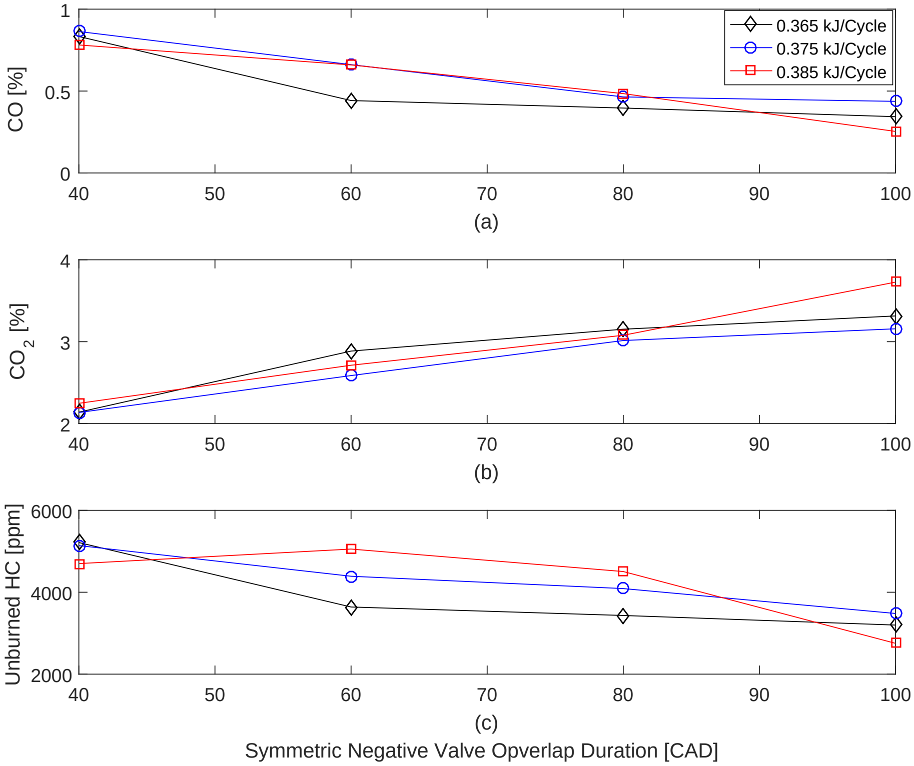

Figure 3.19: Effects of NVO duration on (a) CO, (b) CO_2 and (c) Unburned Hydrocarbon emissions at constant injected fuel energies

Parameter	Values
Engine Speed [rpm]	725-825
T_{Intake} $[^{\circ}C]$	80
P_{Intake}[kPa]	88-90
ϕ	0.26-0.46
$T_{Coolant}$ $[^{\circ}C]$	50
Oil temperature $[^{\circ}C]$	50
ON [PRF]	0
NVO [CAD]	40-100 CAD
Fueling rate [kJ per cycle]	0.3-0.4

Table 3.4: Engine Operating Conditions

niques like VVT with SNVO are used. The EVVT system is used to modulate the amount of trapped residual gas cycle by cycle for combustion timing control. SNVO gives good command for combustion timing control as detailed in this chapter. Effects of NVO duration on engine energy distribution is detailed in next chapter.

Chapter 4

HCCI Engine Energy Distribution[1]

The effects of NVO duration on HCCI engine energy distribution and waste heat recovery are investigated using VVT with SNVO strategy. This analysis is based on experimental data and helpful for engine control around its optimum operating condition (higher thermal efficiencies and lower emissions). Exergy analysis is performed to understand the relative contribution of different loss mechanisms in HCCI engines and how VVT changes these contributions. The results indicate that VVT with SNVO is an effective actuator for combustion and CHP first and second law efficiency improvement, specifically at low injected fuel energies. Combustion efficiency has an important role in HCCI engine energy distribution and the CHP power to heat ratio is improved as combustion efficiency improves. Brake thermal efficiency is improved at higher combustion efficiencies for appropriate combustion timings. Incomplete combustion is one major source of energy losses in HCCI engines. Power to energy loss ratio is defined for energy distribution analysis in HCCI engines as it includes fraction of the fuel energy lost due to incomplete combustion. Higher power to energy losses ratios are obtained at higher combustion efficiencies where combustion timings are near TDC.

---

[1] This chapter is based on [43]

4.1 Background – HCCI Exergy

Micro Combined Heat and Power (CHP) is an effective technology for generating heat and electricity in residential buildings [140]. This technology can replace the conventional heating boilers to provide heat and hot water and the majority of the building electricity [141]. Micro CHP plants are mainly used in countries that have high electricity prices and where CO_2 emission reduction is of concern [140, 141]. HCCI engines present a new opportunity for the micro CHP market since these engines are fuel efficient and can work with wide variety of fuels including natural gas and biofuels [142]. The potential for HCCI-CHP has not been studied while CI and SI have been [143–152]. HCCI combined with VVT actuation is flexible enough to examine the potential of HCCI-CHP systems. VVT has been used for combustion timing control extensively [18, 22, 42] but there is no literature on the effects of VVT on HCCI engine energy distribution. In this work, the effects of VVT on engine energy distribution are detailed experimentally for the first time. The results indicate VVT is an effective actuator for combustion and CHP first and second law efficiency improvement, specifically at low injected fuel energies.

Existing internal combustion engines micro CHP units generate power in a range of 1-100 kW and are used mainly for residential and commercial buildings [140]. Micro CHP systems can also be integrated with turbines and fuel cells as the power source [140, 153]. Compared to internal combustion engines, fuel cells have a higher efficiency and they do not produce NO_X and particulate matter emissions. CHP units with fuel cells are being tested, mainly in Japan and Germany, but have the disadvantage of high capital costs [140]. Turbines are typically used for micro CHP systems with 30-200 kW output which is suitable for commercial buildings [140]. The turbine micro CHP units are slower to start and ramp to full load compared to internal combustion engines [140, 141, 154]. Although the internal combustion engines maintenance costs are higher than comparable gas turbines, the maintenance can be handled by in-house staff or local service organizations [155]. The micro CHP systems with internal combustion engine are currently the most economical option due to their lower capital costs [155].

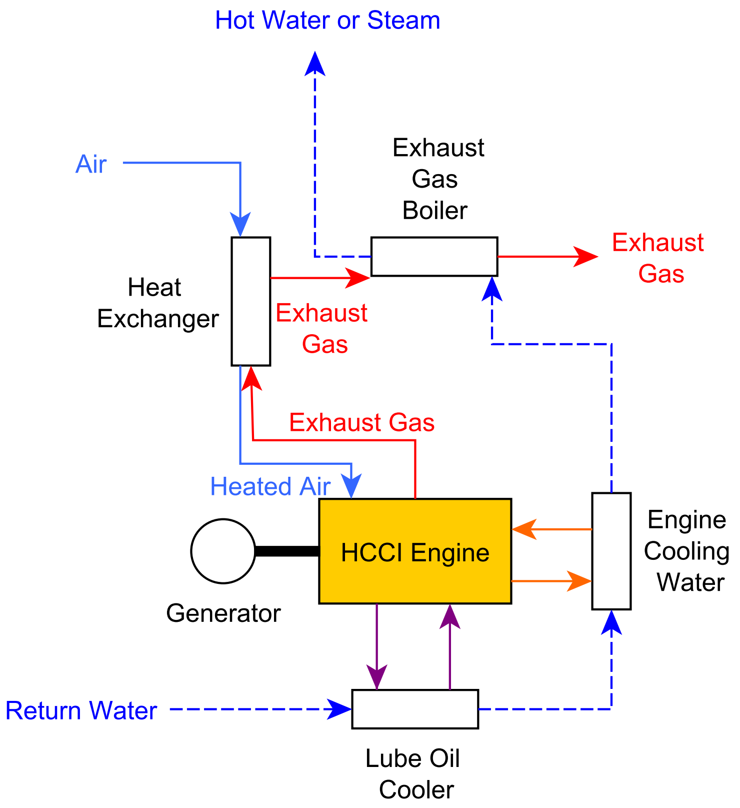

Figure 4.1: HCCI engine flow diagram for a micro CHP unit

A schematic of a micro CHP unit with HCCI engine is shown in Figure 4.1. The air/fuel mixture is burned in combustion chamber in HCCI mode and exhaust gas flow is used for the intake charge heating. Since only part of the fuel energy released during combustion is converted to the mechanical work, there is potential to recover the rest of the released heat. An energy balance including heat loss to the exhaust gas and cooling water is shown in Figure 4.2. The heat from the lube oil, cooling water and exhaust gas can be recovered using intermediate heat exchangers as shown in Figure 4.1. HCCI engine design can be optimized for fuel efficiency at specific loads and speeds for this reason.

There are relatively few studies on HCCI engine energy distribution and exergy analysis. A summary of these studies is provided next. A crank angle based exergy analysis is performed for a HCCI engine using a multi-zone thermo-kinetic model [156]. Four loss mechanisms for HCCI engines are introduced including combustion irreversibility (16.4%-21.5%), heat loss to exhaust (12.0%-18.7%), heat transfer to the cylinder walls (3.9%-17.1%) and chemical exergy lost due to incomplete combustion (4.7%-37.8%). The model developed in [156] is used to define optimal operating points for a gasoline fueled HCCI engine [157]. The results show that exergy losses to the exhaust gas are reduced with delayed combustion timing, however, the exergy losses to the unburned species then increase. The optimal combustion timing is determined using the balance of the exergy losses to the unburned species and the exergy losses to the coolant and exhaust gas. Exergy efficiency sensitivity to the intake pressure and equivalence ratio are also detailed for wide engine operating ranges. It is found that late combustion timing with higher fuel equivalence ratios and higher boosted intake pressures are preferred at high loads. For low loads, it is recommended to keep the fuel equivalence ratio high and gradually reduce the boosted intake manifold pressure to the ambient pressure.

A crank angle based single zone model is developed for the second law analysis of a HCCI engine burning Natural Gas/DME fuel [158]. The exergy efficiency is improved by an increase in excess air ratios of the DME and the irreversibility decreases with increasing intake temperature. A crank angle based single zone model is developed for HCCI engine second law analysis [159]. It is found that an increase in the inlet charge temperature reduces the maximum pressure, indicated work and entropy generation per cycle. The results also show that availability is increased with increasing engine speed since heat loss to the cylinder walls is reduced. An Ammonia-Water Cogeneration Cycle (AWCC) is used to recover heat from the exhaust gas and cooling water of a HCCI engine in [160]. A crank angle based single zone thermodynamic model is used to show that fuel energy saving ratio can be improved up to 28% using the proposed trigeneration system. An ammonia water and steam Rankine cycles are used for heat recovery from exhaust gases of spark ignition and compression ignition engines [161]. The simulation results indicate that high exhaust gas temperature from the spark ignition engine increases the power output of the ammonia water cycle relative to the Rankine cycle. In addition, the power output of both the ammonia water and the Rankine cycles are reduced due to lower exhaust gas temperature when a compression ignition engine is used.

The performance of a HCCI engine based cogeneration system is compared to the performance of cogeneration system with other prime movers including stoichiometric spark ignition engine, lean burn spark ignition engine, diesel engine, microturbine, and fuel cell [142]. The major factors considered for the evaluation are the electric and heating efficiency, $\mathrm{NO_X}$ emission, and the fuel consumption and cost. The analysis is performed for two different cases. In the first case, the cogeneration facility requires combined heat and power while in the second case the requirement is for power and chilling. The results indicate that HCCI engine based cogeneration systems are of interest because of their low cost, high efficiency and low emissions. A natural gas HCCI engine is turbocharged [162] to improve engine performance characteristics and the engine power generating efficiency is investigated for CHP application. The results indicate that the HCCI engine improves the CHP power generating efficiency and reduces the $\mathrm{NO_X}$ emission.

Major parameters affecting first and second law efficiencies of internal combustion engines including HCCI are detailed in [163] and different methods are introduced for improving engine efficiency. The effects of intake pressure boosting and variable valve timing on exergy flows of a HCCI engine are detailed using a physical model [164]. It is found that combustion irreversibility is increased at low loads with positive valve overlap and the combustion irreversibility is decreased by changing from the positive valve overlap to negative valve overlap. Cycle temperature is reduced with positive valve overlap and the energy lost to the cylinder walls and exhaust is reduced. The pumping work is lower with positive valve overlap and the brake thermal efficiency increases with positive valve overlap at boosted intake pressure. Energy distribution analysis is performed for a HCCI engine and the engine efficiency is compared to a port fuel injection SI and a lean burn SI engine [165]. The analysis indicates that combustion irreversibility increases at low combustion temperatures and the HCCI engine offers only modest efficiency improvements compared the lean burn SI engine.

Energy and exergy analysis of a wet ethanol HCCI engine integrated with organic Rankine cycle is performed using a thermodynamic model [166]. It is found that the first and second law efficiencies of the combined power cycle are highly sensitive to the turbocharger pressure ratio. The effects of organic Rankine cycle evaporator pinch point temperature, turbocharger efficiency, and ambient temperature on the first and second law efficiencies are negligible. The largest exergy loss is in the HCCI engine ($\sim$ 68.7%), and the second largest exergy loss occurs in catalytic converter ($\sim$ 3.13%). Combined first and second law analysis are performed for a HCCI engine working with ethanol and the effects of the intake manifold pressure, ambient temperature, and compressor efficiency on engine exergy efficiency are examined [167]. The results indicate that the first and second law efficiencies are improved by increasing the turbocharger pressure ratio and the efficiencies are reduced when the ambient temperature increases. The exergy analysis indicates that the first and second law efficiencies are more sensitive to the turbocharger pressure ratio compared to the turbocharger compressor efficiency and ambient temperature.

A second law analysis is performed for a HCCI engine based on a single-zone model [168]. Blends of n-heptane and natural gas fuel are used and the exergy analysis indicates that exergy destruction is decreased when the natural gas fraction increases in the fuel blend. The effects of EGR on HCCI combustion is investigated and the results indicate that the chemical exergy of the in-cylinder charge is reduced by increasing the EGR rate. The optimum EGR rate is defined based on exergy analysis for a specific engine operating conditions. First and second law analysis are performed for a system consisting of a turbocharged natural gas HCCI engine, a regenerator and a catalyst [169]. The effects of intake manifold pressure, ambient temperature, fuel equivalence ratio, engine speed and turbocharger compressor efficiency on system exergy efficiency are investigated. The results indicate that thermal and exergy efficiencies are improved at higher intake pressure, fuel equivalence ratios and engine speeds. Increased ambient temperature has adverse effects on both thermal and exergy efficiencies. The effects of fueling rate, intake temperature and engine speed on the thermal efficiency of a HCCI-like Low-Temperature Gasoline Combustion (LTGC) engine are studied in [112]. The results indicate that combustion timing, combustion efficiency, mixture properties and the fraction of the injected fuel energy lost to the cylinder walls and the exhaust are key parameters that affect thermal efficiency. In the reminder of this chapter, engine experiments and detailed analysis of HCCI engine energy distribution using VVT as the main actuator is detailed for the first time. The effects of SNVO duration on HCCI engine energy distribution and exergy are detailed below.

4.2 Energy and Exergy Analysis

Energy and exergy analysis is performed based on the measured experimental data listed in Table 3.1. All engine operating parameters are held constant including engine speed, IVC and EVO timings, while NVO duration is changed for several injected fuel energies. The injected fuel energy is assumed to follow the six different energy pathways as shown in Figure 4.2 and only part of injected fuel energy is turned into the useful work. The first energy pathway is part of the injected fuel energy lost due to incomplete combustion. To calculate how much energy is lost due to incomplete combustion, combustion efficiency is calculated first. Combustion efficiency, η_{Comb} is defined as

$$\eta_{Comb} = \frac{c_1 Q_{HR}}{m_f LHV_f} + c_2 \tag{4.1}$$

where Q_{HR} is the net energy released during combustion. The values of m_f

and LHV_f are the injected fuel mass and fuel low heating value respectively while c_1=55.271 and c_2=44.176 are defined using MATLAB Model Based Calibration Toolbox (The details are in Appendix E). These constants are parameterized based on the combustion efficiency values calculated from 14 measured emission points shown in Figure 4.3[136]. The constants are for tested conditions and how they vary as a function of engine speed and for other engines has not been investigated. The net heat release is calculated as

$$Q_{HR} = \int_{\theta_1}^{\theta_{99}} \left(\frac{dQ_{HR}}{d\theta} \right) d\theta \tag{4.2}$$

where θ_1 and θ_{99} are defined as the crank angle for 1% and 99% mass fraction respectively. The apparent heat release rate, $\frac{dQ_{HR}}{d\theta}$ is calculated using a single zone model as

$$\frac{dQ_{HR}}{d\theta} = \frac{1}{k-1} V \frac{dP}{d\theta} + \frac{k}{k-1} P \frac{dV}{d\theta} \tag{4.3}$$

where k, P and V are the specific heat ratio, measured in-cylinder pressure and the in-cylinder volume respectively. A graphical approach [125] is used to define the window limits used to calculate apparent heat release rate. The cylinder volume is calculated at each crank angle from slider crank mechanism eqn. [7]. The fuel energy lost due to incomplete combustion, Q_{IC} is calculated as

$$Q_{IC} = (1 - \eta_{Comb}) m_f LHV_f \tag{4.4}$$

where η_{Comb} is from eqn. 4.1. Referring to Figure 4.2, part of injected fuel energy is lost due to pumping work. Pumping work is found to be almost con-

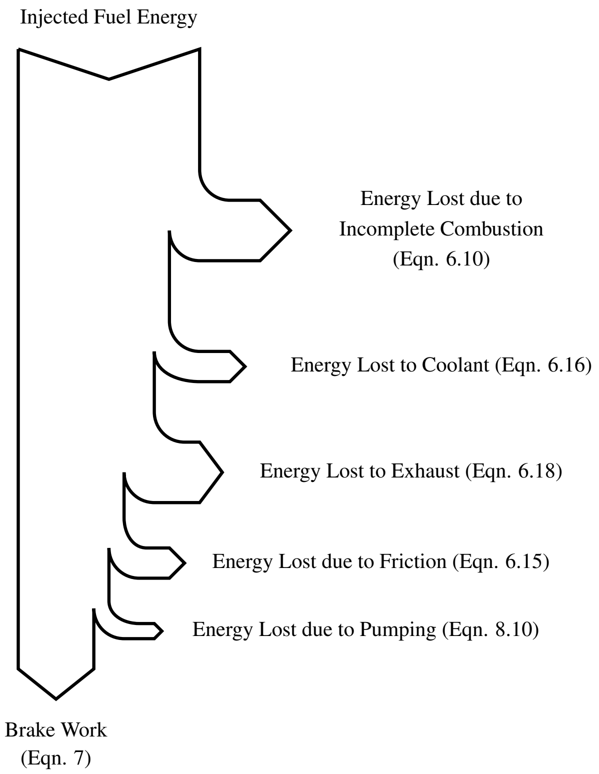

Figure 4.2: Energy balance of a HCCI engine

stant for different NVO durations. Pumping work, $W_{Pumping}$ is calculated from the measured cylinder pressure trace as

$$W_{Pumping} = \int_{TDC-Int}^{BDC-Int} PdV + \int_{BDC-Exh}^{TDC-Exh} PdV \tag{4.5}$$

Next, part of injected fuel energy lost due to friction (see Figure 4.2) is calculated as

$$W_{friction} = W_{ind} - W_{brake} \tag{4.6}$$

where $W_{friction}$, W_{ind} and W_{brake} are the friction, indicated and brake work respectively. Brake work, W_{brake} is

$$W_{brake} = 120\frac{P_{brake}}{\omega} \tag{4.7}$$

where P_{brake} and ω are brake power and engine speed respectively. Brake power is calculated from the measured engine torque and speed as

$$P_{brake} = \frac{2\pi}{60}\tau\omega \tag{4.8}$$

where τ is the measured torque. Brake thermal efficiency, $\eta_{th,brake}$ represents the fraction of injected fuel energy turned into useful work and is calculated as

$$\eta_{th,brake} = \frac{W_{brake}}{m_f LHV_f} \tag{4.9}$$

The net indicated work, W_{ind} is calculated from the measured pressure traces as

$$W_{ind} = \oint_{cycle} PdV \tag{4.10}$$

The amount of injected fuel energy lost due to heat transfer to the coolant, Q_{cool} is calculated as

$$Q_{cool} = \oint_{Cycle} \frac{dQ_{cool}}{d\theta}d\theta \tag{4.11}$$

where $\frac{dQ_{cool}}{d\theta}$ is the rate of heat transfer to the coolant and is calculated as

$$\frac{dQ_{cool}}{d\theta} = \frac{Ah_c}{\omega}(T_{cyl} - T_{wall}) \tag{4.12}$$

where the parameters A, ω, T_{cyl} and T_{wall} are the in-cylinder area exposed to the gas, engine speed, in-cylinder gas temperature and cylinder wall temperature respectively. The in-cylinder gas temperature is calculated using ideal gas law [7, 13] and the wall temperature is assumed to be constant (T_{wall}=400°K [13, 84]). The parameter h_c is the heat transfer coefficient and is calculated from the modified Woschni's correlation [84] as

$$h_c = \alpha_s L^{-0.2} {P_{cyl}}^{0.8} {T_{cyl}}^{-0.73} \bar{\vartheta}^{0.8} \tag{4.13}$$

where L is the instantaneous chamber height. The scaling factor, α_s is used for tuning of the coefficient to match specific engine geometry (α_s=1.2 [13]). The mean piston speed, $\bar{\omega}$ is calculated as

$$\bar{\vartheta} = C\bar{S}_p \tag{4.14}$$

where C=6.18 during gas exchange period and C=2.28 for the closed part of the cycle [84]. Finally, the amount of injected fuel energy lost to the exhaust, Q_{exh} is calculated from an energy balance (see Figure 4.2) as

$$Q_{exh} = m_f LHV_f - Q_{cool} - W_{friction} - W_{brake} - Q_{IC} - W_{Pumping} \tag{4.15}$$

The brake thermal efficiency is the engine first law efficiency and indicates the fraction of the injected fuel energy turned into useful work. The second law efficiency however is a comparison of the system's thermal efficiency to the maximum possible efficiency [170]. From this point of view, exergy analysis is more useful for the HCCI engine heat lost recovery analysis to understand the relative contribution of different loss mechanisms that result in performance reduction of HCCI engine. The theoretical maximum useful work that a system can produce is called exergy [170] and is calculated as

$$X = Q\left(1 - \frac{T_0}{T}\right) \tag{4.16}$$

where Q, T_0 and T are the waste heat, ambient temperature and the waste heat temperature respectively (T_0=25 C). The exergy efficiency is the ratio of the exergy content of an energy source to the exergy content of the fuel [171] and is calculated as

$$\eta = \frac{X}{m_f x_f} \tag{4.17}$$

where x_f is the fuel exergy ($x_f = 1.0354 \times LHV_f$ [172]).

The next step is to define exergy efficiency of the exhaust and coolant. The exergy efficiency of the exhaust gas, η_{exh} is calculated as

$$\eta_{exh} = \frac{Q_{exh}\left(1 - \frac{T_0}{T_{exh}}\right)}{m_f x_f} \tag{4.18}$$

where Q_{exh} is calculated from eqn. 4.15 and T_{exh} is the measured exhaust gas temperature. The coolant exergy efficiency, η_{cool} is calculated as

$$\eta_{cool} = \frac{Q_{cool}\left(1 - \frac{T_0}{T_{cool}}\right)}{m_f x_f} \tag{4.19}$$

where Q_{cool} is calculated from eqn. 4.11 and T_{cool} is the coolant temperature. In the experiment, the coolant temperature is measured and remains almost constant (T_{cool}= 50±3°C).

For a CHP system analysis, the first and second law efficiencies are needed. The first law efficiency of a CHP system is calculated [171] as

$$\eta_I = \frac{W_{el} + Q_{cool} + Q_{exh}}{m_f LHV_f} \tag{4.20}$$

where W_{el} is electric work that is obtained by coupling the engine to a generator. The electric generator efficiency is assumed to be 0.9 [140] and the electric work is calculated as $W_{el} = 0.9W_{brake}$.

The second law efficiency of a CHP system, η_{II} is defined [171] as

$$\eta_{II} = \frac{W_{el} + X_{cool} + X_{exh}}{m_f x_f} \tag{4.21}$$

where X_{cool} and X_{exh} are the coolant and exhaust exergies respectively and are calculated from eqn. 4.16. Finally, the power to heat ratio of a CHP system is calculated [140] as

$$\alpha = \frac{W_{el}}{Q_{cool} + Q_{exh}} \tag{4.22}$$

The power to heat ratio gives information about the quality of the CHP unit and the CHP potential for specific application is determined with this factor. Power to heat ratio values between 0.5 and 1.2 for existing micro CHP units integrated with internal combustion engines are typical [140]. The cogeneration potential for each application depends on the heat load and power to heat ratio values. More low cost electricity can be produced at high power to heat ratios [140, 173, 174].

Combustion efficiency in HCCI engines is lower than gas turbines, SI and Diesel engines and incomplete combustion is one major source of energy losses in HCCI engines [112, 175–177]. A new parameter is defined for HCCI energy distribution analysis as

$$\beta = \frac{W_{el}}{Q_{cool} + Q_{exh} + Q_{IC}} \tag{4.23}$$

where β is the power to energy loss ratio.

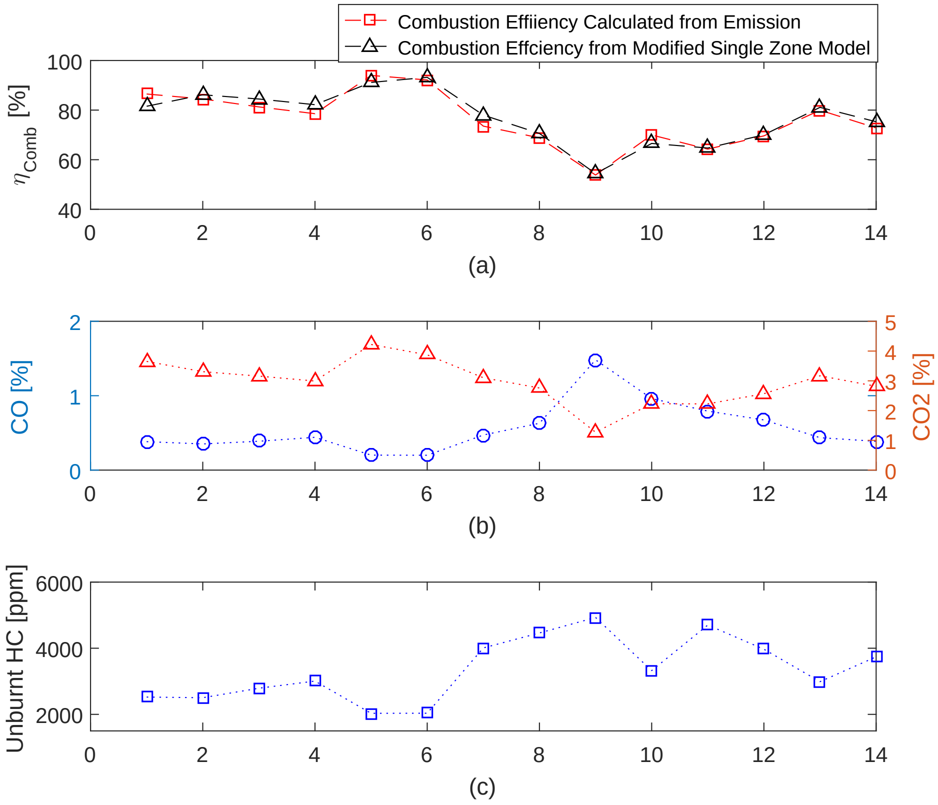

Figure 4.3: (a) Calculated Combustion efficiency (b) measured CO and CO_2 concentrations, and (c) measured unburnt HC [Injected Fuel Energy=0.356-0.395 $\frac{\text{kJ}}{\text{Cycle}}$, NVO=0-100 CAD and ω=825 RPM]

4.3 Experimental Results and Analysis

Energy distribution of the single cylinder HCCI engine with VVT is performed based on the measured steady state points listed in Table 7.2 (the detailed measure-

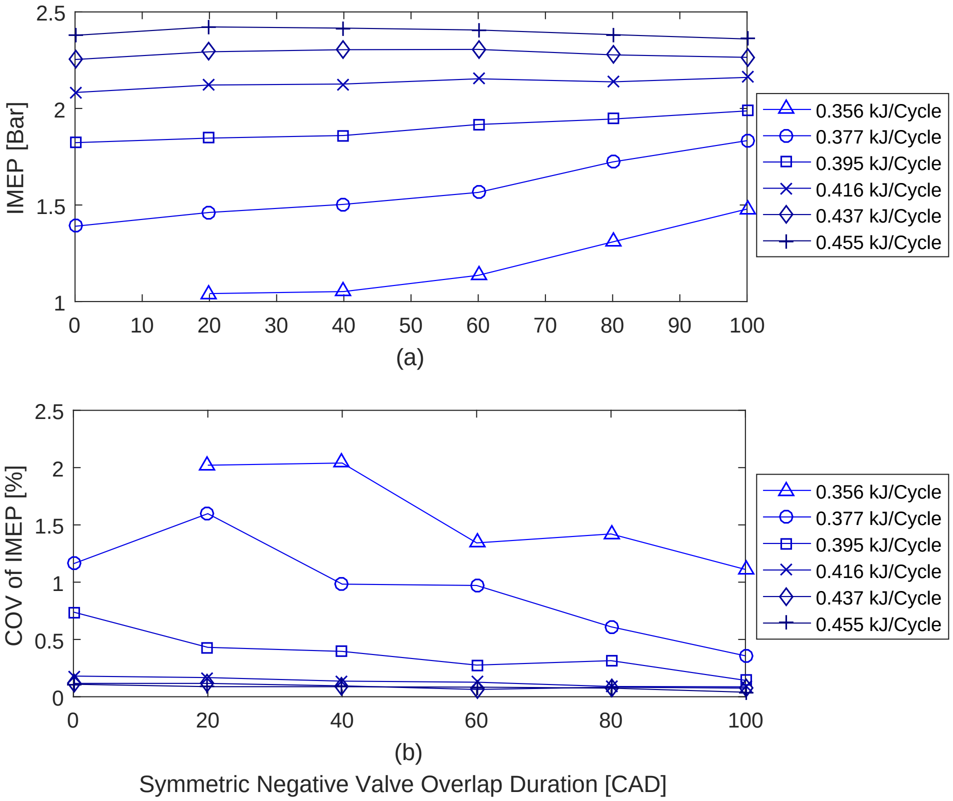

Figure 4.4: SNVO effects on (a) IMEP and (b) COV of IMEP at constant injected fuel energies

ments are summarized in Table B, Appendix B). The operating points are far from misfire as Indicated Mean Effective Pressure (IMEP) is positive [7] (see Figure 4.4(a)) and the combustion is stable as Coefficient of Variation (COV) of IMEP is below 3% [13] for all operating points shown in Figure 4.4(b). Only part of injected fuel energy is converted into the brake work (see Figure 4.2) and brake thermal efficiency is used to define the fraction of the injected fuel energy turned into the useful work. Brake thermal efficiency as a function of NVO for several injected fuel energies is shown in Figure 4.5(a). Brake thermal efficiency increases at low injected fuel energies with increasing NVO duration. Combustion timing advances with increase in NVO duration as shown in Figure 4.5(b). Combustion timing is the crank

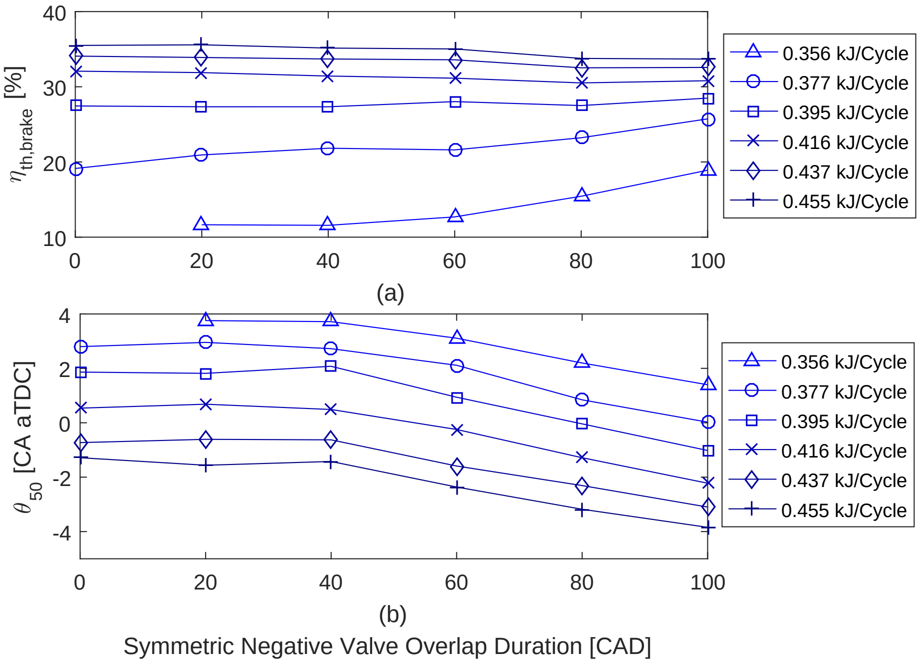

Figure 4.5: NVO effects on (a) the brake thermal efficiency and (b) combustion timing at constant injected fuel energies

angle of fifty percent fuel mass fraction burned in this work. The expansion ratio increases with the advanced combustion timing and the brake thermal efficiency is improved. At high injected fuel energies, brake thermal efficiency is almost constant. For these operating points, combustion timing is advanced to before TDC which increases the compression work. The increased compression work cancels the increased expansion work and the brake thermal efficiency remains almost constant. The effects of NVO duration on the fraction of the injected fuel energy lost to the exhaust due to incomplete combustion is shown in Figure 4.6(a). At low injected fuel energies, combustion efficiency is improved with increase in NVO duration as shown in Figure 4.6(b). Combustion timing is advanced with increase in NVO duration and mixture has enough time to completely burn and reactions are quenched later. At higher SNVO durations, more residual gas is trapped and it gives

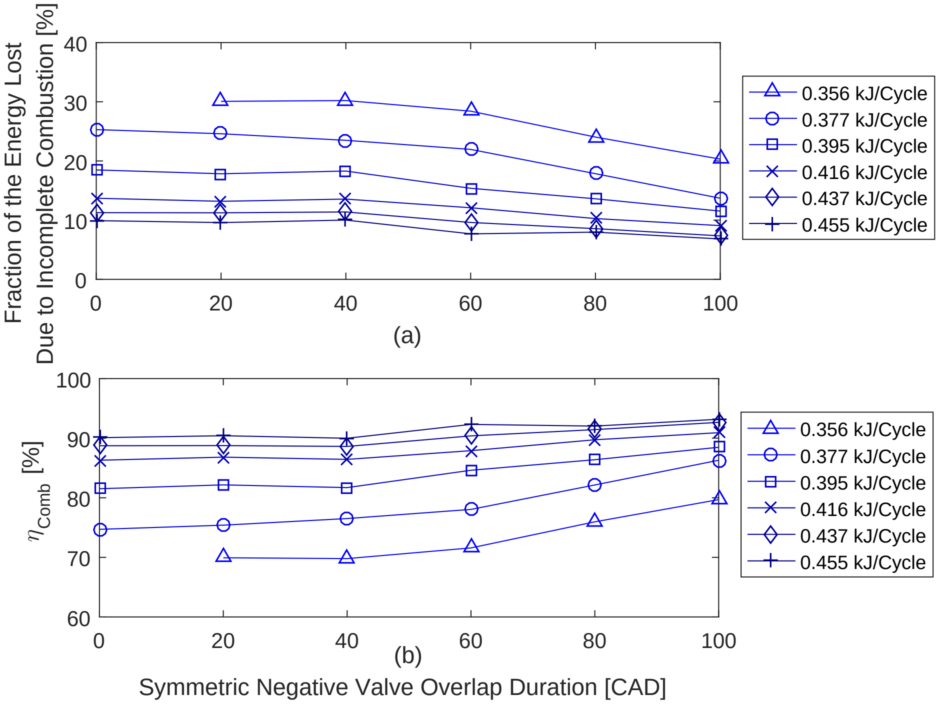

Figure 4.6: (a) Fraction of the injected fuel energy lost due to incomplete combustion and (b) combustion efficiency versus NVO duration at constant injected fuel energies

the unburned HC and CO remaining from the previous cycle a second chance to react. Combustion efficiency at high injected fuel energies is high and effects of NVO duration on combustion efficiency is negligible.

The waste heat recovery from the coolant and exhaust improves the engine fuel efficiency. About one-third of the injected fuel energy is lost to the coolant and exhaust. The fraction of the injected fuel energy lost to the coolant slightly increases with increase in NVO duration as shown in Figure 4.7(a). Combustion timing is advanced and the cycle temperature is increased when NVO increases at constant injected fuel energies. The effects of NVO duration on the fraction of the injected fuel energy lost to the exhaust is shown in Figure 4.7(b). The fraction of the fuel energy lost to the exhaust increases with increase in NVO duration specifically at

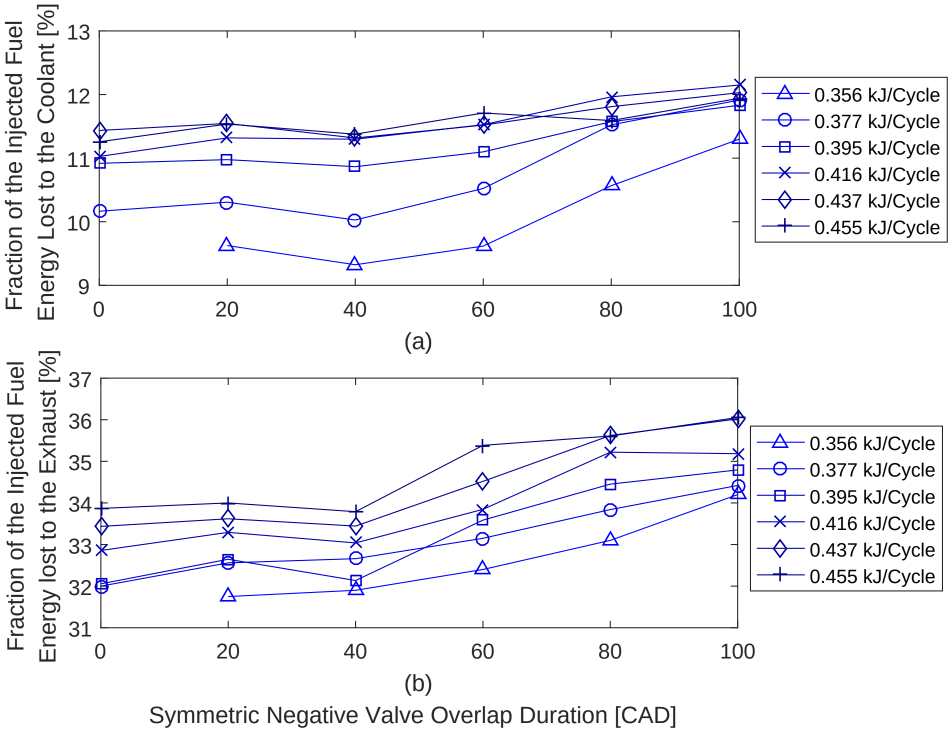

Figure 4.7: NVO effects on the fraction of the injected fuel energy lost to the (a) coolant and (b) exhaust at constant injected fuel energies

low injected fuel energies. Combustion efficiency improves and combustion timing advances with an increase in NVO duration. The advanced combustion timing and higher combustion efficiencies increase the exhaust gas temperature and exhaust loses. At high loads, NVO effects on the fraction of the injected fuel energy lost to the exhaust is negligible. The quality of the waste heat flows are evaluated with the calculation of the exhaust and coolant exergy efficiencies. The coolant exergy efficiency is below 1% for all operating points as shown in Figure 4.8(a). The coolant exergy efficiency increases with increase in SNVO duration as the fraction of the injected fuel energy lost to the coolant is increased with advanced combustion timing and improved combustion efficiency. Effects of SNVO duration on exhaust gas exergy efficiency is shown in Figure 4.8(b). Exhaust gas exergy efficiency increases

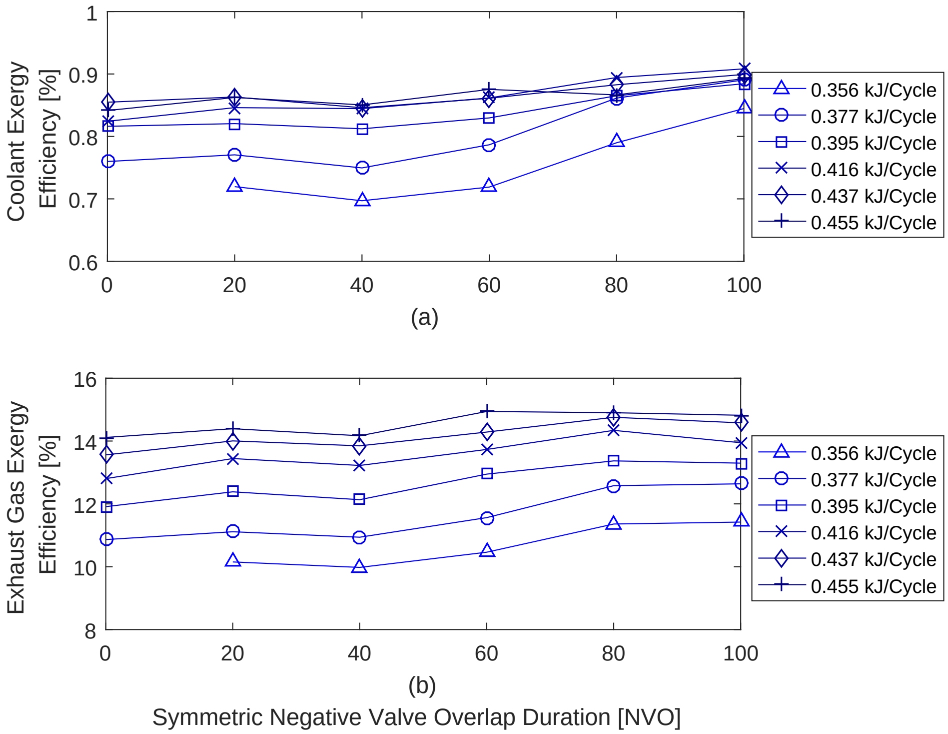

Figure 4.8: NVO effects on the (a) exhaust gas exergy efficiency and (b) coolant exergy efficiency at constant injected fuel energies

with increase in SNVO duration as the fraction of the injected fuel energy lost to the exhaust increases. The coolant exergy efficiency is negligible compared to the exhaust exergy efficiency. This is attributed to a much higher exhaust gas temperature compared to the coolant water temperature so the fraction of the fuel energy lost to the exhaust is higher than the fraction of the fuel energy wasted to the coolant. The coolant exergy efficiency increases with increase in NVO duration as the fraction of the injected fuel energy lost to the coolant is increased with advanced combustion timing and improved combustion efficiency.

The effects of NVO duration on CHP first law efficiency is shown in Figure 4.9(a). The maximum first law efficiency is about twice the maximum brake thermal efficiency, indicating that engine waste heat recovery is potentially impor-

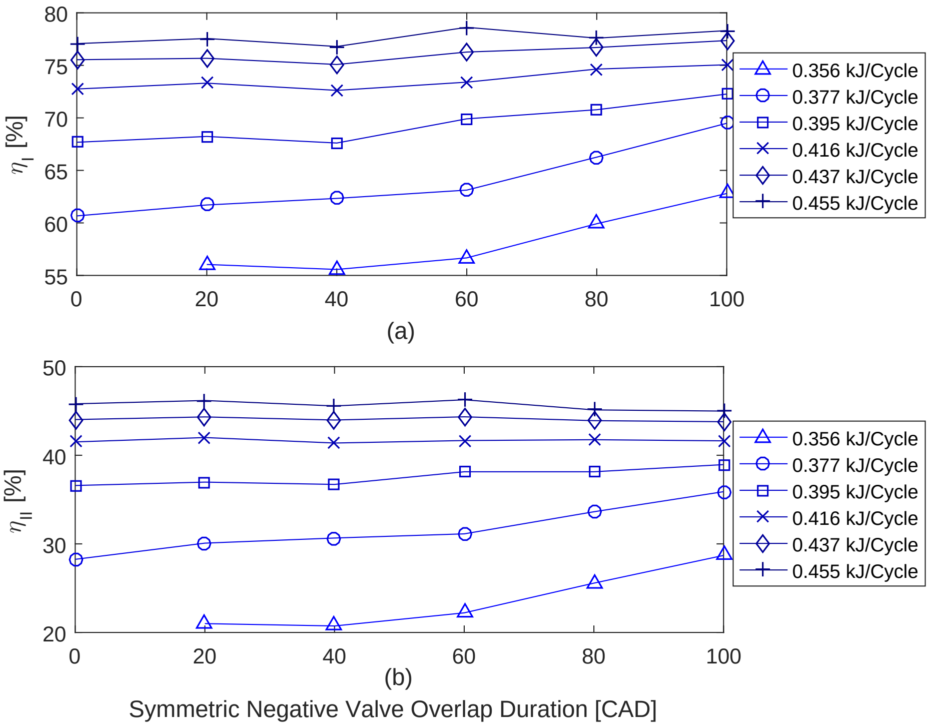

Figure 4.9: NVO effects on the (a) η_I, first law, and (b) η_{II}, second law CHP efficiency, at constant injected fuel energies

tant. At low injected fuel energies, CHP first law efficiency increases with increase in NVO duration as combustion efficiency is improved. The fraction of the injected fuel energy lost to the coolant and exhaust increases with improved combustion efficiency while brake work increases with advanced combustion timing. At high injected fuel energies, NVO duration has negligible effects on CHP first law efficiency. The fraction of the fuel energy lost to the coolant and exhaust increases with increase in NVO duration, however, the brake work reduces as compression work is increased. The effects of NVO duration on the CHP second law efficiency is shown in Figure 4.9(b). The second law efficiency is about 30% lower than the first law efficiency because the coolant and exhaust exergies are smaller compared to the amount of energy lost to the exhaust gas and cylinder walls. At low injected fuel

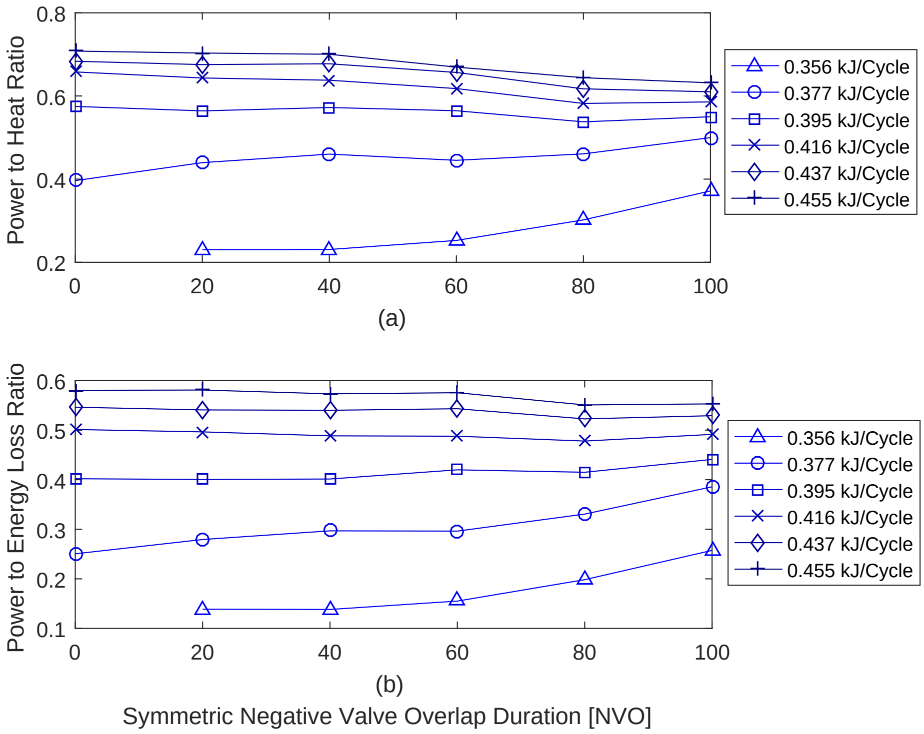

Figure 4.10: NVO effects on the (a) α, power to heat ratio, and (b) β, power to energy loss ratio, at constant injected fuel energies

energies, the second law efficiency improves with increase in NVO duration. At high injected fuel energies, the brake work reduces with increase in NVO duration, however, the coolant and exhaust exergies are increased. The increase in coolant and exhaust exergies cannot compensate the brake work reduction and the second law efficiency, η_{II}, deteriorates slightly.

The effects of NVO duration on the CHP power to heat ratio is shown in Figure 4.10(a). The power to heat ratio improves with increase in NVO duration at low injected fuel energies. At low injected fuel energies, brake work and heat losses to the coolant and exhaust are increased with increase in NVO duration. The increase in brake work is higher compared to the increase in energy losses to the coolant and exhaust and the power to heat ratio is increased as a result. At high injected fuel energies, the power to heat ratio, α, reduces slightly with increase in NVO duration. Brake work reduces with increase in compression work and the fraction of the fuel energy lost to the exhaust and coolant increases due to advanced combustion timing and higher combustion efficiencies. The calculated power to heat ratio values shown in Figure 4.10(a) are between 0.25 and 0.7 that is closed to the values reported for micro-CHP units integrated with gas turbines [140]. The effects of NVO duration on CHP power to energy loss ratio is shown in Figure 4.10(b). At low injected fuel energies, power to energy loss ratio increases with an increase in NVO duration, however, it is almost constant at high injected fuel energies. The power to energy loss ratio is 20% less than power to heat ratio at high injected fuel energies. At low injected fuel energies, the power to heat ratio is twice the power to energy loss ratio. These results indicate that combustion efficiency has significant role in HCCI engine energy distribution.

4.4 Discussion

HCCI engine energy distribution analysis is performed to characterize NVO effects on the distribution of supplied fuel energy. Coolant and exhaust exergies are calculated for HCCI engine waste heat recovery analysis. The results indicate that VVT with SNVO is an effective actuator for combustion and CHP first and second law efficiency improvement, specifically at low injected fuel energies. Combustion efficiency has an important role in HCCI engine energy distribution and the CHP power to heat ratio is improved with improve in combustion efficiency. Brake thermal efficiency is improved at higher combustion efficiencies when combustion timings is appropriate. Incomplete combustion is one major source of energy losses in HCCI engines. Power to energy losses ratio is defined for energy distribution analysis in HCCI engines as it includes fraction of the fuel energy lost due to incomplete combustion. Higher power to energy losses ratios are obtained at higher combustion efficiencies where combustion timings are near TDC.

Chapter 5

Detailed Physical Model (DPM)[1]

HCCI four stroke cycle is modeled as a sequence of continuous processes: intake, compression, combustion, expansion and exhaust. For the cycle simulation, the system of interest is the instantaneous contents of a cylinder. This system is open to the transfer of mass, enthalpy and energy in the form of work and heat. The cylinder is modeled as a time variant volume and the cylinder contents are divided into fourteen continuous zones. Quasi steady, adiabatic, one dimensional flow equations are used to predict mass flows past the intake and exhaust valves. The intake and exhaust manifolds are modeled as constant volumes whose pressure and temperature are determined by solving each manifold mass and energy equations. Intake charge and exhaust gas are modeled as ideal gases. A reduced order reaction mechanism for n-heptane is used for combustion simulation. The chemical kinetic reaction mechanism is from [178]. It is a reduced mechanism consists of 29 species and 52 reactions and is generated from the detailed n-heptane reaction mechanism [179]. The reaction mechanism is detailed in Appendix G. Despite extensive work on the modeling of HCCI combustion as detailed in Chapter 1, to date no physical control oriented model can provide accurate and fast prediction of the combustion timing

---

[1] This chapter is mainly based on [64]

with the variation of trapped residual gas. Thus the focus of this chapter is on developing detailed physical based model that is required for control oriented modeling.

5.1 Modeling Assumptions

The Detailed Physical Model (DPM) is a crank angle based model and is developed by solving conservation of mass and energy at each crank angle. Figure 5.1(a) shows the zone configurations used in this work. This configuration has been widely used in literature [180–185]. The drawback of this zone configuration is that the temperature difference between cylinder head, piston top and cylinder walls are not considered in the modeling. Other zone configurations are proposed in [186, 187] (see Figure 5.1 (b)&(c)) that considers different boundary temperature for each combustion chamber surface temperature but they suffer from extensive computational time. The zone distribution shown in Figure 5.1(a) is sufficient for predicting the combustion timing with less computational time. The gas properties are considered to be lumped in each zone with uniform pressure distribution for all zones. The fuel is n-heptane and the reaction mechanism is taken from [179]. The reaction mechanism and the species thermodynamic properties are listed in Appendix G (the file is in Cantera format). Heat transfer between zones are considered while mass transfer is ignored. Mass transfer between zones is needed when emission analysis is of interest [188, 189]. A one dimensional quasi-steady orifice model is used for gas exchange modeling. The orifice model along with the conservation of mass and energy gives the average temperature, pressure and gas composition at IVC. The model details are provided next.

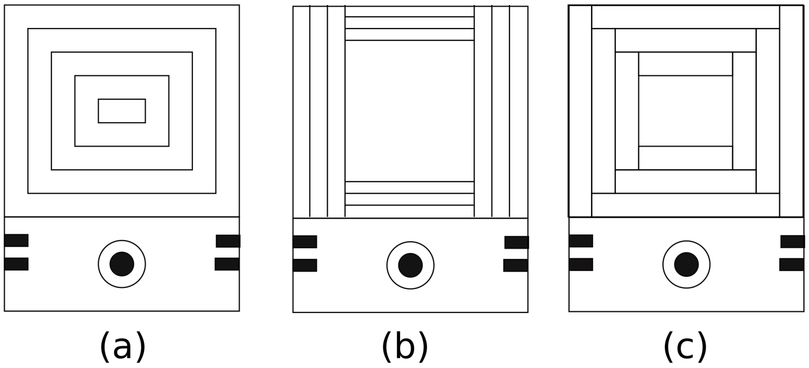

Figure 5.1: Zone Configurations

5.2 DPM Model Structure

Conservation of mass is used to develop a differential equation for the change in species concentration and energy conservation is used to obtain a differential equation for the change in system temperature. For the in-cylinder content, conservation of energy can be written as [115]:

$$\dot{U} = \sum_{j} \dot{m}_j h_j + \dot{Q}_W - \dot{W} \tag{5.1}$$

where $\dot{U}$ is the rate of change of the internal energy of the system, $\dot{Q}_W$ is the heat transfer rate into the system, $\dot{W}$ is the rate at which the system does work by boundary displacement and h_j is the enthalpy of the jth specie entering or leaving the system. The first term on the right hand side of eqn. 5.1 is zero during closed part of the cycle. Conservation of mass (eqn. 5.1) for the k^{th} zone can be written as

$$\dot{U}_i = \dot{Q}_{W,k} - \dot{W}_k \tag{5.2}$$

The internal energy of the k$^{\text{th}}$ zone is then calculated as the sum of the internal energy of all species [186]

$$U_k = \sum_{k=1}^{N_s} m_{k,i} u_{k,i} \tag{5.3}$$

where k represents the zone number. Differentiating eqn. 5.3 with respect to time gives

$$\dot{U}_k = \sum_{i=1}^{N_s} (m_{k,i}\dot{u}_{k,i} + \dot{m}_{k,i}u_{k,i}) \tag{5.4}$$

For an ideal gas the change in internal energy of a zone can be written as

$$\dot{u}_k = \bar{c_v}\dot{T}_k \tag{5.5}$$

The conservation of gas species in each zone can be calculated as

$$\dot{y}_{k,i} = \frac{\dot{\omega}_{k,i}M_i}{\rho_k} + \sum_i \frac{\dot{m}_i}{m_{cyl}}(\bar{y}_i - y_i^{cyl}) \tag{5.6}$$

where $\dot{\omega}_j$ is the net chemical production rate for each species and M_j is the molar mass of each species. The second term on the right hand side of eqn. 5.6 is zero during closed part of the cycle as there is no mass transfer between zones and $\bar{y}_i$ is the mass fraction of the specie entering or leaving the cylinder during open part of the cycle. The y_i^{cyl} is the in-cylinder mass fraction of each specie during open part of the cycle. The Cantera [96] is used for the calculation of the net chemical production rate, internal energy and enthalpy of the gas species. Figure 5.2 shows how Cantera is integrated to the cycle simulation. The rate of change of mass of each specie in k^{th} zone is calculated as

$$\dot{m}_{k,i} = m_k\dot{y}_{k,i} \tag{5.7}$$

$\dot{W}$ in eqn 5.1 is calculated as

$$\dot{W} = P_{cyl}\dot{V}_k \tag{5.8}$$

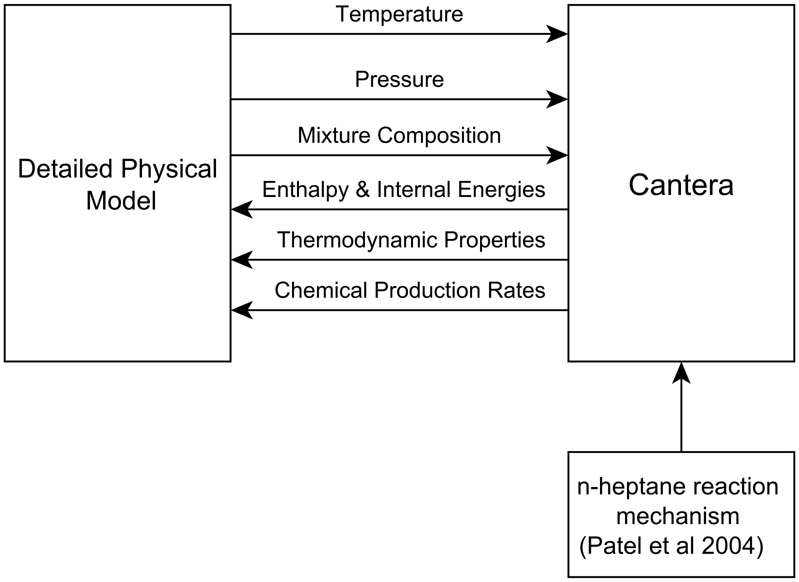

Figure 5.2: Cantera implementation in cycle simulation

where $\dot{V}_k$ and P_{cyl} are obtained from ideal gas law by summing over zones

$$P_{cyl} = \frac{\sum_k m_k R_k T_k}{V_{cyl}} \tag{5.9}$$

$$\dot{V}_k = \dot{V}_{cyl} \frac{m_k R_k T_k}{\left(\sum_k m_k R_k \dot{T}_k\right)^2} \left(m_k R_k \dot{T}_k \sum_k m_k R_k T_k - m_k R_k T_k \sum_k m_k R_k \dot{T}_k\right) \tag{5.10}$$

The cylinder volume, as a function of engine crank angle θ, are calculated using the slider crank mechanism [84]

$$V_{cyl} = V_c + \frac{\pi B^2}{4}[l + a - a\cos\theta - \sqrt{l^2 - (a\sin\theta)^2}] \tag{5.11}$$

where V_c is the cylinder clearance volume, B is the cylinder bore, l is the connecting rod length and $L = 2a$ is the stroke. The rate of change of temperature in each zone can be expressed by substituting eqns 5.4, 5.5, 5.6, 5.7, 5.8 and 5.9 into eqn. 5.2, resulting in:

$$\dot{T}_k = \frac{1}{\bar{c}_p}\left(\dot{Q} - \sum_i u_i \dot{y}_{k,i} + \frac{R_k T_k}{\sum_k m_k R_k T_k}\sum_k m_k R_k \dot{T}_k - \frac{R_k T_k}{V_{cyl}}\dot{V}_{cyl}\right) \tag{5.12}$$

The heat transfer rate between the cylinder wall and the adjacent zone is calculated using modified Woschni heat transfer model [124]. The modified Woschni's correlation has shown good results for HCCI engines and is used here to determine the heat transfer coefficient [84, 124]:

$$\dot{Q} = A_W h_c (T_{cyl} - T_{wall}) \tag{5.13}$$

$$h_c = 3.26 B^{-0.2} {p_{cyl}}^{0.8} {T_{cyl}}^{-0.55} \bar{n}^{0.8} \tag{5.14}$$

$$\bar{n} = C_1 \bar{S}_p \tag{5.15}$$

where A_W is the cylinder wall area available for heat transfer, h_c is the heat transfer coefficient, and T_{wall} is the in-cylinder wall surface temperature (T_{wall}= 420 K). C_1 is 6.18 during induction and exhaust and 2.28 otherwise. B is the cylinder bore and $\bar{S}_p$ is the mean piston speed. The heat transfer between each zones due to the temperature difference is calculated based on a simple conduction model developed in [186]. Residual gas mass and temperature distribution at IVC are obtained by the model proposed in [186].

Governing equations describing the exhaust manifold dynamics are similar to those described by the HCCI combustion dynamics. The following two coupled differential equations describe exhaust manifold dynamics [190]:

$$\dot{m}_{man} = \dot{m}_{in} - \dot{m}_{out} \tag{5.16}$$

$$\dot{U} = \sum_j m_j h_j + \dot{Q} \tag{5.17}$$

where $U = m_{man}c_vT_{man} = \frac{1}{\gamma-1}p_{man}V_{man}$ and $h_j = c_{p,j}T$.

Eqns. 5.16 and 5.17 are coupled with the ideal gas law:

$$p_{man}V_{man} = m_{man}RT_{man} \tag{5.18}$$

Rearranging Eqns 5.16 and 5.17 using Eqn 5.18 and neglecting heat transfer gives

$$\dot{p}_{man} = \frac{\gamma R}{V_{man}}(\dot{m}_{in}T_{in} - \dot{m}_{out}T_{man}) \tag{5.19}$$

$$\begin{aligned}\dot{T}_{man} = \frac{T_{man}R}{p_{man}V_{man}c_v}(\bar{c_p}\dot{m}_{in}T_{in} \\ - \bar{c_p}\dot{m}_{out}T_{man} - \bar{c_v}(\dot{m}_{in} - \dot{m}_{out})T_{man})\end{aligned} \tag{5.20}$$

where γ is the heat capacity ratio and c_p and c_v are the specific heat at constant pressure and volume respectively. The conservation of manifold gas species can be expressed as

$$\dot{y}_{man} = \sum_j \frac{\dot{m}_j}{m_{man}}(y_j - y_{man}) \tag{5.21}$$

The adiabatic formulations 5.19, 5.20 and 5.21 estimate the exhaust manifold behavior.

In this study a heater is used to increase the intake manifold temperature to a constant, hence isothermal assumption is used for intake manifold modeling. Eqns 5.19 and 5.20 can be simplified [190] to:

$$\dot{p}_{man} = \frac{RT_{man}}{V_{man}}(\dot{m}_{in} - \dot{m}_{out}) \tag{5.22}$$

$$T_{man} = constant \tag{5.23}$$

The conservation of the intake charge species equation is the same as eqn. 5.21.

A one dimensional quasi steady compressible flow model is used to calculate mass flow rates through the intake and exhaust valves during induction and exhaust strokes. The intake and exhaust manifolds are treated as volumes with known pressure, temperature and mixture composition. When reverse flow to the manifolds occurs, a rapid mixing model is used. At each step of the intake or the exhaust strokes, values for the valve open areas are calculated as

$$A = \pi D L \tag{5.24}$$

where A, D and L are the valve open area, valve head diameter and valve lift respectively. Given the valve open area, the discharge coefficient, and the pressure ratio across a valve, the mass flow rate across the valve is calculated from [115]

$$\dot{m} = C_d A \frac{P_o}{RT_o} \sqrt{\gamma R T_o} \left(\frac{2}{\gamma - 1} \left[\left(\frac{P_s}{P_o} \right)^{\frac{2}{\gamma}} - \left(\frac{P_s}{P_o} \right)^{\frac{\gamma+1}{\gamma}} \right] \right)^{\frac{1}{2}} \tag{5.25}$$

where C_d is discharge coefficient, A is valve open area, P_o is pressure upstream of the valve, P_s is pressure downstream of the valve, T_o is temperature upstream of the valve, γ is ratio of specific heats and R is gas constant. For the case of chocked flow, eqn. 5.25 reduces to [115]

$$\dot{m} = C_d A \frac{P_o}{RT_o} \sqrt{\gamma R T_o} \left(\frac{2}{\gamma + 1} \right)^{\frac{(\gamma+1)}{2(\gamma-1)}} \tag{5.26}$$

The intake throttle is considered as a flow restriction area and eqns. 5.25 and 5.26 are applied for throttle body simulation.

Engine speed is modeled using a constant engine inertia. The differential equation for engine speed is

$$I_{eng} \dot{\Omega} = T_{eng} - T_{load} \tag{5.27}$$

where T_{eng} is engine torque, Ω is engine speed, T_{load} is load torque and I_{eng} is the engine inertia [190].

The state equations for the model are given by eqns. 5.6, 5.9, 5.12, 5.19- 5.22 and 5.27. The system under study can be written in the following general form, where x is the state of the system, u is the control input, w is a disturbance, and f is a nonlinear function.

$$\dot{x} = f(t, x, u, w) \tag{5.28}$$

where $x \in \Re^n$, $u \in \Re^m$ and $w \in \Re^p$. This notation is a vector notation, which allows us to represent the system in a compact form. The main inputs of the model are the intake manifold temperature, valve timing, fuel mass flow rate and the load torque (u^T=[$\dot{m}_f$ T_{int} θ_{IVO} θ_{EVC} T_{load}]). In addition to the inputs, the model also includes certain output variables that can be used to monitor and control the system. These outputs are combustion timing, peak pressure, pressure rise rate and output work (y^T=[θ_{SOC} P_{max} PRR W]. The state variables are chosen due to their physical significance to the combustion process and are: in-cylinder and manifold temperature and pressure, species mass fraction and engine speed (x^T=[T_{cyl} P_{cyl} T_{man} P_{man} y_{man} y_{cyl} Ω]). For the detailed physical model n=483 [14(zones)×29(species in each zone)+14(temperature at each zone)+1 (in-cylinder pressure) +2(manifolds)×29(species)+2 (intake and exhaust manifolds temperatures)+2(intake and exhaust manifolds pressures)] and m=5.

Figures 5.3 and 5.4 show HCCI pressure trace and zonal temperature distribution calculated from the DPM respectively. In Figure 5.3b, pressure trace around TDC of combustion is zoomed to show some important HCCI combustion indices used for HCCI combustion calculation. Figure 5.4 shows a typical plot of the temperatures for each zone. The hottest zone (Zone 1) is the one that ignites first. As zone 1 burns and its volume expands, it compresses the lower temperature zones, which in turn ignite. The period over which the ignition of the various zones occurs determines the rate of heat release and the burn duration in the cylinder. If the temperature of a zone is not high enough, there might be no combustion in that zone, as the case is for zone 14 shown in Figure 5.4. The temperature increase that is observed in zone 14 is a result of compression only, due to the volumetric expansion of the zones that have already ignited. Figure 5.5 shows the DPM structure and the communication between its sub-models.

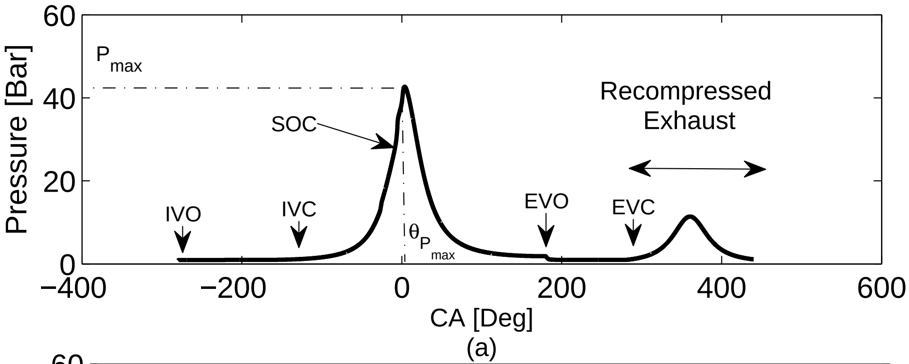

(a)

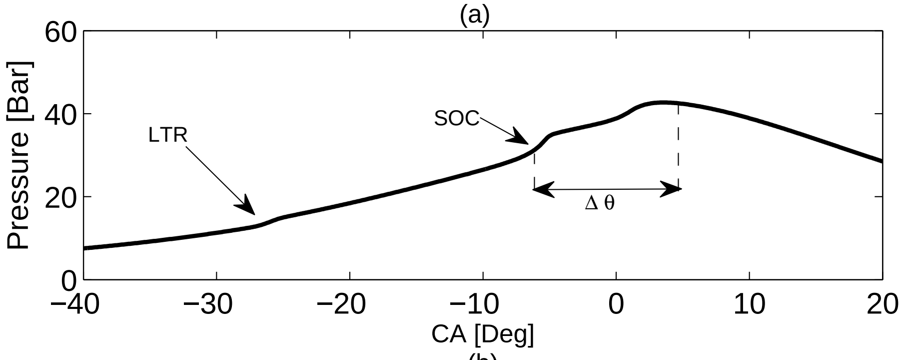

(b)

Figure 5.3: Experiment Pressure Trace [160 Deg NVO, Ω=825 RPM and ϕ=0.3]

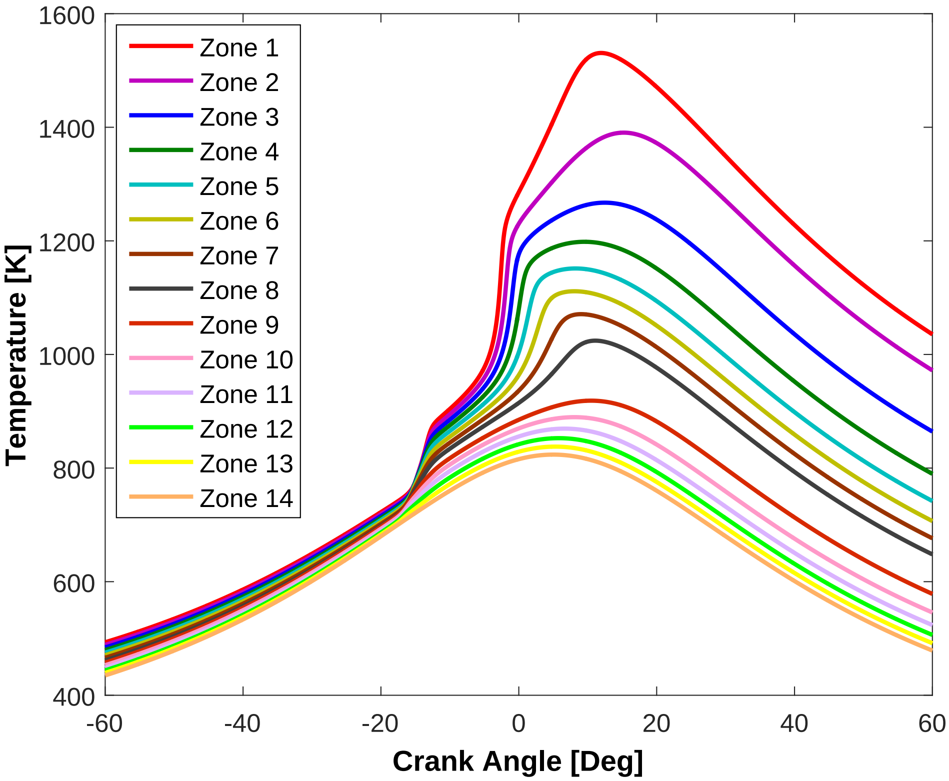

Figure 5.4: Zonal Temperature Distribution [160 Deg NVO, Ω=825 RPM and ϕ=0.3]

5.3 Defining the Numbers of Zones

With the configuration shown in Figure 5.1(a), the next step is to define the number of zones required for HCCI cycle simulation. To do this, the number of zones is increased from 1 to 20 and the model accuracy in predicting the combustion timing (θ_{50}) and burn duration are shown in Figure 5.6. A single zone model, can predict the start of combustion with enough accuracy however it cannot predict the burn duration and combustion timing (θ_{50}) as shown in Figure 5.6. The reason is the whole mixture ignites at the same time resulting in very fast combustion with short burn duration. In a real HCCI engine, the mixture near the walls is cooler than

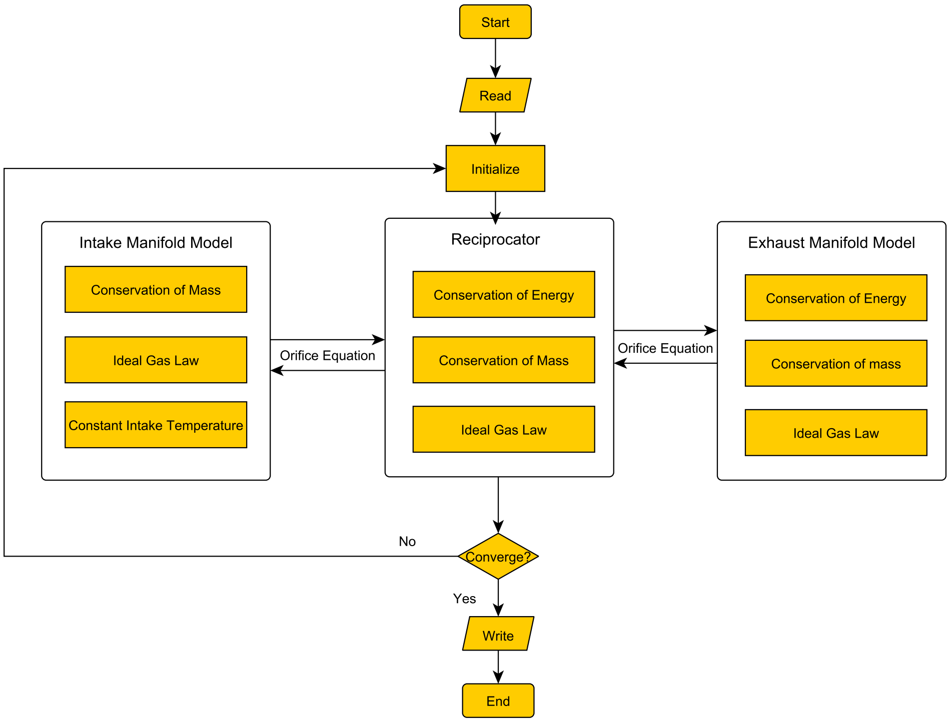

Figure 5.5: Flowchart of DPM simulation program

the mixture in the center of combustion chamber at the end of compression stroke [187]. Figure 5.6 shows the effect of numbers of zones on burn duration and combustion timing (θ_{50}). With one zone, the combustion timing and burn duration is not predicted accurately. Multi-zone models can consider temperature gradients in combustion chamber and have been used widely for estimating the burn duration [185, 191, 192]. Sequential combustion occurs when more than one zones are considered for cycle simulation as shown in Figure 5.4. It is found that with 14 zones, the model is a compromise between good accuracy and acceptable computational time.

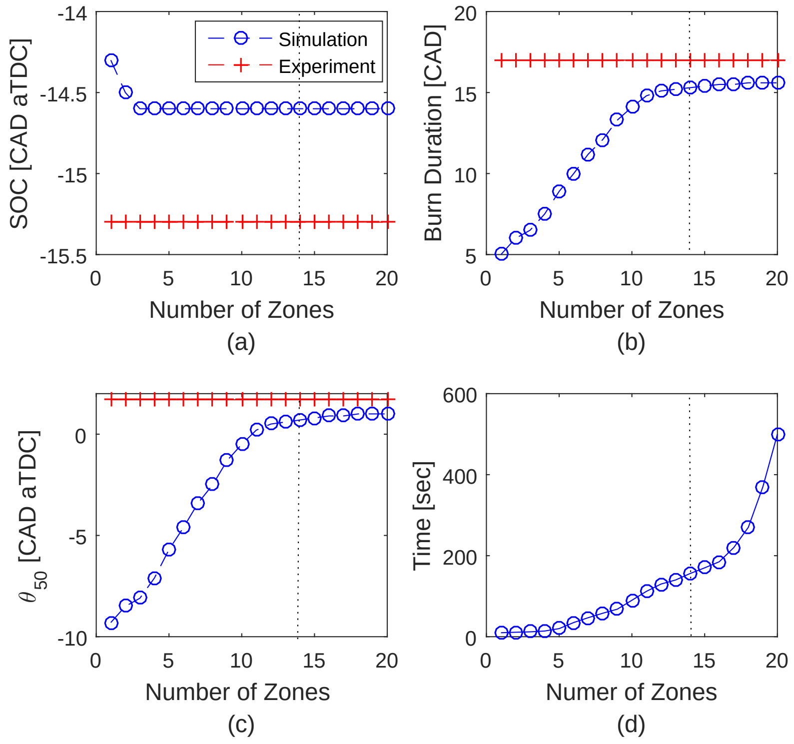

Figure 5.6: Determining the number of zones (a) SOC (b) Burn Duration, (c) combustion timing, and (d) computation time [NVO=20 CAD, ϕ=0.36 and Ω=811 RPM]

Table 5.1: Operating Conditions for Validation

Case Name	A	B	C	D	E
EVC [bTDC]	-300	-330	-320	-320	-300
IVO [bTDC]	300	330	290	300	320
Ω [RPM]	798	799	800	801	803
ϕ	0.37	0.33	0.36	0.33	0.33
T_{int} [C]	80	80	80	78.9	78.4
P_{int} [Bar]	0.88	0.88	0.88	0.89	0.89

5.4 Model Validation

The model is validated against experimental data from the single cylinder engine. The simulations are conducted for a range of equivalence ratios with different valve timings. The test points that are used for model validation are listed in Table 5.1

with each case labeled with the letters A through E for future reference.

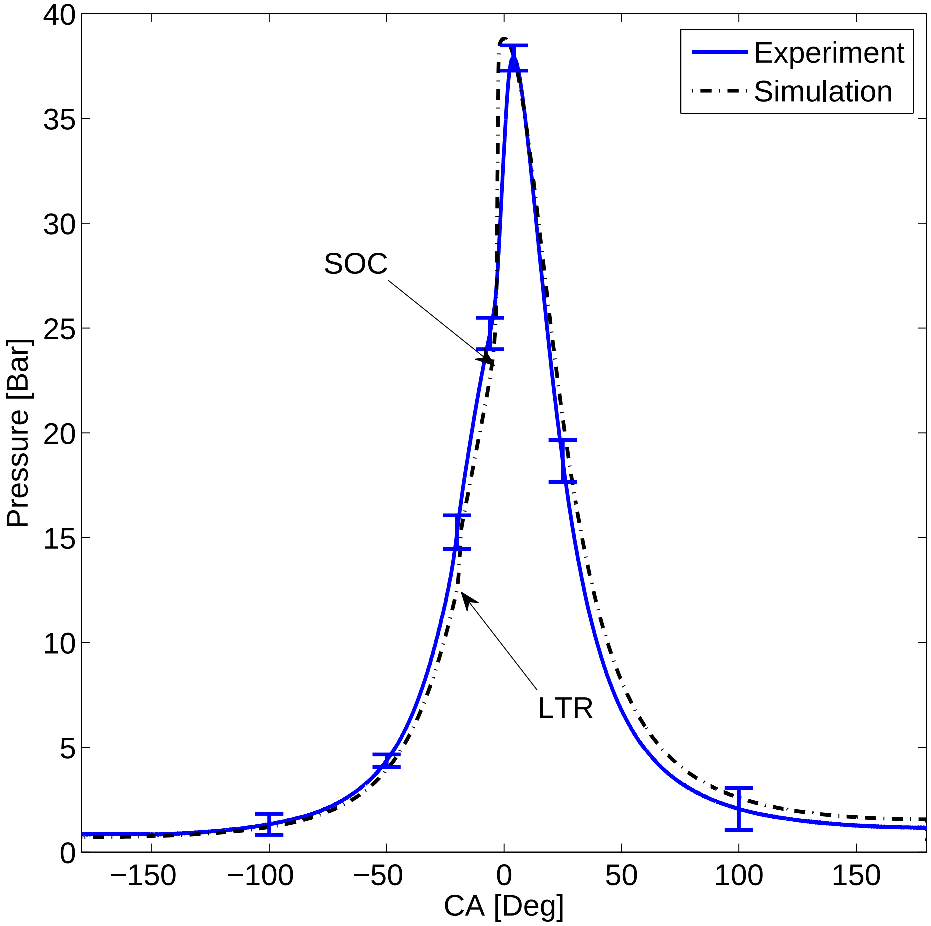

Figure 5.7: Experiment Pressure Trace vs. Models - Case A (see Table 5.1)

Figures 5.7- 5.11 compare cylinder pressure from the DPM model to the corresponding experimental cylinder pressure traces that is averaged for 300 cycles. The detailed physical model matches the experimental pressure trace quite well during compression, combustion and expansion. Start of combustion is predicted within 1.5 CAD in each case. The predicted peak pressure is slightly higher (about 4.5%) for each case and this is attributed to the higher combustion efficiency in simu-

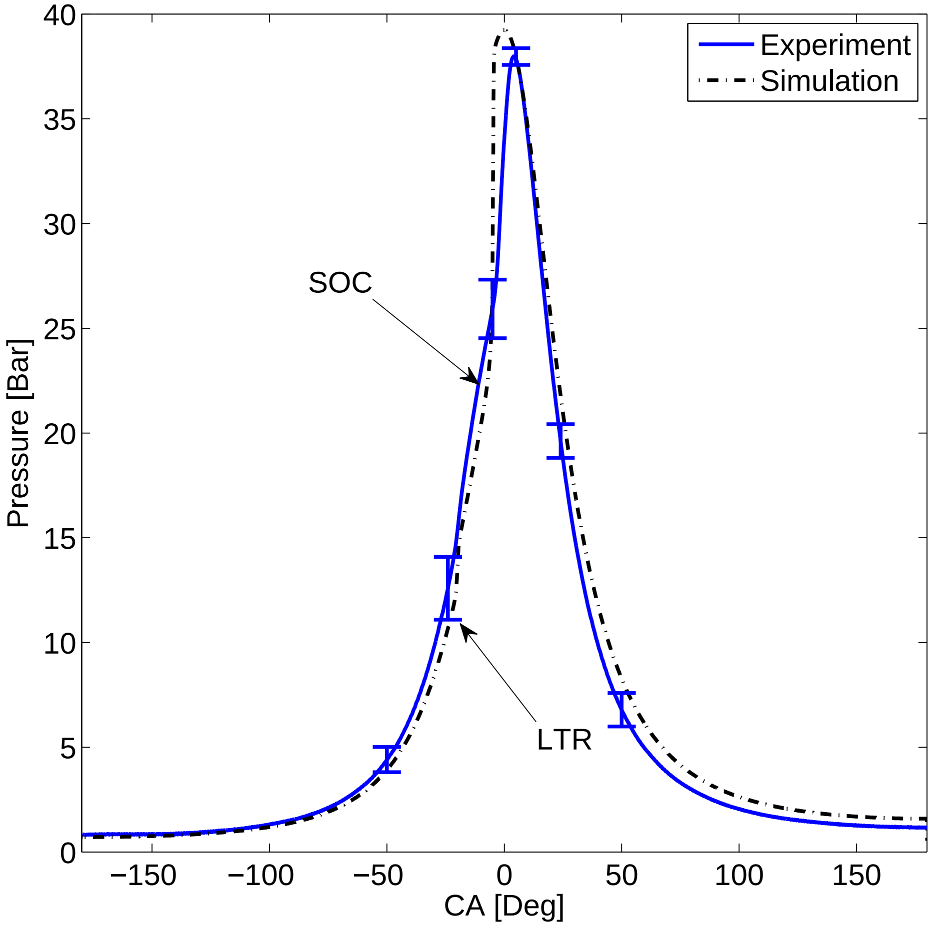

Figure 5.8: Experiment Pressure Trace vs. Models - Case B (see Table 5.1)

lation. The detailed physical model does not consider the effects of turbulence, combustion chamber wall temperature gradients and low temperature regions, such as crevices on combustion. This can cause inaccurate prediction of IMEP and thermal efficiency, but the model is still useful as it is able to capture the effects of valve timing. In each case, the detailed physical model predicts the effective compression ratio slightly lower and this cause another discrepancy between the simulation and measured cylinder pressure values during compression. DPM shows a small abrupt pressure increase during compression before main combustion and it is caused by

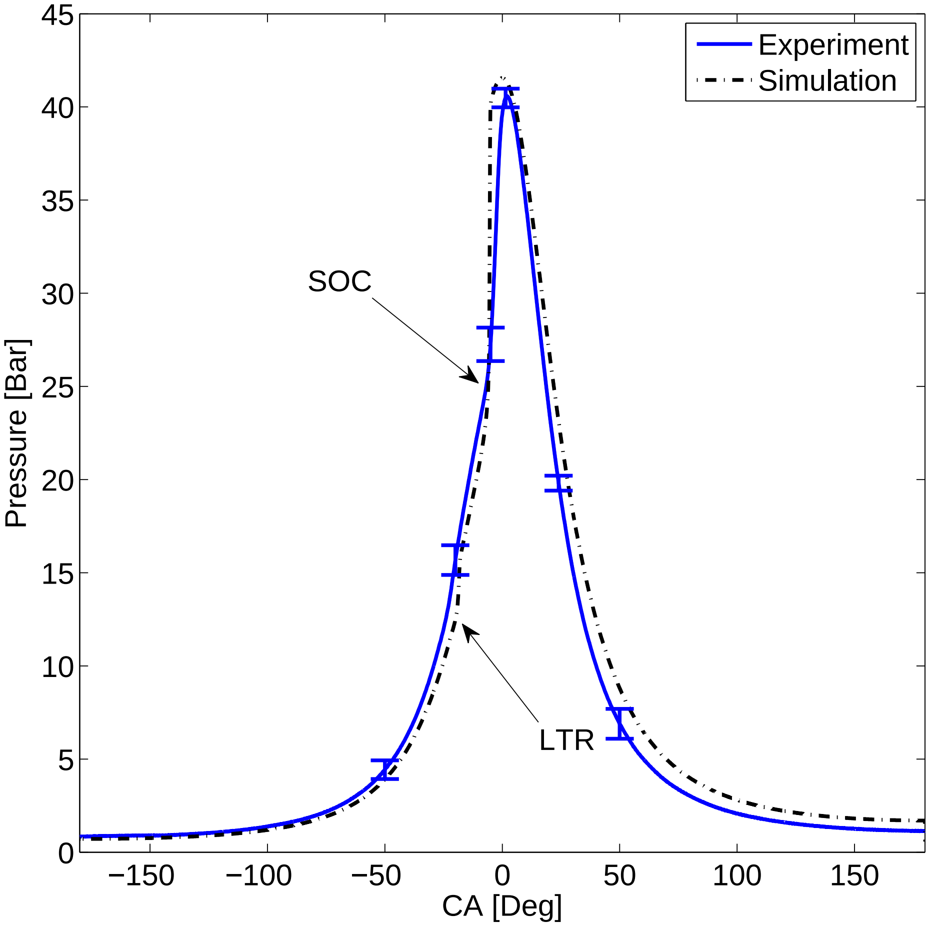

Figure 5.9: Experiment Pressure Trace vs. Models - Case C (see Table 5.1)

early heat release due to Low Temperature Reactions (LTR). Table 5.2 compares some more combustion indices i.e. the prediction and measured location of occurrence of the start of combustion and the predicted and measured peak pressure. This table shows that the physical model is accurate for control and thermodynamics analysis of the HCCI engine. The detailed physical model is computationally efficient needing 156 sec to simulate an HCCI cycle on a 2.66 GHz Intel PC.

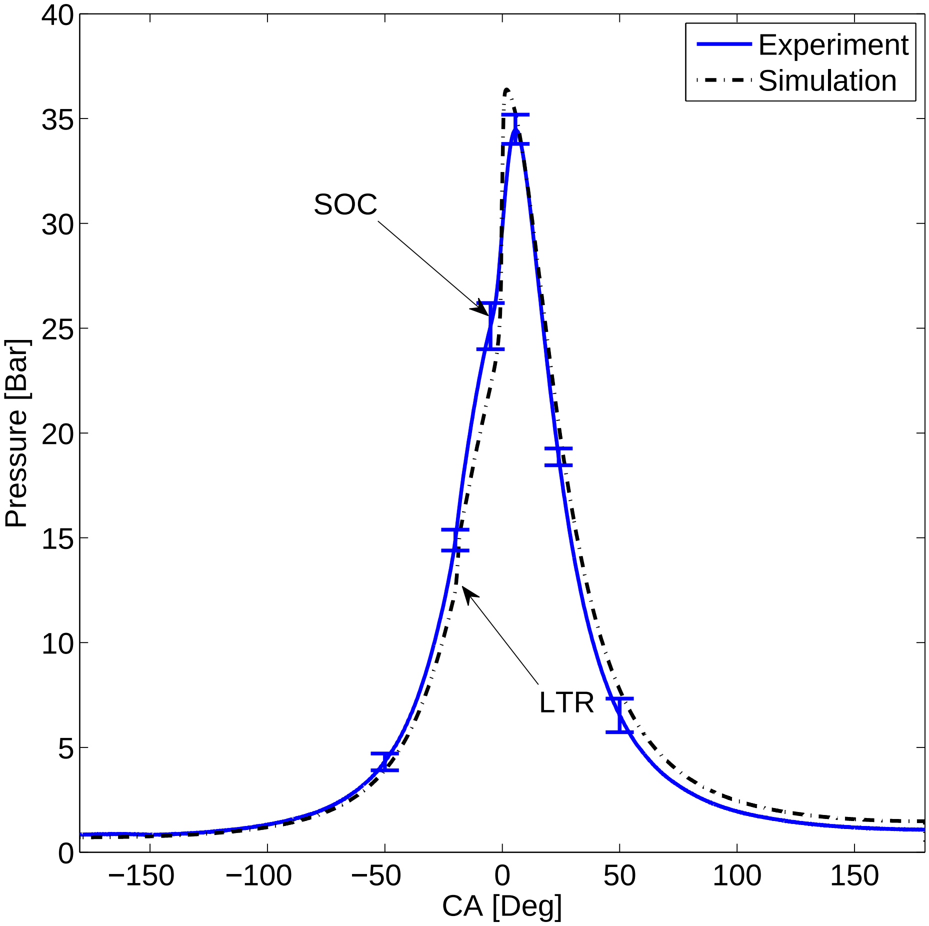

Figure 5.10: Experiment Pressure Trace vs. Models - Case D (see Table 5.1)

Table 5.2: Comparison of predicted and experimental values of peak pressure and start of combustion

Case Name	A	B	C	D	E
Measured SOC [CA aTDC]	-4.3	-6.2	-6.5	-3.7	-0.1
Detailed Physical Model SOC [CA aTDC]	-3.8	-5.8	-6.2	-2.2	-0.8
Measured P_{max} [Bar]	37.9	38	40.5	34.5	31.9
Detailed Physical Model P_{max} [Bar]	38.8	39.2	41.5	36.4	33.26
Measured $\theta_{P_{max}}$ [CA aTDC]	4	4	1.9	5.6	6.1
Detailed Physical Model $\theta_{P_{max}}$ [CA aTDC]	0	-0.1	-0.1	1.9	4

The detailed physical model is further validated against experimental data. Fig-

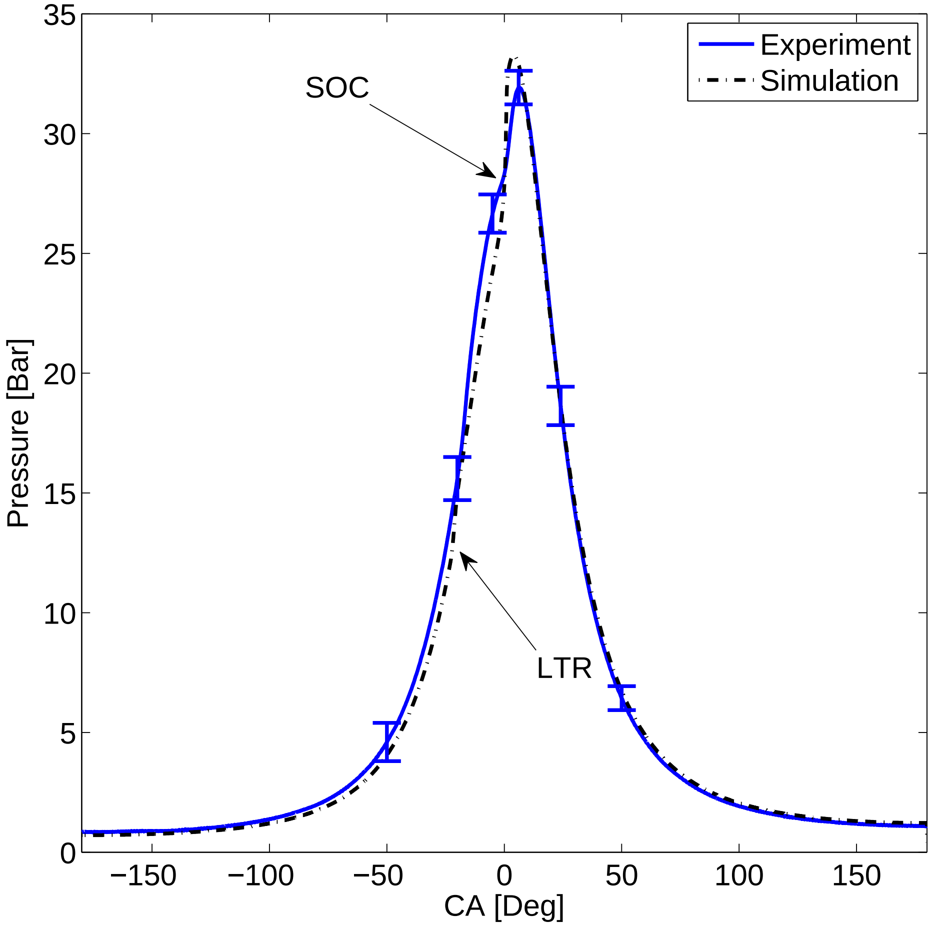

Figure 5.11: Experiment Pressure Trace vs. Models - Case E (see Table 5.1)

ure 5.12 shows predicted and measured combustion timing (θ_{50}) when IVO timing changes while holding all other parameters constant. The detailed physical model predictions are within 1-3 crank angle degrees of the measured θ_{50} values. As shown in Figure 5.12, combustion timing advances when IVO timing is retarded. When IVO is retarded, in-cylinder gas temperature is reduced due to expansion but more fresh charge is inducted into the cylinder due to low in-cylinder pressure at IVO. Mixture composition has key role on HCCI combustion timing control and in this case and combustion advances because the trapped charge fuel equivalence ratio is increased by late IVO. Figure 5.13 shows predicted and measured θ_{50} when EVC timing changes, keeping other operating parameters constant. As shown in Figure 5.13, detailed physical model predictions are acceptable within 2 crank angle degrees. Combustion timing retards when EVC timing is advanced. When EVC is advanced, in-cylinder gas temperature is increased because more residual gas is trapped but since the pressure is high at IVO so part of the residual gas goes to the intake manifold and dilutes the fresh charge. Combustion timing retards because the trapped charge fuel equivalence ratio is reduced by advanced EVC.

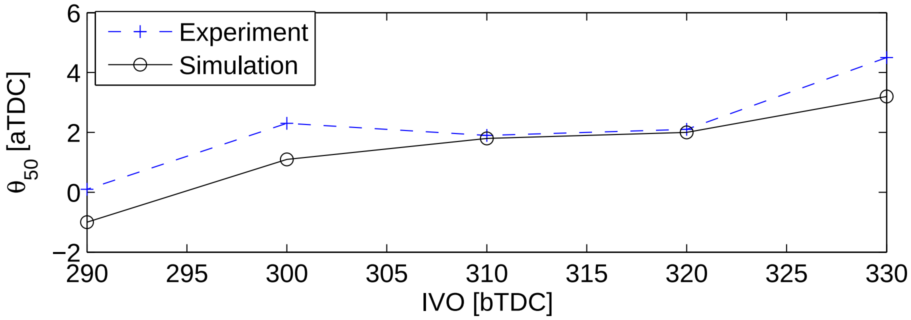

(a) Injected Fuel Energy = 0.36 kJ

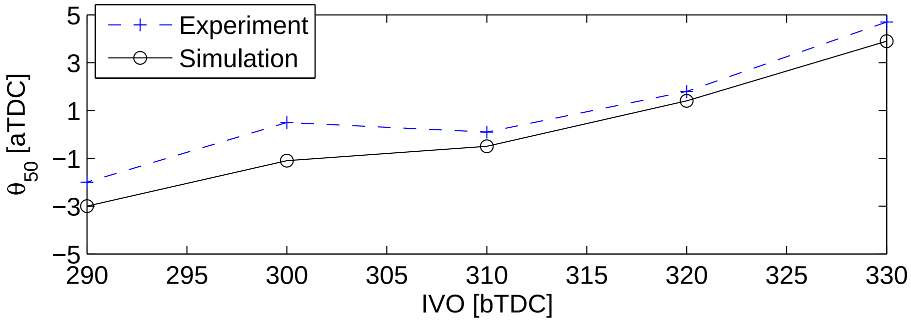

Injected Fuel Energy = 0.39 kJ

Figure 5.12: Comparison of predicted and measured θ_{50} for IVO timing changes (EVC=-320 bTDC, T_{int}=88^oC, P_{int}=0.88 Bar and Ω=819 RPM)

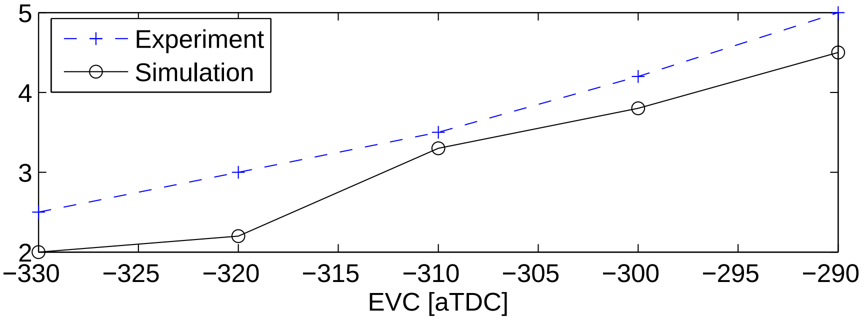

(a) Injected Fuel Energy = 0.36 kJ

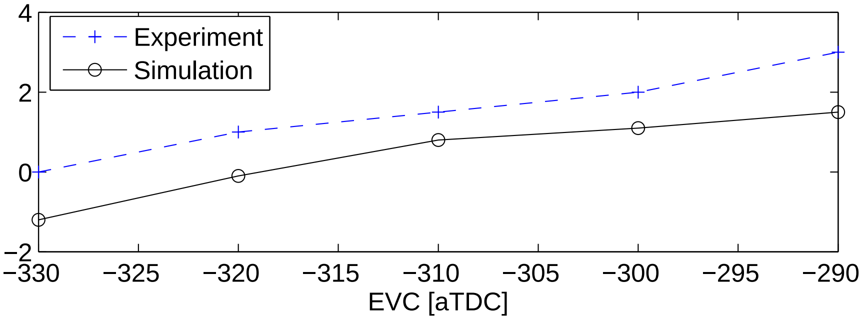

(b) Injected Fuel Energy = 0.39 kJ

Figure 5.13: Comparison of predicted and measured θ_{50} for EVC timing changes (IVO=+320 bTDC, T_{int}=88^oC, P_{int}=0.88 Bar and Ω=819 RPM)

5.5 Variable Valve Timing Implementation with DPM

The detailed physical model developed in previous section is used to study the effect of variable valve timing on HCCI combustion using symmetric NVO strategy. Fully variable valve timing can be used to control HCCI combustion by trapping residual gas from the previous combustion cycle. Controlling HCCI with NVO is a practical method since pumping losses are minimized. NVO effects on HCCI combustion are examined for six different cases of NVO equals 0, 20, 40, 60, 80 and 100 CAD. The fueling rate, intake manifold temperature and engine speed are kept constant and only the valve timing changes. With longer NVO duration, more mass of hot combustion products is trapped in the cylinder at EVC. The high temperature in the cylinder, combined with the shorter duration of the intake valve opening, results in introducing less fresh charge in the cylinder and eventually the total fresh charge captured in the cylinder is less for longer NVOs. Even though the trapped mass and the temperature after IVC changes widely with NVO, the pressure during compression is almost the same for all cases, as it can be seen in figure 5.14. This is due to the fact that the intake pressure and IVC timing are the same for all cases.

The in-cylinder pressure from the detailed physical model and the crank angle of fifty are shown in figures 5.14 and 5.15 respectively. When NVO increases, the amount of trapped residual gas as well as the in-cylinder gas temperature increases. The trapped residual gas dilutes the in-cylinder mixture leading to lower equivalence ratio. The fresh charge is mixed with trapped residual gas which contains oxygen, and as a result the equivalence ratio in the cylinder decreases as NVO increases. Combustion timing is advanced when the in-cylinder gas temperature increases with larger amounts of trapped residual gas. The peak pressure increases due to advanced combustion timing until NVO reaches 40 CAD, however, the peak pressure then decreases and the combustion duration increases due to lower equivalence ratio of the trapped mixture at NOVs higher than 40 CAD. The effects of NVO duration on IMEP is shown in Figure 5.15. IMEP increases as NVO duration increases until NVO reaches 40 CAD and it reduces afterwards. The main reason is the decreased equivalence ratio of the trapped mixture due to higher NVO durations. The DPM is validated further against the measured steady-state operating points for NVO durations and injected fuel energies listed in Table 3.1. As shown in Figure 5.16, the detailed physical model is accurate enough to be careful for HCCI combustion analysis as it captures combustion timing with average errors of

1.1 CAD. IMEP values from DPM are compared to the measurements in Table 3.1. The DPM predicts higher values for IMEP as higher combustion efficiencies are predicted by the DPM. The DPM captures IMEP with average error of 0.25 Bar (see Figure 5.17). The results in this chapter indicates that the DPM can be used as virtual setup for control development and implementation.

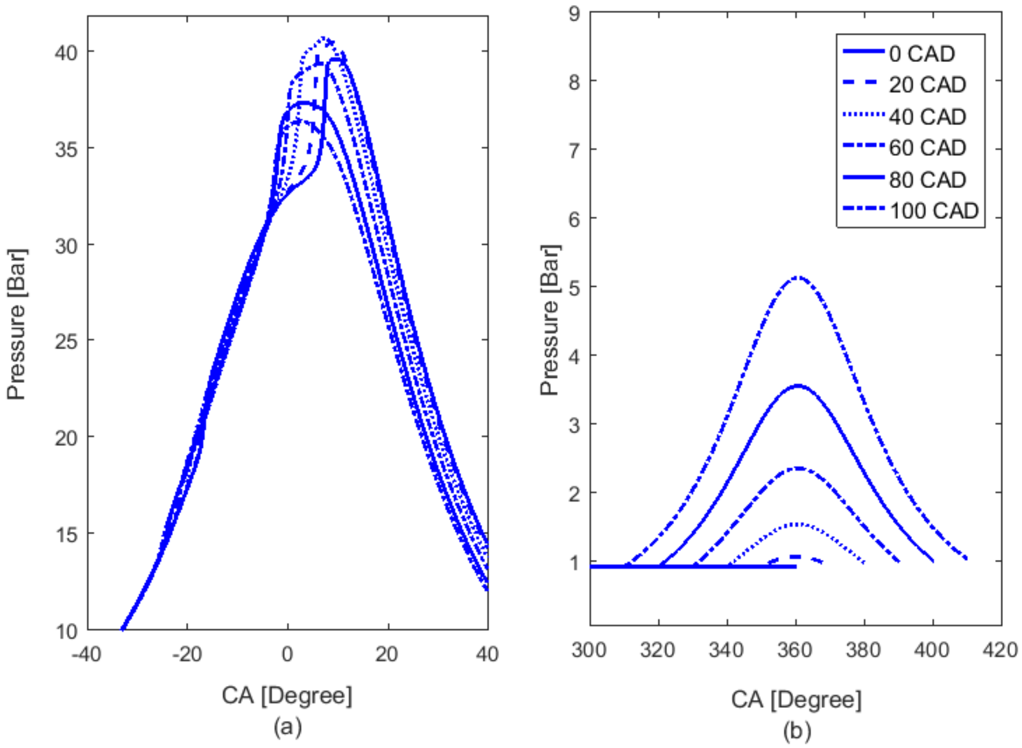

Figure 5.14: Pressure Trace of HCCI engine with variable NVO at 825 RPM (a) combustion (b) re-compression [$\mathrm{Em}_{\mathrm{finj}}$=0.25 kJ]

5.6 Discussion

A detailed multi-zone HCCI model has been developed and implemented in a full cycle simulation of an HCCI engine for predicting HCCI combustion characteristics and subsequent controller development. Validation of the DPM against experiments in a single cylinder research engine have been conducted over a wide range of en-

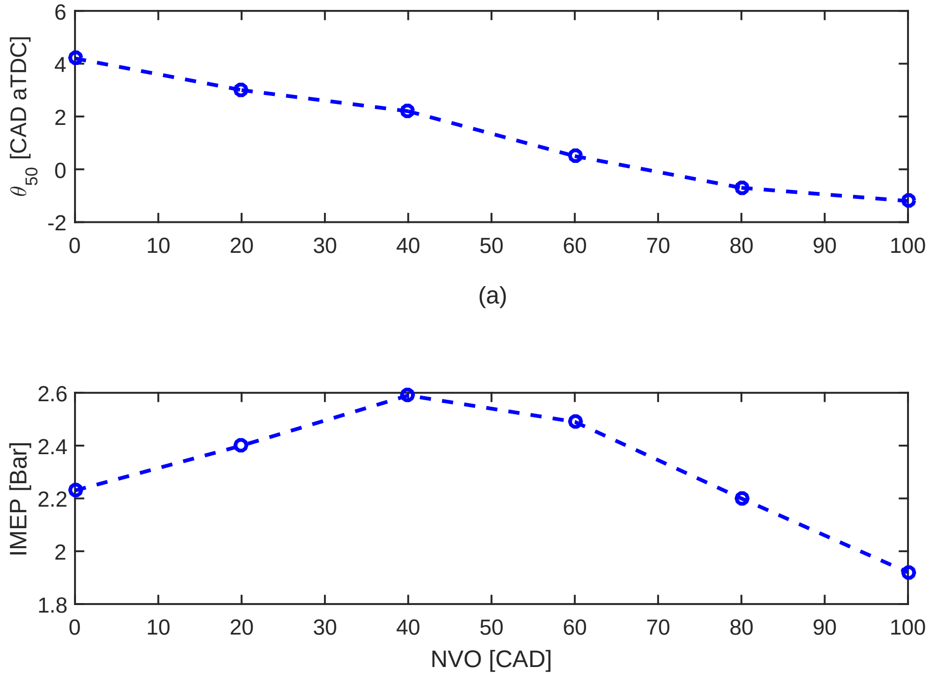

(a)

(b)

Figure 5.15: Effects of symmetric NVO on (a) combustion timing (θ_{50}) and (b) IMEP at 825 RPM [$\mathrm{Em_{finj}}$=0.25 kJ]

gine loads and valve timings at 825 RPM that shows good agreement. The DPM shows that VVT modulates the amount of trapped residual gas and is one effective way for HCCI combustion timing control. Use of a VVT with NVO strategy is investigated with DPM. The simulation results indicate that VVT with NVO affects combustion timing and IMEP considerably and will be used as an effective actuator for combustion timing control.

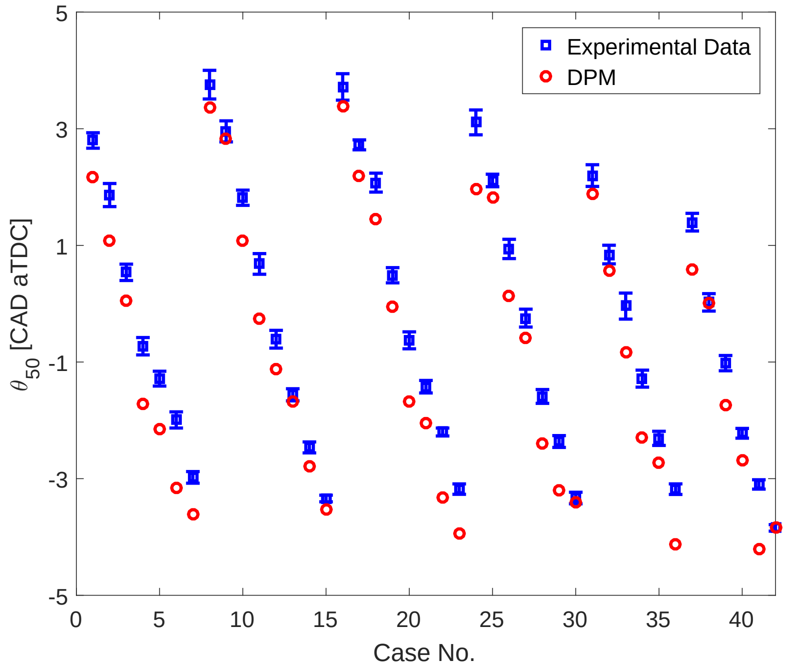

Figure 5.16: Steady state validation of the DPM, combustion timing (θ_{50})

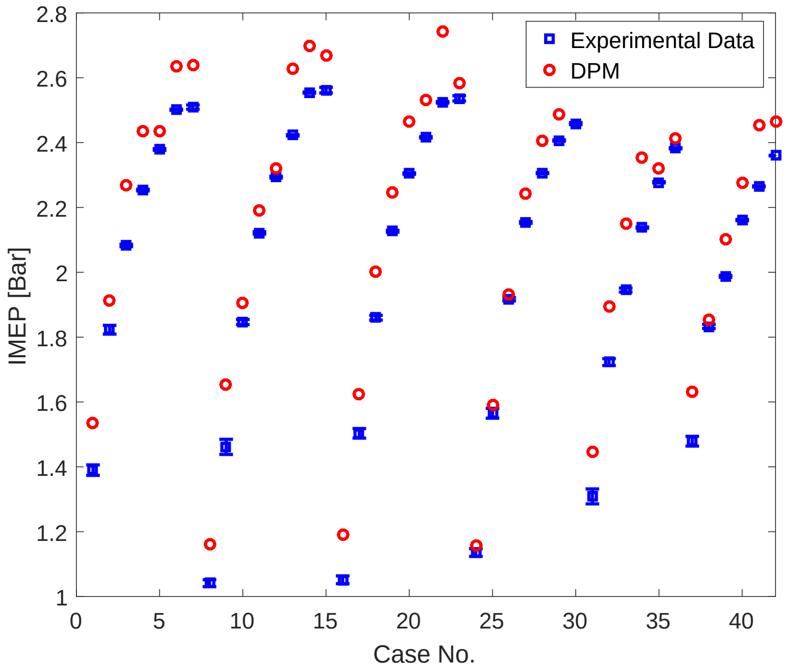

Figure 5.17: Steady state validation of the DPM, load (IMEP)

Chapter 6

Combustion Timing Control[1]

Combustion timing is challenging to control in HCCI engines. There are many factors affecting combustion timing in HCCI engines including mixture temperature, pressure and composition at IVC. In this chapter, NVO is used as the main actuator to adjust the amount of trapped residual gas for combustion timing control. Two controllers are designed for HCCI combustion timing control: PI and feedforward/feedback. First, PI controller gains are tuned in simulation using the DPM and the controller is then implemented on a single cylinder engine. Next, the PI controller performance is improved by developing a feedforward/feeback controller that relates combustion timing to the valve timing using a control oriented model. The controller uses combustion timing as feedback to zero the steady state error using a constant gain integrator. Experimental results show good tracking of combustion timing for both controllers.

6.1 PI controller

A PI controller is developed that uses θ_{50} as a measured input and adjusts the intake and exhaust valves timing (IVO, EVC) using symmetric NVO to get a varied

---

[1] This chapter is based on [42, 193]

amount of the trapped residual gas in the cylinder to adjust the combustion timing. SNVO is used as a variable valve timing strategy. Using simulation the DPM is used to design a PI controller for θ_{50} control. The controller is a standard PI control that is synchronous with the engine cycle (k)

$$u_k = u_{k-1} + (k_p + 0.5k_iT)e_k + 0.5k_iTe_{k-1} \tag{6.1}$$

$$EVC_k = EVC_{k-1} + u_k \tag{6.2}$$

$$IVO_k = IVO_{k-1} - u_k \tag{6.3}$$

where $e = \theta_{50}(Ref) - \theta_{50}(Meas)$ is the error and T, k_p and k_i are the sample time, proportional and integral gains respectively (k_p = 2 and k_i = 3). The designed controller is tested in simulation on the DPM [64] and the tracking performance of the designed controller is shown in Figure 6.1. The PI controller can track the desired θ_{50} trajectory with a rise time of 3 to 4 engine cycles and the maximum overshoot of 0.8 CAD. No steady state error is observed which is attributed to the integral term. The effect of measurement noise on tracking performance of the PI controller is studied by adding a Gaussian disturbed noise with standard deviation of 1.2 CAD to the measurement of θ_{50} after cycle 55 (see Figure 6.1(a)). The noise level was determined based on the available experimental data. The PI controller maintained tracking despite the measurement noise in the feedback signal.

The controller is also tested with the disturbances of varying engine loads and varying engine speed. In Figures 6.2 and 6.3, the disturbance rejection properties of both controllers are compared for positive and negative disturbance step changes.

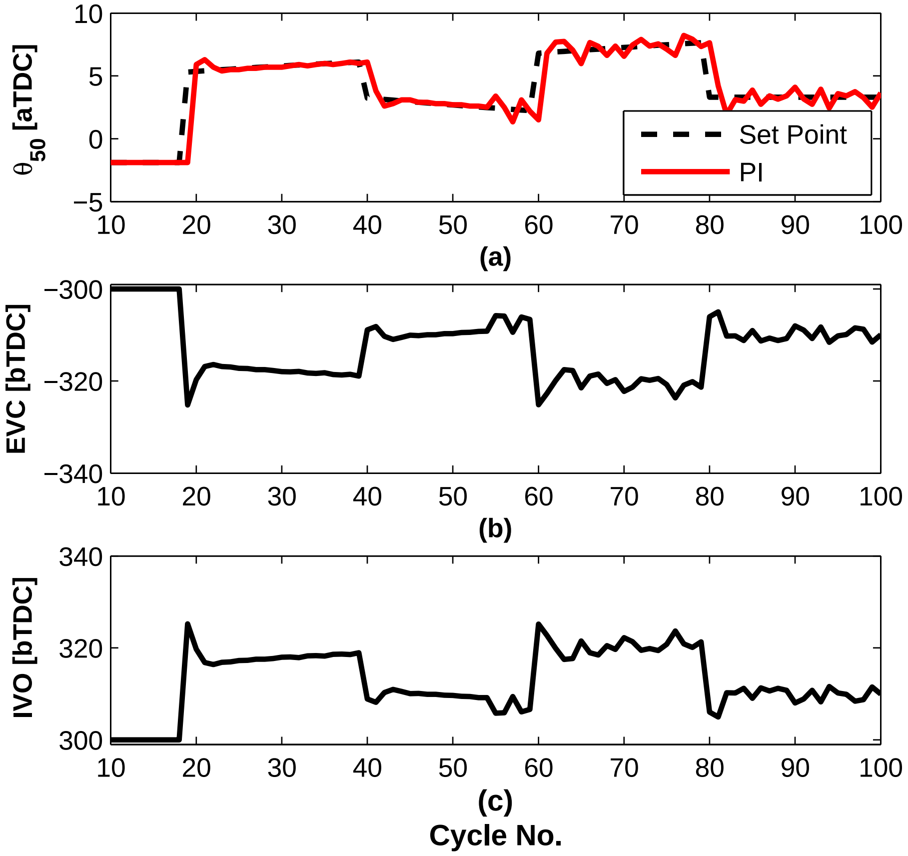

Figure 6.1: Simulation: Tracking Performance of PI controller (a) Engine Plant Output (b and c) controller inputs

The results show that the PI controller has a reasonable disturbance rejection characteristic and the integral action causes the steady state error to go zero.

6.2 Feedforward/Feedback controller

The controller performance in tracking the combustion timing is improved with a Feedforward/Feedback controller. Valve timing is the main actuator and combustion timing is used as feedback to the controller. Similar to the PI controller, symmetric NVO is used as variable valve timing strategy. The controller is based on a model that relates combustion timing to the valve timing in feedforward and

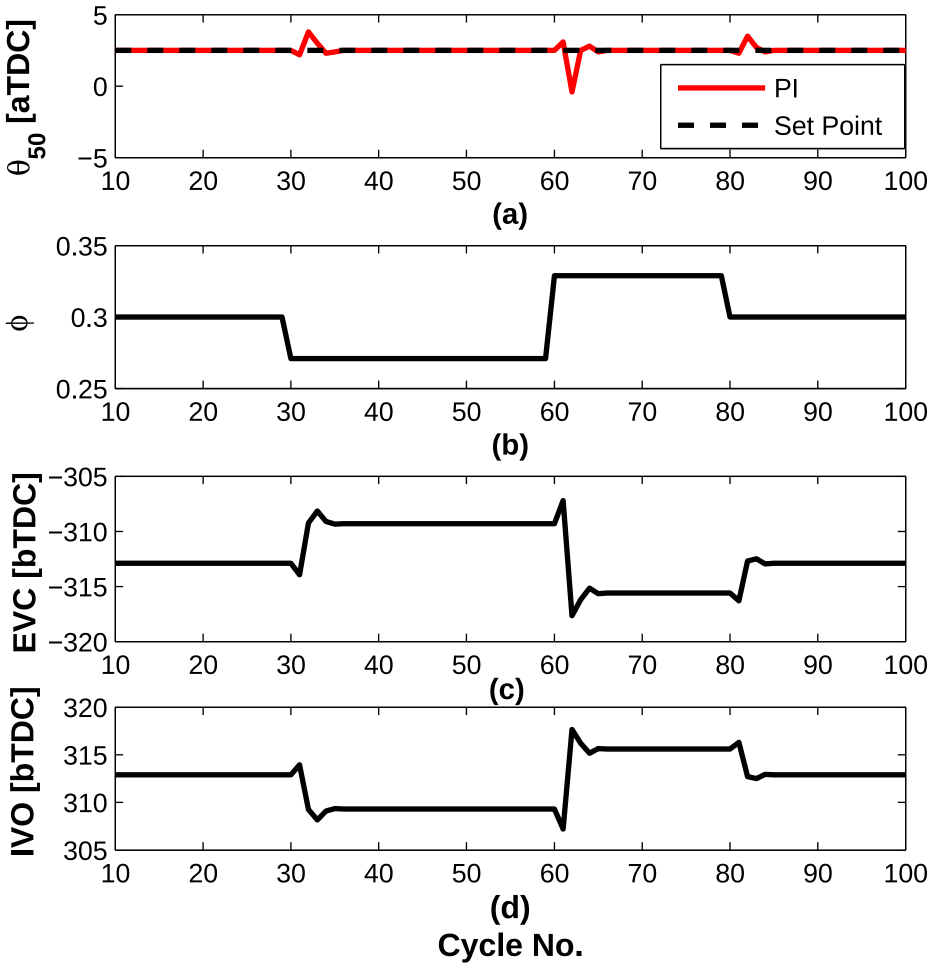

Figure 6.2: Simulation - Disturbance rejection: fuel equivalence ratio (a) θ_{50} (b) Disturbance (c and d) Controller Inputs

combustion timing is used as feedback to zero the steady state error using a constant gain integrator.

First, a control oriented model is developed for the feedforward part of the controller. The model inputs are intake manifold pressure and temperature, fueling rate, engine speed and valve timing and the model output is combustion timing. The crank angle at which 50% of the energy is released, θ_{50}, is used as an indicator for combustion timing. Fueling rate and engine speed variations are considered as

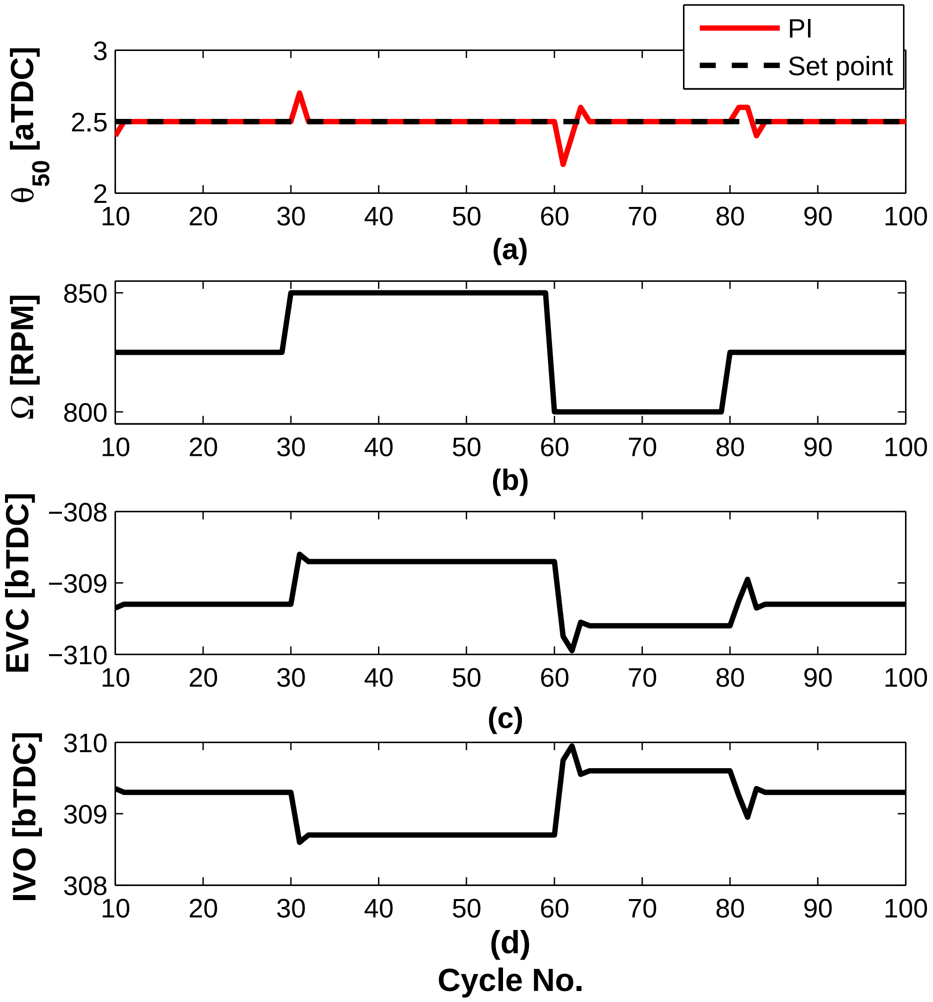

Figure 6.3: Simulation - Disturbance rejection: Engine speed (a) θ_{50} (b) Disturbance (c and d) Controller Inputs

disturbances to the plant. The model is developed for n-heptane fuel and can be easily reformulated for other fuels since it is parameterized by the DPM explained in Chapter 5.

Mixture temperature at IVC is determined first since it has an important effect on HCCI combustion timing. It is assumed that the inducted premixed air fuel is mixed with the trapped residual from the previous cycle instantaneously at the

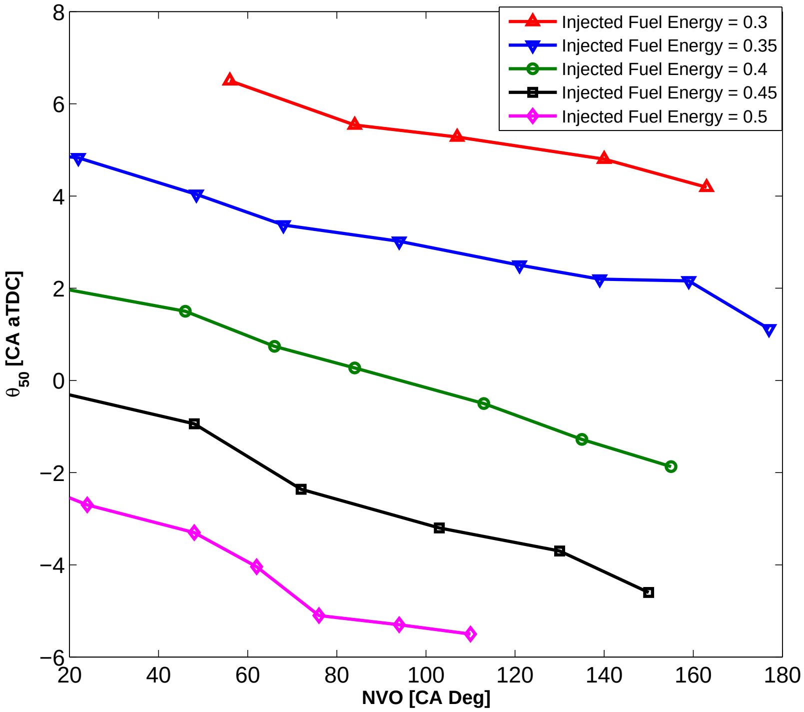

Figure 6.4: The implemented lookup table [n = 825 RPM]

instant of IVC. Mixture temperature at IVC is calculated as:

$$T_{IVC} = \frac{\lambda m_{fuel} L_{st} c_{p,air} T_{int} + \frac{P_{em} V_{EVC}}{R_{resid}} c_{p,resid} + m_{fuel} c_{p,fuel} T_{fuel}}{\lambda m_{fuel} L_{st} c_{p,air} + m_{fuel} c_{p,fuel} + \frac{P_{em} V_{EVC}}{R_{resid} T_{em}} c_{p,resid}} \tag{6.4}$$

and the residual gas mass fraction is calculated from:

$$x_{resid} = \frac{\frac{P_{em} V_{EVC}}{R_{resid} T_{em}}}{\frac{P_{em} V_{EVC}}{R_{resid} T_{em}} + m_{fuel} + \lambda m_{fuel} L_{st}} \tag{6.5}$$

A simplified integrated Arrhenius model [194, 195] is used for HCCI combustion timing simulation and for n-heptane it is [196]:

$$K_{th} = \int_{IVC}^{SOC} \frac{A exp\left(\frac{-E_a}{R_u T_{TDC}}\right) [C_7 H_{16}]^a_{TDC} [O_2]^b_{TDC}}{\omega} d\theta \tag{6.6}$$

where ω is the engine speed and the parameters A, $\frac{Ea}{Ru}$, a and b are empirical constants determined from literature [195, 196] and are listed in Table 6.1. Oxygen and

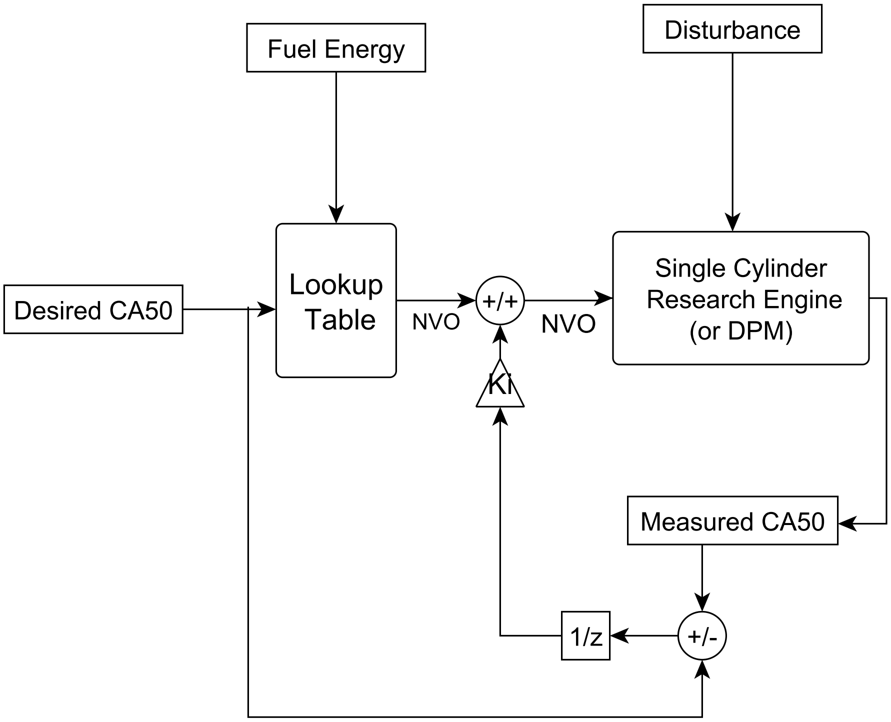

Figure 6.5: Controller structure

fuel concentrations at TDC are determined from:

$$[O_2]_{TDC} = \frac{0.0073 m_{air}}{V_{TDC}} \tag{6.7}$$

$$[C_7H_{16}]_{TDC} = \frac{m_{fuel}}{100 V_{TDC}} \tag{6.8}$$

where V_{TDC} is the in-cylinder volume at TDC and m_{air} is calculated as:

$$m_{air} = \lambda m_{fuel} L_{st} \tag{6.9}$$

and L_{st} is 15.1 for n-heptane.

Substituting eqns. 6.7 and 6.8 into eqn. 6.6, the Start of Combustion (SOC), θ_{SOC}, is calculated as:

$$\theta_{SOC} = \theta_{IVC} + \frac{\omega K_{th} exp\left(\frac{E_a}{R_u T_{TDC}}\right)}{A(\frac{m_{fuel}}{100V_{TDC}})^a(\frac{0.0073m_{air}}{V_{TDC}})^b} + \theta_{Offset} \tag{6.10}$$

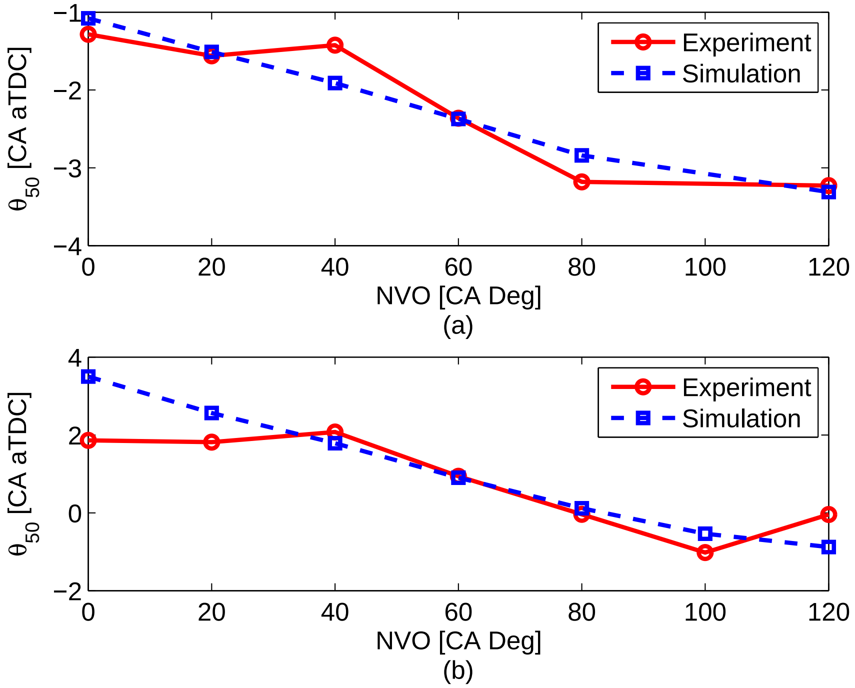

Figure 6.6: Comparison of predicted and measured θ_{50} for NVO variation (a) Injected Fuel Energy = 0.46 kJ, (b) Injected Fuel Energy = 0.39 kJ [n = 791 RPM]

DPM simulations at over 150 engine operating points between $2.5 \leq \lambda \leq 4$ and $0 \leq \text{NVO} \leq 100$ are used to parameterize θ_{offset} and K_{th} and are listed in Table 6.1. These values are obtained by minimizing the difference between θ_{SOC} from the DPM and eqn. 6.10. In eqn. 6.10, T_{TDC} is calculated assuming isentropic compression as:

$$T_{TDC} = \left(\frac{V_{IVC}}{V_{TDC}}\right)^{\gamma-1} T_{IVC} \tag{6.11}$$

where γ is the heat capacity ratio of the trapped mixture. It is also assumed that once the predetermined threshold, K_{th}, in eqn. 6.10 is exceeded, the combustion process is initiated. Combustion duration, $\Delta\theta$, is calculated based on a correlation [72] as:

$$\Delta\theta = C(1 + x_{resid})^{D} \lambda^{E} \tag{6.12}$$

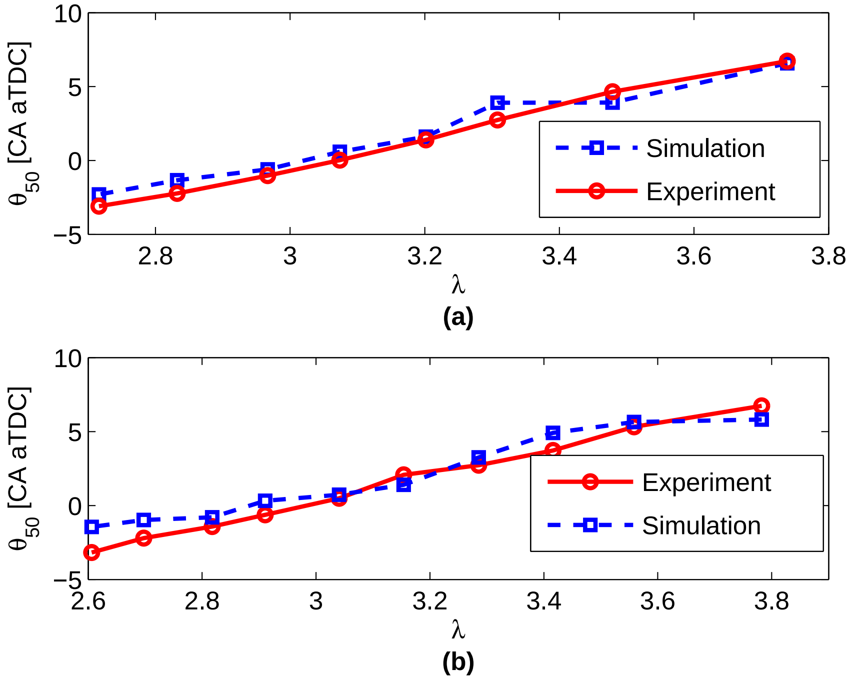

Figure 6.7: Comparison of predicted and measured θ_{50} for λ variation (a) NVO= 100 CAD (b) NVO= 40 CAD [n= 791 RPM]

where C, D, and E are constants which are determined from experimental data and are listed in Table 6.1. Finally, θ_{50} is calculated as:

$$\theta_{50} = \theta_{SOC} + 0.5\Delta\theta \tag{6.13}$$

Table 6.1: Model parameters

$A\ [\left(\frac{\mathrm{mol}}{\mathrm{cm}^3}\right)^{1-\mathrm{a}-\mathrm{b}} \mathrm{Sec}^{-1}]$	4.63×10^{11}
$\frac{Ea}{Ru}$ [K]	1.5×10^{3}
a [-]	0.25
b [-]	1.5
K_{th} [-]	2.3×10^{-6}
θ_{offset} [rad]	2.9613
C [-]	6.72
D [-]	0.25
E [-]	-0.12

The controller uses combustion timing, θ_{50}, as feedback and adjusts the trapped

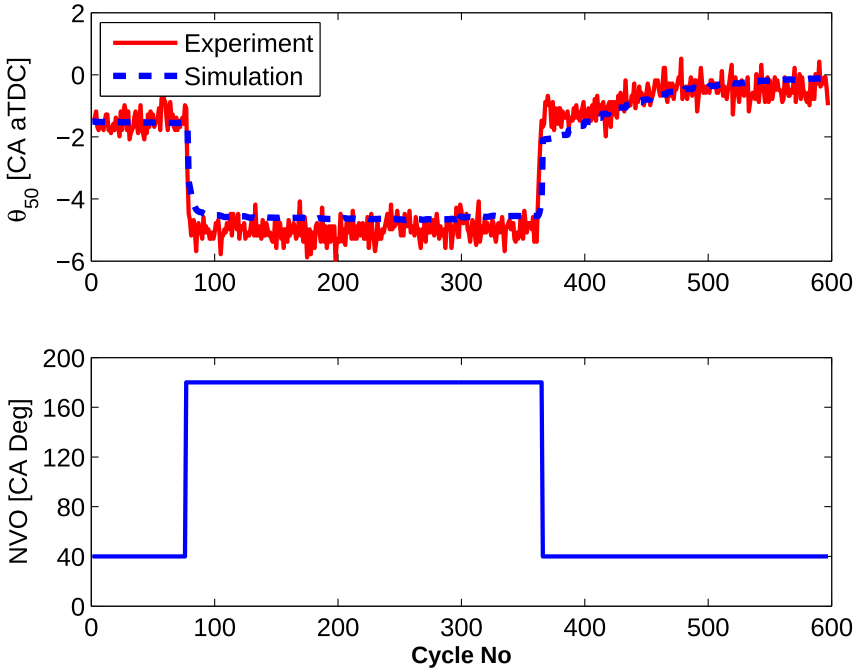

Figure 6.8: NVO duration step: Comparison between predicted and measured θ_{50} [n=788 RPM, and Injected fuel energy=0.45 kJ]

residual gas mass fraction with EVC and IVO timing for combustion timing control. Measured cylinder pressure is used to determine combustion timing. However, combustion timing is needed as a function of in-cylinder volume at EVC. First, λ that appears in eqns. 6.5, 6.9 and 6.10, is written as a function of in-cylinder volume at EVC:

$$\lambda = 0.0662 \frac{\eta_v P_{int}(V_{IVC} - V_{EVC})}{R_{int} T_{int} m_{fuel}} \tag{6.14}$$

where volumetric efficiency (η_v) is calculated as in [137]. Substitution of eqns 6.12, 6.5, 6.10 and 6.14 into eqn 6.13, results in combustion timing (θ_{50}) expressed as a

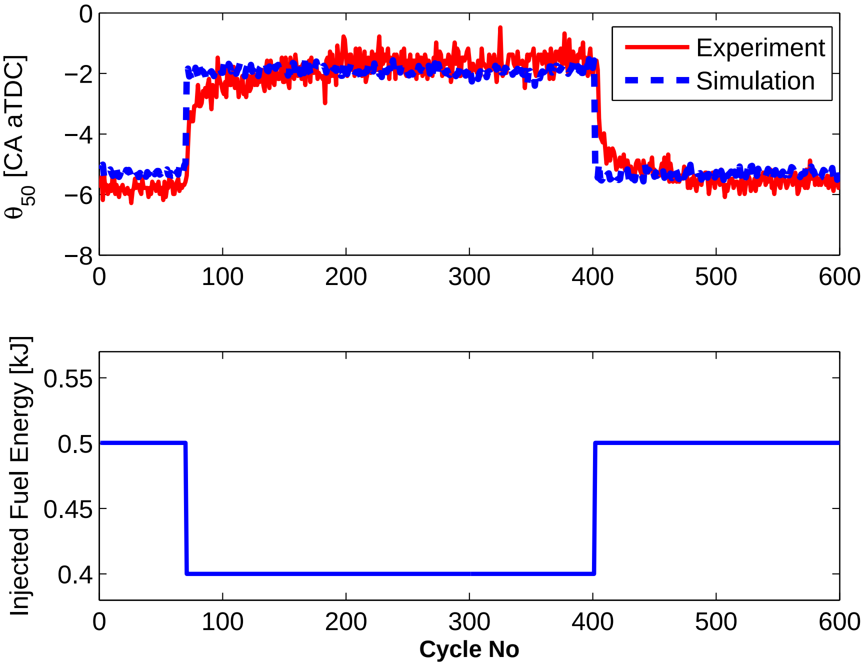

Figure 6.9: Fueling rate step: Comparison between predicted and measured θ_{50} [n=791 RPM, NVO=120 CA Deg]

function of in-cylinder volume at EVC as:

$$\theta_{50} = \frac{\omega K_{th}}{A} \times \frac{exp\left(\frac{E_a R_u^{-1}\left(\frac{V_{IVC}}{V_{TDC}}\right)^{1-\gamma}}{\frac{\frac{\eta_v P_{int}(V_{IVC}-V_{EVC})}{R_{int}} c_{p,air} + \frac{P_{em}V_{EVC}}{R_{resid}} c_{p,resid} + m_{fuel} c_{p,fuel} T_{fuel}}{\frac{\eta_v P_{int}(V_{IVC}-V_{EVC})}{R_{int}T_{int}} c_{p,air} + m_{fuel} c_{p,fuel} + \frac{P_{em}V_{EVC}}{R_{resid}T_{em}} c_{p,resid}}}\right)}{\left(\frac{m_{fuel}}{100V_{TDC}}\right)^a \left(\frac{0.0073\frac{\eta_v P_{int}(V_{IVC}-V_{EVC})}{R_{int}T_{int}}}{V_{TDC}}\right)^b}$$
$$+ 0.5C\left(1 + \frac{\frac{P_{em}V_{EVC}}{R_{resid}T_{em}}}{\frac{P_{em}V_{EVC}}{R_{resid}T_{em}} + m_{fuel} + \frac{\eta_v P_{int}(V_{IVC}-V_{EVC})}{R_{int}T_{int}}}\right)^D \times$$
$$\left(0.0662\frac{\eta_v P_{int}(V_{IVC}-V_{EVC})}{R_{int}T_{int}m_{fuel}}\right)^E + \theta_{IVC} + \theta_{Offset} \tag{6.15}$$

Given a desired θ_{50}, it is difficult to solve eqn. 6.15 for V_{EVC} so Trust Region Reflective Algorithm [197] is used for solving this equation. EVC timing is determined from slider crank mechanism [84] equation using V_{EVC} from eqn. 6.15 as:

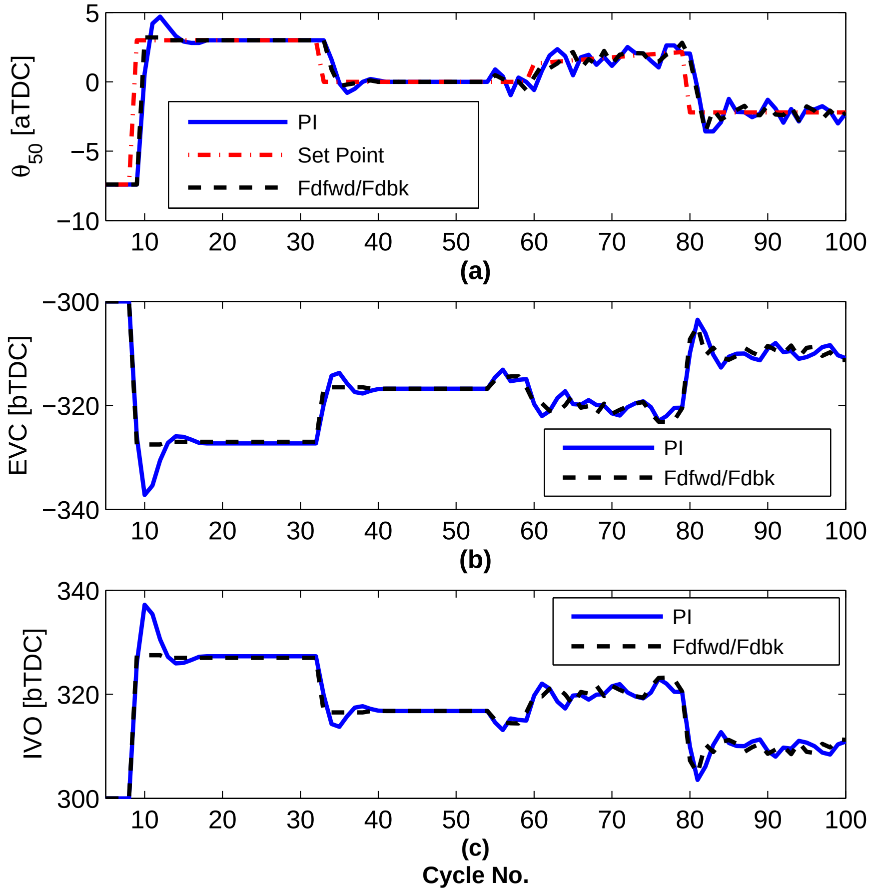

Figure 6.10: Simulation - Tracking performance of the manually tuned PI and feedforward/feedback controllers (a) θ_{50} as controller output (b and c) Controller Inputs [n= 850 RPM, Injected Fuel Energy=0.5 kJ]

$$V_{EVC} = V_c + \frac{\pi B^2}{4}[l + a - a\cos\theta_{EVC} - \sqrt{l^2 - (a\sin\theta_{EVC})^2}] \tag{6.16}$$

The slider crank mechanism equation was explained in eqn. 5.11 Chapter 5. The IVO timing is

$$\theta_{IVO} = -\theta_{EVC} \tag{6.17}$$

since symmetric NVO is implemented. A constant gain discrete time integrator is

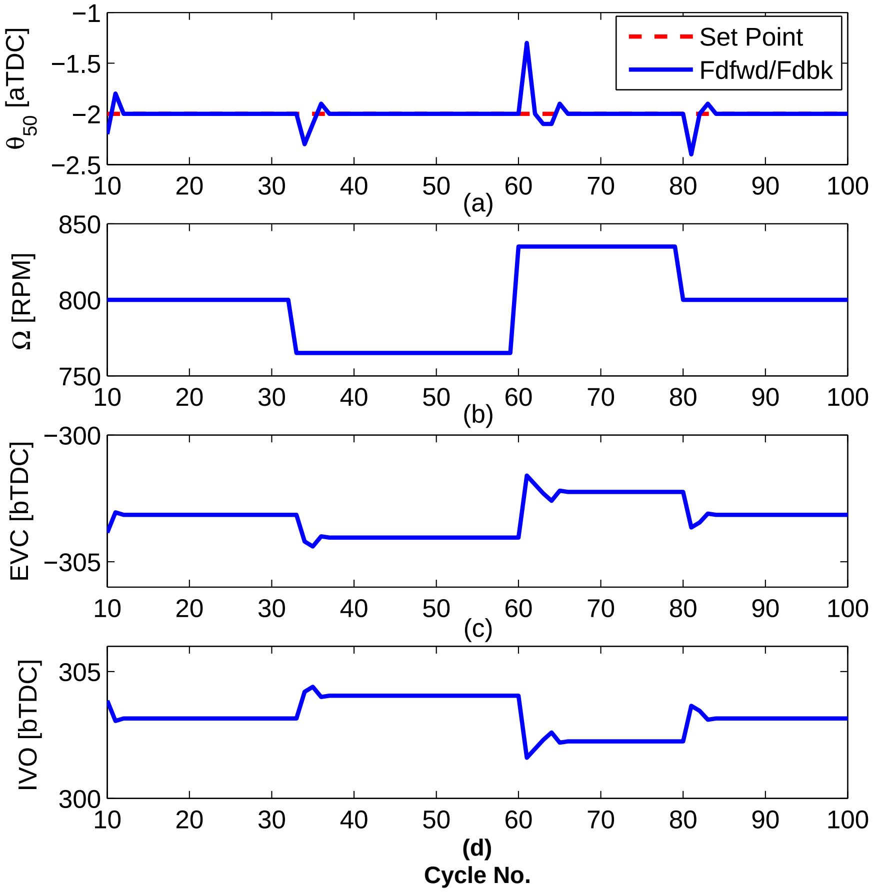

Figure 6.11: Simulation - Disturbance rejection: Engine speed (a) θ_{50} as controller output (b) Disturbance (c and d) Controller Inputs

used to zero the steady error as:

$$u_k = u_{k-1} + k_i T e_k \tag{6.18}$$

$$\theta_{EVC,k} = \theta_{EVC,k-1} + u_k \tag{6.19}$$

where e = $\theta_{50}(Ref) - \theta_{50}$(Meas) is the error and T, k and k_i are the sample time, cycle number, and integral gain respectively (k_i = 3 is tuned and $\theta_{EVC,1}$ is initialized using eqns 6.16 and 6.17). For realtime implementation on the engine,

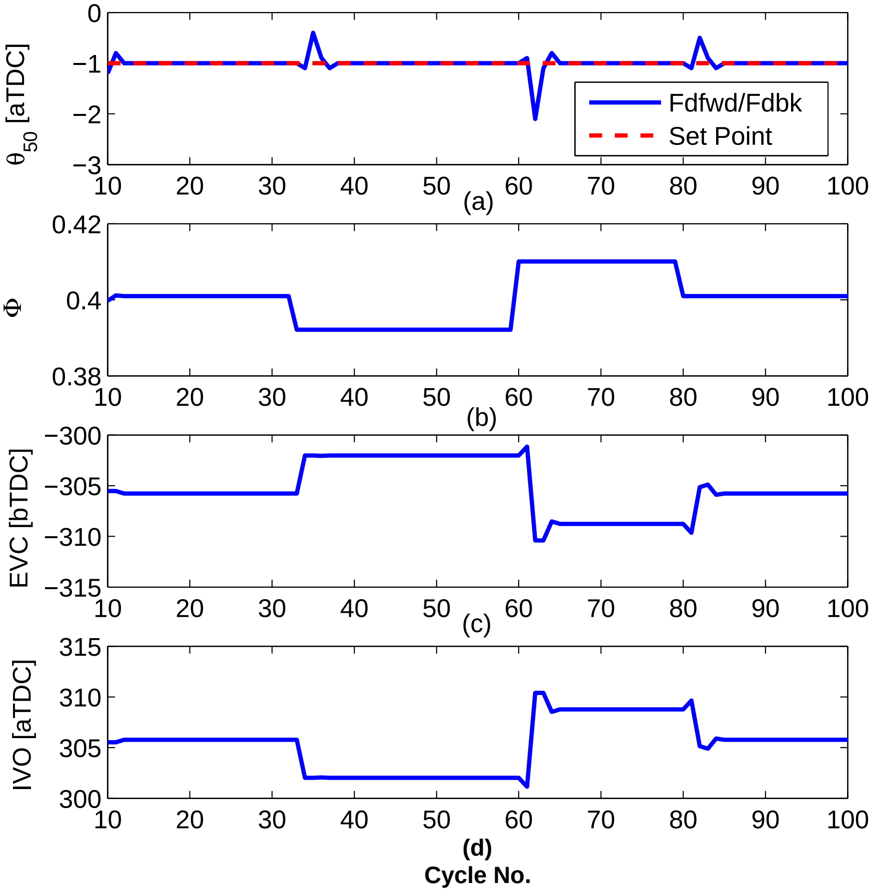

Figure 6.12: Simulation - Disturbance rejection: Engine load (a) θ_{50} as controller output (b) Disturbance (c and d) Controller Inputs

eqns. 6.15 and 6.16 are solved for different desired combustion timings and fueling rates and the values are tabulated in a lookup table. A linear interpolation lookup table is used to reduce realtime processing. The lookup table is shown in Figure 6.4 and the controller structure is shown in Figure 6.5.

The model accuracy is investigated before control implementation. Both steady-state and transient performance of the model are tested by comparing predicted θ_{50} to the experiments. The test points used for model validation have not been used for model parametrization. For steady state validation, fueling rate is kept constant and

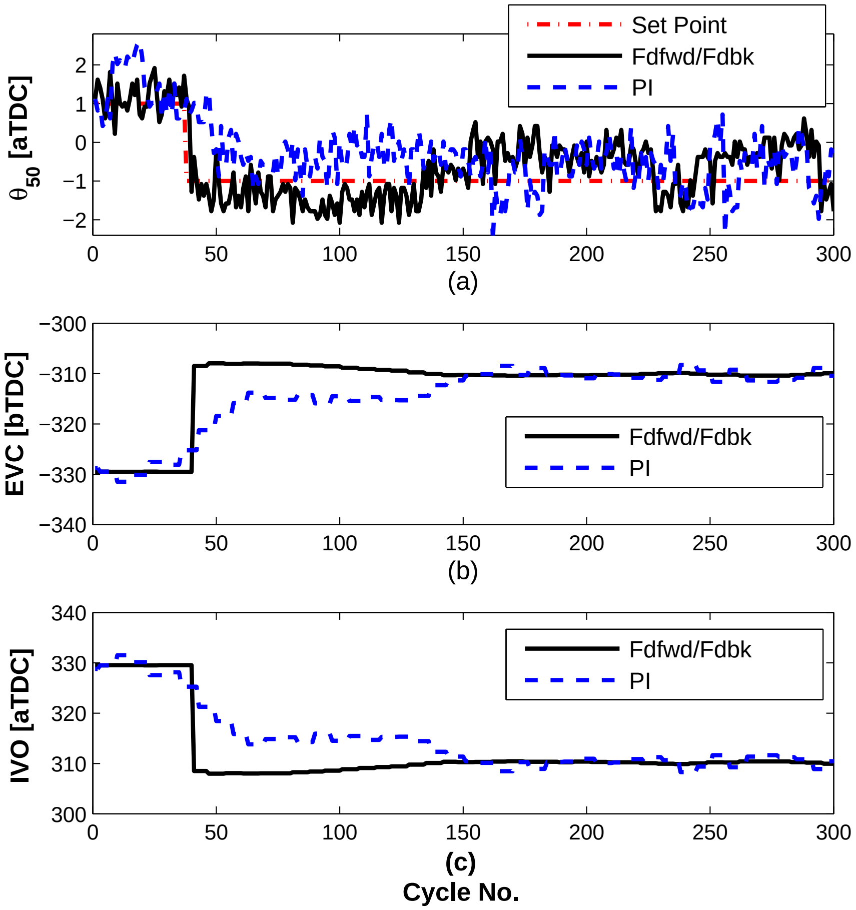

Figure 6.13: Experiment - Tracking performance of the manually tuned PI and feedforward/feedback controllers (step down) (a) θ_{50} as controller output (b and c) Controller Inputs[n= 788 RPM, Injected Fuel Energy=0.4 kJ]

the NVO duration is varied. Figure 6.6 shows θ_{50} versus the NVO duration for two different fueling rates and the model accuracy is sufficient for control purposes. The difference between measured and the predicted combustion timing is attributed to the assumptions used in the Arrhenius integral simplification. In-cylinder residual gas mass fraction increases when NVO timing increases causing mixture temperature at IVC to increase and the combustion timing to advance. The model is further validated by holding the valve timing constant and varying the fueling rates. Figure 6.7 shows the variation of θ_{50} with respect to λ for two different NVOs. The

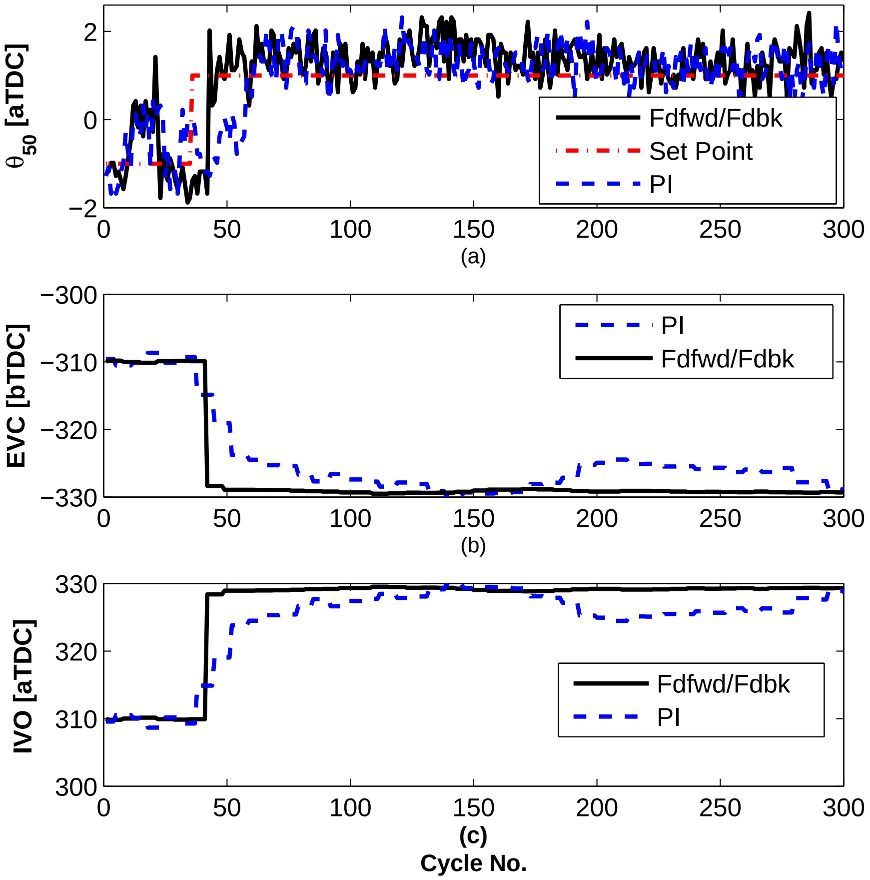

Figure 6.14: Experiment - Tracking performance of the manually tuned PI and feedforward/feedback controllers (step up) (a) θ_{50} as controller output (b and c) Controller Inputs [n= 788 RPM, Injected Fuel Energy=0.4 kJ]

reactivity of the mixture tends to increase from lean to rich conditions.

The transient response to steps in NVO are shown in Figure 6.8. As expected, θ_{50} advances when NVO duration increases. The resulting θ_{50} of the model and engine are plotted showing that the model captures the transient dynamics accurately. Experimental and simulated combustion timing for transient fueling rate are compared in Figure 6.9. The simulation model reaches the final value earlier compared to the experimental data since the fuel transport dynamics [72] are not considered in the model. Predicted θ_{50} is in good agreement with the experiment and the model captures the overall dynamic trend of changes in fueling rate sufficiently accurately for control purposes.

The feedforward/feedback controller performance in tracking the desired combustion timing is examined in simulation. Combustion timing (θ_{50}) as the controller inputs and valve timing (EVC, IVO) as the main actuators for varying the amount of the residual gas in the cylinder are used for cycle by cycle combustion timing control. The DPM explained in chapter 5 is used to test and tune the performance of the controller using simulation. Figure 6.10 shows the controller tracking performance for combustion timing set point changes. Both the PI and Fdfwd/Fdbk controllers track the desired trajectory with no steady state error but the new Feedforward/Feedback controller has less overshoot. The effect of measurement noise on the tracking performance of both controllers is studied by adding a Gaussian noise with standard deviation of 1.2 CAD to the measured θ_{50} starting at cycle 55 (see Figure 6.10). The noise level is chosen based on noise levels in typical experimental data. The Feedforward/Feedback controller has less oscillations than the PI controller when there is measurement noise. The disturbance rejection properties of the controller are evaluated for step changes in the engine speed and load. The disturbance rejection of the Feedforward/Feedback controller is tested for positive and negative step changes in Figures 6.11 and 6.12 in simulation. The Feedforward/Feedback controller rejects disturbance from the engine speed and engine load by maintaining θ_{50} within 1 crank angle degree.

The Feedforward/Feedback controller is experimentally tested and compared to the PI controller. First the desired combustion timing is advanced by two degrees (see figure 6.13) and then it returned back to its original value (see figure 6.14). Both controllers track the desired trajectory but the Feedforward/Feedback controller has faster response and smoother tracking performance in both cases. Theses results indicate that the Feedforward/Feedback controller performance has improved tracking of the desired combustion timing and performs well in maintaining a desirable engine combustion timing during load and engine speed disturbances.

6.3 Discussion

PI and Fdfwd/Fdbk controllers that control HCCI combustion timing by varying valve timing cycle-by-cycle is developed using a detailed engine model and then validated on a single cylinder engine. The PI and Fdfwd/Fdbk gains are determined using DPM in simulation and the same gains are used when the controllers implemented. Performance of the Fdfwd/Fdbk controller is compared to the PI controller and the results show that the Fdfwd/Fdbk controller performance has improved tracking of the desired combustion timing and performs well in maintaining a desirable engine combustion timing during load and engine speed disturbances.

Chapter 7

Combustion Timing and Load Control[1]

A Model Predictive Control (MPC) for combustion timing and load control of a single cylinder HCCI engine is designed. First, a nonlinear control oriented model for cycle by cycle combustion timing and output work control is developed. The control oriented model is developed based on the DPM (see chapter 5) using physical model order reduction techniques. Since the detailed physical model is based on physics and has a chemical kinetic model of the fuel this will allow different fuels and engine configurations to be easily examined if the appropriate fuel chemical kinetics are known. In previous studies [18, 22, 46, 50, 51, 61, 63, 65, 87], either knock integral [198, 199] or Arrhenius type models [65, 200] are used for combustion timing prediction. Such models rely on extensive experimental data for parametrization and they are only valid for limited engine operating ranges. For the case studied here with primary reference fuels, the reaction mechanism is available in [98]. The nonlinear control oriented model is then linearized around one operating point and engine experimental validation results show that it has sufficient accuracy for combustion timing and output work prediction. Then SNVO is

---

[1] This chapter is based on [25]

used for HCCI combustion timing control while the fueling rate is used for output work control. Again, the crank angle of fifty percent fuel mass fraction burned, θ_{50}, is used as the cycle by cycle measurement of combustion timing. In simulation, the DPM, presented in chapter 5, provides θ_{50} and IMEP while in the experiment, cylinder pressure is used. A schematic of the steps needed to obtain the control oriented model are shown in Figure 7.1. MPC is used as it has the ability to incorporate constraints on inputs and outputs explicitly. This approach is very useful in this highly constrained problem. Laguerre functions are mainly used for the cases when the discrete-time impulse response of a dynamic system is available by a Laguerre model [95]. This approach simplifies the traditional MPC algorithm used in [18, 21, 92, 93] and reduces the computation time [95] useful for the engine real time implementation. The controller performance is tested in simulation with noisy measurement considering constraints on inputs and outputs. The ability of the controller to reject engine load and speed disturbances is examined. Finally the controller is implemented on the dSPACE MicroAutoBox to control the single cylinder research engine and the results are compared to the PI and feedforward/feedback controllers developed in chapter 6.

7.1 Control Oriented Model

The control oriented model developed for MPC is different from the one developed for Feedforward/Feedback controller. A discrete nonlinear control oriented model is developed based on the DPM in chapter 5 and the methods described in [18, 50, 201, 202, 7] for model order reduction. The DPM has 483 states with 5 inputs and 4 outputs as described in chapter 5. For the control oriented HCCI

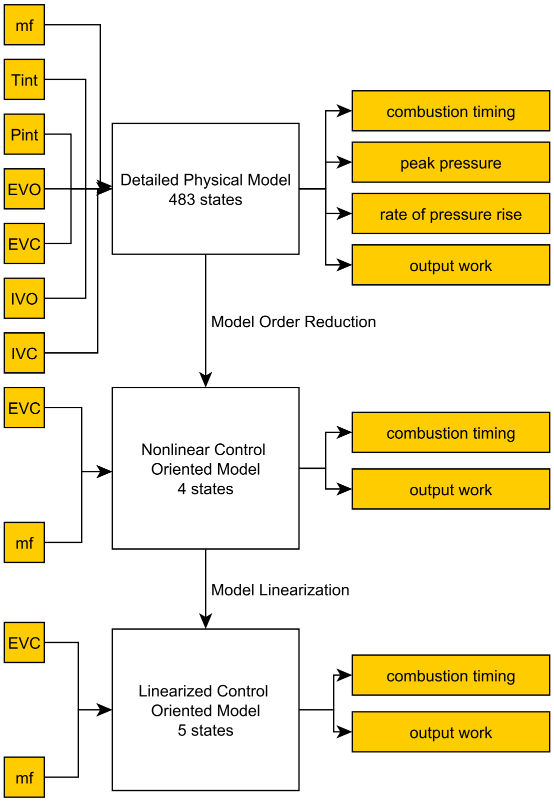

Figure 7.1: Control Oriented Model development steps

engine model, compression, combustion and expansion are modeled as a sequence of continuous processes. The four states of the nonlinear control oriented model are: residual gas mole fraction (α), fuel equivalence ratio (ϕ), in-cylinder temperature at IVC (T_{IVC}) and crank angle of fifty percent fuel mass fraction burned (θ_{50}). These states are found to be important variables affecting HCCI combustion [9, 13]. The control oriented model can be easily modified for other fuels by a model parametrization using the DPM with the appropriate fuel chemical kinetics. Mixture temperature and composition at the beginning of compression are determined first by assuming that the fresh intake charge and residual gas from previous cycle mix instantaneously in the cylinder at IVC. Mixture composition at the beginning of compression is assumed to be:

$$\begin{aligned}
&\phi_k C_7H_{16} + 11(O_2 + 3.76N_2) + \frac{\alpha_k(\phi_k + 52.36)}{(4\phi_{k-1} + 52.36)(1 - \alpha_k)}(7\phi_{k-1}CO_2 \\
&+ 8\phi_{k-1}H_2O + 41.36N_2 + 11(1 - \phi_{k-1})O_2)
\end{aligned} \tag{7.1}$$

where ϕ and k represent the fuel equivalence ratio and cycle number respectively. Mixture composition in eqn. 7.1 is determined by assuming that the exhaust gas fuel equivalence ratio is the same as mixture fuel equivalence ratio before combustion [203]. The residual gas mole fraction, α, is calculated as:

$$\alpha_k = \frac{\frac{P_{exh,k-1}V_{EVC,k-1}}{T_{RES,k-1}}}{\frac{P_{int,k}V_{IVC,k}}{T_{IVC,k}}}. \tag{7.2}$$

Mixture temperature at IVC is determined by using the intake charge composition and applying the first law of thermodynamics to the system. In-cylinder gas temperature at IVC, T_{IVC}, is calculated as:

$$T_{IVC,k} = \frac{C_1 T_{int,k} + \alpha_k C_2 T_{RES,k-1}}{C_1 + \alpha_k C_2} \tag{7.3}$$

where

$$\begin{aligned}
C_1 &= \phi_k C_{p,C_7H_{16}} + 11C_{p,O_2} + 41.36C_{p,N_2} \\
C_2 &= 7\phi_{k-1}C_{p,CO_2} + 8\phi_{k-1}C_{p,H_2O} + 41.36C_{p,N_2} + \\
&\quad 11(1 - \phi_{k-1})C_{p,O2}.
\end{aligned}$$

The specific heat values are assumed to be constant. The in-cylinder pressure at IVC is assumed to be equal to the intake manifold pressure. Temperature and pressure at the crank angle of fifty percent fuel mass fraction burned with the assumption of isentropic compression can then be calculated as

$$T_{50,k} = T_{IVC,k}\left(\frac{V_{IVC,k}}{V_{50,k}}\right)^{\gamma-1} \tag{7.4}$$

$$P_{50,k} = P_{IVC,k}\left(\frac{V_{IVC,k}}{V_{50,k}}\right)^{\gamma} \tag{7.5}$$

where γ is specific heat ratio. Mixture temperature, pressure and composition at IVC are important factors that influencing HCCI combustion timing [1, 9, 13]. To obtain a model that is more suitable for real-time combustion timing control, the DPM is reduced to a fitted set of algebraic equations for predicting fuel equivalence ratio, start of combustion, combustion duration and crank angle of fifty percent fuel mass fraction burned. The model is:

$$\phi_k = 2.0743T_{RES,k}^{-5.0268} + 0.795m_{fuel,k}Q_{LHV} - 0.0082\alpha_k^{2.4260} + 0.0172 \tag{7.6}$$

$$\theta_{soc,k} = -0.0047T_{IVC,k} - 0.9479\phi_k + 1.9579 \tag{7.7}$$

$$\Delta\theta_k = 0.8153\theta_{soc,k} + 0.1925 \tag{7.8}$$

$$\theta_{50,k} = \theta_{soc,k} + 0.5\Delta\theta_k \tag{7.9}$$

Constants in eqns. 7.6, 7.7, 7.8 and 7.9 are parametrized using the DPM without considering external EGR. Temperature after combustion, T_{AC}, is calculated by applying first law of thermodynamics to the trapped in-cylinder mixture as [51, 92, 202]

$$T_{AC,k} = \frac{(C_1 + \alpha_k C_2)T_{50,k} + C_5}{C_2(1+\alpha_k)} \tag{7.10}$$

where $C_5 = Q_{LHV}\phi_k\beta$ and β is the percentage of system energy lost by heat transfer during combustion (β=0.12). By applying the ideal gas law to the system, the in-cylinder pressure after combustion, P_{AC} for cycle k is calculated as [51, 92, 202]

$$P_{AC,k} = \frac{N_{AC,k}}{N_{BC,k}}P_{50,k}\frac{T_{AC,k}}{T_{50,k}} \tag{7.11}$$

where

$$N_{AC,k} = 4\phi_k + 52.36 + \alpha_k(4\phi_{k-1} + 52.36)$$

$$N_{BC,k} = \phi_k + 52.36 + \alpha_k(4\phi_{k-1} + 52.36).$$

The expansion process is assumed to be isentropic so the in-cylinder gas temperature and pressure at EVO is calculated as

$$T_{EVO,k} = (\frac{V_{50,k}}{V_{EVO,k}})^{\gamma-1} T_{AC,k} \tag{7.12}$$

$$P_{EVO,k} = (\frac{V_{50,k}}{V_{EVO,k}})^{\gamma} P_{AC,k}. \tag{7.13}$$

At EVO, blowdown to the exhaust manifold pressure is occurred assuming that the in-cylinder mixture isentropically expands to the exhaust manifold pressure. Residual gas temperature after blowdown, T_{RES}, is calculated as [7]

$$T_{RES,k} = \left(\frac{P_{exh,k}}{P_{EVO,k}}\right)^{\frac{\gamma-1}{\gamma}} T_{EVO,k} \tag{7.14}$$

Finally, engine output work is calculated from a correlation obtained from the DPM as

$$\text{IMEP}_k = 13.7327 \times m_{f,k} Q_{LHV} - 3.887. \tag{7.15}$$

To write the model in state space form where the states can be written as a function of the inputs and state variables of the previous cycle the model equations are rearranged.

The *first state* equation is residual mole fraction which is given in eqn. 7.2. Eqns. 7.3, 7.4, 7.5, 7.10, 7.11, 7.12, 7.13 and 7.14 can then be sequentially substituted into eqn. 7.2 to obtain the state equation for the residual mole fraction which is:

$$\begin{aligned}\alpha_k = & \\ & \frac{\mathrm{P_{exh}\,T_{int}\,V_{EVC,k-1}} \left(\frac{\mathrm{V_{50,k-1}}}{\mathrm{V_{EVO,k-1}}}\right)^{1-\gamma}}{\mathrm{P_{int}\,V_{IVC}} \left(\mathrm{Q_{LHV}}\,\beta\,\phi_{\mathrm{k-1}} + \mathrm{T_{IVC,k}} \left(\frac{\mathrm{V_{IVC}}}{\mathrm{V_{50,k-1}}}\right)^{\gamma-1} A_2\right)} \times \\ & \frac{\left(\alpha_{\mathrm{k-1}} + 1\right)\, A_1}{A_4^{\frac{\gamma-1}{\gamma}}}\end{aligned} \tag{7.16}$$

where

$$\begin{aligned}A_1 = & 41.36 C_{p,N_2} + 7\,\mathrm{C_{p,CO_2}}\,\phi_{\mathrm{k-1}} + 8\,\mathrm{C_{p,H_2O}}\,\phi_{\mathrm{k-1}} \\ & - \mathrm{C_{p,O_2}}\,\left(11\,\phi_{\mathrm{k-1}} - 11\right) \\ A_2 = & 41.36 C_{p,N_2} + 11\,\mathrm{C_{p,O_2}} + \mathrm{C_{p,C_7H_{16}}}\,\phi_{\mathrm{k-1}} + \alpha_{\mathrm{k-1}}\,A_1 \\ A_3 = & \mathrm{Q_{LHV}}\,\beta\phi_{\mathrm{k-1}} + \mathrm{T_{IVC,k}} \left(\frac{\mathrm{V_{IVC}}}{\mathrm{V_{50,k-1}}}\right)^{\gamma-1} A_2 \\ A_4 = & \left(\frac{\mathrm{P_{exh}\,T_{IVC,k-1}}\,\left(\alpha_{\mathrm{k-1}} + 1\right)}{\mathrm{P_{int}} \left(\frac{\mathrm{V_{IVC}}}{\mathrm{V_{50,k-1}}}\right) \left(\frac{\mathrm{V_{50,k-1}}}{\mathrm{V_{EVO,k-1}}}\right)^{\gamma}}\right) \times \\ & \left(\frac{\left(\phi_{\mathrm{k-1}} + \alpha_{\mathrm{k-1}}\,\left(4\,\phi_{\mathrm{k-1}} + 41.56\right) + 41.56\right)\, A_1}{A_3\left(4\,\phi_{\mathrm{k-1}} + \alpha_{\mathrm{k-1}}\,\left(4\,\phi_{\mathrm{k-1}} + 41.56\right) + 41.56\right)}\right).\end{aligned}$$

The *second state* equation is the temperature at IVC. Substituting eqns 6.7, 6.8, 6.14, 5.13, 6.12, 6.13, 6.15 and 6.16 into eqn 6.6 yields the second of these state update equations.

$$T_{IVC,k} = \frac{\left(T_{int}B_{10} - \frac{B_1^{-1}B_4B_{10}B_5}{(\alpha_{k-1}+1)F_3}\right)}{\left(B_{10} + \frac{B_{14}}{P_{int}V_{IVC}B_2B_5}\right)} + B_5 \tag{7.17}$$

where

$$
\begin{aligned}
B_1 =& \left(\frac{V_{50,k-1}}{V_{EVC}}\right)^{1-\gamma} \\
B_2 =& \alpha_{k-1}(4\phi_{k-1} + 52.36) \\
B_3 =& 41.36C_{p,N_2} + 7C_{p,CO_2}\phi_{k-1} + 8C_{p,H_2O}\phi_{k-1} \\
& - C_{p,O_2}(11\phi_{k-1} - 11) \\
B_4 =& Q_{LHV}\beta\phi_{k-1} + T_{IVC,k-1}\left(\frac{V_{IVC}}{V_{50,k-1}}\right)^{\gamma-1} \times \\
& (41.36C_{p,N_2} + 11C_{p,O_2} + C_{p,C_7H_{16}}\phi_{k-1} + \alpha_{k-1}B_3) \\
B_5 =& \left(\frac{P_{exh}T_{IVC,k-1}V_{50,k-1}(\alpha_{k-1}+1)}{P_{int}V_{IVC}B_4(4\phi_{k-1} + B_2 + 52.36)\left(\frac{V_{50,k-1}}{V_{EVO}}\right)^{\gamma}}\right)^{\frac{\gamma-1}{\gamma}} \\
& \times \left(\left(\phi_{k-1} + B_2 + 52.36\right)B_3\right)^{\frac{\gamma-1}{\gamma}} \\
B_6 =& \frac{B_1^{-1}B_4B_5}{(\alpha_{k-1}+1)B_3} \\
B_7 =& \left(\frac{P_{exh}T_{int}V_{EVC,k-1}B_1(\alpha_{k-1}+1)B_3}{P_{int}V_{IVC}B_4B_5}\right)^{2.426} \\
B_8 =& 10000B_6^{5.0268} \\
B_9 =& C_{p,C_7H_{16}}(0.795m_{f,k-1}Q_{LHV} - 0.0082B_7 \\
& + \frac{20743}{B_8} + 0.0172) \\
B_{10} =& 41.36C_{p,N_2} + 11C_{p,O_2} + B_9 \\
B_{11} =& C_{p,O_2}(8.745m_{f,k-1}Q_{LHV} - 0.0902B_7 + \frac{228173}{B_8} \\
& - 10.8108) \\
B_{12} =& C_{p,CO_2}(5.65m_{f,k-1}Q_{LHV} - 0.0082B_7 + \frac{145201}{B_8} \\
& + 0.0124) + 41.36C_{p,N_2} \\
B_{13} =& C_{p,H_2O}(6.37m_{f,k-1}Q_{LHV} - 0.0656B_7 + \frac{16.5944}{B_6^{5.0268}} + \\
& 0.1376) + B_{12} - B_{11} \\
B_{14} =& P_{exh}T_{int}V_{EVC,k-1}B_1(\alpha_{k-1}+1)B_{13}B_3
\end{aligned}
$$

The *third state* equation is fuel equivalence ratio. Similar to the second state update equation, eqns. 6.7, 6.8, 6.14, 5.13, 6.12, 6.13, 6.15 and 6.16 are substituted into eqn. 5.10 resulting in:

$$\begin{aligned}\phi_k &= 0.795\mathrm{m_{f,k-1}}\mathrm{Q_{LHV}} + \frac{2.0743}{C_7^{0.5027}} - 0.0082\times \\ &\frac{\left(\mathrm{P_{exh}}\,\mathrm{T_{int}}\,\mathrm{V_{EVC,k-1}}\left(\frac{\mathrm{V_{50,k-1}}}{\mathrm{V_{EVO}}}\right)^{1-\gamma}\,(\alpha_{\mathrm{k-1}}+1)\;C_1\right)^{2.4}}{C_6} \\ &+ 0.0172\end{aligned} \tag{7.18}$$

where

$$\begin{aligned}
C_1 =& 41.36\mathrm{C_{p,N2}} + 7\,\mathrm{C_{p,co_2}}\,\phi_{\mathrm{k-1}} \\
&+ 8\,\mathrm{C_{p,H_2O}}\,\phi_{\mathrm{k-1}} - \mathrm{C_{p,O_2}}\;(11\,\phi_{\mathrm{k-1}} - 11) \\
C_2 =& C_1^{\frac{\gamma-1}{\gamma}}(\phi_{\mathrm{k-1}} + \alpha_{\mathrm{k-1}}\,(4\,\phi_{\mathrm{k-1}} + 52.36) + 52.36)^{\frac{\gamma-1}{\gamma}} \\
C_3 =& 41.36\mathrm{C_{p,N2}} + 11\,\mathrm{C_{p,O_2}} + \mathrm{C_{p,C_7H_{16}}}\,\phi_{\mathrm{k-1}} + \alpha_{\mathrm{k-1}}\,C_1 \\
C_4 =& \mathrm{P_{exh}}\,\mathrm{T_{IVC,k-1}}\,(\frac{\mathrm{V_{IVC}}}{\mathrm{V_{50,k-1}}})^{\gamma-1}\;(\alpha_{\mathrm{k-1}}+1)\,(\phi_{\mathrm{k-1}}+ \\
&\alpha_{\mathrm{k-1}}\;(4\,\phi_{\mathrm{k-1}} + 52.36) + 52.36)\,C_1 \\
C_5 =& (4\,\phi_{\mathrm{k-1}} + \alpha_{\mathrm{k-1}}\,(4\,\phi_{\mathrm{k-1}} + 52.36) + 52.36)\mathrm{P_{int}}\,(\frac{\mathrm{V_{IVC}}}{\mathrm{V_{EVO}}})^{\gamma} \\
&\times (\mathrm{Q_{LHV}}\,\beta, \phi_{\mathrm{k-1}} + \mathrm{T_{IVC,k-1}}\,(\frac{\mathrm{V_{IVC}}}{\mathrm{V_{50,k-1}}})^{\gamma-1}\;41.36\mathrm{C_{p,N2}} \\
C_6 =& \mathrm{P_{int}}\,\mathrm{V_{IVC}}\,(\mathrm{Q_{LHV}}\,\beta, \phi_{\mathrm{k-1}} + \mathrm{T_{IVC,k-1}}\,(\frac{\mathrm{V_{IVC}}}{\mathrm{V_{50,k-1}}})^{\gamma-1}\;\times \\
&C_3)\left(\frac{C_4}{C_5}\right)^{\frac{\gamma-1}{\gamma}}
\end{aligned}$$

$$
\begin{aligned}
C_7 =& ((\alpha_{\mathrm{k-1}} + 1)\ C_1)^{-1}(\frac{\mathrm{V}_{\mathrm{50,k-1}}}{\mathrm{V}_{\mathrm{EVO}}})^{\gamma-1} \times \\
& (\mathrm{Q}_{\mathrm{LHV}}\,\beta, \phi_{\mathrm{k-1}} + \mathrm{T}_{\mathrm{IVC,k-1}}\,(\frac{\mathrm{V}_{\mathrm{IVC}}}{\mathrm{V}_{\mathrm{50,k-1}}})^{\gamma-1} \times \\
& (41.36\mathrm{C}_{\mathrm{p,N2}} + 11\,\mathrm{C}_{\mathrm{p,O_2}} + \mathrm{C}_{\mathrm{p,C_7H_{16}}}\,\phi_{\mathrm{k-1}} \\
& + \alpha_{\mathrm{k-1}}\,C_1))\,{C_5}^{-1}\times \\
& (\mathrm{P}_{\mathrm{exh}}\,\mathrm{T}_{\mathrm{IVC,k-1}}\,(\frac{\mathrm{V}_{\mathrm{IVC}}}{\mathrm{V}_{\mathrm{50,k-1}}})^{\gamma-1}\,(\alpha_{\mathrm{k-1}} + 1)\,)^{\frac{\gamma-1}{\gamma}} C_2 \\
& + 11\,\mathrm{C}_{\mathrm{p,O_2}} + \mathrm{C}_{\mathrm{p,C_7H_{16}}}\,\phi_{\mathrm{k-1}} + \alpha_{\mathrm{k-1}}\,C_1))
\end{aligned}
$$

The *fourth state* equation is crank angle of fifty percent fuel mass fraction burned, θ_{50}. Eqns. 6.18, 7.18, 6.9 and 6.10 are substituted into eqn. 8.10, and the result is:

$$
\begin{aligned}
\theta_{50,k} =& 0.0109D_9 - 2.7677D_8^{-1} - 1.0607m_{f,k-1}Q_{LHV} \\
& - 0.0066(T_{int}\,(41.36C_{p,N_2} + 11C_{p,O_2} + D_5) \\
& + \frac{P_{exh}T_{int}V_{EVC,K-1}F_{10}}{P_{int}V_{IVC}}) \\
& \times (41.36C_{p,N_2} + 11C_{p,O_2} + D_5 + D_{11})^{-1} + 2.829
\end{aligned}
\tag{7.19}
$$

where

$$
\begin{aligned}
D_1 =& \left(\frac{V_{IVC}}{V_{50,k-1}}\right)^{\gamma-1} \\
D_2 =& 41.36C_{p,N_2} + 7C_{p,CO_2}\phi_{k-1} \\
& + 8C_{p,H_2O}\phi_{k-1} - C_{p,O_2}\left(11\phi_{k-1} - 11\right) \\
D_3 =& \left(\frac{V_{50,k-1}}{V_{EVO}}\right)^{1-\gamma} \\
D_4 =& \alpha_{k-1}\left(4\phi_{k-1} + 52.36\right) \\
D_5 =& C_{p,C_7H_{16}}(0.795m_{f,k-1}Q_{LHV} \\
D_6 =& Q_{LHV}\beta\phi_{k-1} + T_{IVC,k-1}D_1 \\
& (41.36C_{p,N_2} + 11C_{p,O_2} + C_{p,D_6H_{16}}\phi_{k-1} + \alpha_{k-1}D_2) \\
& + 2.0743D_8^{-1} - 0.0082D_9 + 0.0168) \\
D_7 =& \left(\frac{P_{exh}T_{IVC,k-1}D_1(\alpha_{k-1}+1)(\phi_{k-1} + D_4 + 52.36)D_2}{P_{int}\left(\frac{V_{IVC}}{V_{EVO}}\right)^{\gamma} D_6(4\phi_{k-1} + D_4 + 52.36)}\right)^{\frac{\gamma-1}{\gamma}} \\
D_8 =& \frac{\left(\frac{V_{50,k-1}}{V_{EVO}}\right)^{\gamma-1} D_6D_7}{(\alpha_{k-1}+1)D_2} \\
D_9 =& \left(\frac{P_{exh}T_{int}V_{EVC,k-1}D_3(\alpha_{k-1}+1)D_2}{P_{int}V_{IVC}D_7D_6}\right)^{2.426} \\
D_{10} =& 41.36C_{p,N_2} + C_{p,H_2O}(m_{f,k-1}Q_{LHV} + 16.59D_8^{-1} \\
& - 0.0656D_9 + 0.1376) + C_{p,CO_2}(92.75m_{f,k-1}Q_{LHV} \\
& + 14.52D_8^{-1} - 0.0574D_9 + 0.1204) \\
& - C_{p,O_2}(8.75m_{f,k-1}Q_{LHV} + 22.8173D_8^{-1} \\
& - 0.083D_9 - 10.81) \\
D_{11} =& \frac{P_{exh}T_{int}V_{EVC,k-1}D_3(\alpha_{k-1}+1)D_{10}D_2}{P_{int}V_{IVC}D_6D_7}.
\end{aligned}
$$

Eqns. 7.16—7.19 are now in a form suitable for nonlinear state-space control development. This nonlinear discrete control oriented model can capture the dynamics of the trapped residual gas in the HCCI engine cycle by cycle. Figure 7.2 shows the response of the nonlinear COM to a step change in NVO duration and fueling rate compared with the response of the detailed physical model. A good dynamic match between the nonlinear control oriented model and the detailed physical model is observed. Then, the nonlinear COM is linearized around one operating point and the linearized model behavior is compared to both nonlinear control oriented model and the detailed physical model in Figure 7.2. The operating point is selected based on the measured experimental data in [9] to ensure that the selected point is far away from both misfire and ringing regions.

The linear state space model is given by:

$$\begin{aligned} x_{k+1} &= Ax_k + Bu_k \\ y_k &= Cx_k + Du_k \end{aligned} \tag{7.20}$$

where A, B, C and D depend on the operating condition that the model is linearized around. The operating condition that the nonlinear COM was linearized around is listed in Table 7.1. The model states, inputs and outputs are: $x = \begin{bmatrix} T_{ivc} & \alpha & \phi & m_f Q_{LHV} & \theta_{50} \end{bmatrix}^T$, $u = \begin{bmatrix} m_f Q_{LHV} & \theta_{EVC} \end{bmatrix}^T$ and $y = \begin{bmatrix} \theta_{50} & \text{IMEP} \end{bmatrix}^T$ respectively. $m_f Q_{LHV}$ is added as a new fifth state to the linearized model to make matrix D in eqn. 7.63 zero. The A, B and C matrixes of eqn. 7.63 are then:

$$A = \begin{bmatrix} 0.1415 & -4.4917 & 14.79502 & 0 & 1.4264 \\ -0.0004 & 0.0144 & -0.0477 & 0 & -0.0046 \\ 0.0000 & -0.00002 & 0.00008 & 0 & 0.00000 \\ 0 & 0 & 0 & 0 & 0 \\ -0.00093 & 0.02975 & -0.09799 & 0 & -0.00944 \end{bmatrix}$$

$$B = \begin{bmatrix} 0.2672 & -10.3807 \\ 0 & -0.3226 \\ 0.795 & 0.0005 \\ 1.0000 & 0 \\ -1.0625 & 0.0679 \end{bmatrix} \tag{7.21}$$

$$C = \begin{bmatrix} 0 & 0 & 0 & 0 & 1.00 \\ 0 & 0 & 0 & 13.732 & 0 \end{bmatrix}$$

As seen in eqn. 7.64, the fourth state has no dynamics.

Table 7.1: Operating point for linearization of COM

T_{int}	80^o C
ϕ	0.3
T_{IVC}	86^oC
θ_{EVC}	40 Deg CA bTDC
m_fQ_{LHV}	0.42 kJ
θ_{50}	4.63 Deg CA aTDC
P_{int}	88.6 kPa
ω	820 RPM

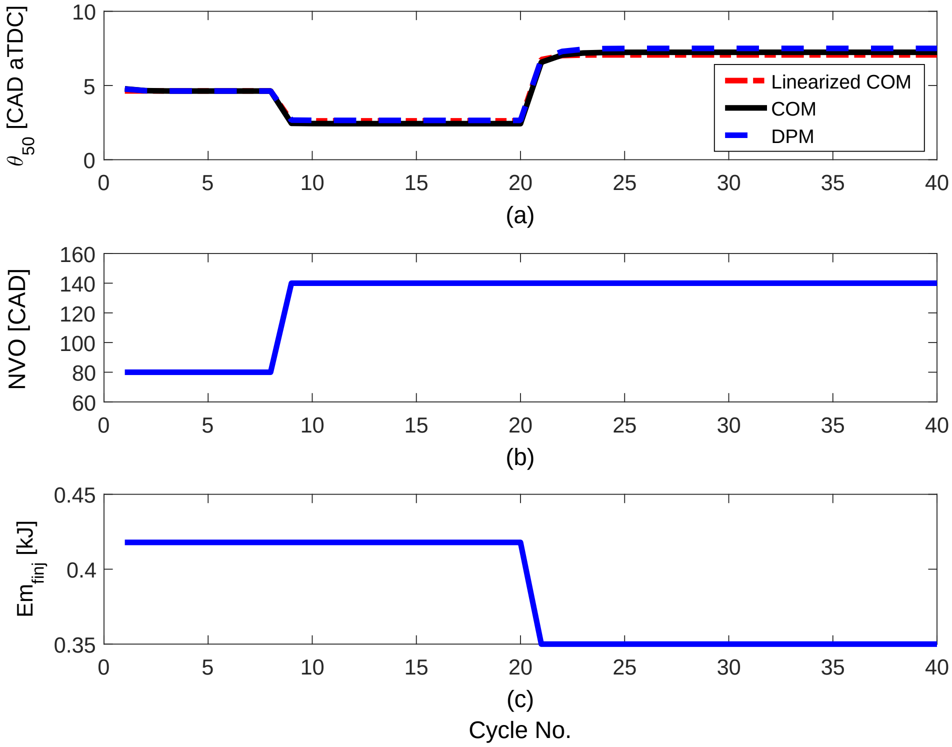

Figure 7.2: Comparison of the DPM, COM and the linear model for a step change in NVO and then fueling rate (a) combustion timing, (b)NVO [CAD] and [c] Injected Fuel Energy

Table 7.2: Steady state engine operating conditions

T_{int}	78^o - 85^o C
ϕ	0.3 - 0.4
θ_{EVC}	0 - 90 Deg CA bTDC
$m_f Q_{LHV}$	0.33 - 0.49
P_{int}	88 - 95 kPa
ω	813 - 825 RPM
NVO	0 - 180 CA Deg

7.2 Model Validation

Experimental data from the single cylinder engine [9] is compared with the nonlinear control oriented model and the DPM when NVO duration and fueling rate are varied. In all cases, the charge is lean (ϕ < 1). First, NVO duration is kept constant and fueling rate is varied. As shown in Figure 7.3, combustion timing is advanced when fueling rate is increased. The reason is the reactivity of the fuel tends to increase from very lean to rich conditions. Both models show earlier combustion timing as the mixture becomes rich. This is consistent with the literature [9, 13]. Next, the fueling rate is kept constant and NVO duration is changed. Figure 7.4 shows the effects of NVO duration on combustion timing. When NVO duration increases, the amount of trapped residual gas as well as the in-cylinder gas temperature at IVC increases. Combustion timing is advanced when the in-cylinder gas temperature at IVC increases with larger amounts of trapped residual gas. This is consistent with the previous studies [9, 139]. These results confirm that both control oriented and the detailed physical models seem to capture the fueling rate and the trapped residual gas effects on combustion timing. In Figure 7.5, both nonlinear control oriented and the detailed physical models are further validated against 42 engine steady state operating conditions listed in Table 7.2. These results show that the detailed physical and control oriented models capture combustion timing with average errors of 1.1 CAD and 1.7 CAD respectively. The control oriented model is suitable for real time requiring only 6.4 msec to simulate an HCCI cycle on a 2.66 GHz Intel PC. The DPM requires 156 sec for an HCCI cycle which is also relatively fast for this type of simulation but unsuitable for realtime.

Figure 7.6 shows the performance of the detailed physical model, control oriented model and the linearized control oriented model in predicting θ_{50} during transient valve timing experiments. The linear model is compared to the detailed physical model in Figure 7.7. As shown in this figure, the linear model states track the detailed physical model well. The linear model captures the system dynamics behavior and the maximum error in combustion timing prediction is 1.2 CA Deg compared to the detailed physical model.

The linearized control oriented model is used for MPC design considering constraints on inputs and outputs. Combustion timing and engine output work are used as controller inputs and the outputs are SNVO duration and fueling rate. Constraints on combustion timing and output work are sufficient for safe engine operation mode. Constraints on SNVO duration and fueling rate are determined based on the experimental limits. The valve timing response is slowed down to have smooth transient combustion timing response when the engine operating mode changes. The fueling rate response is kept fast in order to reach the desired load quickly.

Details of the input and output constraints are explained in controller structure section. The main objective of the controller is the tracking of the desired output work and combustion timing. The desired combustion timing and output work tra-

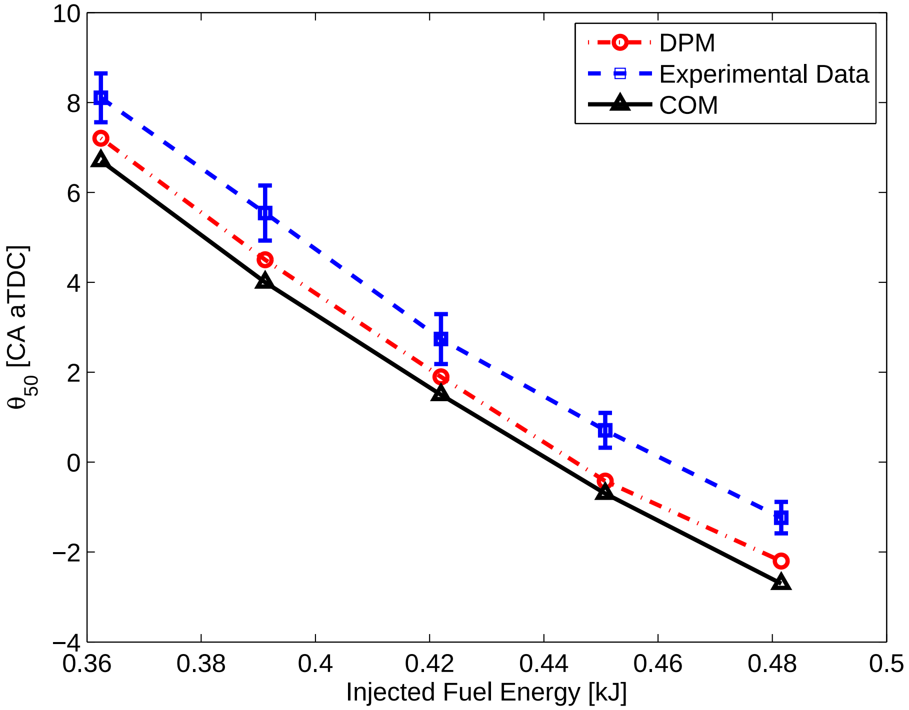

Figure 7.3: Steady state model validation – NVO=60 Deg CA, ω=817 RPM, P_{int}= 88.3 kPa, T_{int}=80^oC and fueling rate is varied at constant airflow rate

jectories are considered as step functions to check the response to a fast system transient.

7.3 MPC structure

The controller is designed based on the method detailed in [95]. In order to ensure that integrators are embedded in the state space model derived in eqn. 7.20, the model is changed to suit this design purpose as in [95]. Taking a difference operation on both sides of the eqn. 7.20 yields:

$$x_{k+1} - x_k = A(x_k - x_{k-1}) + B(u_k - u_{k-1}) \tag{7.22}$$

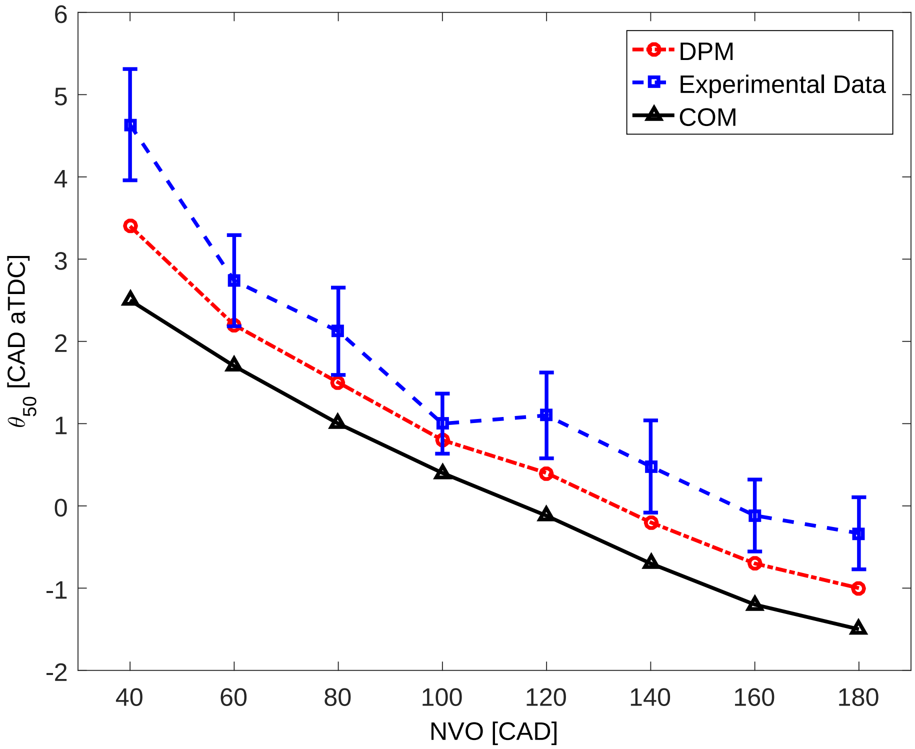

Figure 7.4: Steady state model validation – Injected Fuel Energy = 0.42 KJ, ω=817 RPM, P_{int}=88.343 kPa, T_{int}=$80^{o}C$ and NVO duration is varied

The state-space equation then can be re-written as

$$\Delta x_{k+1} = A\Delta x_k + B\Delta u_k \tag{7.23}$$

where Δu_k is the input to the state-space model, also called the rate of change of the control signal. In order to relate the output y_k to the state variable x_k, a new state variable vector is defined as $x(k) = \begin{bmatrix}\Delta {x_k}^T & y_k\end{bmatrix}^T$ where superscript T indicates matrix transpose. From eqn. 7.23, the output can be written as

$$y_{k+1} = y_k + CA\Delta x_k + CB\Delta u_k \tag{7.24}$$

The augmented model can be written as

$$x_{k+1} = A_e x_k + B_e \Delta u_k \tag{7.25}$$

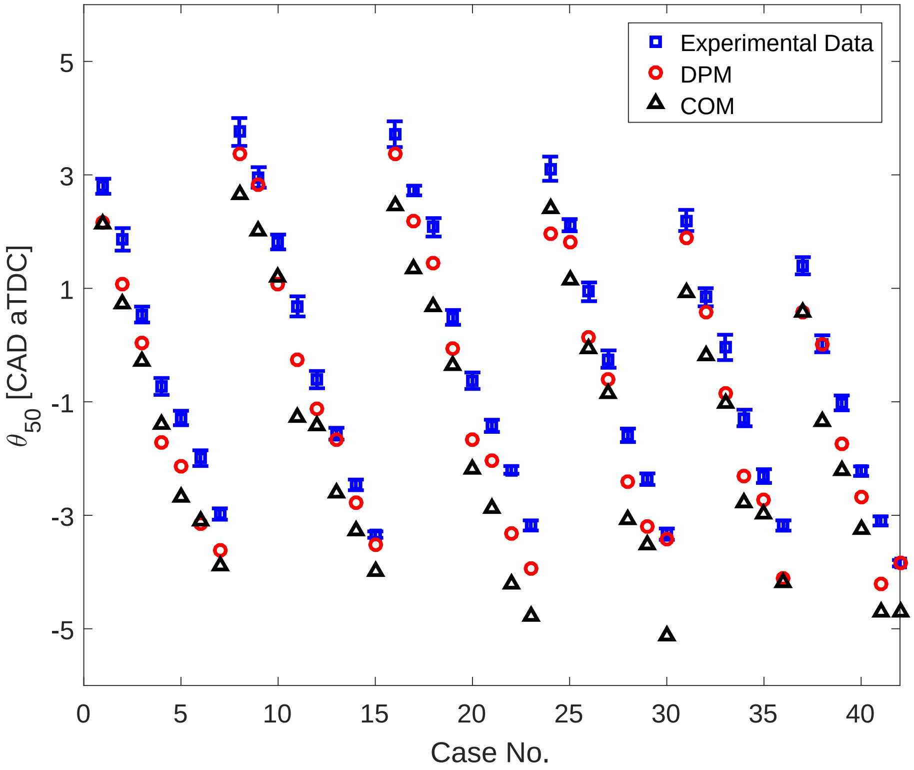

Figure 7.5: Steady state validation of COM and DPM

$$y(k) = C_e x_k$$

where

$A_e = \begin{bmatrix} A_n & 0_n^T \\ C_n A_n & I_{q\times q} \end{bmatrix}$, $B_e = \begin{bmatrix} B_n \\ C_n B_n \end{bmatrix}$ and $C_e = \begin{bmatrix} 0_{q\times n} & Iq \times q \end{bmatrix}$. The subscripts q and n are respectively the number of outputs and the states. $0_{q\times n}$ is a $q \times n$ zero matrix and $I_{q\times q}$ is a $q \times q$ identity matrix.

Typically MPC for the case of rapid sampling and complicated process dynamics may require a very large number of parameters, leading to poorly numerically conditioned solutions and heavy computational load when implemented online [95]. Instead, Laguerre function approach can be used. In this method, a set of Laguerre

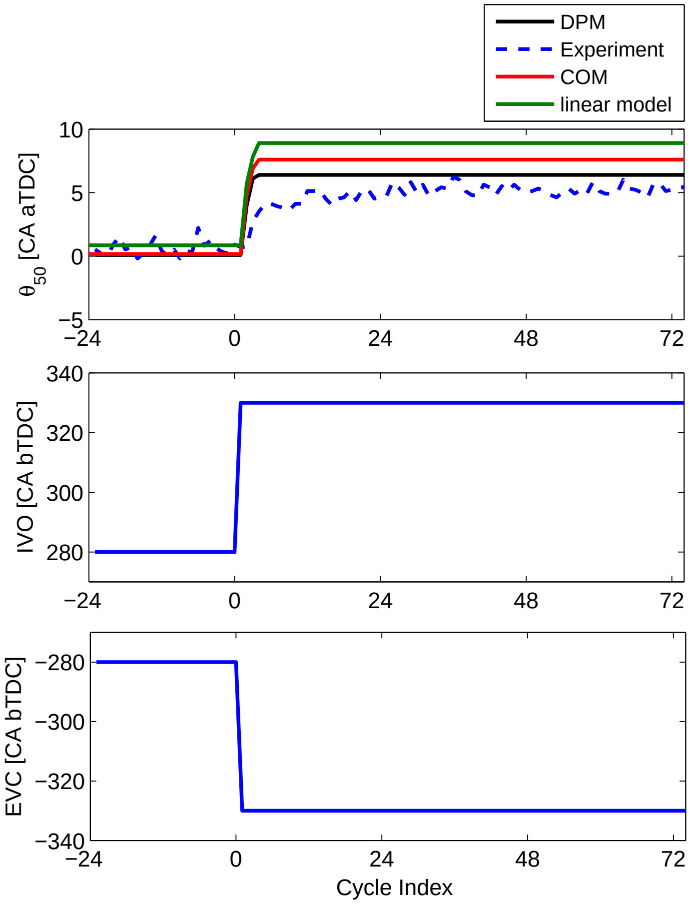

Figure 7.6: Transient model validation

functions are used to capture the control signal dynamic as

$$\Delta u_(k_i + k) = \Sigma_{j=1}^{N} c_j(k_i) l_j(k) \tag{7.26}$$

where k_i is the initial time, k is the future sampling time, c_j is the Laguerre coefficients and N is used to describe the complexity of the control trajectory. Eqn. 7.26 can be written in vector form as

$$\Delta u(k_i + k) = L(k)^T \eta \tag{7.27}$$

where $L(k)^T$ is the transposed Laguerre function and η comprises N Laguerre coefficients. The objective of MPC is to bring outputs as close as possible to the

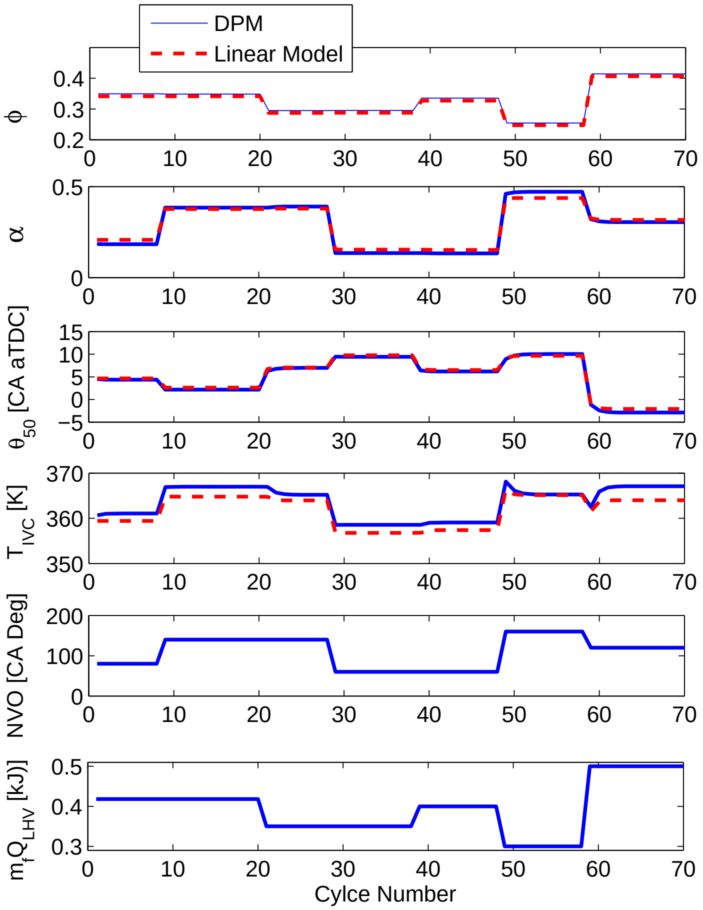

Figure 7.7: Linear model versus DPM [ω=825 RPM, P_{int}=95 kPa and T_{int}=80^{o}C]

reference signal. For this reason, the control parameter vector, ΔU is defined that minimizes the following cost function:

$$J = (R_s - Y)\,(Rs - Y) + \Delta U^T \bar{R} \Delta U \tag{7.28}$$

where R_S is the reference signal and R is tuning parameter. The ΔU and Y are the control signals and plant outputs respectively where

$$\Delta U = \begin{bmatrix} \Delta u(k_i) & \Delta u(k_i+1) & \Delta u(k_i+2) & \ldots & \Delta u(k_i+N_c-1) \end{bmatrix} \tag{7.29}$$

$$\Delta Y = \begin{bmatrix} y(k_i) & y(k_i+1) & y(k_i+2) & \ldots & y(k_i+N_p) \end{bmatrix} \tag{7.30}$$

where N_p and N_c are prediction horizon and control horizon respectively.

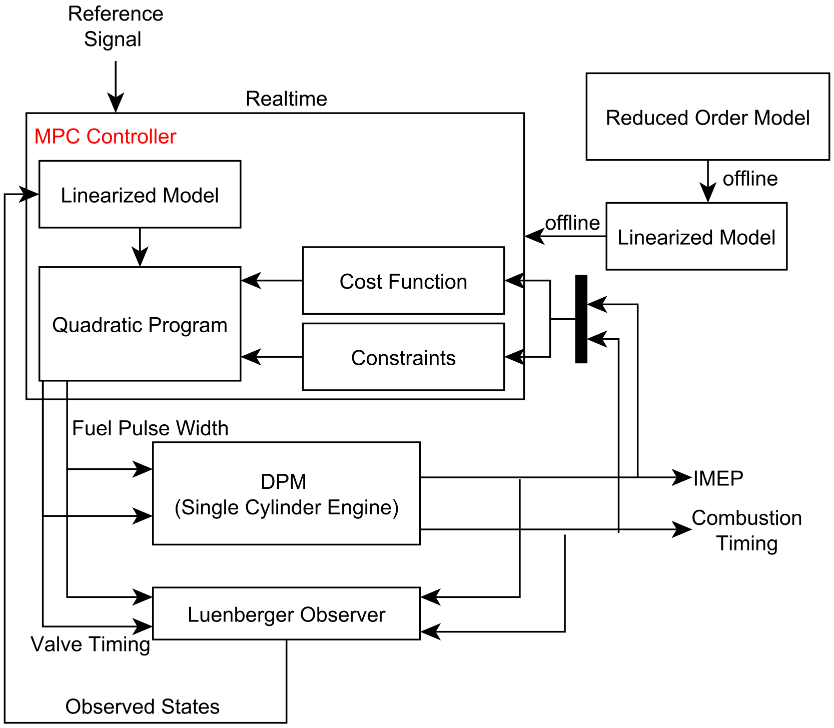

Figure 7.8: MPC Structure

The Laguerre network in eqn. 7.27 is defined using the following difference equation [95]:

$$L(k+1) = A_l L(k) \tag{7.31}$$

where

$$L(0) = \sqrt{\beta}\begin{bmatrix}1 & -a & a^2 & -a^3 & \ldots & (-1)^{N-1}a^{N-1}\end{bmatrix}^T \tag{7.32}$$

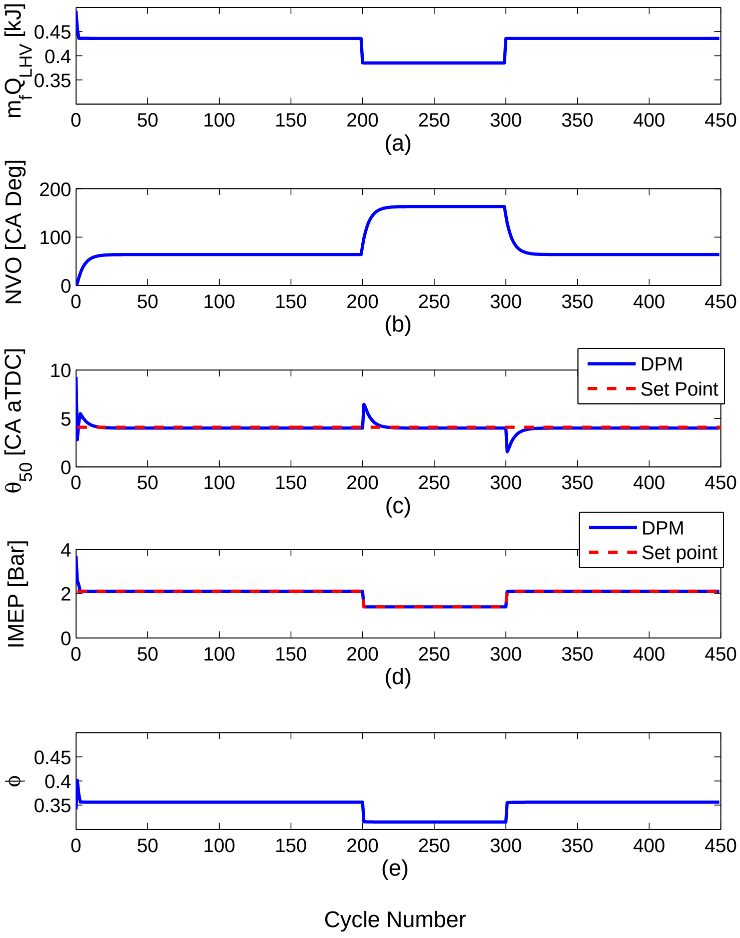

Figure 7.9: Simulated MPC - Controller performance (unconstrained inputs & outputs): (a) & (b) controller outputs (c) & (d) system outputs (e) fuel equivalence ratio [ω=825 RPM, P_{int}=95 kPa and T_{int}=80^{o}C]

A_l is $N \times N$ matrix and is defined as

$$A_l = \begin{bmatrix} a & 0 & 0 & \dots & 0 \\ \beta & a & 0 & \dots & 0 \\ -a\beta & \beta & a & \dots & 0 \\ \vdots & \ddots & \ddots & \ddots & \vdots \\ (-1)^N a^{N-2}\beta & (-1)^{N-1} a^{N-3}\beta & (-1)^{N-2} a^{N-4}\beta & \dots & a \end{bmatrix} \tag{7.33}$$

and

$$\beta = 1 - a^2 \tag{7.34}$$

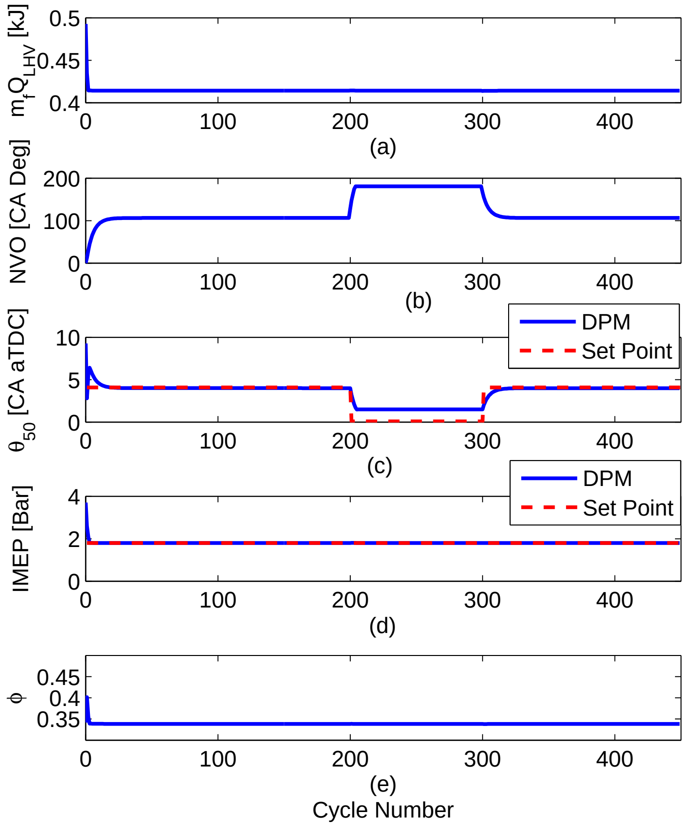

Figure 7.10: Simulated MPC - Controller performance (constrained inputs): (a) & (b) controller outputs (c) & (d) system outputs (e) fuel equivalence ratio [ω=825 RPM, P_{int}=95 kPa and T_{int}=80^{o}C] NVO saturation

Traditional MPC [18] corresponds to the case that parameter a=0 and $N = N_c$ in the Laguerre network (N_c is control Horizon). The number of parameters in the MPC optimization can be reduced considerably with choosing appropriate a and N that is required for implementation. For example, a larger value of a can be selected to achieve a long control horizon with a smaller number of parameters N required in the optimization procedure. The parameters a and N plays important role in closed loop performance of the controller [95].

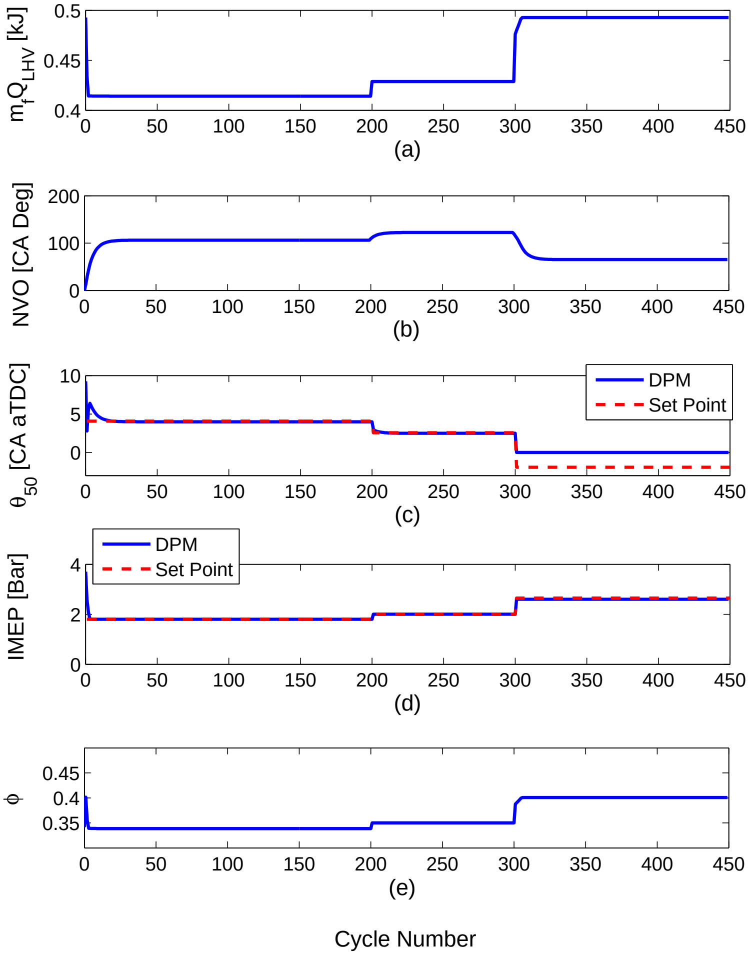

Figure 7.11: Simulated MPC - Controller performance (constrained output (θ_{50})): (a) & (b) controller outputs (c) & (d) system outputs (e) fuel equivalence ratio [ω=825 RPM, P_{int}=95 kPa and T_{int}=80^{o}C]

For a Two-Input-Two-Output system the input signal is written as

$$\Delta u(k) = \begin{bmatrix} \Delta u_1(k) & \Delta u_2(k) \end{bmatrix} \tag{7.35}$$

and the input matrix is partitioned as

$$B = \begin{bmatrix} B_1 & B_2 \end{bmatrix} \tag{7.36}$$

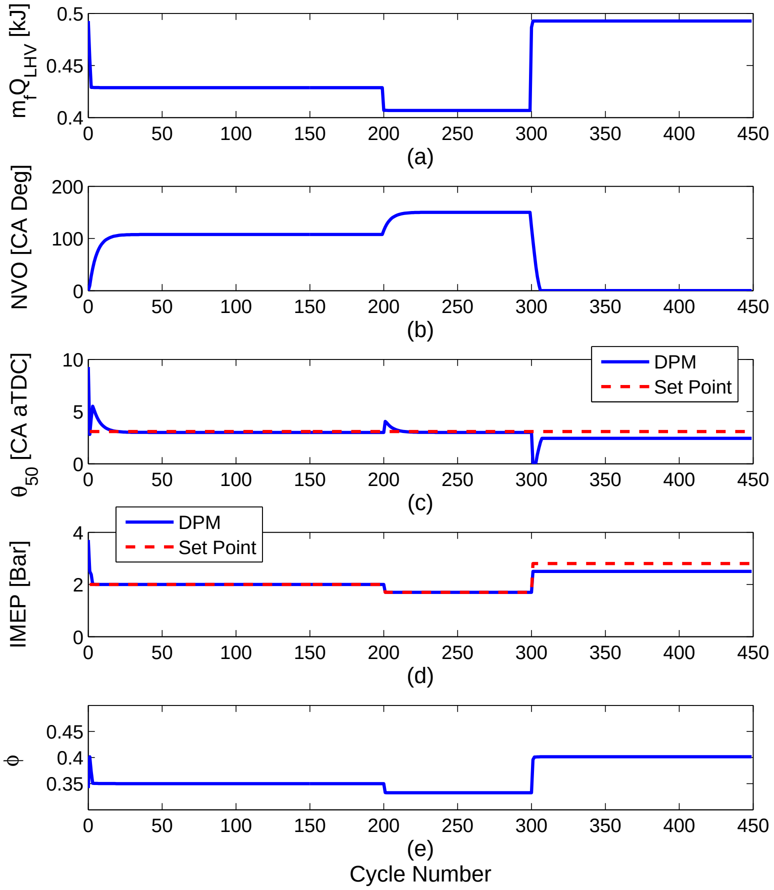

Figure 7.12: Simulated MPC - Controller performance (constrained output (IMEP)): (a) & (b) controller outputs (c) & (d) system outputs (e) fuel equivalence ratio [ω=825 RPM, P_{int}=95 kPa and T_{int}=80^{o}C]

Each control signal is written based on Lagauerre parameter as

$$\Delta u_i = L_i(k)^T \eta_i \tag{7.37}$$

where a_i and N_i are determined for each signal individually. Within this framework, the control horizon concept used in previous studies [21, 18, 93, 92] is eliminated. N_i is used to describe the complexity of the input signal trajectory in conjunction with the Laguerre function pole locations. Larger values for pole locations can be selected to achieve a longer control horizon with a smaller number of N_i in the

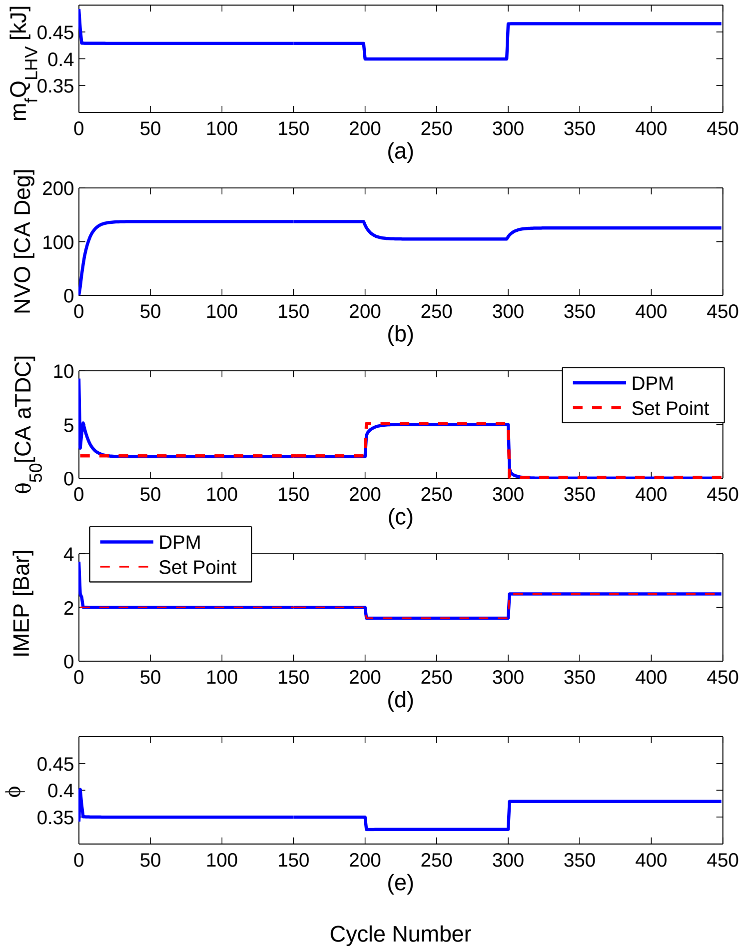

Figure 7.13: Simulated MPC - Controller performance (both desired IMEP and θ_{50} are changed at the same time): (a) & (b) controller outputs (c) & (d) system outputs (e) fuel equivalence ratio [ω=825 RPM, P_{int}=95 kPa and T_{int}=80^{o}C]

optimization procedure. The Laguerre function is used to speed up calculations for real-time implementation. For this two input-two output system each input signal is designated to have a Laguerre pole location at 0.5. η_i and $L_i(k)$ in eqn. 7.37 are the Laguerre function description of the ith control input and $L_i(k)$ is written as

$$L_i(k)^T = \left[l_1^i(k) \quad l_2^i(k) \quad \ldots \quad {l^i}_{N_i}(k) \right] \tag{7.38}$$

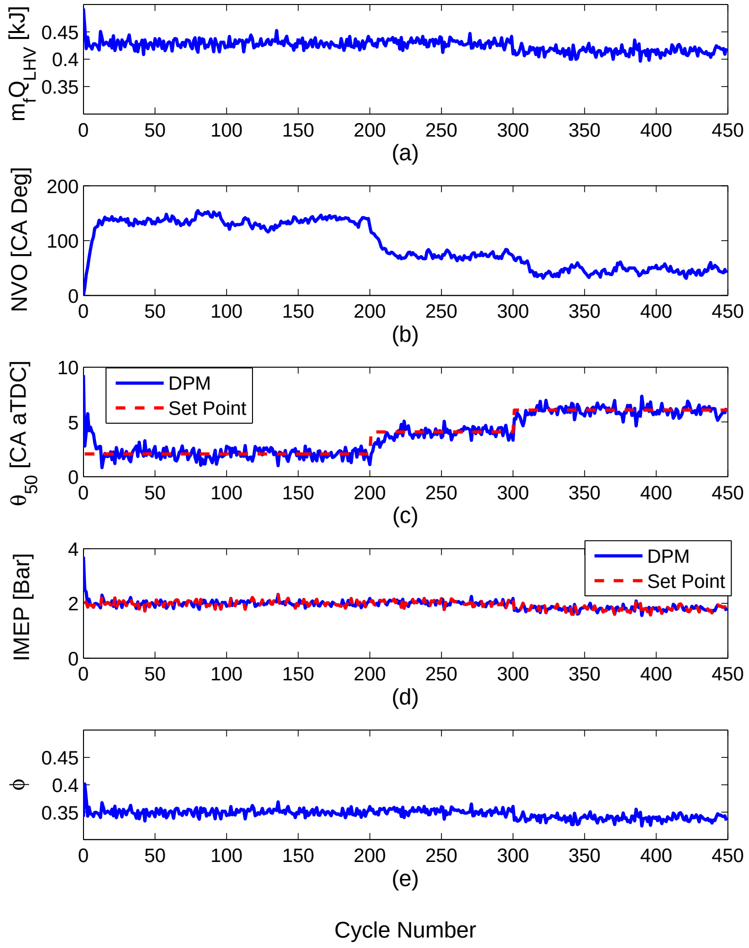

Figure 7.14: Simulated MPC - Controller performance considering measurement noise: (a) & (b) controller outputs (c) & (d) system outputs (e) fuel equivalence ratio [ω=825 RPM, P_{int}=95 kPa and T_{int}=80^{o}C]

The prediction of the future state at time k is defined as

$$x(k_i + k) = A^k x(k_i) + \phi(k)^T \eta \tag{7.39}$$

where the parameters η^T and $\phi(k)$ are defined as

$$\eta^T = \begin{bmatrix} \eta_1^T & \eta_2^T \end{bmatrix} \tag{7.40}$$

$$\phi(k)^T = \sum_{j=0}^{k-1} A^{k-j-1} \left[B_1 L_1(j)^T \ B_2 L_2(j)^T \right] \tag{7.41}$$

$\phi(k)^T$ is computed recursively using the convolution sum detailed in [95]. The optimal control cost function is defined as

$$\begin{aligned} J =& \eta^T \Omega \eta + 2\eta^T \psi x(k) \\ & + \sum_{m=1}^{N_p} x(k)^T (A^T)^m Q A^m x(k) \end{aligned} \tag{7.42}$$

where Ω and ψ are:

$$\Omega = \sum_{m=1}^{N_p} \phi(m) Q \phi(m)^T + R_L \tag{7.43}$$

$$\psi = \sum_{m=1}^{N_p} \phi(m) Q A^m \tag{7.44}$$

with the weighting matrices Q and R_L. The global optimal solution of the cost function (eqn. 7.42) is [95]

$$\eta = -\Omega^{-1} \psi x(k_i) \tag{7.45}$$

The control law is then realized as

$$\Delta u(k_i) = \begin{pmatrix} L_1(0)^T & {0_2}^T \\ {0_1}^T & L_2(0)^T \end{pmatrix} \eta \tag{7.46}$$

where ${0_i}^T$ represents a zero block row vector with identical dimension to $L_i(0)^T$. The control signal, Δu can be written in the form of linear state feedback control as

$$\Delta u(k_i) = -K_{MPC} x(k_i) \tag{7.47}$$

where the $x(k_i)$ is defined using Luenberger observer [204]. Typically, the Luenberger observer has the following structure

$$\begin{aligned}\hat{x}(k+1) &= A_e\hat{x}(k) + K_{ob}\left[y(k) - \hat{y}(k)\right] + B_e u(k) \\ \hat{y}(k) &= C_e\hat{x}(k)\end{aligned} \tag{7.48}$$

where A_e, B_e and C_e matrices are determined from eqn. 7.25. $\hat{x}$ is the estimated state and y is available from the measurement. The state feedback control gain, K_{MPC} (see eqn 7.47) is

$$K_{MPC} = \begin{pmatrix} L_1(0)^T & {0_2}^T \\ {0_1}^T & L_2(0)^T \end{pmatrix} \Omega^{-1}\psi \tag{7.49}$$

and the closed loop feedback control is

$$x(k+1) = \left(A - BK_{MPC}\right)x(k) \tag{7.50}$$

The important aspect of MPC is the ability to handle constraints on actuators and system outputs explicitly. The constrained control requires real-time optimization using quadratic programming detailed in [95, 205]. To impose constraints on the rate of change of the input signal, the cost function, eqn. 7.42 is minimized subject to

$$\Delta u_{min} < \Delta u(k_i + k) < \Delta u_{max} \tag{7.51}$$

where Δu_{min} and Δu_{max} are the minimum and maximum rate of change of plant control signal respectively. $\Delta u(k_i + k)$ is defined in eqn. 7.46. Similarly, the constraints on the control signals yield to the following inequality for the future sample time k:

$$u_{min} < \begin{pmatrix} \sum_{i=0}^{k-1} L_1(i)^T & {0_2}^T \\ {0_1}^T & \sum_{i=0}^{k-1} L_2(i)^T \end{pmatrix} \eta + u(k_i - 1) < u_{max} \tag{7.52}$$

where u_{min} and u_{max} are the minimum and maximum values of the plant input signal respectively. Finally the output constraints are yield to the following inequality:

$$y_{min} < y(k_i + k) < y_{max} \tag{7.53}$$

where y_{min} and y_{max} are the minimum and maximum values of the plant output. The output, y is defined from eqn. 7.39 as

$$y(k_i + k) = CA^k x(k_i) + C\phi(k)^T \eta \tag{7.54}$$

In this work, constraints are applied one cycle ahead (k=k_i+1) to reduce the cost function optimization calculation time. The minimum and maximum values of the plant input and output signals used are listed in Table 7.3. The input constraints are hard constraints due to actuator limits while the output constraints are soften by slack variables. Other constraints can be considered by rearranging the COM. For example constraints on the rate of pressure rise or air-fuel ratio have been investigated in [18, 46]. A schematic of the controller structure is shown in Figure 7.8.

Table 7.3: Minimum and maximum values of the input and output signals

	Minimum	Maximum
Injected Fuel Energy [kJ]	0.3	0.5
Injected Fuel Energy Rate [$\frac{kJ}{Cycle}$]	-0.1	0.1
NVO [CA Deg]	0	180
NVO Rate [$\frac{CADeg}{Cycle}$]	-20	20
IMEP [Bar]	0.68	2.5
θ_{50} [CA Deg aTDC]	0	8

7.4 MPC Performance in Simulation

The controller is tested in simulation using the DPM as the virtual engine. The MPC is tested with constant engine speed, intake manifold pressure and temperature first and then effects of load and speed disturbances are examined. Controller performance, without considering constraints on inputs and outputs, is shown in Figure 7.9 and both θ_{50} and IMEP closely track the setpoint. Examining the figure closely, at cycle 200 when the desired IMEP is reduced, EVC timing is advanced and NVO duration is increased to trap more residual gas which maintains the combustion timing at 4 Deg CA aTDC.

Controller performance considering input constraints is shown in Figure 7.10. In this case, the desired IMEP is held constant while the desired combustion timing is advanced. To advance the combustion timing, NVO duration is increased by controller to increase the trapped residual gas. At cycle 204, the NVO duration reaches the maximum constraint of 180 Deg CA so the NVO duration saturates at 180 Deg CA. The value of θ_{50} does not track the desired trajectory. This is attributed to NVO saturation after cycle 204 where the controller keeps fueling rate constant to maintain IMEP (load).

The controller performance with an output constraint is shown in Figure 7.11. The combustion timing lower limit is set to 0 CA Deg after TDC to avoid engine ringing. After cycle 300, the controller does not track the desired combustion trajectory since the desired trajectory is set at 2 CA Deg bTDC. To check the controller performance to a constraint on output work, a maximum limit for IMEP of 2.5 bar based on experiments [9] is set. This limit is based on the engine ringing limit.

Thus in Figure 7.12, when the desired IMEP is increased to 2.8 bar after cycle 300 the controller, maintains the maximum limit of 2.5 bar. In this case, the controller maintains the engine output at the maximum load limit while trying to maintain the combustion timing at 3 CA Deg aTDC. However, the NVO duration reaches the lower limit of 0 CA Deg so the desired combustion timing is not obtained after cycle 300 due to the constraint. The constraints on θ_{50} and output work are used for safe engine operation. The upper and lower bounds are determined from experimental ringing and misfire limits [9].

The controller performance is tested in simulation when both desired combustion timing and load are varied and the results are shown in Figure 7.13. The controller is able to track both desired combustion timing and load accurately when they are changed simultaneously. Figure 7.14 shows the controller performance considering the sensor noise effects. The effect of measurement noise on tracking performance of the MPC is studied by adding a Gaussian disturbed noise with standard deviation of 1.2 CAD to the measurement of θ_{50}. The noise level is determined based on measurements in [9]. The controller maintains tracking despite the measurement noise in the feedback signal. The controller is also tested with the disturbances of engine load and speed. Figures 7.15 and 7.16 show the disturbance rejection properties of the controller for positive and negative disturbance step changes in fuel equivalence ratio and engine speed. The results show that the controller has reasonable disturbance rejection for these cases.

For implementation on the engine an observer is designed. The observer design is explained in section 7.3. When the controller is run in simulation, states like temperature at IVC, θ_{50}, fuel equivalence ratio and residual mole fraction are available from the detailed physical model. However, for real time implementation, there is no sensor on the engine to measure those states so an observer is required to predict them. Further constraints, like constraints on the air-fuel ratio and rate of pressure rise can be considered by augmenting the linearized control oriented model.

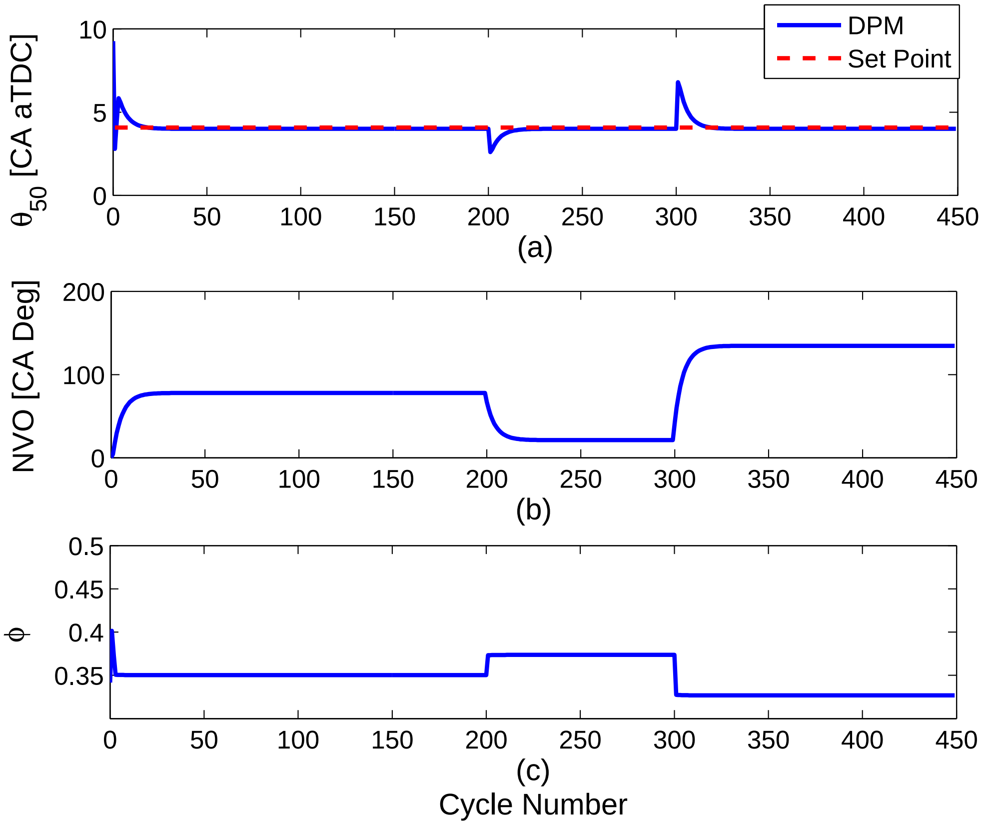

Figure 7.15: Simulated MPC - Disturbance rejection: Engine load (a) θ_{50} (b) Controller Input and (c) Disturbance [ω=825 RPM, P_{int}=95 kPa and T_{int}=80^{o}C]

7.5 MPC Implementation

The model developed in section 7.1 is based on the model developed in [25] and is modified for controller implementation. The nonlinear HCCI model used for implementation is slightly different from the one developed in section 7.1 and has

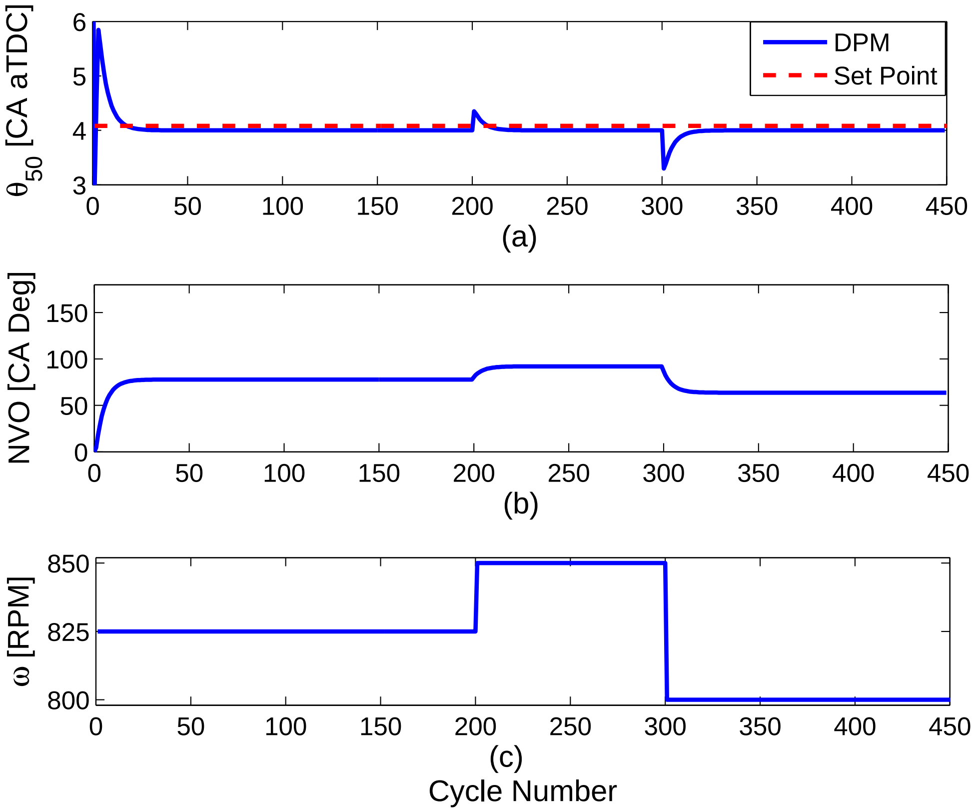

Figure 7.16: Simulated MPC - Disturbance rejection: Engine speed (a) θ_{50} (b) Controller Input and (c) Disturbance [IMEP=1.9 Bar, P_{int}=95 kPa and T_{int}=80^oC]

four states. The modified nonlinear model states are

$$x = [T_{IVC} \quad \alpha \quad \phi \quad \theta_{50}]^T \tag{7.55}$$

where T_{IVC}, α, ϕ and θ_{50} are IVC temperature, residual fraction, fuel equivalence ratio, and combustion timing respectively. The model has two inputs and two outputs:

$$u = [Q_{LHV} \times m_f \quad \theta_{EVC}]^T \tag{7.56}$$

$$y = [\theta_{50} \quad IMEP]^T \tag{7.57}$$

where Q_{LHV}, m_f and θ_{EVC} are fuel heating value, fueling rate and EVC timing respectively.

The modifications in the nonlinear model is mainly related to the IMEP sub-model. In section 7.1, IMEP is modeled as a linear function of injected fuel energy. IMEP modeling in section 7.1 is performed based on the method detailed in [18], however, IMEP is a function of combustion efficiency and it changes with changes in SNVO duration (see chapter 3). Hence, fuel equivalence ratio, combustion timing and IMEP models are modified using experimental data as

$$\phi_k = 0.0007 T_{RES,k-1} m_{fuel,k} Q_{LHV} + 0.19 \tag{7.58}$$

$$\theta_{50,k} = 1.176\theta_{soc,k} + 0.1602 \tag{7.59}$$

$$\text{IMEP}_k = 0.046 \times T_{IVC,k}\phi_k - 3.88 \tag{7.60}$$

The nonlinear model state variables are then normalized. The normalized model is used for model order reduction later to reduce MPC calculation time. The linearized model has a large difference of magnitude among the state variables that could affect the decision of the importance of each state. The importance of each state variable on the relationship between input and output is then examined and the non-dominant states are truncated. The state variables are divided by standard state variable as

$$\tilde{x} = \frac{x}{x_s} \tag{7.61}$$

where $\tilde{x}$ is the non-dimensional state variable. The normalized non-linear state space model is derived as

$$\dot{\tilde{x}} = \frac{1}{x_s} f(\tilde{x} x_s, u) \tag{7.62}$$

The operating point listed in Table 7.4 is used to normalize the non-linear model which means that all of the normalized state variables are 1 at this operating point.

Table 7.4: Operating Condition used to Normalize Nonlinear COM

T_{IVC}	363.5 K
α	0.107 [-]
ϕ	0.3 [-]
θ_{50}	2.72 CAD aTDC
$IMEP$	1.5 Bar

The normalized state-space model is re-linearized around the operating point listed in Table 7.5. This operating point is selected close to the operating point that both PI and feedforward/feedback controllers implemented in chapter 6. A first order approximation of Taylor expansion is used to linearize the model. The linear state-space model is given by

$$\begin{aligned} x_{k+1} &= Ax_k + Bu_k \\ y_k &= Cx_k + Du_k \end{aligned} \tag{7.63}$$

where A, B, C and D depend on the operating point that the model is linearized around. The model states, inputs and outputs are defined in Eqns. 7.55, 7.56 and

7.57. The A, B and C matrices are

$$
A = \begin{bmatrix} 0.1129 & -0.0005 & 0.0045 & 0.000 \\ -1.1953 & 0.0048 & -0.0473 & -0.0004 \\ 0.3424 & -0.0014 & 0.0136 & 0.0001 \\ -7.2144 & 0.0288 & -0.2858 & -0.0021 \end{bmatrix}
$$

$$
B = \begin{bmatrix} 0.0002 & -0.0178 \\ 0 & -2.4634 \\ 0.9741 & 0 \\ -6.9582 & 0.7538 \end{bmatrix} \tag{7.64}
$$

$$
C = \begin{bmatrix} 0 & 0 & 0 & 1 \\ 7.7047 & 0 & 3.4357 & 0 \end{bmatrix}
$$

and D is a zero matrix. All model states are controllable and observable according to Popov-Belevitch-Hautus (PBH) tests [204].

Table 7.5: Operating Condition used to Linearize Normalized Nonlinear COM

T_{IVC}	385.06 K
α	0.23 [-]
ϕ	0.3 [-]
θ_{50}	-1.019 CAD aTDC
$m_f Q_{HV}$	0.39 kJ
ω	817 RPM
θ_{EVC}	50 CAD bTDC

The open loop responses of the DPM, the nonlinear COM and linearized model are compared in simulation and are shown in Figure 7.17. There are differences between nonlinear model and the DPM, however, the linearized model have enough accuracy for control design. The linear model still follows the DPM with high accuracy. MPC is implemented based on the linearized COM. The model is embedded with two integrators, one for IMEP and one for combustion timing as indicated in section 7.3. The MPC is implemented (based on the algorithm explained in section 7.3) with slight modifications in constraint handling as discussed in the next section.

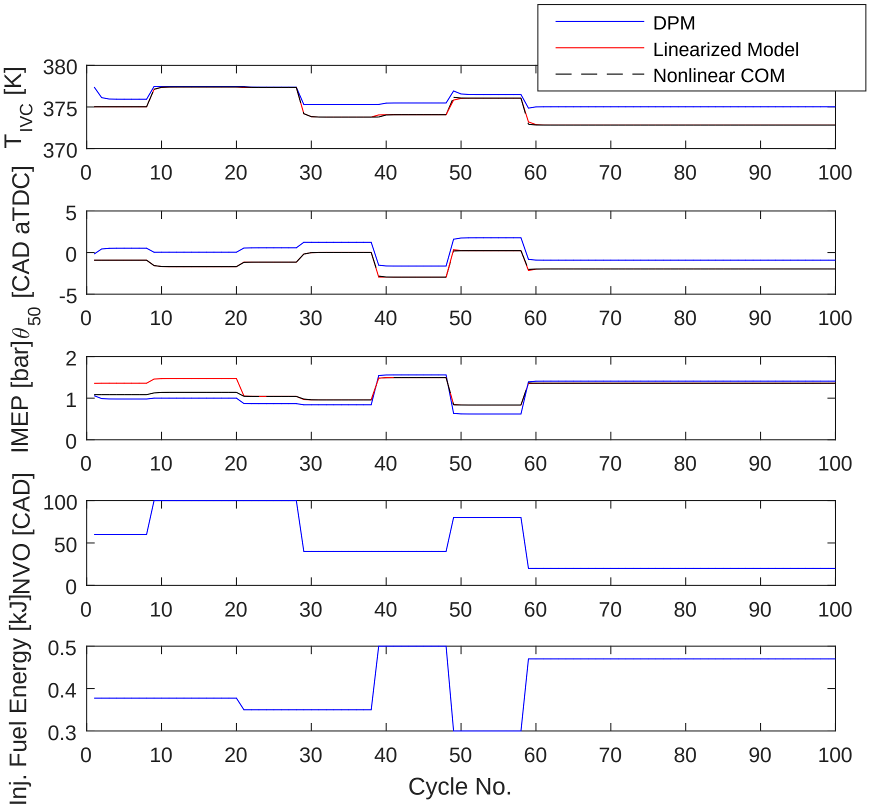

Figure 7.17: Comparison of the DPM, COM and the linearized COM in the open loop simulation

7.5.1 Constraint Handling for Controller Implementation

The constraints on rate of change of control signal is

$$\Delta u_{min} \leq \Delta u \leq \Delta u_{max} \tag{7.65}$$

The cost function, eqn. 7.42 is minimized considering constraints on the rate of change of control signal. For this reason, the global optimal solution ($\eta = -\Omega^{-1}\psi x(k_i)$) is obtained first. The optimal solution is the global optimal solution if

$$\Delta u_{min} \leq L(0)^T \eta \leq \Delta u_{max} \tag{7.66}$$

If $L(0)^T\eta < \Delta u_{min}$ where $\eta = -\Omega^{-1}\psi x(k_i)$ then control signal is defined as $\Delta u(k_i) = \Delta u_{min}$. Similarly, when $L(0)^T\eta > \Delta u_{max}$ where $\eta = -\Omega^{-1}\psi x(k_i)$, the control signal is defined as $\Delta u(k_i) = \Delta u_{max}$. The optimal control signal is then defined as $u(k_i) = u(k_i - 1) + \Delta u(k_i)$.

The constraints on control signal is

$$u_{min} \leq u \leq u_{max} \tag{7.67}$$

The optimal solution of the cost function is the global optimal solution ($\eta = -\Omega^{-1}\psi x(k_i)$) if

$$u_{min} \leq u(k_i - 1) + L(0)^T\eta \leq u_{max} \tag{7.68}$$

If $u(k_i - 1) + L(0)^T < u_{min}$ with $\eta = -\Omega^{-1}\psi x(k_i)$ then $u(k_i) = u_{min}$. The rate of change of control signal is then defined as $\Delta u(k_i) = u_{min} - u(k_i - 1)$. Similarly if $u(k_i - 1) + L(0)^T > u_{max}$ with $\eta = -\Omega^{-1}\psi x(k_i)$ then $u(k_i) = u_{max}$ and $\Delta u(k_i) = u_{max} - u(k_i - 1)$.

Constraints on the outputs are hard to implement and it strongly depends on the model/observer accuracy. At sample time k_i, the prediction of the states one cycle ahead is

$$x(k_i + 1) = Ax(k_i) + BL(0)^T\eta \tag{7.69}$$

and the predicted output one cycle ahead is

$$y(k_i + 1) = CAx(k_i) + CBL(0)^T\eta \tag{7.70}$$

If the output constraints are applied one cycle ahead of time and the inequality of $y_{min} \leq CAx(k_i) + CBL(0)^T\eta \leq y_{max}$ is valid then the optimal solution of the cost function, eqn. 7.42, is the global optimal solution ($\eta = -\Omega^{-1}\psi x(k_i)$). However, if

$CAx(k_i)+CBL(0)^T\eta < y_{min}$ where $\eta = -\Omega^{-1}\psi x(k_i)$ then the output constraint is active. To find the optimal solution of the cost function, the inequality is rearranged as [95]

$$-\phi(k)^T\eta < -y_{min} + CA^{N_p}x(k_i) \tag{7.71}$$

If the constraint on upper limit is violated, then the inequality is

$$\phi(k)^T\eta < y_{max} - CA^{N_p}x(k_i) \tag{7.72}$$

Hildreth's quadratic programming procedure [95, 206] as a dual method is then used to minimize the cost function (eqn. 7.42) subject to the inequalities in eqns. 7.66, 7.68, 7.71 and 7.72. The most important constraints are related to the control signal and the rate of change of the control signal. Secondary constraints are related to the outputs as the effectiveness of these constraints are related to the model accuracy. Also, when observer is used for state estimations the implementation of the output constraints becomes more difficult. In this work, the most important constraints are considered on the amplitude of control signal, the less important constraints are applied to the rate of change of control signal and the least important constraints are considered on the outputs.

7.5.2 Tuning of the Laguerre Function parameters [95, 44]

The cost function of MPC with Laguerre function, eqn. 7.42, is equivalent to

$$J = \Sigma_{k=1}^{Np}(r(k_i) - y(k_i+k))^T(r(k_i) - y(k_i+k)) + \eta^T R_L \eta \tag{7.73}$$

where R_L is a diagonal matrix ($N \times N$) with positive values on its diagonal and r is the set-point signal for the output y. The cost function in eqn. 7.73 is based on the minimization of the error between the set-point signal and the output signal. The cost function is reformulated with the link to Discrete-time Linear Quadratic Regulators (DLQR), where the objective is to minimize the following cost function [44]

$$J = \Sigma_{k=1}^{Np} x(k_i + k)^T Q x(k_i + k) + \eta^T R_L \eta \tag{7.74}$$

where the matrices Q and R_L are weighting matrices.The DLQR is used to tune the Laguerre parameters for MPC design. Both MPC and DLQR cost functions are identical when $r(k_i) = 0$ and $Q = C^T C$. When $r(k_i) \neq 0$ with $Q = C^T C$, the DLQR cost function (eqn. 7.74) is identical to the MPC cost function (eqn. 7.73) with the new state variables defined as

$$x(k_i + m) = \left[\Delta x(k_i + k)^T \;\; y(k_i + k) - r(k_i) \right]^T \tag{7.75}$$

Thus, the unconstrained MPC control is completely identical to the optimal DLQR solution when receding control is applied. The DLQR function in MATLAB is used for tuning the MPC before implementation.

The linearized COM is used for MPC implementation based on the algorithm explained in section 7.3 and shown in Figure 7.18. The Laguerre function parameters are tuned for the linearized model as explained above. The Laguerre parameters are tuned so that the closed loop eigenvalues of the MPC are identical to the closed loop eigenvalues of the DLQR. The tuned parameters are listed in table 7.6 for $N_p = 10$. N_p is the prediction horizon and is defined based on transient measurements.

Experimental transient measurements are performed to investigate effects of fueling rate and valve timing on HCCI combustion. Figure 7.19 shows effects of

Table 7.6: Tuned Laguerre Coefficients (N_p=10)

a_1	0.5	a_2	0.5
N_1	6	N_2	6

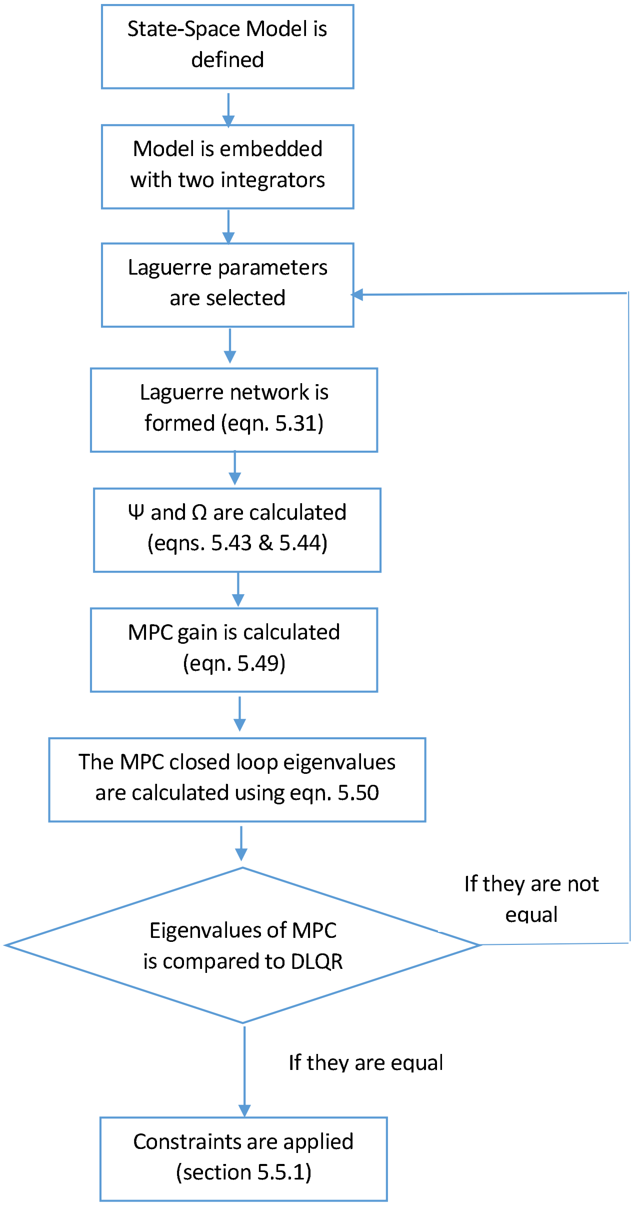

Figure 7.18: MPC Algorithm including Laguerre tuning

fueling rate on combustion timing. Fueling rate is reduced at cycle 100 and the combustion timing is retarded to 4.3 CAD aTDC. This figure indicates that changing fuel quantity at cycle 100 influences combustion phasing on the next cycle and

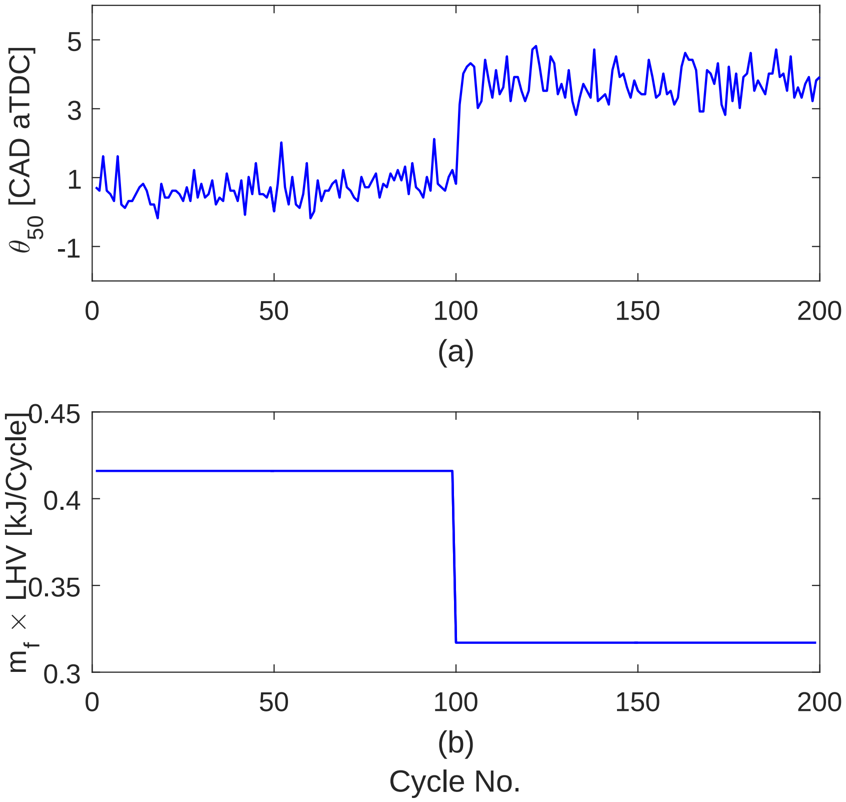

(a)

(b)

Figure 7.19: Experiment - Effect of fueling rate on combustion timing [NVO= 40 CAD]

it takes 2-3 cycles for combustion timing to reach steady state condition.

The NVO duration effects on combustion timing is shown in Figure 7.20. The amount of trapped residual gas is reduced by reducing the NVO duration and the combustion timing is retarded as the IVC temperature is reduced. It takes 20 cycles for combustion timing to reach steady state condition after NVO changed at cycle 26. These results are consistent with the literature [18]. The prediction horizon for MPC implementation is selected as 10 since both actuators are used for combustion timing and load control and fast dynamic of the fueling rate compensates the relatively slow dynamics of valve timing. Figure 7.21 shows that both MPC and DLQR eigenvalues are almost identical with the tuned Laguerre parameters listed in Table

7.6 and N_p=10 (all eigenvalues are located on the real axis).

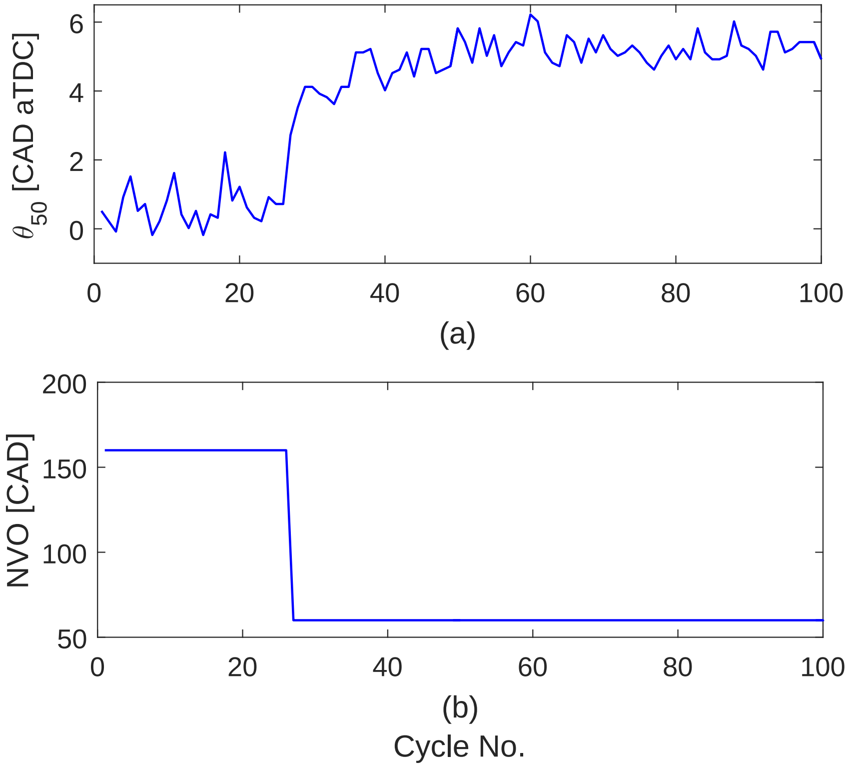

Figure 7.20: Experiment - Effect of NVO on combustion timing [Injected Fuel Energy= 0.3 $\frac{kJ}{Cycle}$]

7.5.3 Observer Implementation

The MPC explained in section 7.3 requires observer as two states (T_{IVC} and α) are not available from the experimental measurements. A full state Luenberger observer is used in this work as discussed in 7.3. All states are estimated based on measurements of θ_{50} and IMEP from Baseline CAS system. The observer is constructed based on the augmented model and it is validated against experimental data. The results shown in Figure 7.22 indicates that the observer has good accuracy for controller implementation. Both fueling rate and NVO duration are changed in

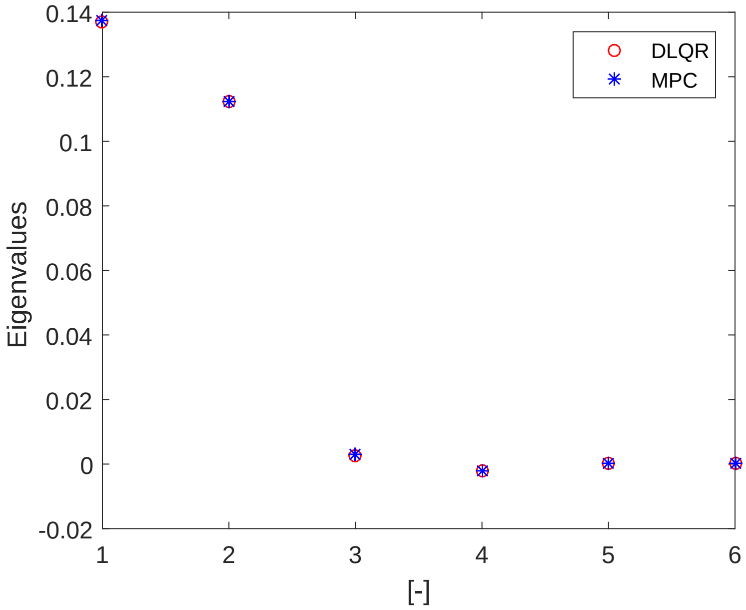

Figure 7.21: Comparison of the closed-loop eigenvalues between MPC and DLQR

this experiment. Other states are not validated as they are not available from the measurements. The IMEP is slightly increased with increase in fueling rate at cycle 48 since the combustion timing is advanced before TDC that increases compression work. The observer accuracy can be improved if exact timing of the inputs and outputs are considered for observer design as detailed in [18]. Kalman filter is used in [18] as observer, however a simple full state Luenberger observer shows good accuracy in predicting model states and it is used for MPC implementation in this work.

7.5.4 MPC Implementation

In chapter 6, PI and feedforward/feedback controllers were developed and implemented for combustion timing control. The MPC controller performance is tested for the same experiments and the results are shown in Figs. 7.23 and 7.24. All controllers can track combustion timing with no steady state error. The Fdfwd/Fdbk

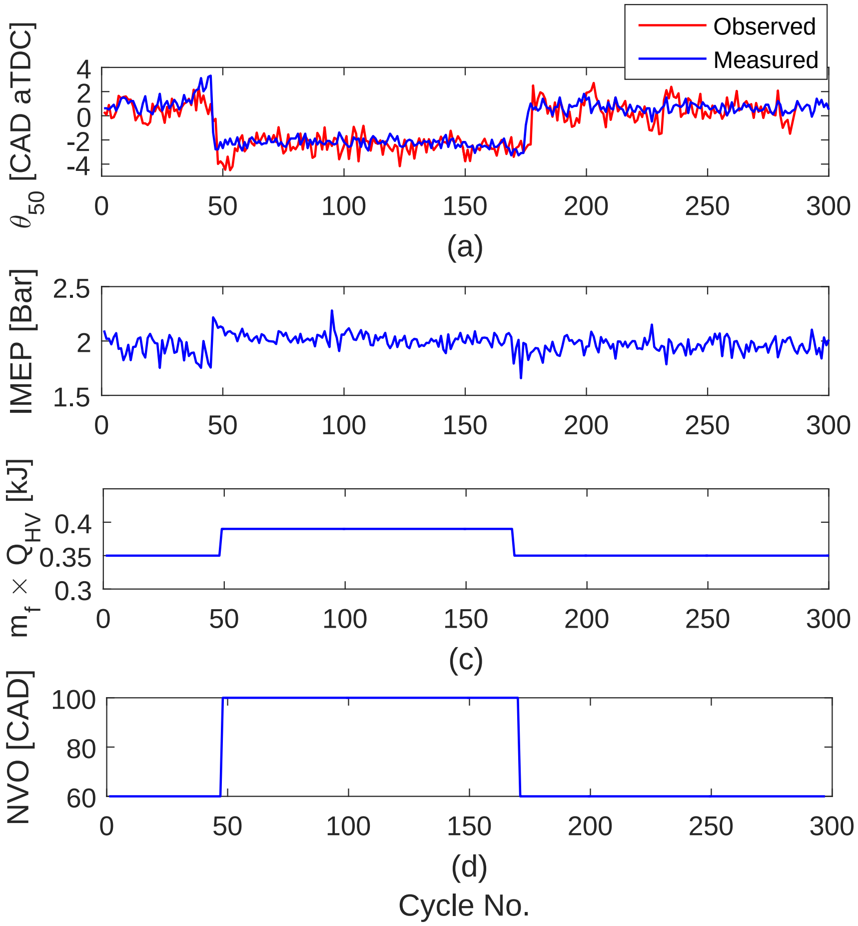

Figure 7.22: Experiment - Observer Validation: (a) combustion timing (b) load (c) & (d) Inputs: Injected Fuel Energy and NVO duration

controller has fast closed loop response and the MPC closed loop response can be adjusted by modulating the weight factors in the cost function (Q and R_L in eqns. 7.42 and 7.43). The fluctuations in the valve timings are higher in MPC compared to the other controllers that is mainly related to the fast model transient dynamics. The valve timing fluctuations are manageable by further validating the control approach.

The controller performance is tested in tracking load at constant combustion timing in Figure 7.25. Controller is able to track load fairly accurately. The steady

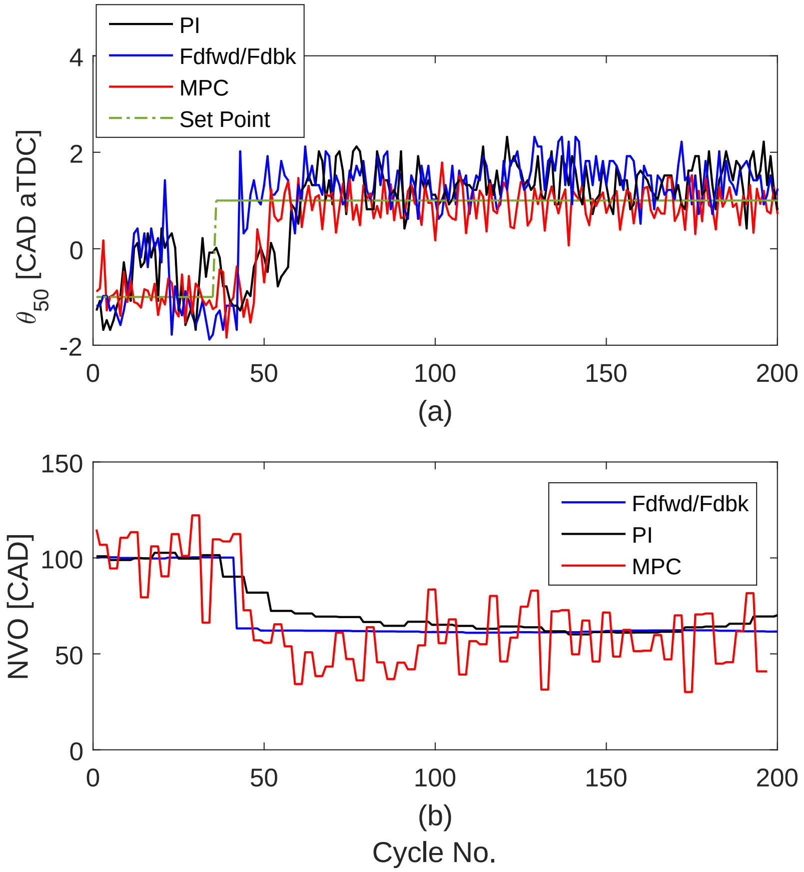

Figure 7.23: Experiment - Tracking performance of the manually tuned PI, feedforward/feedback and MPC (step up) (a) θ_{50} as controller output (b and c) Controller Inputs[n= 788 RPM, Injected Fuel Energy=0.4 kJ]

state error is negligible due to the integral action of the augmented model. It is seen that the controller is able to track both load and combustion timing considering constraints on the valve timing and fueling rate. At cycle 44, desired IMEP is reduced from 2 Bar to 1.4 Bar and the controller can track it by reducing the fueling rate. The controller increases the NVO duration to trap more residual gas and keep the combustion timing at 1 CAD aTDC. At cycle 150, the desired IMEP is returned back to its original value, 2 Bar. The fueling rate is increased by the controller to meet the desired IMEP. The controller reduces the NVO duration to trap less residual gas and keep the combustion timing constant.

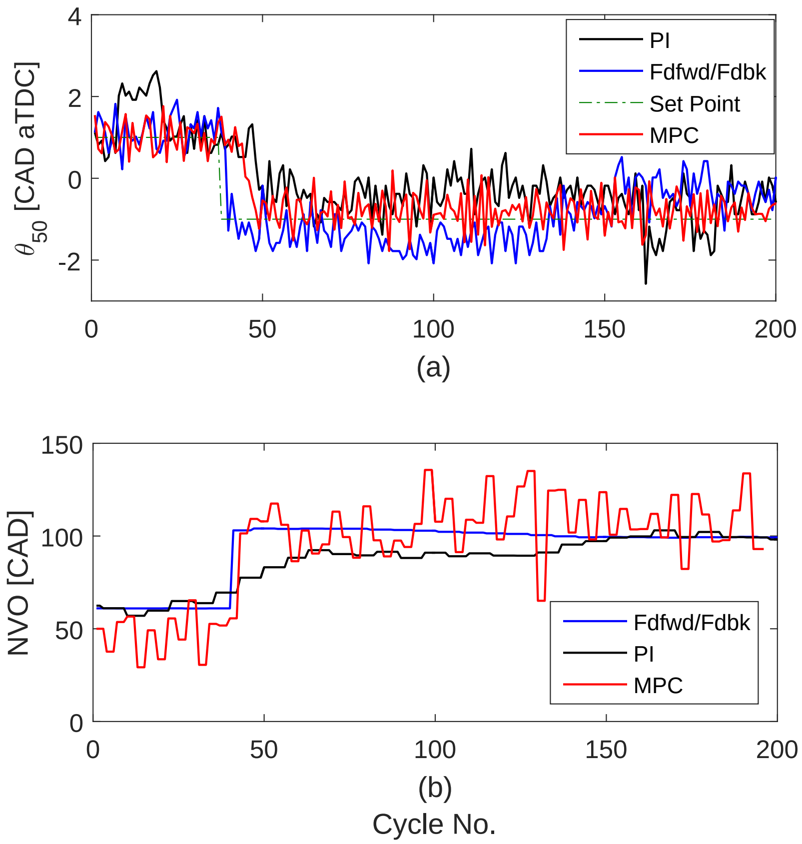

Figure 7.24: Experiment - Tracking performance of the manually tuned PI, feedforward/feedback and MPC (step down) (a) θ_{50} as controller output (b and c) Controller Inputs[n= 788 RPM, Injected Fuel Energy=0.4 kJ]

Figure 7.26 shows the controller performance in tracking combustion timing and load when both desired values are changed. First, desired combustion timing is retarded to 1 CAD aTDC at cycle 44. The controller reduces NVO to trap less residual gas and retard combustion timing. Then, the desired IMEP is reduced at cycle 56 to 1.4 Bar. The controller reduces fueling rate to track the desired IMEP. The combustion timing tends to be retarded at lower fueling rates, hence, the controller increases NVO duration to trap more residual gas and keep combustion timing constant at 1 CAD aTDC. Figure 7.26 (c) and (d) indicates that the controller is able to keep actuators within the constraint limits.

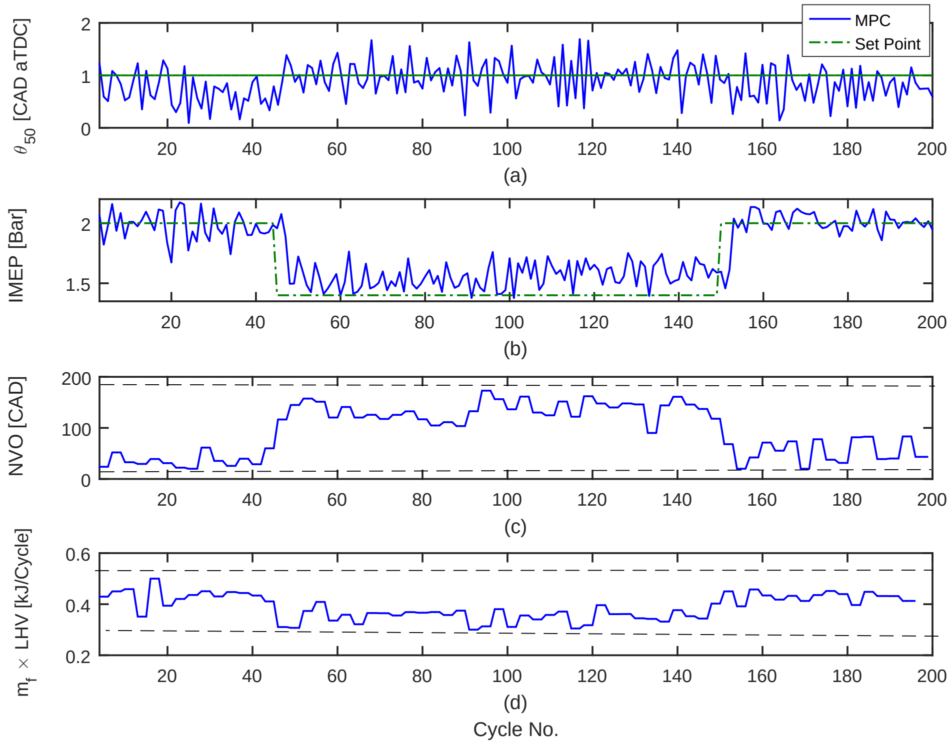

Figure 7.25: Experiment - MPC implementation: (a) combustion timing (b) load (c) & (d) Inputs: NVO duration and Injected Fuel Energy

The MPC performance for the case that constraints are applied on outputs is more complicated than the input constraints. The constraints on output need to be introduced cautiously as they can cause instability of the closed-loop system and severe deterioration of the closed-loop performance. The output constraints are tested for engine speed disturbance rejection as shown in Figure 7.27. Engine speed is increased at cycle 22 from 725 RPM to 950 RPM. The combustion timing is retarded by increase in engine speed. At higher speeds, the low temperature heat release is reduced that retards the combustion timing [207, 208]. The constraints are imposed on both IMEP and combustion timing. The combustion timing and IMEP higher limits are set to 1.7 CAD aTDC and 1.9 Bar while the lower limits are

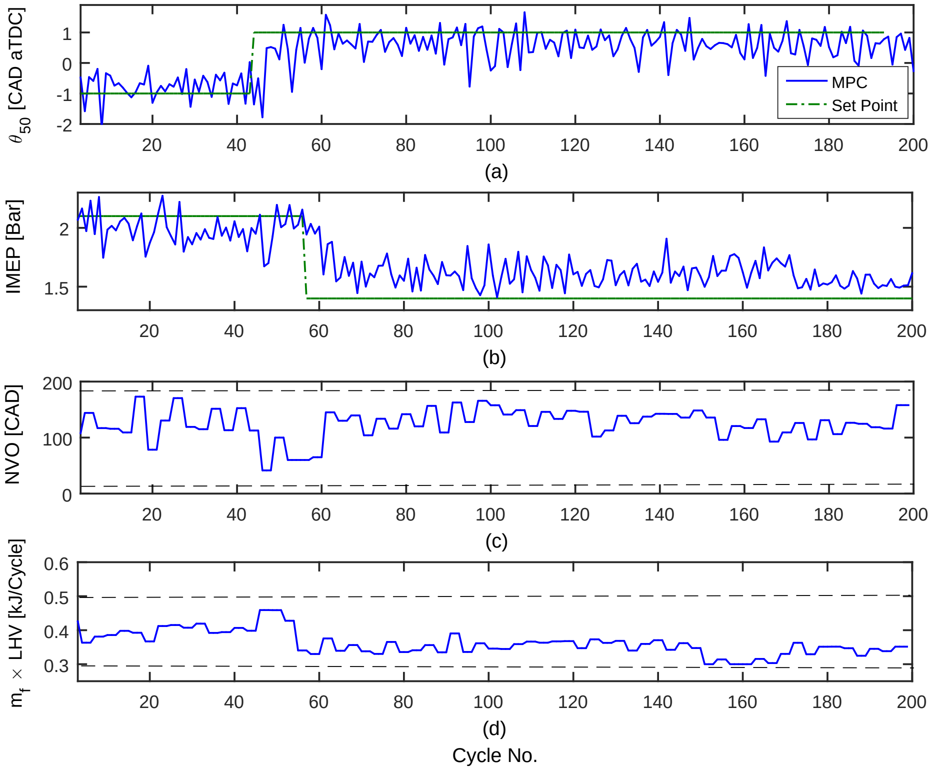

Figure 7.26: Experiment - MPC implementation: (a) combustion timing (b) load (c) & (d) Inputs: NVO duration and Injected Fuel Energy

set to 0.5 CAD bTDC and 1.1 Bar respectively. These values are different from the values listed in Table 7.3. At cycle 78, the combustion timing reaches the higher limit and then cross the limit. The output constraints are activated at cycle 117 and the controller increases NVO duration to return the combustion timing back to its initial value with trapping more residual gas (highlighted in Figure 7.3 (c)). The controller does not change the fueling rate as the IMEP is almost constant with increase in engine speed. The constraint violation between cycles 78 and 117 is due to the slack variable in optimization algorithm. Figure 7.27 shows that the controller is not able to return the combustion timing to the desired value however it can keep the combustion timing within the limit defined by the constraints . In addition, the

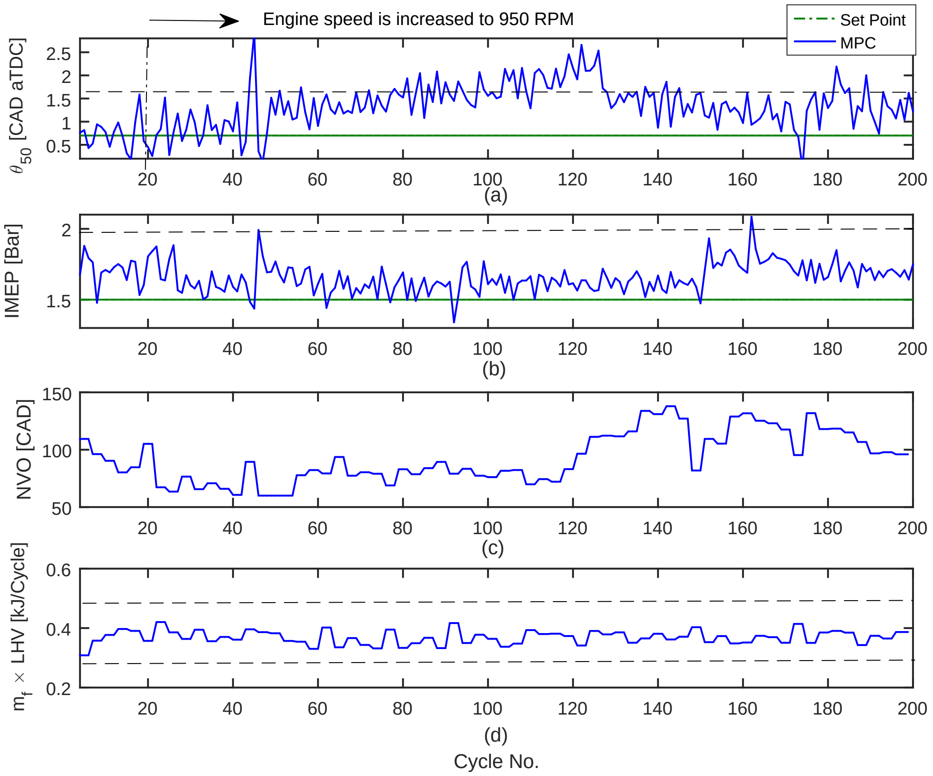

Figure 7.27: Experiment - MPC implementation: (a) combustion timing (b) load (c) & (d) Inputs: NVO duration and Injected Fuel Energy

controller keeps the actuator within the limit defined in Table 7.3.

7.6 Discussion

The MPC developed in this chapter shows good performance for cycle by cycle control of combustion timing and load. Symmetric NVO and fueling rates are used as the main actuators while the IMEP and combustion timing are used as feedback to the controller. The hard constraints are imposed on the controller inputs considering experimental setup physical limitations. The output constraints are defined based on engine operating region and are relaxed with slack variables. The controller shows good performance in simulation and single cylinder experiments. The controller was implemented for a narrow operating region, the region that the model is linearized around. To implement the controller a proportional integral observer is used that compensates model/plant mismatch. The output constraint is hard to implement due to model-plant mismatch. To further extend the control range, MPC controller can be designed using LPV method [209] by linearizing the model around several operating points.

Chapter 8

HCCI Control Oriented Modeling Considering Combustion Efficiency[1]

In chapter 4, it is found that combustion efficiency has important effect on HCCI engine energy distribution. The detailed physical model developed in chapter 5 estimates higher values for combustion efficiency so it is not possible to drive a control oriented model that considers combustion efficiency with the approach explained in chapter 7. In this chapter, the effects of valve timing and fueling rate on combustion efficiency are first investigated experimentally. Then, the influence of combustion efficiency on HC and CO emissions is detailed. Next, a control oriented model is developed for HCCI engine combustion efficiency and emission control based on measurements. This model includes the effect of trapped residual gas and fueling rate on combustion timing and output power. This model is useful for combustion timing and load control in HCCI engines considering the constraints on combustion efficiency and emission. This is, to the authors knowledge, the first time that combustion efficiency is included in HCCI control oriented modeling.

---

[1] This chapter is based on [136]

8.1 SNVO and Fueling Rate Effects on Combustion Efficiency

SNVO duration is varied for several injected fuel energies while other parameters are kept constant. The experimental conditions are listed in Table 2.1. The measurements are used to develop and validate the control oriented model. Combustion timing, burn duration and engine output power are measured while combustion efficiency is calculated using a modified single zone model as [136]

$$\eta_{Comb} = \frac{c_1 Q_{HR}}{m_f LHV_f} + c_2 \tag{8.1}$$

where Q_{HR}, m_f and LHV_f are the net energy released during combustion, the injected fuel mass and n-heptane low heating value respectively. c_1 and c_2 are constants and are listed in Table 8.1.

The effects of SNVO on combustion efficiency and combustion timing at constant injected fuel energies are shown in Figure 8.1. The IVC temperature increases at higher NVOs and the combustion timing advances as a result (see Figure 8.1(a)). With advanced combustion timing, the trapped mixture has enough time to more completely burn and the reactions are quenched later which improves combustion efficiency (see Figure 8.1(b)). Combustion efficiency is improved considerably at low loads with increasing NVO duration compared to high loads. Next, the effects of combustion efficiency on unburnt HC, CO and $\mathrm{CO_2}$ at constant injected fuel energies are shown in Figure 8.2 for engine operation without ringing or misfire. The CO and HC are reduced at higher combustion efficiencies while $\mathrm{CO_2}$ is increased as shown in Figure 8.2(a) through (c). Engine emissions are related to combustion efficiency and can be influenced by valve timing and fueling rate as actuators.

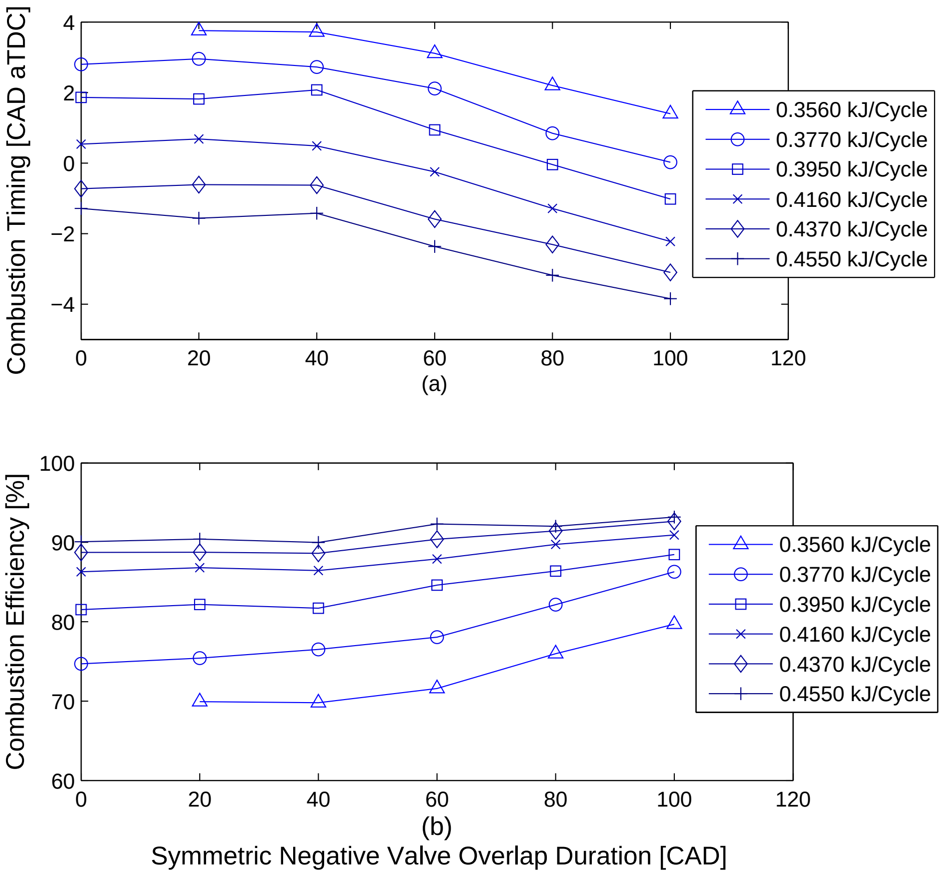

Figure 8.1: Effects of SNVO duration on (a) combustion timing (b) combustion efficiency at constant injected fuel energies

8.2 Control Oriented Model

A control oriented model of a single cylinder HCCI engine is developed and parameterized using measured experimental data. The model is based on physics and is developed to consider the effects of valve timing and fueling rate on combustion timing, engine output power and **combustion efficiency**. At the start of the cycle, fresh charge is inducted into the cylinder and intake charge is assumed to instantaneously mix with the trapped residual gas at IVC. In-cylinder gas temperature at

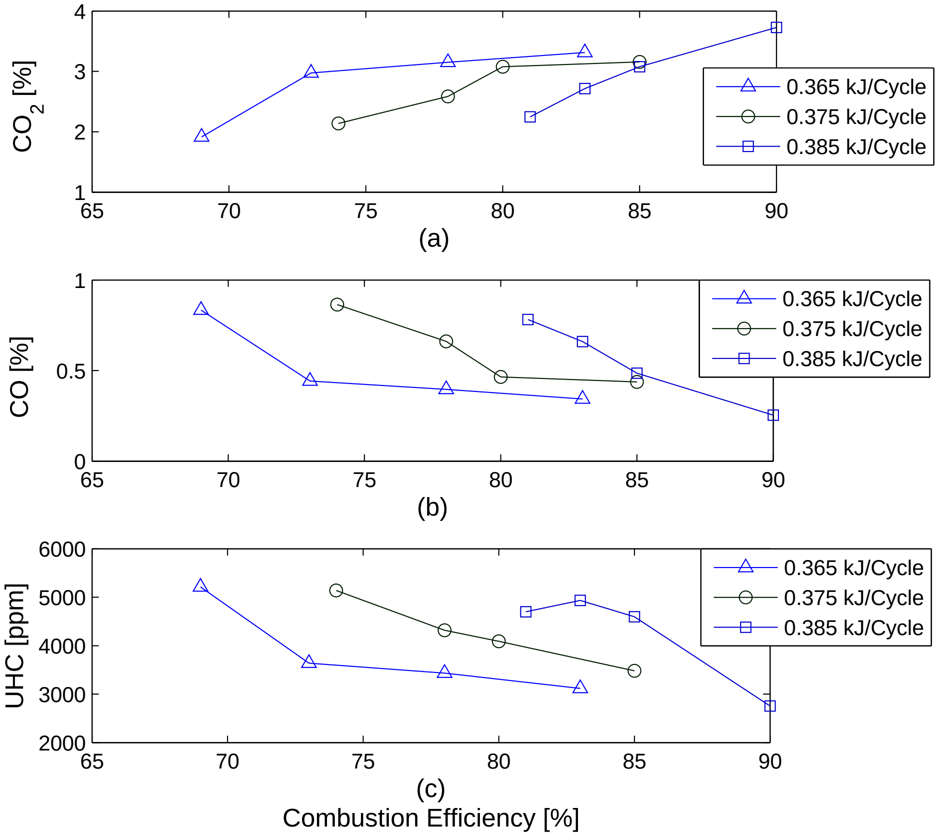

Figure 8.2: (a) $\mathrm{CO_2}$ (b) CO and (c) Unburnt HC versus combustion efficiency at constant injected fuel energies

IVC, T_{IVC} is calculated as

$$T_{IVC,k} = \frac{x_{r,k} c_{p,r} T_{exh,k-1} + (1 - x_{r,k}) c_{p,i} T_{int,k}}{c_{p,IVC}} \tag{8.2}$$

where $c_{p,r}$, $c_{p,i}$ and $c_{p,IVC}$ are residual gas, intake charge and IVC trapped charge specific heat values at constant pressure. x_r and k are residual mass gas fraction and cycle number respectively. All model constant values are listed in Table 8.1. Residual gas mass fraction, x_r is calculated as [7]

$$x_{r,k} = \frac{M_r y_{r,k}}{M_i - M_i y_{r,k} + M_r y_{r,k}} \tag{8.3}$$

where M_i and M_r are the exhaust and intake gas mean molecular weights. Residual gas mole fraction, y_r is calculated as

$$y_{r,k} = \frac{P_{exh,k-1}}{P_{IVC,k}} \frac{V_{EVC,k-1}}{V_{IVC,k}} \frac{T_{IVC,k}}{T_{exh,k-1}} \tag{8.4}$$

where V_{EVC} and V_{IVC} are the in-cylinder volume at EVC and IVC respectively and are calculated form slider-crank mechanism equation [7]. The intake process is assumed to take place at atmospheric pressure

$$P_{IVC,k} = P_{int,k} \tag{8.5}$$

as our HCCI engine usually operates at wide-open throttle with the variable valve timing used to control the amount of trapped charge.

The crank angle of fifty percent fuel mass fraction burned, θ_{50} is calculated as

$$\theta_{50,k} = \theta_{soc,k} + 0.5\Delta\theta_k \tag{8.6}$$

Sensitivity analysis is performed to define the parameters which have important effect on start of combustion. The start of combustion, θ_{soc} is calculated as

$$\theta_{soc,k} = c_3 T_{IVC,k}\phi_k + c_4\phi_k + c_5 T_{IVC,k} + c_6 \tag{8.7}$$

where ϕ is fuel equivalence ratio and c_i are model constants determined using Matlab Model-Based Calibration toolbox and are listed in Table 8.1. The other submodels including burn duration, fuel equivalence ratio, combustion efficiency and IMEP are parameterized with the same method.

Burn duration, $\Delta\theta$ is calculated as

$$\Delta\theta_k = c_7\theta_{soc,k} + c_8 \tag{8.8}$$

Temperature and pressure at the crank angle of fifty percent fuel mass fraction burned, with the assumption of isentropic compression, are calculated as

$$P_{50,k} = P_{int,k}\left(\frac{V_{IVC,k}}{V_{50,k}}\right)^{\gamma} \tag{8.9}$$

$$T_{50,k} = T_{IVC,k}\left(\frac{V_{IVC,k}}{V_{50,k}}\right)^{\gamma-1} \tag{8.10}$$

where V_{50} is the in-cylinder volume at the crank angle fifty of mass fraction burned. γ is assumed constant and is parameterized using the experimental data.

The first law of thermodynamics is applied to the system to calculate in-cylinder gas temperature after combustion. Temperature after combustion, T_{AC} is calculated as

$$T_{AC,k} = T_{50,k} + \frac{c_9\phi_k\eta_{c,k}LHV_f}{c_pAF_{stoich}} \tag{8.11}$$

where η_c and AF_{stoich} are combustion efficiency and stoichiometric air fuel ratio respectively and c_p is the specific heat ratio at θ_{50}. The fuel equivalence ratio, ϕ is calculated as

$$\phi_k = c_{10}T_{IVC,k}y_k + c_{11}T_{IVC,k} + c_{12}y_k + c_{13}m_{f,k}LHV_f + c_{14} \tag{8.12}$$

Combustion efficiency, η_c in Eqn. 8.11, is calculated as

$$\eta_{c,k} = c_{15}\theta_{50,k} + c_{16}T_{IVC,k} + c_{17}y_{r,k} + c_{18}\phi_k^{c_{19}} + c_{20} \tag{8.13}$$

By applying the ideal gas law before and after combustion, the in-cylinder pressure after combustion is calculated as

$$P_{AC,k} = \frac{P_{50,k}T_{AC,k}}{T_{50,k}} \tag{8.14}$$

The expansion process is assumed to be isentropic and the in-cylinder gas temperature and pressure at Exhaust Valve Opening (EVO) is calculated as

$$T_{EVO,k} = \left(\frac{V_{50,k}}{V_{EVO,k}}\right)^{\gamma_e-1}T_{AC,k} \tag{8.15}$$

$$P_{EVO,k} = (\frac{V_{50,k}}{V_{EVO,k}})^{\gamma_e} P_{AC,k} \tag{8.16}$$

where γ_e is determined using experimental data and V_{EVO} is the in-cylinder volume at EVO.

At EVO, blowdown to the exhaust manifold pressure is assumed to occur as an isentropic process. The residual gas temperature after blowdown is calculated as [7]

$$T_{exh,k} = \left(\frac{P_{exh,k}}{P_{EVO,k}}\right)^{\frac{\gamma_e - 1}{\gamma_e}} T_{EVO,k} \tag{8.17}$$

where P_{exh} is the exhaust manifold pressure.

Finally, engine output work is calculated from a correlation obtained from experimental data:

$$\text{IMEP}_k = c_{21}\eta_k m_{f,k} LHV_f + c_{22}\eta_k + c_{23} m_{f,k} LHV_f + c_{24}\theta_{50,k} + c_{25} \tag{8.18}$$

The control oriented model, in standard state-space form where the states can be written as a function of the inputs and state variables of the previous cycle, is

$$\begin{aligned} x_{k+1} &= f(x_k, u_k, w_k) \\ y_k &= g(x_k, u_k, w_k) \end{aligned} \tag{8.19}$$

where x is the state of the system, u is the control input and w is a disturbance. The states, the inputs and the outputs for this system are

$$\begin{aligned} x &= \begin{bmatrix} T_{ivc} & \phi & \eta_c & \theta_{50} \end{bmatrix}^T \\ u &= \begin{bmatrix} m_f Q_{LHV} & \theta_{EVC} \end{bmatrix}^T \\ y &= \begin{bmatrix} \theta_{50} & \text{IMEP} \end{bmatrix}^T \end{aligned} \tag{8.20}$$

Table 8.1: Model parameters and constants

c_1	55.271	c_2	44.176	c_3	0.00788
c_4	-4.043	c_5	-0.0036	c_6	1.493
c_7	1.7365	c_8	0.581	c_9	0.76
c_{10}	0.0012	c_{11}	-0.000077	c_{12}	-0.3582
c_{13}	0.6734	c_{14}	0.071	c_{15}	-0.044
c_{16}	0.039	c_{17}	2.86	c_{18}	17.47
c_{19}	3.99	c_{20}	67.79	c_{21}	-0.2764
c_{22}	0.1385	c_{23}	29.90	c_{24}	0.075
c_{25}	-12.36	$c_{p,r}$	1.079	$c_{p,i}$	1.15
$c_{p,IVC}$	1.046	c_p	1.113	M_i	29.39
M_r	28.74	γ_e	1.3	γ	1.29

8.3 Model Validation

For the steady state experimental data range listed in Table 7.2, the control oriented model is compared to the experiment in Figure 8.3. Figure 8.3 shows that the model captures combustion timing, combustion efficiency and engine output power with average errors of 0.65 CAD, 7.54% and 0.09 Bar respectively. The model is then compared for SNVO duration variations at a constant fueling rate in Figure 8.4. The amount of trapped residual gas increases with an increase in SNVO and the in-cylinder gas temperature at IVC increases. Combustion timing advances with increased IVC temperature and the combustion efficiency increases as shown in Figure 8.4. IMEP increases with increasing SNVO until SNVO reaches 60 CAD then decreases due to increased compression work. The predicted values from the control oriented model match the experiments well. Then, fueling rate is varied and SNVO duration is kept constant and the simulation is compared to experiment in Figure 8.5. The effects of fueling rate on combustion timing, combustion efficiency and output power at constant SNVO are shown in Figure 8.5. Combustion timing advances with increase in fueling rate as the fuel reactivity tends to increase from lean to rich conditions [13]. IMEP increases as fueling rate is increased and combustion efficiency increases with advanced combustion timing. These results indicate that control oriented model captures the fueling rate and the trapped residual gas effects on combustion timing well.

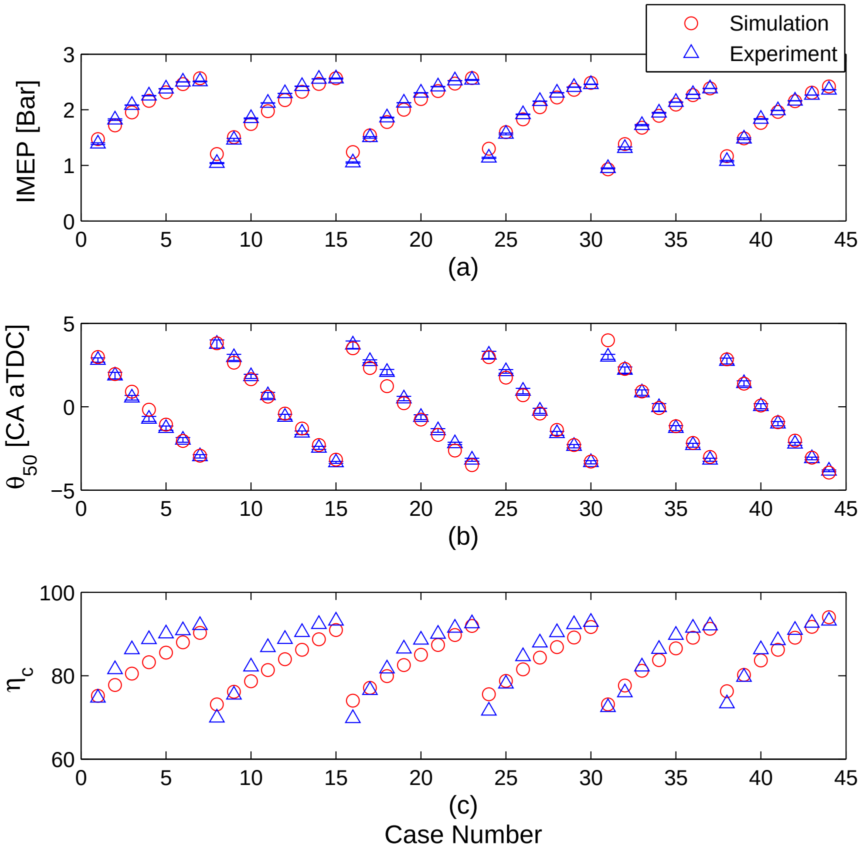

Figure 8.3: Steady state validation (a) engine output power (b) combustion timing and (c) combustion efficiency

Transient validation is performed using the detailed physical model developed in chapter 5 and experimental data. The results are shown in Figure 8.6 and 8.7. The control oriented model captures the trends of the detailed physical model when step

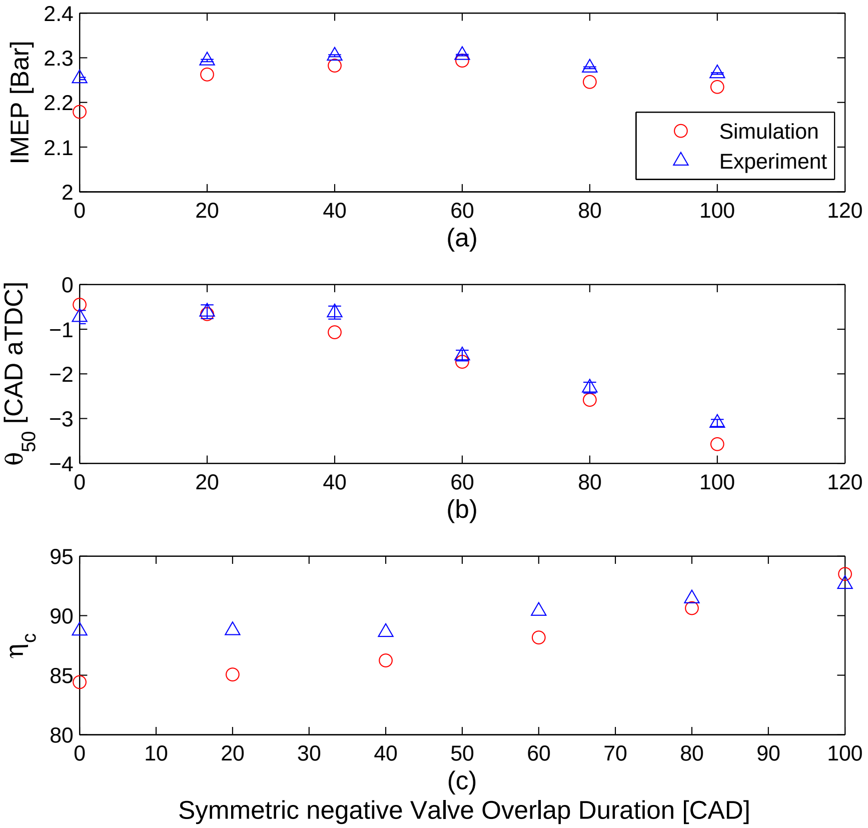

Figure 8.4: Steady state validation for SNVO sweep at $m_f LHV_f$= 0.4374 $\frac{kJ}{Cycle}$, ω=825 RPM, P_{int}=88.4 kPa, T_{int}=80^oC (a) engine output power (b) combustion timing and (c) combustion efficiency

changes are applied to the fueling rate and SNVO duration. The control oriented model does not match the detailed physical model and experimental values exactly and this is attributed to the much simpler structure of the control oriented model. However, the control oriented model ability to predict state values make the control oriented model useful for model-based controller design that includes combustion efficiency.

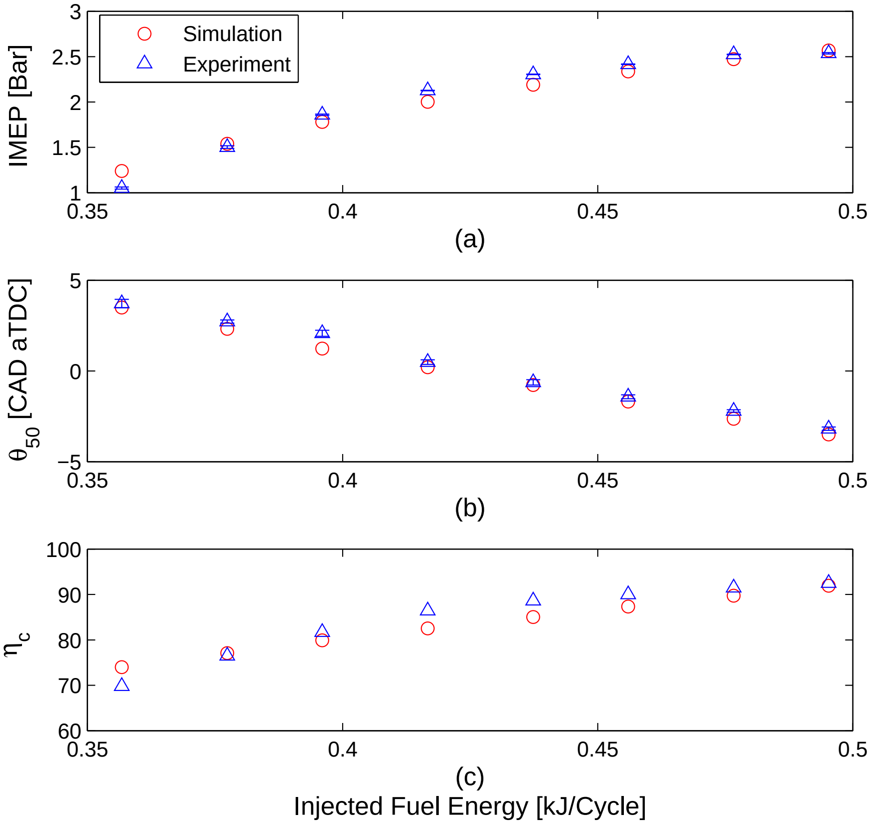

Figure 8.5: Steady state validation for fuel sweep at SNVO= 40 CAD, ω=825 RPM, P_{int}=88.4 kPa, T_{int}=80^oC (a) engine output power (b) combustion timing and (c) combustion efficiency

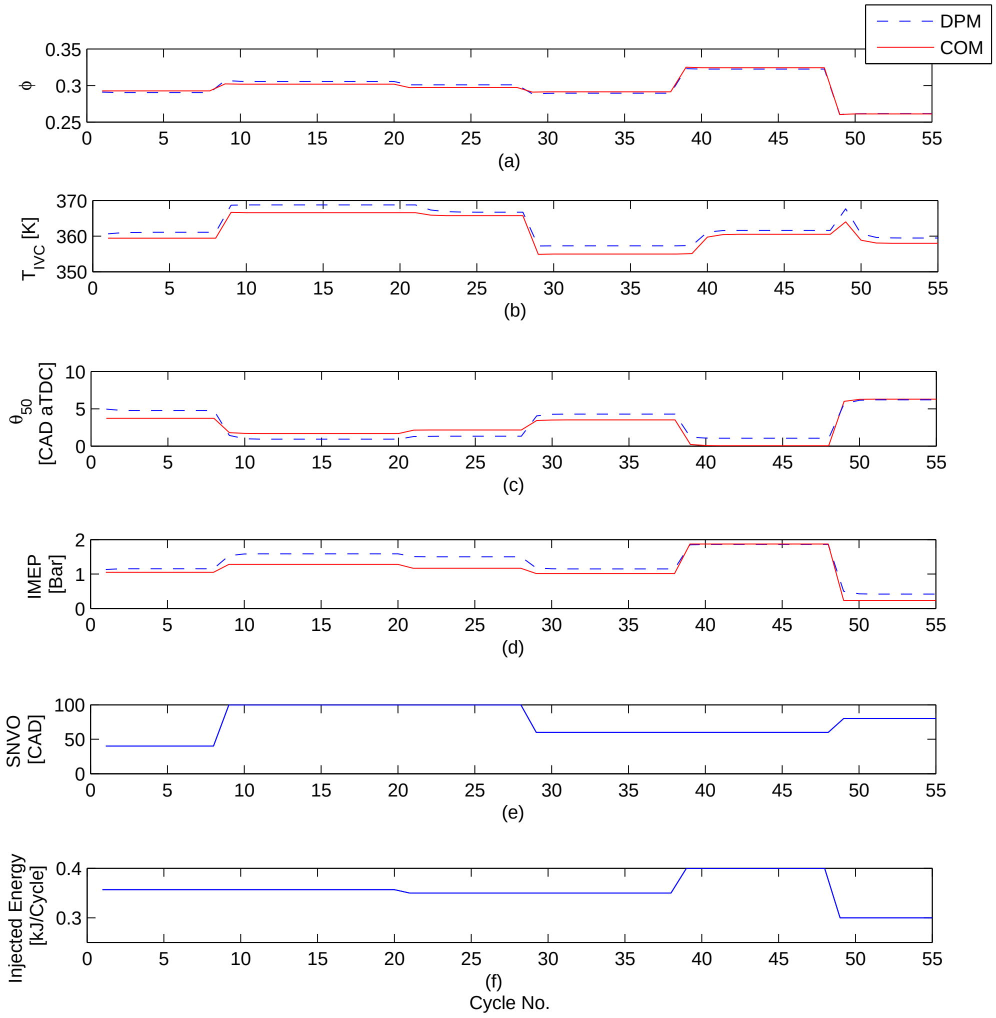

Figure 8.6: Transient COM validation against DPM [ω=825 RPM, P_{int}=88.4 kPa and T_{int}=80^{o}C]

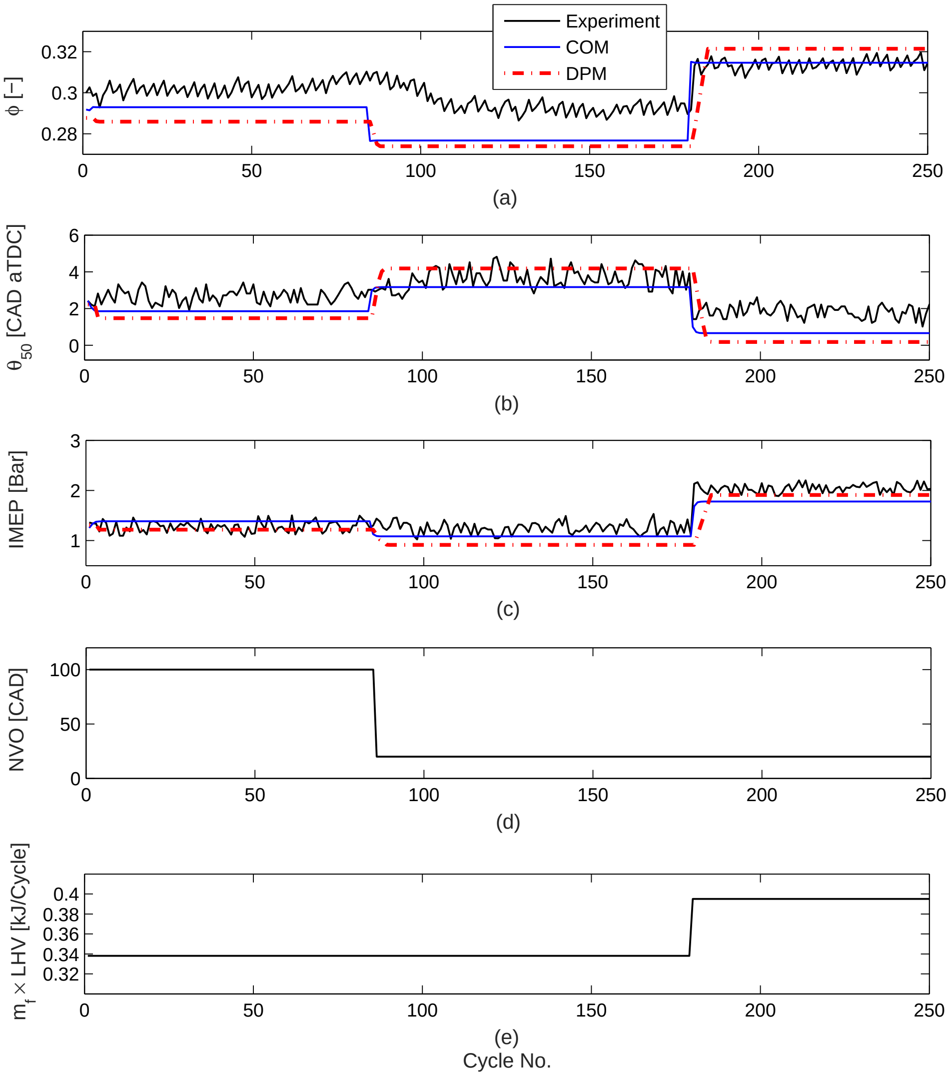

Figure 8.7: Transient COM validation against experiments [ω=818 RPM, P_{int}=88.9 kPa and T_{int}=86°C]

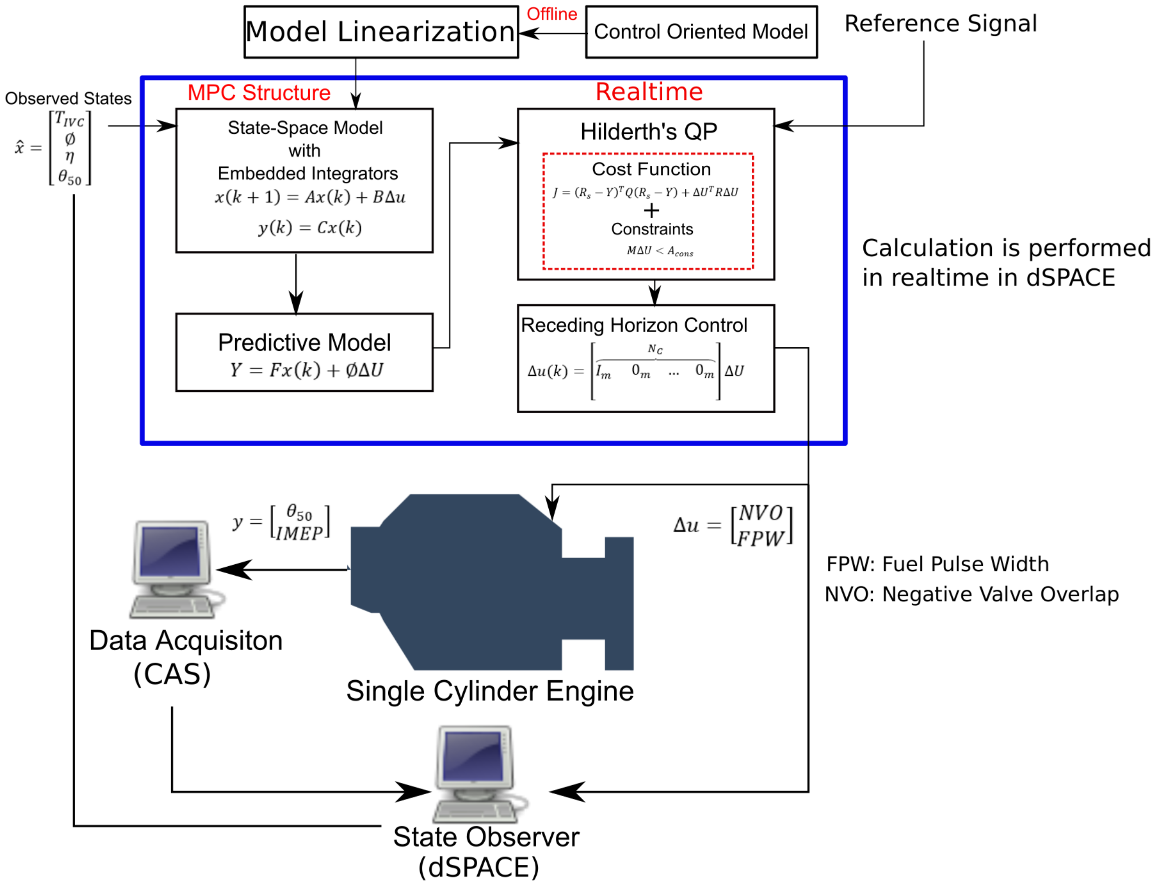

Figure 8.8: Proposed MPC structure using new COM

8.4 Discussion

A physics based nonlinear control oriented model is developed for HCCI combustion timing and output work control considering combustion efficiency. The model includes the effect of trapped residual gas and fueling rate on HCCI combustion and the model parametrization for different fuels and engines is straightforward. The model is validated against the experimental data and a detailed physical model. The nonlinear model shows acceptable accuracy in predicting HCCI combustion timing, load and combustion efficiency. The model can be used as the basis for feedback control design of HCCI engine considering constraints on combustion efficiency and emission. Figure 8.8 shows how the new developed control oriented model can be used for control development and implementation.

Chapter 9

Conclusions

A significant challenge of HCCI is the lack of a direct combustion timing control. Symmetric Negative Valve Overlap (SNVO) is a promising strategy to control combustion timing which can improve fuel efficiency and reduce CO and $\mathrm{CO_2}$ emissions in HCCI internal combustion engines.

Although HCCI is a complex process, this thesis shows that an HCCI engine with SNVO can be modeled in a straightforward way for control development. The purpose of the modeling is to capture the combustion timing and output work of the engine using simple models that are useful for control development and capture the effects of SNVO on the system outputs. A Detailed Physical Model (DPM) of HCCI combustion that has fourteen-zones and includes VVT and fueling rate dynamics is derived and compared to experimental results. The DPM is both accurate (average errors of 1.1 CAD for combustion timing and 0.25 Bar for IMEP) and computationally simple enough (156 sec per engine cycle on a 2.66 GHz Intel PC) to use as a software-in-the-loop model for control strategy development. Then using model order reduction a much simpler nonlinear model is obtained and parameterized using the DPM.

The reduced order model is developed as a sequence of key processes that occur during HCCI combustion. These include: adiabatic mixing of inducted reactants and trapped residual gas from the previous cycle; isentropic compression up to the point where combustion initiates; constant volume combustion; isentropic volumetric expansion; and isentropic exhaust. The resulting model is linearized about an operating condition and then is used to synthesize MPC with Laguerre function. The DPM is again used for closed-loop simulations to tune the controller gains. Then the MPC controller is implemented on a single cylinder engine confirming that the MPC with Laguerre function is suitable for real time implementation. For the engine operating points tested, the MPC control strategy is quite effective at tracking the desired combustion timing and output work with errors of 0.7 CAD and 0.2 Bar; however, due to plant model mismatch some actuators fluctuations are observed during fast transients. The MPC controller considers constraints and despite actuator fluctuations shows better combustion timing tracking performance when compared to the PI and Feedforward/Feedback controllers.

Energy distribution of HCCI engine indicates that combustion efficiency plays an important role in engine energy distribution. Since combustion efficiency is correlated to the engine emission, a higher combustion efficiency value indicates less CO and unburnt HC formation which is useful in the control design. A new control oriented modeling that considers combustion efficiency has been developed and can be used when the fuel reaction mechanism is not available. This new control oriented model can be used for control design and since combustion efficiency and input valve timing is highly constrained an MPC strategy is suggested for future work.

9.1 Future Work

In this thesis, significant research is conducted towards practical HCCI control development and implementation on a single cylinder research engine. However a number of research questions still need to addressed before this technology can be used in production automobiles. A summary of important extensions of this work are:

9.1.1 Further Improving the DPM

- The DPM could be extended to a multi-cylinder HCCI engine simulation by considering the effects of cylinder to cylinder cross-talk. This would enable DPM to be used for HCCI multi-cylinder engine control development and implementation.

- The DPM performance in predicting engine emissions could be improved by considering mass transfer between zones.

- The DPM could be coupled to a catalyst model for combined catalyst-engine control.

- The DPM could be integrated to a vehicle simulator such as ADVISOR (Advanced Vehicle Simulator). This helps further HCCI performance analysis and provides platform for HCCI control development for a driving cycle (such as FTP-75).

9.1.2 Further Improving the MPC

- The MPC actuator fluctuations could be reduced by further validating the control approach and incorporating an adaptive scheme where the model is updated during operation. Another approach is to use Linear Parameter Varying (LPV) model formulation [210] to improve controller performance by linearizing the model over several operating points.
- The MPC framework developed in this work could be implemented in a multi-cylinder HCCI engine by modifying the control oriented model to include cylinder to cylinder cross-talk. Another approach is to design output disturbance estimator to reject the un-modeled cylinder coupling effects [93].

References

[1] Hua Zhao. *HCCI and CAI engines for the automotive industry*. CRC Press, 2006.

[2] Joel Hiltner, Scott Fiveland, Rey Agama, and Martin Willi. System efficiency issues for natural gas fueled HCCI engines in heavy-duty stationary applications. SAE Technical Paper 2002-01-0417, 2002.

[3] Kohtaro Hashimoto. Effect of ethanol on the HCCI combustion. SAE Technical Paper SAE 2007-01-2038, 2007.

[4] Kohtaro Hashimoto. Inhibition Effect of Ethanol on Homogeneous Charge Compression Ignition of Heptane. SAE Technical Paper 2008-01-2504, 2008.

[5] Patrick F. Flynn, Russell P. Durrett, Gary L. Hunter, Axel O. zur Loye, O. C. Akinyemi, John E. Dec, and Charles K. Westbrook. Diesel Combustion: An Integrated View Combining Laser Diagnostics, Chemical Kinetics, And Empirical Validation. In *SAE Technical Paper*, SAE 1999-01-0509, 1999.

[6] John Dec. A Conceptual Model of DI Diesel Combustion Based on Laser-Sheet Imaging. *SAE 970873*, page 32, 1997.

[7] John B. Heywood. *Internal combustion engine fundamentals.* New York : McGraw-Hill, c1988., 1988.

[8] John E. Dec. Advanced compression-ignition engines – understanding the in-cylinder processes. *Proceedings of the Combustion Institute*, 32(2):2727 – 2742, 2009.

[9] Alex Schramm. Effects of negative valve overlap on HCCI combustion and its use in the control of HCCI combustion timing. Master's thesis, University of Alberta, 2014.

[10] Shazam Williams, Linjie (Robin) Hu, Tohru Nakazono, Hiroyuki Ohtsubo, and Miwa Uchida. Oxidation Catalysts for Natural Gas Engine Operating under HCCI or SI Conditions. *SAE Int. J. Fuels Lubr.*, 1:326–337, 04 2008.

[11] Xing-Cai LÃij, Wei Chen, and Zhen Huang. A fundamental study on the control of the HCCI combustion and emissions by fuel design concept combined with controllable egr. part 2. effect of operating conditions and EGR on HCCI combustion. *Fuel*, 84(9):1084 – 1092, 2005.

[12] M. J. Atkins. Experimental Examination of the effects of Fuel Octane and Diluent on HCCI Combustion. Master's thesis, University of Alberta, 2004.

[13] M. Shahbahkti. *Modeling and Experimental Study of an HCCI Engine for Combustion Timing Control.* PhD thesis, University of Alberta, 2009.

[14] Göran Haraldsson, Per Tunestl, Bengt Johansson, and Jari Hyvönen. HCCI Combustion Phasing with Closed-Loop Combustion Control Using Variable

Compression Ratio in a Multi Cylinder Engine. SAE Technical Paper 2003-01-1830, 2003, 05 2003. doi: 10.4271/2003-01-1830.

[15] Paul M. Najt and David E. Foster. Compression-ignited homogeneous charge combustion. *SAE Int. J. Engines*, SAE Technical Paper 830264, 1983. doi:10.4271/830264.

[16] Adrian Audet and Charles Robert Koch. Actuator Comparison for Closed Loop Control of HCCI Combustion Timing. SAE Technical Paper 2009-01-1135, 2009.

[17] Craig Slepicka and Charles Robert Koch. Iterative Learning on Dual-fuel Control of Homogeneous Charge Compression Ignition. *8th IFAC International Symposium on Advances in Automotive Control*, page 6, 2016.

[18] Nikhil Ravi, Hsien-Hsin Liao, Adam F. Jungkunz, Anders Widd, and J. Christian Gerdes. Model predictive control of HCCI using variable valve actuation and fuel injection. *Control Engineering Practice*, 20(4):421 – 430, 2012. Special Section: IFAC Symposium on Advanced Control of Chemical Processes - ADCHEM 2009, doi: 10.1016/j.conengprac.2011.12.002.

[19] Gabriel Ingesson, Lianhao Yin, Rolf Johansson, and Per Tunestal. Simultaneous control of combustion timing and ignition delay in multi-cylinder partially premixed combustion. *SAE Int. J. Engines*, 8:2089–2098, 09 SAE 2015-24-2424, 2015.

[20] Gabriel Ingesson, Lianhao Yin, Rolf Johansson, and Per Tunestal. A Double-

Injection Control Strategy For Partially Premixed Combustion. *8th IFAC International Symposium on Advances in Automotive Control*, page 8, 2016.

[21] J. Bengtsson, P. Strandh, R. Johansson, P. Tunestl, and B. Johansson. Model predictive control of Homogeneous Charge Compression Ignition (HCCI) engine dynamics. In *Computer Aided Control System Design, 2006 IEEE International Conference on Control Applications, 2006 IEEE International Symposium on Intelligent Control, 2006 IEEE*, pages 1675–1680, Oct 2006. doi: 10.1109/CACSD-CCA-ISIC.2006.4776893.

[22] G.M. Shaver, M. Roelle, and J.C. Gerdes. Decoupled control of combustion timing and work output in residual-affected HCCI engines. In *Proceedings of the 2005 American Control Conference*, pages 3871–3876 vol. 6, June 2005. doi: 10.1109/ACC.2005.1470578.

[23] Yuki Iwashiro, Tadashi Tsurushima, Yoshiaki Nishijima, Yasuo Asaumi, and Yuzo Aoyagi. Fuel Consumption Improvement and Operation Range Expansion in HCCI by Direct Water Injection . SAE Technical paper 2002-01-0105, 2002.

[24] J. M. Kang and M. Druzhinina. HCCI engine control strategy with external EGR. In *Proceedings of the 2010 American Control Conference*, pages 3783–3790, June 2010. doi: 10.1109/ACC.2010.5531558.

[25] Khashayar Ebrahimi and Charles Koch. Model Predictive Control for Combustion Timing and Load Control in HCCI Engines. SAE International, SAE 2015-01-0822, 2015.

[26] Rolf D. Reitz and Ganesh Duraisamy. Review of high efficiency and clean reactivity controlled compression ignition (RCCI) combustion in internal combustion engines. *Progress in Energy and Combustion Science*, 46:12 – 71, 2015.

[27] S L Kokjohn, R M Hanson, D A Splitter, and R D Reitz. Fuel reactivity controlled compression ignition (RCCI): a pathway to controlled high-efficiency clean combustion. *International Journal of Engine Research*, 12(3):209–226, 2011.

[28] Zhongzhao Li, Jianyong Zhang, Kaiqiang Zhang, Lei Zhu, Xingcai Lu, and Zhen Huang. An experimental study of the high-load extension of a homogeneous charge compression ignition engine with gasoline and n-heptane. *Proceedings of the Institution of Mechanical Engineers, Part D: Journal of Automobile Engineering*, 228(9):1105–1115, 2014.

[29] Xiaoye Han, Prasad Divekar, Graham Reader, Ming Zheng, and Jimi Tjong. Active injection control for enabling clean combustion in ethanol-diesel dual-fuel mode. *SAE Int. J. Engines*, SAE 2015-01-0858, 2015.

[30] Jari Hyvönen, Göran Haraldsson, and Bengt Johansson. Supercharging HCCI to Extend the Operating Range in a Multi-Cylinder VCR-HCCI Engine. SAE International, SAE 2003-01-3214.

[31] Qiang Fang, Junhua Fang, Jian Zhuang, and Zhen Huang. Influences of pilot injection and exhaust gas recirculation (EGR) on combustion and emissions

in a HCCI-DI combustion engine. *Applied Thermal Engineering*, 48(0):97 – 104, 2012.

[32] John E. Dec, Yi Yang, and Nicolas Dronniou. Boosted HCCI - Controlling Pressure-Rise Rates for Performance Improvements using Partial Fuel Stratification with Conventional Gasoline. *SAE Int. J. Engines*, SAE 2011-01-0897, 2011.

[33] V Manente, B Johansson, and W Cannella. Gasoline partially premixed combustion, the future of internal combustion engines? *International Journal of Engine Research*, 12(3):194–208, 2011.

[34] Magnus Christensen and Bengt Johansson. Homogeneous Charge Compression Ignition with Water Injection. *SAE Technical Paper 1999-01-0182, 1999*. doi: 10.4271/1999-01-0182.

[35] Hanho Yun, Nicole Wermuth, and Paul Najt. High Load HCCI Operation Using Different Valving Strategies in a Naturally-Aspirated Gasoline HCCI Engine. *SAE Int. J. Engines*, SAE 2011-01-0899, 2011.

[36] Patrick Borgqvist, Per Tunestal, and Bengt Johansson. Investigation and Comparison of Residual Gas Enhanced HCCI using Trapping (NVO HCCI) or Rebreathing of Residual Gases. SAE International, SAE 2011-01-1772, 2011.

[37] Patrick Borgqvist, Per Tunestal, and Bengt Johansson. Comparison of Negative Valve Overlap (NVO) and Rebreathing Valve Strategies on a Gasoline

PPC Engine at Low Load and Idle Operating Conditions. *SAE Int. J. Engines*, pages 366–378, SAE 2013-01-0902, 2013.

[38] Mark C. Sellnau, James Sinnamon, Kevin Hoyer, and Harry Husted. Full-Time Gasoline Direct-Injection Compression Ignition (GDCI) for High Efficiency and Low NOx and PM. *SAE Int. J. Engines*, pages 300–314, SAE 2012-01-0384, 2012.

[39] Abdel-Fattah M. Mahrous, Adam Potrzebowski, Miroslaw L. Wyszynski, Hongming Xu, Athanasios Tsolakis, and Pavel Luszcz. A 1D Analysis into the Effect of Variable Valve Timing on HCCI Engine Parameters. SAE Technical Paper, 2008-01-2459, 2008. doi: 10.4271/2008-01-2459.

[40] Jun-Mo Kang, Chen-Fang Chang, and Tang-Wei Kuo. Sufficient condition on valve timing for robust load transients in HCCI engines. SAE Technical Paper 2010-01-1243, 2010.

[41] Khashayar Ebrahimi, Alex Schramm, and Charles Robert Koch. Effects of asymmetric valve timing with constant NVO duration on HCCI engine combustion characteristics. In *Combustion Institute/Canadian Section (CI/CS) Spring Technical Meeting , Windsor, ON*, 2014.

[42] Khashayar Ebrahimi, Alexander Schramm, and Charles Robert Koch. Feedforward/feedback control of HCCI combustion timing. In *Proceedings of the 2014 American Control Conference, Portland, USA*, page 6, 2014. doi: 10.1109/ACC.2014.6858910.

[43] Khashayar Ebrahimi and Charles Robert Koch. SNVO effects on energy

distribution of a single cylinder HCCI engine. *Submitted to International Journal of Engine Research*, 2015.

[44] Harald Waschl, IIya Kolmanovsky, Maarten Steinbuch, and Luigi del Re. *Optimization and Optimal Control in Automotive Systems*. Springer, 2014.

[45] R. Pfeiffer, G. Haraldsson, J. O. Olsson, P. Tunestl, R. Johansson, and B. Johansson. System identification and LQG control of variable-compression HCCI engine dynamics. In *Proceedings of the 2004 IEEE International Conference*, volume 2, pages 1442–1447 Vol.2, Sept 2004. doi: 10.1109/CCA.2004.1387578.

[46] Johan Bengtsson, Petter Strandh, Rolf Johansson, Per Tunestl, and Bengt Johansson. Multi-output control of a heavy duty HCCI engine using variable valve actuation and model predictive control, SAE Technical Paper 2006-01-0873, 2006. doi: 10.4271/2006-01-0873.

[47] Petter Strandh, Johan Bengtsson, Rolf Johansson, Per Tunestl, and Bengt Johansson. Cycle-to-cycle control of a dual-fuel HCCI engine. *SAE Technical Ppaper*, 2004-01-0941, 2004. doi: 10.4271/2004-01-0941.

[48] Petter Strandh, Johan Bengtsson, Rolf Johansson, Per Tunestål, and Bengt Johansson. Variable Valve Actuation for Timing Control of a Homogeneous Charge Compression Ignition Engine. SAE International, SAE 2005-01-0147, 2005.

[49] J. Bengtsson, P. Strandh, R. Johansson, P. Tunestål, and B. Johansson. Hy-

brid control of homogeneous charge compression ignition (HCCI) engine dynamics. *International Journal of Control*, 79(5):422–448, 2006.

[50] M. Bidarvatan, M. Shahbakhti, S.A. Jazayeri, and C.R. Koch. Cycle-to-cycle modeling and sliding mode control of blended-fuel HCCI engine. *Control Engineering Practice*, 24(0):79 – 91, 2014. doi: 10.1016/j.conengprac.2013.11.008.

[51] G.M. Shaver, J.C. Gerdes, and M. Roelle. Physics-based closed-loop control of phasing, peak pressure and work output in HCCI engines utilizing variable valve actuation. In *Proceedings of the 2004 American Control Conference*, volume 1, pages 150–155 vol.1, June 2004. ISSN 0743-1619.

[52] C. Felsch, T. Sloane, J. Han, H. Barths, and A. Lippert. Numerical Investigation of Recompression and Fuel Reforming in a SIDI-HCCI Engine. *SAE Technical Paper*, 2007-01-1878, 2007.

[53] James P. Szybist, Joanna McFarlane, and Bruce G. Bunting. Comparison of Simulated and Experimental Combustion of Biodiesel Blends in a Single Cylinder Diesel HCCI Engine. *SAE Technical Paper*, 2007-01-4010, 2007.

[54] Scott B. Fiveland and Dennis N. Assanis. Development and Validation of a Quasi-Dimensional Model for HCCI Engine Performance and Emissions Studies Under Turbocharged Conditions. *SAE Technical Paper*, 2002-01-1757, 2002.

[55] Ming Jia, Maozhao Xie, and Zhijun Peng. A comparative study of multi-zone

combustion models for HCCI engines. *SAE International*, 2008-01-0064, 2008.

[56] Aristotelis Babajimopoulos, George A. Lavoie, and Dennis N. Assanis. Modeling HCCI Combustion With High Levels of Residual Gas Fraction - A Comparison of Two VVA Strategies. *SAE Technical Paper*, 2003-01-3220, 2003.

[57] Russell P. Fitzgerald, Richard Steeper, Jordan Snyder, Ronald Hanson, and Randy Hessel. Determination of Cycle Temperatures and Residual Gas Fraction for HCCI Negative Valve Overlap Operation. *SAE Int. J. Engines*, (2010-01-0343):124–141, SAE 2010-01-0343, 2010.

[58] Hagar Bastawissi, Zhang Yu-Sheng, Medhat Elkelawy, and Alm Bastawissi. Detailed 3D-CFD/Chemistry of CNG-Hydrogen Blend in HCCI Engine. *SAE Technical Paper*, 2010-01-0165, 2010.

[59] Gang Li, Tao Bo, Changyou Chen, and Richard J. R. Johns. CFD Simulation of HCCI Combustion in a 2-Stroke DI Gasoline Engine. *SAE Technical Paper*, 2003-01-1855, 2003.

[60] Yoshishige Ohyama. Air/fuel ratio and residual gas fraction control using physical models for engines with widely variable valve timing. *SAE Technical Paper*, 2002-01-2174, 2002.

[61] G. M. Shaver, J. C. Gerdes, M. J. Roelle, P. A. Catton, and F. E. Christopher. Dynamic Modeling of Residual-Affected Homogeneous Charge Compression Ignition Engines with Variable Valve Actuation. *Journal of Dy-*

namics System, Measurement, and Control, 127:374 –381, 2005. doi: 10.1115/1.1979511.

[62] Roy Ogink and Valeri Golovitchev. Gasoline HCCI Modeling: Computer Program Combining Detailed Chemistry and Gas Exchange Processes. *SAE Technical Paper*, 2001-01-3614, 2001.

[63] N. Ravi, M.J. Roelle, H. H. Liao, A.F. Jungkunz, C. F. Chang, S. Park, and J.C. Gerdes. Model-Based Control of HCCI Engines Using Exhaust Recompression. *IEEE Transactions on Control Systems Technology*, 18(6):1289–1302, Nov 2010.

[64] Khashayar Ebrahimi, Charles Koch, and Alex Schramm. A control oriented model with variable valve timing for HCCI combustion timing control, 04 2013.

[65] G.M. Shaver, M. Roelle, and J.C. Gerdes. A two-input two-output control model of HCCI engines. In *Proceedings of the 2006 American Control Conference*, June 2006. doi: 10.1109/ACC.2006.1655401.

[66] N. Ravi, N. Chaturvedi, J. Oudart, D. Cook, E. Doran, A. Kojic, and M. Pimpare. Control-oriented physics-based modeling of engine speed effects in hcci. In *2012 IEEE 51st IEEE Conference on Decision and Control (CDC)*, pages 4947–4952, Dec 2012.

[67] D.J. Rausen, A.G. Stefanopoulou, J. M. Kang, J.A. Eng, and T.W. Kuo. A mean-value model for control of homogeneous charge compression ignition

(HCCI) engines. *Journal of Dynamic Systems, Measurement, and Control*, (3):355, 2005.

[68] http://www.sandia.gov/chemkin/docs/SENKINabs.html.

[69] https://www.avl.com/web/ast/boost.

[70] S. Karagiorgis, N. Collings, K. Glover, and T. Petridis. Dynamic modeling of combustion and gas exchange processes for controlled auto-ignition engines. *Proceedinds of the 2006 American Control Conference*, pages 1880 –1885, 2006.

[71] A. Audet. Closed Loop Control of HCCI using Camshaft Phasing and Dual Fuel. Master's thesis, University of Alberta, 2008.

[72] Mahdi Shahbakhti and Charles Robert Koch. Dynamic Modeling of HCCI Combustion Timing in Transient Fueling Operation. *SAE Int. J. Engines*, 2:1098–1113, SAE 2009-01-1136, 2009.

[73] M. Bidarvatan, V. Thakkar, M. Shahbakhti, B. Bahri, and A. Abdul Aziz. Grey-box modeling of HCCI engines. *Applied Thermal Engineering*, 70(1):397 – 409, 2014.

[74] Bahram Bahri, Azhar Abdul Aziz, Mahdi Shahbakhti, and Mohd Farid Muhamad Said. Analysis and modeling of exhaust gas temperature in an ethanol fuelled HCCI engine. *Journal of Mechanical Science and Technology*, 27(11):3531–3539, 2013.

[75] M. Dehghani Firoozabadi, M. Shahbakhti, C.R. Koch, and S.A. Jazayeri.

Thermodynamic control-oriented modeling of cycle-to-cycle exhaust gas temperature in an HCCI engine. *Applied Energy*, 110:236 – 243, 2013.

[76] Göran Haraldsson, Per Tunestl, Bengt Johansson, and Jari Hyvönen. HCCI combustion phasing with closed-loop combustion control using variable compression ratio in a multi cylinder engine, SAE Technical Paper 2003-01-1830, 2003. doi: 10.4271/2003-01-1830.

[77] Jan-Ola Olsson, Per Tunestl, and Bengt Johansson. Closed-loop control of an HCCI engine. *SAE Technical Paper*, 2001-01-1031, 2001. doi: 10.4271/2001-01-1031.

[78] Göran Haraldsson, Per Tunestl, Bengt Johansson, and Jari Hyvönen. HCCI closed-loop combustion control using fast thermal management. *SAE Technical Paper*, 2004-01-0943, 2004. doi: 10.4271/2004-01-0943.

[79] Fredrik Agrell, Hans-Erik ngström, Bengt Eriksson, Jan Wikander, and Johan Linderyd. Integrated simulation and engine test of closed loop HCCI control by aid of variable valve timings. *SAE Technical Paper*, 2003-01-0748, 2003. doi: 10.4271/2003-01-0748.

[80] N. J. Killingsworth, S. M. Aceves, D. L. Flowers, F. Espinosa-Loza, and M. Krstic. Hcci engine combustion-timing control: Optimizing gains and fuel consumption via extremum seeking. *IEEE Transactions on Control Systems Technology*, 17(6):1350–1361, Nov 2009.

[81] C. M. Tsai, C. R. Koch, and M. Saif. Cycle adaptive feedforward approach

control of an electromagnetic valve actuator. In *47th IEEE Conference on Decision and Control (CDC), Cancun, Mexico,*, pages 5698 – 5703, 2008.

[82] Donghoon Lee, A.G. Stefanopoulou, S. Makkapati, and M. Jankovic. Modeling and control of a heated air intake homogeneous charge compression ignition (HCCI) engine. In *Proceedings of the 2010 American Control Conference*, pages 3817–3823, June 2010. doi: 10.1109/ACC.2010.5531442.

[83] Nenghui Zhou, Hui Xie, Nan Li, Tao Chen, and Hua Zhao. Study on layered close loop control of 4-stroke gasoline HCCI engine equipped with 4VVAS, SAE Technical Paper 2008-01-0791, 2008, doi:10.4271/2008-01-0791.

[84] J. S. Souder. *Closed-Loop Control of a Multi-Cylinder HCCI Engine*. PhD thesis, University of California, Berkeley, 2004.

[85] Johannes Franz, Frank Schwarz, Michael Guenthner, Joerg Reissing, Andreas Mueller, and Christian Donn. Closed loop control of an HCCI multi-cylinder engine and corresponding adaptation strategies. *SAE Technical Paper*, 2009-24-0079, 2009. doi: 10.4271/2009-24-0079.

[86] K. Hoffmann, P. Drews, D. Seebach, K.-G. Stapf, S. Pischinger, and D. Abel. Optimized closed loop control of controlled auto ignition cai. F2008-06-046. In *FISITA word automotive congress proceedings*, volume 3 of *World automotive congress; FISITA*, pages 136 – 145, 2008.

[87] Mehran Bidarvatan and Mahdi Shahbakhti. Two-Input Two-Output Control of Blended Fuel HCCI Engines. In *SAE Technical Paper*, SAE Technical Paper, 2013-01-1663, 2013, doi: 10.4271/2013-01-1663.

[88] Mehran Bidarvatan and Mahdi Shahbakhti. Integrated HCCI engine control based on a performance index. *Journal of Engineering for Gas Turbines and Power*, (10):101601. ISSN 0742-4795, doi: 10.1115/1.4027279.

[89] Meysam Razmara, Mehran Bidarvatan, Mahdi Shahbakhti, and Rush Robinett. Innovative Exergy-Based Combustion Phasing Control of IC Engines. In *SAE Technical Paper*. SAE International, SAE 2016-01-0815, 2016.

[90] Mehran Bidarvatan, Mahdi Shahbakhti, and Seyed Ali Jazayeri. Model-Based Control of Combustion Phasing in an HCCI Engine. *SAE Technical Paper*, 2012-01-1137, 2012.

[91] A. Widd, K. Ekholm, P. Tunestal, and R. Johansson. Experimental evaluation of predictive combustion phasing control in an HCCI engine using fast thermal management and VVA. In *2009 IEEE Control Applications, (CCA) Intelligent Control, (ISIC)*, pages 334–339, July 2009.

[92] Dinggen Li and Di Wang. Multivariable control of residual-affected HCCI engines based on Model Predictive Control, SAE Technical paper 2013-01-2511, 2013, doi: 10.4271/2013-01-2511.

[93] S. M. Erlien, A. F. Jungkunz, and J. C. Gerdes. Multi-Cylinder HCCI Control With Cam Phaser Variable Valve Actuation Using Model Predictive Control. In *Proceedings of the 2012 ASME Dynamic Systems and Control Conference*, volume 2, pages 823 – 832, 2013. doi:10.1115/DSCC2012-MOVIC2012-8585.

[94] Vijay Manikandan Janakiraman, XuanLong Nguyen, and Dennis Assanis.

Nonlinear Model Predictive Control of A Gasoline HCCI Engine Using Extreme Learning Machines. *CoRR*, abs/1501.03969, 2015.

[95] Liuping Wang. *Model predictive control system design and implementation using MATLAB*. Advances in industrial control. London : Springer, c2009., 2009.

[96] http://www.cantera.org/docs/sphinx/html/index.html.

[97] https://www-pls.llnl.gov/.

[98] https://www.erc.wisc.edu/chemicalreaction.php.

[99] R. Seethaler, M. Mashkournia, R. R. Chladny, J. Zhao, and C. R. Koch. Closed loop electromagnetic valve actuation motion control on a single cylinder engine. In *SAE Paper 2013-01-0594*, page 8, 2013.

[100] M. Mashkournia. Electromagnetic variable valve timing on a single cylinder engine in HCCI and SI. Master's thesis, University of Alberta, 2012.

[101] R. R. Chladny. *Modeling and control of automotive gas exchange valve solenoid actuators*. PhD thesis, University of Alberta, 2007.

[102] Thomas Stolk and Alexander Von Gaisberg. Elektromagnetischer aktuator, German Patent Application DE 10025491 A1, 2001.

[103] A. Ghazimirsaied. *Extending HCCI Low Load Operation Using Chaos Prediction and Feedback Control*. PhD thesis, University of Alberta, 2012.

[104] M. Mashkournia. Electromagnetic Variable Valve Timing on a Single Cylinder Engine in HCCI and SI. M.Sc. thesis, University of Alberta, 2012.

[105] http://www.epa.gov/climatechange/EPAactivities/regulatory-initiatives.html.

[106] http://articles.sae.org/11963/.

[107] http://articles.sae.org/12604/.

[108] http://energy.gov/eere/vehicles/2014-doe-vehicle-technologies-office-annual-merit-review.

[109] Anders Widd, Rolf Johansson, Patrick Borgqvist, Per Tunestal, and Bengt Johansson. Investigating Mode Switch from SI to HCCI using Early Intake Valve Closing and Negative Valve Overlap. In *SAE Technical Paper, SAE 2011-01-1775*.

[110] M Shahbakhti and C R Koch. Characterizing the cyclic variability of ignition timing in a homogeneous charge compression ignition engine fuelled with n-heptane/iso-octane blend fuels. *International Journal of Engine Research*, 9(5):361–397, 2008.

[111] James P. Szybist and Bruce G. Bunting. The effects of fuel composition and compression ratio on thermal efficiency in an hcci engine. SAE International, SAE 2007-01-4076, 2007.

[112] Jeremie Dernotte, John E. Dec, and Chunsheng Ji. Energy Distribution Analysis in Boosted HCCI-like / LTGC Engines - Understanding the Trade-Offs to Maximize the Thermal Efficiency. *SAE Int. J. Engines SAE 2015-01-0824*, 8, 2015.

[113] John E. Dec, Yi Yang, and Nicolas Dronniou. Improving efficiency and using E10 for higher loads in boosted hcci engines. *SAE Int. J. Engines*, SAE 2012-01-1107, 2012.

[114] Chunsheng Ji, John E. Dec, Jeremie Dernotte, and William Cannella. Effect of Ignition Improvers on the Combustion Performance of Regular-Grade E10 Gasoline in an HCCI Engine. *SAE 2014-01-1282, SAE Int. J. Engines*, 7:790–806, 04 2014.

[115] D. N. Assanis. *Turbocharged Turbocompounded diesel engine system for studies of low heat rejection engine performance*. PhD thesis, Massachusetts Institue of Technology, 1985.

[116] Sebastian Hensel, Fatih Sarikoc, Florian Schumann, Heiko Kubach, and Ulrich Spicher. Investigations on the heat transfer in hcci gasoline engines. *SAE Int. J. Engines*, 2:1601–1616, 06 2009.

[117] http://www.epa.gov/chp/.

[118] John E. Dec and Magnus Sjöberg. A Parametric Study of HCCI Combustion - the Sources of Emissions at Low Loads and the Effects of GDI Fuel Injection. In *SAE Technical Paper*. SAE International, 03 SAE 2003-01-0752, 2003.

[119] John E. Dec and Yi Yang. Boosted HCCI for High Power without Engine Knock and with Ultra-Low NOx Emissions - using Conventional Gasoline. *SAE Int. J. Engines*, SAE 2010-01-1086, 2010.

[120] Samveg Saxena, Jyh-Yuan Chen, and Robert Dibble. Maximizing Power Output in an Automotive Scale Multi-Cylinder Homogeneous Charge Compression Ignition (HCCI) Engine. In *SAE Technical Paper*, SAE 2011-01-0907, 2011.

[121] Samveg Saxena, Silvan Schneider, Salvador Aceves, and Robert Dibble. Wet ethanol in HCCI engines with exhaust heat recovery to improve the energy balance of ethanol fuels. *Applied Energy*, 98(0):448 – 457, 2012.

[122] Samveg Saxena and Iván D. Bedoya. Fundamental phenomena affecting low temperature combustion and hcci engines, high load limits and strategies for extending these limits. *Progress in Energy and Combustion Science*, 39(5):457 – 488, 2013.

[123] Ming Zheng, Xiaoye Han, Usman Asad, and Jianxin Wang. Investigation of butanol-fuelled HCCI combustion on a high efficiency diesel engine. *Energy Conversion and Management*, 98:215 – 224, 2015.

[124] Junseok Chang, Orgun Güralp, Zoran Filipi, Dennis N. Assanis, Tang-Wei Kuo, Paul Najt, and Rod Rask. New Heat Transfer Correlation for an HCCI Engine Derived from Measurements of Instantaneous Surface Heat Flux. In *SAE Technical Paper*. SAE International, SAE 2004-01-2996, 2004.

[125] Charles F. Marvin. Combustion time in the engine cylinder and its effect on engine performance. Technical Report 276, NACA, 1927.

[126] Niklas Ivansson. Estimation of the residual gas fraction in an HCCI-engine using cylinder pressure. Master's thesis, Linköping University, 2003.

[127] Samveg Saxena, Jyh-Yuan Chen, and Robert W. Dibble. Characterization of Ion Signals under Ringing Conditions in an HCCI Engine. SAE 2011-01-177, 2011.

[128] Zhi Wang, Fang Wang, and Shi-Jin Shuai. Study of Engine Knock in HCCI Combustion using Large Eddy Simulation and Complex Chemical Kinetics. In *SAE Technical Paper*. SAE International, SAE 2014-01-2573, 2014.

[129] Masoud Mashkournia, Adrian Audet, and Charles Robert Koch. Knock detection and control in an hcci engine using dwt. In *Proceedings of the ASME 2011 Dynamic Systems and Control Conference, Morgantown, USA*, pages 391–399. ASME, 2011.

[130] Morgan M. Andreae, Wai K. Cheng, Thomas Kenney, and Jialin Yang. On HCCI Engine Knock. In *SAE Technical Paper*. SAE International, 07 SAE 2007-01-1858, 2007.

[131] Tadashi Tsurushima, Eiji Kunishima, Yasuo Asaumi, Yuzo Aoyagi, and Yoshiteru Enomoto. The Effect of Knock on Heat Loss in Homogeneous Charge Compression Ignition Engines. In *SAE Technical Paper*. SAE International, SAE 2002-01-0108, 2002.

[132] http://www.automotive-iq.com/lubricants-and-fuels/articles/fueling-the-future-of-the-si-engine.

[133] http://jalopnik.com/293027/gm-rolls-out-prototypes-powered-by-hcci.

[134] J. A. Eng. Characterization of Pressure Waves in HCCI Combustion. In *SAE Technical Paper*. SAE International, 10 SAE 2002-01-2859, 2002.

[135] C. J. Chiang, A. G. Stefanopoulou, and M. Jankovic. Nonlinear Observer-Based Control of Load Transitions in Homogeneous Charge Compression Ignition Engines. *IEEE Transactions on Control Systems Technology*, 15(3):438–448, May 2007.

[136] Khashayar Ebrahimi, Masoud Aliramezani, and Charles Robert Koch. An HCCI control oriented model that includes combustion efficiency. *IFAC-PapersOnLine*, 49(11):327 – 332, 2016. 8th IFAC Symposium on Advances in Automotive Control AAC 2016Norrköping, Sweden, 20Ů23 June 2016.

[137] L Kocher, E Koeberlein, DG Van Alstine, K Stricker, and G Shaver. Physically based volumetric efficiency model for diesel engines utilizing variable intake valve actuation. *INTERNATIONAL JOURNAL OF ENGINE RESEARCH*, 13(2):169 – 184, n.d.

[138] Akhilendra Pratap Singh and Avinash Kumar Agarwal. Effect of Intake Charge Temperature and EGR on Biodiesel Fuelled HCCI Engine. SAE International, SAE 2016-28-0257, 2016.

[139] Aristotelis Babajimopoulos, Dennis N. Assanis, and Scott B. Fiveland. An Approach for Modeling the Effects of Gas Exchange Processes on HCCI Combustion and Its Application in Evaluating Variable Valve Timing Control Strategies. SAE Technical Paper, 2002-01-2829, 2002, doi: 10.4271/2002-01-2829.

[140] Asko Vuorinen. *Planning of Optimal Power Systems*. Vammalan Kirjapaino Oy, Vammala, Finland, 2009.

[141] R. Beith. *Small and micro combined heat and power (CHP) systems : advanced design, performance, materials and applications.* Woodhead Publishing series in energy: no. 18. Cambridge, UK ; Philadelphia, PA : Woodhead Pub., 2011., 2011.

[142] Salvador M. Aceves, Joel Martinez-Frias, and Gordon M. Reistad. Analysis of Homogeneous Charge Compression Ignition (HCCI) engines for cogeneration applications. *Journal of Energy Resources Technology*, (1):16, 2006.

[143] http://www.wartsila.com/energy/solutions/applications/combined-heat-and-power-(chp)-plants.

[144] https://powergen.gepower.com/applications/chp.html.

[145] J.G. Brammer and A.V. Bridgwater. The influence of feedstock drying on the performance and economics of a biomass gasifierŰengine CHP system. *Biomass and Bioenergy*, 22(4):271 – 281, 2002.

[146] H.I. Onovwiona and V.I. Ugursal. Residential cogeneration systems: review of the current technology. *Renewable and Sustainable Energy Reviews*, 10(5):389 – 431, 2006.

[147] Alan Moran, Pedro J Mago, and Louay M Chamra. Thermoeconomic modeling of micro-CHP (micro-cooling, heating, and power) for small commercial applications. *International Journal of Energy Research*, 32(9):808–823, 2008.

[148] J.L. Mit’guez, S. Murillo, J. Porteiro, and L.M. López. Feasibility of a new

domestic CHP trigeneration with heat pump: I. design and development. *Applied Thermal Engineering*, 24(10):1409 – 1419, 2004.

[149] M Talbi and B Agnew. Energy recovery from diesel engine exhaust gases for performance enhancement and air conditioning. *Applied Thermal Engineering*, 22(6):693 – 702, 2002.

[150] Aysegul Abusoglu and Mehmet Kanoglu. Exergetic and thermoeconomic analyses of diesel engine powered cogeneration: Part 1 Ű formulations. *Applied Thermal Engineering*, 29(2Ű3):234 – 241, 2009.

[151] M. Mostafavi and B. Agnew. Thermodynamic analysis of combined diesel engine and absorption refrigeration unitŮnaturally aspirated diesel engine. *Applied Thermal Engineering*, 17(5):471 – 478, 1997.

[152] G. Pepermans, J. Driesen, D. Haeseldonckx, R. Belmans, and W. DŠhaeseleer. Distributed generation: definition, benefits and issues. *Energy Policy*, 33(6):787 – 798, 2005.

[153] CHP for Commercial Buildings: Fuel Cell, Engine, and Turbine Technologies for Cogeneration in Commercial, Institutional, and Municipal Buildings: Global Market Analysis and Forecasts. *PR Newswire*, 2015.

[154] P. Stathopoulos and C.O. Paschereit. Retrofitting micro gas turbines for wet operation. A way to increase operational flexibility in distributed CHP plants. *Applied Energy*, 154:438 – 446, 2015.

[155] Catalog of CHP Technologies – Section 2. Technology Characterization - Re-

ciprocating Internal Combustion Engines, Combined Heat and Power Partnership, U.S. Environmnetal Protection Agency , 03 2015.

[156] Samveg Saxena, Ivan Dario Bedoya, Nihar Shah, and Amol Phadke. Understanding loss mechanisms and identifying areas of improvement for HCCI engines using detailed exergy analysis. *J. Eng. Gas Turbines Power*, (GTP-13-110):10, 2013.

[157] Samveg Saxena, Nihar Shah, Ivan Bedoya, and Amol Phadke. Understanding optimal engine operating strategies for gasoline-fueled HCCI engines using crank-angle resolved exergy analysis. *Applied Energy*, 114(0):155 – 163, 2014.

[158] Samad Jafarmadar and Nader Javani. Exergy analysis of natural gas/DME combustion in Homogeneous Charge Compression Ignition engines (HCCI) using zero-dimensional model with detailed chemical kinetics mechanism. *International Journal of Exergy*, (3), 2014.

[159] Rasool Fatehi Ghahfarokhi, Shahram Khalilarya, and Rahim Ebrahimi. Energy and exergy analyses of Homogeneous Charge Compressin Ignition (HCCI) engine. *Thermal Science*, (1):107, 2013.

[160] N. Sarabchi, R. Khoshbakhti Saray, and S.M.S. Mahmoudi. Utilization of waste heat from a HCCI engine in a tri-generation system. *Energy*, 55:965 – 976, 2013.

[161] Maria Jonsson and Jinyue Yan. Ammonia water bottoming cycles: a compar-

ison between gas engines and gas diesel engines as prime movers. *Energy*, 26(1):31 – 44, 2001.

[162] Kazunobu Kobayashi, Takahiro Sako, Yoshimi Sakaguchi, Satoshi Morimoto, Sumihiro Kanematsu, Kiyoshi Suzuki, Tohru Nakazono, and Hiroyuki Ohtsubo. Development of HCCI natural gas engines. *Journal of Natural Gas Science and Engineering*, 3(5):651 – 656, 2011.

[163] Robert M. Wagner, Tom E. Briggs, Tim J. Theiss, Gurpreet Singh, and Bob Gemmer. Defining engine efficiency limits, 17th DEER Conference, Detroit, MI, USA, 2011.

[164] S. Mamalis and D. N. Assanis. Second-Law Analysis of Boosted HCCI Engines: Modeling Study. *Journal of Energy Engineering*, 141(2):1 – 9, 2015.

[165] J. T. Farrell, J. G. Stevens, and W. Weissman. A second law analysis of high efficiency low emission gasoline engine concepts. In *SAE Technical Paper, SAE 2006-01-0491*. SAE International, 2006.

[166] Abdul Khaliq and Shailesh K. Trivedi. Second law assessment of a wet ethanol fuelled HCCI engine combined with organic Rankine cycle. *Journal of Energy Resources Technology*, (2):22201, 2012.

[167] Abdul Khaliq, Shailesh K. Trivedi, and Ibrahim Dincer. Investigation of a wet ethanol operated HCCI engine based on first and second law analyses. *Applied Thermal Engineering*, 31(10):1621 – 1629, 2011.

[168] A.K. Amjad, R. Khoshbakhi Saray, S.M.S. Mahmoudi, and A. Rahimi. Availability analysis of n-heptane and natural gas blends combustion in HCCI engines. *Energy*, 36(12):6900 – 6909, 2011.

[169] Mohamed Djermouni and Ahmed Ouadha. Thermodynamic analysis of an HCCI engine based system running on natural gas. *Energy Conversion and Management*, 88(0):723 – 731, 2014.

[170] Yunus A. Çengel and Michael A. Boles. *Thermodynamics : an engineering approach.* New York : McGraw-Hill Education, [2015], 2015.

[171] Agnese Magno, Ezio Mancaruso, and Bianca Maria Vaglieco. Effects of a biodiesel blend on energy distribution and exhaust emissions of a small CI engine . *Energy Conversion and Management*, 96:72 – 80, 2015.

[172] James P Szybist, Kalyana Chakravathy, and C Stuart Daw. Analysis of the impact of selected fuel thermochemical properties on internal combustion engine efficiency. *Energy & Fuels*, 26(5):2798–2810, 2012.

[173] Tuula Savola and Carl-Johan Fogelholm. Increased power to heat ratio of small scale CHP plants using biomass fuels and natural gas. *Energy Conversion and Management*, 47(18Ű19):3105 – 3118, 2006.

[174] Christos A Frangopoulos. A method to determine the power to heat ratio, the cogenerated electricity and the primary energy savings of cogeneration systems after the european directive. *Energy*, 45(1):52–61, 2012.

[175] Daesu Jun and Norimasa Iida. A Study of High Combustion Efficiency and

Low CO Emission in a Natural Gas HCCI Engine. SAE Technical Paper 2004-01-1974, 2004.

[176] A.H. Lefebvre. Fuel effects on gas turbine combustion-ignition, stability, and combustion efficiency. *Am. Soc. Mech. Eng., (Pap.); (United States)*, 1984.

[177] Michel De Paepe, Peter DŠHerdt, and David Mertens. Micro-CHP systems for residential applications. *Energy Conversion and Management*, 47(18Ű19):3435 – 3446, 2006.

[178] http://www.erc.wisc.edu/chemicalreaction.php.

[179] https://www-pls.llnl.gov.

[180] Salvador M. Aceves, Joel Martinez-Frias, Daniel L. Flowers, J. Ray Smith, Robert W. Dibble, John F. Wright, and Randy P. Hessel. A Decoupled Model of Detailed Fluid Mechanics Followed by Detailed Chemical Kinetics for Prediction of Iso-Octane HCCI Combustion. SAE International, 09 2001.

[181] M. Bissoli, A. Frassoldati, A. Cuoci, E. Ranzi, M. Mehl, and T. Faravelli. A new predictive multi-zone model for HCCI engine combustion. *Applied Energy*, 178:826 – 843, 2016.

[182] N.P. Komninos. Modeling HCCI combustion: Modification of a multi-zone model and comparison to experimental results at varying boost pressure. *Applied Energy*, 86(10):2141 – 2151, 2009.

[183] José Antonio Vélez Godiño, Miguel Torres García, Fco José Jiménez-Espadafor Aguilar, and Elisa Carvajal Trujillo. Numerical study of HCCI

combustion fueled with diesel oil using a multizone model approach. *Energy Conversion and Management*, 89:885 – 895, 2015.

[184] N.P. Komninos and D.T. Hountalas. Improvement and validation of a multi-zone model for HCCI engine combustion concerning performance and emissions. *Energy Conversion and Management*, 49(10):2530 – 2537, 2008.

[185] Ming Jia, Maozhao Xie, and Zhijun Peng. A Comparative Study of Multi-zone Combustion Models for HCCI Engines. SAE International, 04 SAE 2008-01-0064, 2008.

[186] P. Kongsereeparp. *Chemical kinetic based simulation for an HCCI engine and its combustion*. PhD thesis, University of Alberta, 2008.

[187] Paitoon Kongsereeparp and M. David Checkel. Novel method of setting initial conditions for multi-zone hcci combustion modeling. In *SAE Technical Paper*. SAE International, 04 2007.

[188] N.P. Komninos. Investigating the importance of mass transfer on the formation of HCCI engine emissions using a multi-zone model. *Applied Energy*, 86(7Ű8):1335 – 1343, 2009.

[189] N.P. Komninos. Assessing the effect of mass transfer on the formation of HC and CO emissions in HCCI engines, using a multi-zone model. *Energy Conversion and Management*, 50(5):1192 – 1201, 2009.

[190] Lino Guzzella. *Introduction to modeling and control of internal combustion engine systems*. Springer, 2004.

[191] Hongming Xu, Michael Liu, Shadi Gharahbaghi, Steve Richardson, Miroslaw Wyszynski, and Thanos Megaritis. Modelling of HCCI Engines: Comparison of Single-zone, Multi-zone and Test Data. In *SAE Technical Paper*. SAE International, SAE 2005-01-2123, 2005.

[192] Mattia Bissoli, Alberto Cuoci, Alessio Frassoldati, Tiziano Faravelli, Eliseo Ranzi, Tommaso Lucchini, Gianluca D'Errico, and Francesco Contino. Detailed Kinetic Analysis of HCCI Combustion Using a New Multi-Zone Model and CFD Simulations. *SAE Int. J. Engines*, pages 1594–1609, SAE 2013-24-0021, 2013.

[193] K. Ebrahimi and C.R. Koch. HCCI combustion timing control with Variable Valve Timing. In *Proceedings of 2013 American Control Conference*, pages 4429–4434, June 2013. doi: 10.1109/ACC.2013.6580522.

[194] Gregory M. Shaver. Stability analysis of residual-affected HCCI using convex optimization. *Control Engineering Practice*, 17(12):1454 – 1460, 2009. Special Section: The 2007 IFAC Symposium on Advances in Automotive Control.

[195] Joshua Bradley Bettis. Thermoynamic Based Modeling for Nonlinear Control of Combustion Phasing in HCCI Engines . Master's thesis, Missouri University of Science and Technology, 2010.

[196] Stephen R. Turns. *An introduction to combustion : concepts and applications.* New York : McGraw-Hill, c2012., 2012.

[197] http://www.mathworks.com/help/optim/ug/equation-solving-algorithms.html.

[198] Kevin Swan, Mahdi Shahbakhti, and Charles Robert Koch. Predicting start of combustion using a modified knock integral method for an HCCI engine. In *SAE Technical Paper*, SAE Technical Paper, 2006-01-1086, doi: 10.4271/2006-01-1086 2006.

[199] Mahdi Shahbakhti, Robert Lupul, and Charles Robert Koch. Predicting HCCI Auto-Ignition Timing by Extending a Modified Knock-Integral Method. SAE Technical Paper, 2007-01-0222, 2007, doi: 10.4271/2007-01-0222.

[200] Jean Baptiste Millet, Fadila Maroteaux, and Frédéric Ravet. Modeling of HCCI Combustion by One Step Reaction Function: In View of Assisting the Optimization of Engine Management System. SAE Technical Paper, 2007-24-0033,2007, doi: 10.4271/2007-24-0033.

[201] G. M. Shaver, J. C. Gerdes, P. Jane, P. A. Catton, and C. F. Edwards. Modeling for control of HCCI engines. *Proceedings of the American Control Conference*, page 749Ű754, 2003, doi: 10.1109/ACC.2003.1239111.

[202] J. B. Bettis. Thermodynamic based modeling for nonlinear control of combustion phasing in HCCI engines. Master's thesis, Missouri University of Science and Technology, 2010.

[203] L. Guzzella, C. R. Koch, and M. Scherer. USA 6212467: Electronic Engine Control System, USA Patent, 2001.

[204] Chi-Tsong Chen. *Linear system theory and design.* New York: Oxford University Press, 1999.

[205] Petter Tøndel, Tor Arne Johansen, and Alberto Bemporad. An algorithm for multi-parametric quadratic programming and explicit MPC solutions. *Automatica*, 39(3):489 – 497, 2003. doi: 10.1016/S0005-1098(02)00250-9.

[206] David A Wismer and Rahul Chattergy. *Introduction to nonlinear optimization: a problem solving approach*, volume 1. North Holland, 1978.

[207] Vahid Hosseini, W. Stuart Neill, and Wallace L. Chippior. Influence of Engine Speed on HCCI Combustion Characteristics using Dual-Stage Autoignition Fuels. In *SAE Technical Paper*. SAE International, SAE 2009-01-1107, 2009.

[208] Ida Truedsson, William Cannella, Bengt Johansson, and Martin Tuner. Engine Speed Effect on Auto-Ignition Temperature and Low Temperature Reactions in HCCI Combustion for Primary Reference Fuels. In *SAE Technical Paper*. SAE International, SAE 2014-01-2666, 2014.

[209] Andrew P. White, Guoming Zhu, and Jongeun Choi. *Linear Parameter Varying Control for Engineering Applications*. 2013.

[210] Anders Widd. Predictive Control of HCCI Engines using Physical Models, 2009.

[211] Robert J. Moffat. Describing the uncertainties in experimental results. *Experimental Thermal and Fluid Science*, 1(1):3 – 17, 1988.

[212] Dowdell RB Abernethy RB, Benedict RP. Asme measurement uncertainty. *ASME. J. Fluids Eng.*, (doi: 10.1115/1.3242450.):107(2):161–164, 1985.

[213] Roy D. Lienhard John H. Beckwith, T. G. (Thomas G.) Marangoni. *Mechanical measurements*. Number ISBN: 0201847655. 2007.

[214] Dennis N. Assanis, Zoran Filipi, Scott B. Fiveland, and Michalis Syrimis. A Methodology for Cycle-By-Cycle Transient Heat Release Analysis in a Turbocharged Direct Injection Diesel Engine. SAE International, SAE 2000-01-1185, 2000.

[215] `http://www.mathworks.com/products/mbc/`.

[216] Stephen Pace and Guoming G. Zhu. Air-to-Fuel and Dual-Fuel Ratio Control of an Internal Combustion Engine. *SAE Int. J. Engines*, pages 245–253, SAE 2009-01-2749, 2009.

[217] Junsoo Kim, Seungsuk Oh, Kangyoon Lee, Myoungho Sunwoo, Wootai Kim, Chunwoo Lee, and Myongho Kim. Individual Cylinder Air-Fuel Ratio Estimation Algorithm for Variable Valve Lift (VVL) Engines. SAE International, SAE 2010-01-0785, 2010.

Appendix A

HCCI combustion Indexes

Measured pressure trace provides information about the HCCI combustion indexes. Using the first law of thermodynamics, the rate of heat release, $\frac{dQ_{HR}}{d\theta}$ is calculated [1] as

$$\frac{dQ_{HR}}{d\theta} = \frac{1}{k-1} V \frac{dP}{d\theta} + \frac{k}{k-1} P \frac{dV}{d\theta} \tag{A.1}$$

where k is the specific heat ratio, P is the in-cylinder pressure and V is the instantaneous cylinder volume. The rate of heat release for the measured pressure in Figure A.1(a) is shown in Figure A.1(b). In this work, θ_{10}, θ_{50}, and θ_{90} are defined as the crank angles for 10%, 50%, and 90% mass fraction burned respectively. Start of Combustion (SOC) is defined as the point at which the third derivative of the pressure trace with respect to the crank angle degree exceeds a predefined threshold

$$\frac{d^3P}{d\theta^3} = \left(\frac{d^3P}{d\theta^3}\right)_{threshold} \tag{A.2}$$

The threshold is defined using CAS measurements as $\left(\frac{d^3P}{d\theta^3}\right)_{threshold}$=25 $\frac{kPa}{CAD^3}$ as shown in Figure A.1(c). This threshold value is consistent with the value reported in [13]. Burn Duration (BD) is defined as the crank angle difference between SOC and θ_{90}.

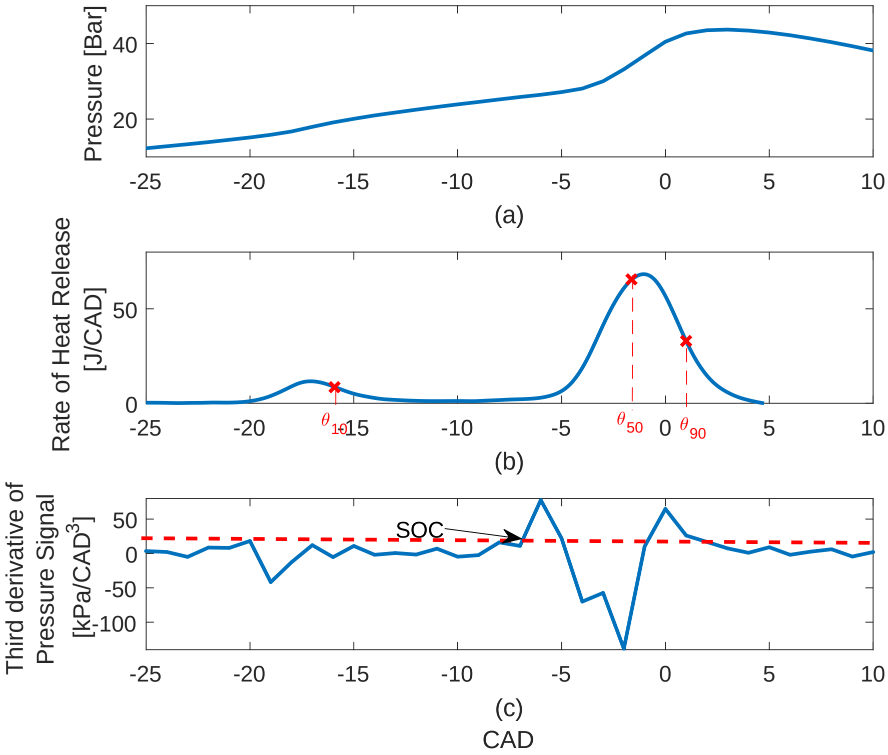

Figure A.1: HCCI combustion indexes (a) Pressure, (b) Rate of Heat Release and (c) Third derivative of pressure signal [NVO=40 Deg CA, ω=817 RPM, P_{int}= 88.3 kPa, T_{int}=80^oC and Em_{finj}=0.456 $\frac{kJ}{Cycle}$]

Appendix B

HCCI Experimental Data

SUMMARY

Table B.1: Summary of HCCI experimental data from single cylinder research engine

#	$\mathrm{Em}_{\mathrm{finj}}$ $\frac{\mathrm{kJ}}{\mathrm{Cycle}}$	NVO [CAD]	θ_{SOC} [CAD aTDC]	θ_{50} [CAD aTDC]	IMEP [Bar]	ϕ [-]	$\mathrm{P}_{\mathrm{IVC}}$ [Bar]	BD [CAD]	$\mathrm{T}_{\mathrm{Int}}$ [^{o}C]	$\mathrm{P}_{\mathrm{EVO}}$ [Bar]	$\mathrm{T}_{\mathrm{Exh}}$ [^{o}C]
1	0.377	0	-5.0	2.7	1.38	0.30	0.86	24.0	77	1.05	157
2	0.395	0	-6.3	1.8	1.82	0.32	0.85	23.0	77	1.13	179
3	0.415	0	-7.4	0.5	2.08	0.33	0.86	20.6	77	1.19	190
4	0.437	0	-8.5	-0.7	2.25	0.34	0.86	18.6	78	1.22	201
5	0.455	0	-9.0	-1.2	2.37	0.36	0.86	17.0	78	1.24	208
6	0.475	0	-9.5	-1.9	2.50	0.38	0.85	15.3	78	1.27	209
7	0.495	0	-10.3	-2.9	2.50	0.39	0.86	14.0	78	1.25	211
8	0.355	20	-3.7	3.7	1.04	0.28	0.86	24.8	79	1.01	133
9	0.377	20	-5.0	2.9	1.46	0.30	0.86	24.0	79	1.08	164
10	0.395	20	-6.3	1.8	1.84	0.31	0.86	23.2	79	1.14	185
11	0.415	20	-7.3	0.6	2.12	0.32	0.86	20.7	79	1.20	201
12	0.437	20	-8.4	-0.6	2.29	0.34	0.86	18.6	79	1.23	209
13	0.455	20	-9.1	-1.5	2.42	0.35	0.86	16.8	79	1.25	214
14	0.475	20	-10.1	-2.4	2.55	0.36	0.86	15.5	79	1.28	222
15	0.495	20	-10.7	-3.3	2.56	0.38	0.86	14.1	79	1.27	217
16	0.355	40	-3.8	3.7	1.05	0.28	0.86	24.8	79	0.99	132
17	0.377	40	-5.2	2.7	1.50	0.30	0.86	24.3	79	1.09	158
18	0.395	40	-6.1	2.0	1.85	0.31	0.86	23.2	80	1.13	185
19	0.415	40	-7.4	0.4	2.12	0.32	0.86	20.3	79	1.18	200
20	0.437	40	-8.4	-0.6	2.29	0.34	0.86	18.2	79	1.25	205
21	0.455	40	-9.0	-1.4	2.41	0.35	0.86	16.8	79	1.23	212
22	0.475	40	-9.7	-2.2	2.52	0.37	0.86	15.2	79	1.26	209
23	0.495	40	-10.5	-3.1	2.50	0.38	0.86	13.9	79	1.26	208
24	0.355	60	-4.5	3.1	1.12	0.28	0.86	24.6	80	1.02	138
25	0.377	60	-5.8	2.1	1.56	0.30	0.86	24.0	80	1.11	167

Continued on next page ...

#	$\mathrm{Em}_{\mathrm{finj}}$ $\frac{\mathrm{kJ}}{\mathrm{Cycle}}$	NVO [CAD]	θ_{SOC} [CAD aTDC]	θ_{50} [CAD aTDC]	IMEP [Bar]	ϕ [-]	$\mathrm{P}_{\mathrm{IVC}}$ [Bar]	BD [CAD]	$\mathrm{T}_{\mathrm{Int}}$ [^{o}C]	$\mathrm{P}_{\mathrm{EVO}}$ [Bar]	$\mathrm{T}_{\mathrm{Exh}}$ [^{o}C]
26	0.395	60	-7.0	0.9	1.91	0.31	0.86	22.0	80	1.19	187
27	0.415	60	-8.0	-0.2	2.15	0.33	0.86	19.7	80	1.21	202
28	0.437	60	-9.3	-1.5	2.3	0.34	0.86	17.3	80	1.23	207
29	0.455	60	-9.9	-2.3	2.4	0.36	0.86	16.2	79	1.22	215
30	0.475	60	-10.8	-3.3	2.45	0.37	0.86	14.9	80	1.26	216
31	0.328	80	-4.5	2.9	0.94	0.28	0.86	25.4	79	0.98	131
32	0.355	80	-5.6	2.1	1.3	0.30	0.86	24.5	80	1.05	153
33	0.377	80	-7.2	0.8	1.72	0.31	0.86	23.3	79	1.12	181
34	0.395	80	-7.9	-0.0	1.94	0.32	0.86	21.3	79	1.15	191
35	0.415	80	-8.9	-1.3	2.13	0.34	0.86	19.1	79	1.2	204
36	0.437	80	-9.6	-2.3	2.27	0.35	0.86	17.1	80	1.23	207
37	0.455	80	-10.4	-3.2	2.38	0.36	0.86	15.6	79	1.27	207
38	0.338	100	-4.8	2.7	1.07	0.30	0.86	25.4	79	0.98	133
39	0.355	100	-6.5	1.4	1.47	0.31	0.86	24.6	80	1.06	159
40	0.377	100	-7.9	0.0	1.83	0.32	0.86	22.7	79	1.12	179
41	0.395	100	-8.7	-1.0	1.98	0.33	0.86	20.6	79	1.15	187
42	0.415	100	-9.7	-2.2	2.16	0.35	0.86	18.5	79	1.17	198
43	0.437	100	-10.3	-3.1	2.25	0.36	0.86	17.0	79	1.19	203
44	0.455	100	-11.0	-3.8	2.35	0.38	0.86	15.6	79	1.2	207

Appendix C

HCCI Emission Data

SUMMARY

Table C.1: Emission - Summary of HCCI experimental data from single cylinder research engine

#	$\mathrm{Em}_{\mathrm{finj}}$ $\frac{\mathrm{kJ}}{\mathrm{Cycle}}$	NVO [CAD]	Speed [RPM]	ϕ [-]	θ_{50} [CAD aTDC]	IMEP [Bar]	CO [%]	CO_2 [%]	THC [ppm]
1	0.364	100	816	0.37	-0.7	1.92	0.38	3.65	3023
2	0.364	80	815.8	0.34	-2.6	1.9	0.35	3.3	3003
3	0.364	60	815.8	0.33	-1.8	1.9	0.38	3.15	3290
4	0.364	40	815.6	0.33	-1	1.91	0.44	2.99	3506
5	0.385	100	815.3	0.39	-4	2	0.2	4.22	2531
6	0.385	80	815.3	0.37	-4.7	2	0.19	3.87	2534
7	0.385	60	816.9	0.34	-0.1	1.97	0.47	3.1	4509
8	0.385	40	816.8	0.33	1.19	1.88	0.62	2.75	4962
9	0.338	40	817.9	0.28	1.29	1.13	1.48	1.27	5430
10	0.338	80	817.7	0.31	-0.39	1.5	0.96	2.23	3822
11	0.338	60	817.6	0.35	-0.1	1.66	0.71	3.14	3253
12	0.338	100	817.9	0.42	1.5	1.63	0.71	3.91	3760
13	0.375	40	818.1	0.32	1.9	1.78	0.79	2.22	5201
14	0.375	60	817.1	0.31	0.79	1.81	0.67	2.56	4470
15	0.375	80	817.1	0.33	-1.2	1.95	0.43	3.16	3489
16	0.375	100	816.9	0.38	-1.6	1.9	0.34	3.91	3114

Appendix D

Experimental Uncertainty

An error analysis is performed to understand the effects of uncertainty in the measurements and calculated parameters. Experimental uncertainty is calculated for a base steady state test under operating conditions listed in Table D.1. The test is repeated four times as listed in Table D.2. There are two types of uncertainties: precision and bias [211]. The precision uncertainty is calculated from the repeated measurements and for small sample size (n < 30) it is calculated [211, 212] as

$T_{coolant}$ [$^\circ C$]	50
T_{oil} [$^\circ C$]	50
T_{int} [$^\circ C$]	80
ω [RPM]	820
Injected Fuel Energy [kJ]	0.38
ON [-]	0
EVC [bTDC]	-320°
IVO [bTDC]	320°
EVO [bTDC]	-180°
IVC [bTDC]	180°

Table D.1: Baseline Engine Conditions

$$P_x = t_{\frac{\alpha}{2},\nu}\frac{S_x}{\sqrt{n}} \tag{D.1}$$

where n, t and $\mathrm{S_x}$ are the number of samples, t-distribution and standard deviation respectively. α and ν in Eqn. D.1 are calculated as

$$\alpha = 1 - c \tag{D.2}$$

$$\nu = n - 1 \tag{D.3}$$

where c is the confidence interval percentile and ν is the degree of freedom. The t-distribution values are available in [213]. Bias uncertainty can not be determined by repeated measurements. The Bias uncertainty is determined by the manufacturers' specifications and the values are in [9]. The total uncertainty, $\mathrm{U_x}$ is then calculated as

$$U_x = \sqrt{{B_x}^2 + {P_x}^2} \tag{D.4}$$

In this work, the ninety fifth percentile confidence interval is calculated for each measured parameter and the values are reported in Table D.2.

Calculated parameters such as IMEP, Maximum Rate of Pressure Rise (MRPR) and combustion timing (θ_{50}) contain uncertainty from multiple measured parameters. The probable uncertainty in calculated parameters are defined based on known uncertainties in the measured variables. The uncertainty is then calculated [211] as

$${\epsilon_F}^2 = \sum_{i=1}^{n} \left(\frac{\partial F}{\partial x_i} \right)^2 {\epsilon_i}^2 \tag{D.5}$$

where the mean square uncertainty in a quantity F is found by adding the mean square uncertainties of all variables contributing to parameter F. ϵ_i is the variance of each measured variable.

The uncertainty of the calculated parameters are listed in Table D.3. The error analysis of combustion timing is a bit complicated compared to the other parameters. The combustion timing is defined as the crank angle that fifty percent of total fuel energy is released. The total heat release is calculated as

$$Q_{HR} = \oint_{Cycle} \left(\frac{dQ}{d\theta} \right) d\theta \tag{D.6}$$

where the rate of heat release is calculated based on measured pressure trace [214] as

$$\frac{dQ}{d\theta} = \frac{k}{k-1} P \frac{dV}{d\theta} + \frac{1}{k-1} V \frac{dP}{d\theta} \tag{D.7}$$

where K, P, V and θ are specific heat ratio, in-cylinder pressure, in-cylinder volume and crank angle respectively. The uncertainties of specific heat ratio calculation, in-cylinder pressure measurement, in-cylinder volume estimation, valve timing, encoder crank angle offset and total injected fuel energy affect the combustion timing uncertainty. For combustion timing error analysis, the combustion timing is calculated based on measurements first and stored as $\theta_{50,0}$. Then, the value of each variable affecting combustion timing is increased by its uncertainty interval and the combustion timing is recalculated and stored as $\theta_{50,i+}$. The $\theta_{50,C_{i+}}$ is then calculated as $\theta_{50,C_{i+}} = \theta_{50,i+} - \theta_{50,0}$. The $\theta_{50,C_{i-}}$ is calculated as the next step by calculating the $\theta_{50,i-}$ and subtracting the $\theta_{50,0}$ from $\theta_{50,i-}$. The $\theta_{50,i-}$ is calculated similar to $\theta_{50,i+}$ except the variables affecting the combustion timing are reduced by their uncertainty intervals. The θ_{50,C_i} is then calculated by taking the average of the absolute values of the $\theta_{50,C_{i-}}$ and $\theta_{50,C_{i+}}$. The uncertainty of combustion timing is finally calculated as the root-sum-square of θ_{50,C_i} [211]. Same approach is used to calculate uncertainty of the other parameters listed in Table D.3.

Parameter	Jan 13 2013	Jan 19 2016	Jan 27 2016	Feb 18 2016	Total uncertainty
T_{Int} [$°C$]	79.6	79.4	79.5	79.9	0.4
$T_{Coolant}$ [$°C$]	47.3	48.1	46.5	45.8	1.6
T_{Oil} [$°C$]	50.2	49.8	49.9	50.1	0.3
$T_{Exhaust}$ [$°C$]	194.7	194.1	196.2	193.1	2
ϕ [-]	0.3	0.32	0.28	0.31	0.01
Ω [RPM]	826	819	823	815	8
P_{Intake} [kPa]	91.2	88.9	85.49	86.87	5
EVC [CAD bTDC]	-325	-315	-325	-320	8
IVO [CAD bTDC]	325	315	325	320	8
EVO [CAD bTDC]	-185	-175	-180	-185	8
IVC [CAD bTDC]	175	182	180	175	6

Table D.2: Uncertainty in Measured Parameters

Parameter	Jan 13 2013	Jan 19 2016	Jan 27 2016	Feb 18 2016	Total uncertainty
IMEP [Bar]	1.6	1.8	1.9	1.5	0.4
θ_{50} [CAD aTDC]	2.1	2.5	3.1	2.8	0.9
η_{Comb} [%]	78	71	74	83	9
$\eta_{Thermal,brake}$ [%]	32	36	30	34	8
MRPR [$\frac{Bar}{CAD}$]	2.7	2.1	3.5	2.9	1

Table D.3: Uncertainty in Calculated Parameters

Appendix E

Combustion Efficiency Model

The exhaust gas temperature in HCCI engines is low as the engine runs with lean mixture [1]. Due to low combustion temperature in HCCI engines, the oxidation does not continue in exhaust manifold and the combustion efficiency is mainly dependent on the concentration of unburnt HC and CO in the exhaust gases [175, 112]. The combustion efficiency is calculated using measured engine emission as [112]

$$\eta_c = 100 - 100 \times \frac{m_{HC} LHV_f + m_{CO} LHV_{CO}}{m_f LHV_f} \tag{E.1}$$

where m_{HC} and m_{CO} are the measured unburnt HC and CO masses respectively in the exhaust. The parameter LHV_{CO} is the lower heating value of CO. Accurate emission measurement for whole engine operating range is time consuming and difficult. To avoid emission measurement, a model used in [9] is further improved. The combustion efficiency in [9] is calculated as

$$\eta_c = 100 \times \frac{Q_{HR}}{m_f LHV_f} \tag{E.2}$$

where Q_{HR} is the net heat release and is calculated from

$$Q_{HR} = \int_{SOC}^{EOC} \left(\frac{dQ_{HR}}{d\theta} \right) d\theta \tag{E.3}$$

where SOC and EOC are the Start of Combustion and End of Combustion respectively. Rate of heat release, $\frac{dQ_{HR}}{d\theta}$ is calculated from a single zone model [214] as

$$\frac{dQ_{HR}}{d\theta} = \frac{1}{\gamma - 1} V \frac{dP}{d\theta} + \frac{\gamma}{\gamma - 1} P \frac{dV}{d\theta} \tag{E.4}$$

where γ, P and V are the specific heat ratio, measured in-cylinder pressure and the in-cylinder volume respectively. The combustion efficiency calculated from eqn. E.2 is compared to the combustion efficiency calculated based on measured emission (Eqn. E.1) in Figure E.1(a). The combustion efficiency values calculated from Eqn. E.2 is less than the values calculated from the measured emission (Eqn. E.1) with the average error of 10.13%. The reason is single zone models are not accurate in predicting burn rate, mixture composition and temperature at IVC [191]. The single zone model accuracy is improved using MATLAB Model-Based Calibration Toolbox as

$$\eta_c = \frac{c_1 Q_{HR}}{m_f LHV_f} + c_2 \tag{E.5}$$

The improved single zone model is parameterized and validated against the combustion efficiency values calculated based on measured emission in Figure E.1(b). The new developed single zone model shows acceptable accuracy with the average error of 2.17% for one SNVO and fuel sweep. Figure E.2 shows the model parametrization algorithm.

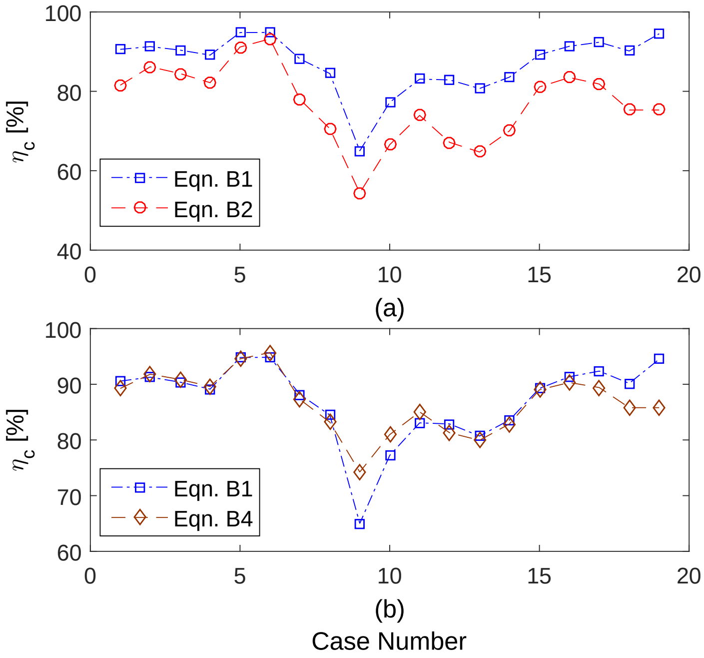

Figure E.1: (a) Combustion efficiency calculated based on measured emission vs combustion efficiency calculated from single zone model, (b) Combustion efficiency calculated based on measured emission vs combustion efficiency calculated from modified single zone model [$m_f LHV_f$= 0.33-0.39$\frac{\text{kJ}}{\text{Cycle}}$, SNVO=40-100 CAD, ω=825 RPM, P_{int}=88.4 kPa and T_{int}=80°C]

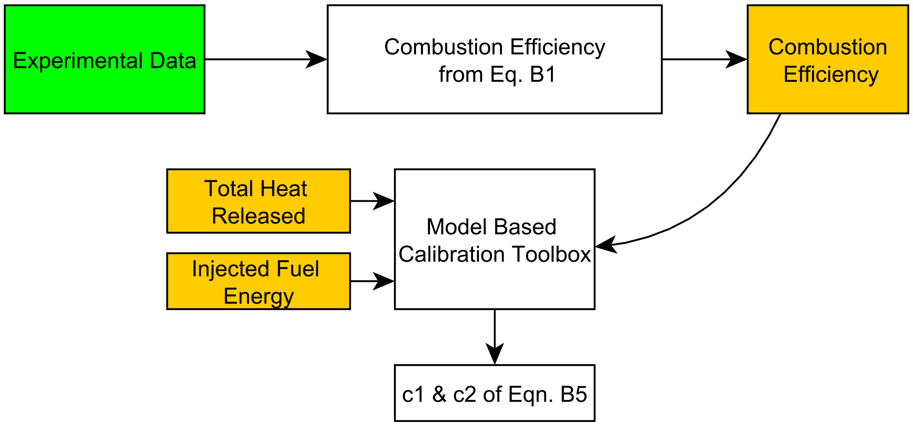

Figure E.2: Model Parametrization Algorithm

Appendix F

Control Oriented Modeling using Experimental Data

As detailed in chapter 8, a control oriented model is developed for HCCI engine that includes combustion efficiency. Measured experimental data is used to develop this model. NVO durations at constant injected fuel energies are changed and 44 operating points are measured at constant speed. n-hepaten is used as the fuel in this experiment. The engine operating conditions are listed in Table 2.1. To obtain a model that is more suitable for real-time engine control, fitted algebraic equations are derived from experimental data. This approach is useful for engine control oriented modeling when reaction mechanism is not available for the fuel. Model Based Calibration toolbox [215] in Matlab is used to calibrate the sub-models and tune the parameters.

F.1 Modeling Procedure

Start of Combustion (SOC) is calculated for each measured operating points first. The SOC is defined as the crank angle that 10% of the fuel energy is released. Sensitivity analysis is performed to define the parameters which have important effect on start of combustion. These parameters are mixture composition and temperature at the beginning of compression [1]. The Start of Combustion, θ_{soc} is then derived as

$$\theta_{soc,k} = 0.00788 T_{IVC,k}\phi_k - 4.043\phi_k - 0.0036 T_{IVC,k} + 1.493 \tag{F.1}$$

where T_{IVC} and ϕ are the IVC temperature and fuel equivalence ratio.

Burn duration sub-model is derived as the next step. Burn Duration is calculated for each operating point as the crank angle rotation between θ_{soc} and θ_{90} (the crank angle that 90% of fuel energy is released during the cycle). The Burn Duration is defined as linear function of start of combustion. The Burn Duration is

$$\Delta\theta_k = 1.7365\theta_{soc,k} + 0.581 \tag{F.2}$$

where θ_{soc} is the start of combustion that is calculated from eqn. F.1.

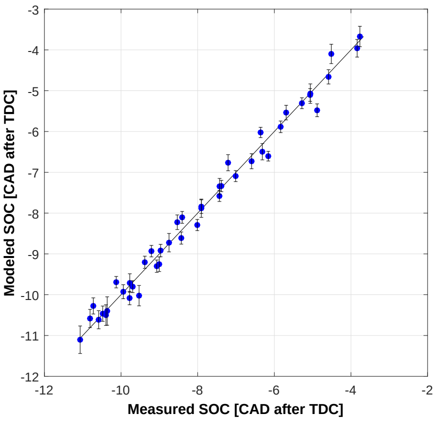

Figure F.1: SOC Model Parametrization – RMSE=0.258 CAD

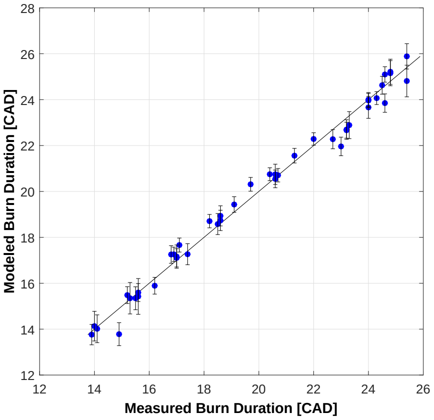

Figure F.2: Burn Duration Model Parametrization – RMSE=0.462 CAD

Figures F.1 and F.2 show the model accuracy in predicting the start of combustion and burn duration. Combustion timing, θ_{50} is then defined as

$$\theta_{50,k} = 0.5 \times \Delta\theta_k + \theta_{soc,k} \tag{F.3}$$

Combustion timing is defined as the crank angle that 50% of fuel energy is released during the cycle.

The next step is to define fuel equivalence ratio sub-model. The fuel equivalence ratio is calculated from the lambda sensor measurements. The main parameters affecting fuel equivalence ratio are residual gas fraction, IVC temperature and the injected fuel energy [216, 217]. The model is derived as

$$\phi_k = 0.0012 T_{IVC,k} y_{r,k} - 7.7 \times 10^{-5} T_{IVC,k} - 0.3582 y_k + 0.6734 m_{f,k} LHV_f + 0.071 \tag{F.4}$$

where y_r is the residual mole fraction. Figure F.3 shows the model accuracy in predicting fuel equivalence ratio.

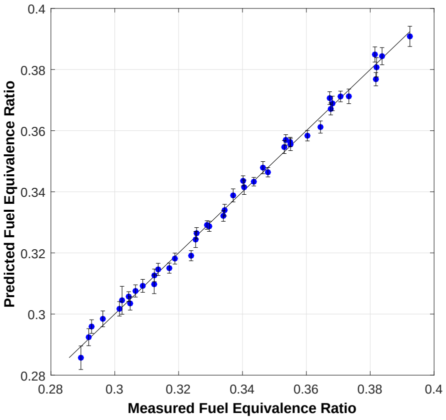

Figure F.3: Fuel Equivalence Ratio Model Parametrization – RMSE=0.00235

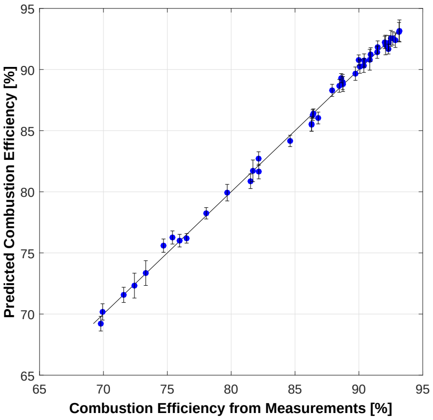

Figure F.4: Combustion Timing Model Parametrization – RMSE=0.516

The next step is to define combustion efficiency sub-model. The combustion efficiency calculation is detailed in Appendix E. Major parameters affecting combustion efficiency is investigated in chapter 4 and Appendix E. These parameters are combustion timing, IVC temperature, residual fraction (NVO duration) and fuel equivalence ratio. The combustion efficiency sub-model, η_c is then derived as

$$\eta_{c,k} = -0.044\theta_{50,k} + 0.039T_{IVC,k} + 2.86y_{r,k} + 17.47\phi_k^{3.99} + 67.79 \tag{F.5}$$

The model accuracy in predicting combustion efficiency is shown in Figure F.4. Finally, IMEP sub-model is derived using the measured data and Matalb Model Based Calibration Toolbox. Injected fuel energy, combustion efficiency and combustion timing are major parameters that affect IMEP as detailed in chapter 3. The IMEP sub-model is then derived as

$$\text{IMEP}_k = -0.2674\eta_k m_{f,k} LHV_f + 0.1385\eta_k + 29.9m_{f,k} LHV_f + 0.075\theta_{50,k} + 0.1385 \tag{F.6}$$

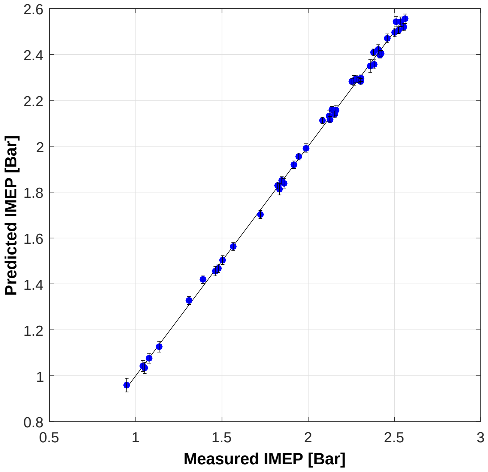

Figure F.5: IMEP Model Parametrization – RMSE=0.029 Bar

Figure F.5 shows the model accuracy in predicting the IMEP. The approach explained in this appendix and chapter 8 can be extended to HCCI engines that work with different fuels including bio-fuels.

Appendix G

n-heptane Reaction Mechanism

```
#
# Generated from n-hepatne reaction mechanism
# by ck2cti on Tue Apr 03 16:02:13 2012
# https://combustion.llnl.gov/
#
units(length = "cm", time = "s", quantity = "mol", act_energy = "cal/mol")


ideal_gas(name = "mech_dat",
      elements = " H  C  O  N ",
      species = """ nc7h16  o2  n2  co2  h2o  co  h2  oh  h2o2  ho2
                   h  o  ch3o  ch2o  hco  ch2  ch3  ch4  c2h3  c2h4
                   c2h5  c3h4  c3h5  c3h6  c3h7  c7h15-2  c7h15o2  c7ket12  c5h11co """,
      reactions = "all",
      initial_state = state(temperature = 300.0,
                        pressure = OneAtm)    )



#-------------------------------------------------------------------------------
#  Species data
#-------------------------------------------------------------------------------

species(name = "nc7h16",
    atoms = " C:7  H:16 ",
    thermo = (
       NASA( [  300.00,  1391.00], [-1.268361870E+000,  8.543558200E-002,
               -5.253467860E-005,  1.629457210E-008, -2.023949250E-012,
               -2.565865650E+004,  3.537329120E+001] ),
       NASA( [ 1391.00,  5000.00], [ 2.221489690E+001,  3.476757500E-002,
               -1.184071290E-005,  1.832984780E-009, -1.061302660E-013,
               -3.427600810E+004, -9.230401960E+001] )
              ),
    note = "2/10/95"
       )

species(name = "o2",
    atoms = " O:2 ",
    thermo = (
       NASA( [  300.00,  1000.00], [ 3.212936000E+000,  1.127486000E-003,
               -5.756150000E-007,  1.313877000E-009, -8.768554000E-013,
               -1.005249000E+003,  6.034738000E+000] ),
       NASA( [ 1000.00,  5000.00], [ 3.697578000E+000,  6.135197000E-004,
               -1.258842000E-007,  1.775281000E-011, -1.136435000E-015,
               -1.233930000E+003,  3.189166000E+000] )
              ),
    note = "121386"
```

```
       )

species(name = "n2",
    atoms = " N:2 ",
    thermo = (
       NASA( [  300.00,  1000.00], [ 3.298677000E+000,  1.408240000E-003,
               -3.963222000E-006,  5.641515000E-009, -2.444855000E-012,
               -1.020900000E+003,  3.950372000E+000] ),
       NASA( [ 1000.00,  5000.00], [ 2.926640000E+000,  1.487977000E-003,
               -5.684761000E-007,  1.009704000E-010, -6.753351000E-015,
               -9.227977000E+002,  5.980528000E+000] )
             ),
    note = "121286"
       )

species(name = "co2",
    atoms = " C:1  O:2 ",
    thermo = (
       NASA( [  300.00,  1000.00], [ 2.275725000E+000,  9.922072000E-003,
               -1.040911000E-005,  6.866687000E-009, -2.117280000E-012,
               -4.837314000E+004,  1.018849000E+001] ),
       NASA( [ 1000.00,  5000.00], [ 4.453623000E+000,  3.140169000E-003,
               -1.278411000E-006,  2.393997000E-010, -1.669033000E-014,
               -4.896696000E+004, -9.553959000E-001] )
             ),
    note = "121286"
       )

species(name = "h2o",
    atoms = " H:2  O:1 ",
    thermo = (
       NASA( [  300.00,  1000.00], [ 3.386842000E+000,  3.474982000E-003,
               -6.354696000E-006,  6.968581000E-009, -2.506588000E-012,
               -3.020811000E+004,  2.590233000E+000] ),
       NASA( [ 1000.00,  5000.00], [ 2.672146000E+000,  3.056293000E-003,
               -8.730260000E-007,  1.200996000E-010, -6.391618000E-015,
               -2.989921000E+004,  6.862817000E+000] )
             ),
    note = "20387"
       )

species(name = "co",
    atoms = " C:1  O:1 ",
    thermo = (
       NASA( [  300.00,  1000.00], [ 3.262452000E+000,  1.511941000E-003,
               -3.881755000E-006,  5.581944000E-009, -2.474951000E-012,
               -1.431054000E+004,  4.848897000E+000] ),
       NASA( [ 1000.00,  5000.00], [ 3.025078000E+000,  1.442689000E-003,
               -5.630828000E-007,  1.018581000E-010, -6.910952000E-015,
               -1.426835000E+004,  6.108218000E+000] )
             ),
    note = "121286"
       )

species(name = "h2",
    atoms = " H:2 ",
    thermo = (
       NASA( [  300.00,  1000.00], [ 3.298124000E+000,  8.249442000E-004,
               -8.143015000E-007, -9.475434000E-011,  4.134872000E-013,
               -1.012521000E+003, -3.294094000E+000] ),
       NASA( [ 1000.00,  5000.00], [ 2.991423000E+000,  7.000644000E-004,
               -5.633829000E-008, -9.231578000E-012,  1.582752000E-015,
               -8.350340000E+002, -1.355110000E+000] )
             ),
    note = "121286"
       )
```

```
species(name = "oh",
    atoms = " O:1  H:1  ",
    thermo = (
       NASA( [  300.00,  1000.00], [ 3.637266000E+000,  1.850910000E-004,
             -1.676165000E-006,  2.387203000E-009, -8.431442000E-013,
              3.606782000E+003,  1.358860000E+000] ),
       NASA( [ 1000.00,  5000.00], [ 2.882730000E+000,  1.013974000E-003,
             -2.276877000E-007,  2.174684000E-011, -5.126305000E-016,
              3.886888000E+003,  5.595712000E+000] )
             ),
    note = "121286"
       )

species(name = "h2o2",
    atoms = " H:2  O:2  ",
    thermo = (
       NASA( [  300.00,  1000.00], [ 3.388754000E+000,  6.569226000E-003,
             -1.485013000E-007, -4.625806000E-009,  2.471515000E-012,
             -1.766315000E+004,  6.785363000E+000] ),
       NASA( [ 1000.00,  5000.00], [ 4.573167000E+000,  4.336136000E-003,
             -1.474689000E-006,  2.348904000E-010, -1.431654000E-014,
             -1.800696000E+004,  5.011370000E-001] )
             ),
    note = "120186"
       )

species(name = "ho2",
    atoms = " H:1  O:2  ",
    thermo = (
       NASA( [  300.00,  1000.00], [ 2.979963000E+000,  4.996697000E-003,
             -3.790997000E-006,  2.354192000E-009, -8.089024000E-013,
              1.762274000E+002,  9.222724000E+000] ),
       NASA( [ 1000.00,  5000.00], [ 4.072191000E+000,  2.131296000E-003,
             -5.308145000E-007,  6.112269000E-011, -2.841165000E-015,
             -1.579727000E+002,  3.476029000E+000] )
             ),
    note = "20387"
       )

species(name = "h",
    atoms = " H:1  ",
    thermo = (
       NASA( [  300.00,  1000.00], [ 2.500000000E+000,  0.000000000E+000,
              0.000000000E+000,  0.000000000E+000,  0.000000000E+000,
              2.547163000E+004, -4.601176000E-001] ),
       NASA( [ 1000.00,  5000.00], [ 2.500000000E+000,  0.000000000E+000,
              0.000000000E+000,  0.000000000E+000,  0.000000000E+000,
              2.547163000E+004, -4.601176000E-001] )
             ),
    note = "120186"
       )

species(name = "o",
    atoms = " O:1  ",
    thermo = (
       NASA( [  300.00,  1000.00], [ 2.946429000E+000, -1.638166000E-003,
              2.421032000E-006, -1.602843000E-009,  3.890696000E-013,
              2.914764000E+004,  2.963995000E+000] ),
       NASA( [ 1000.00,  5000.00], [ 2.542060000E+000, -2.755062000E-005,
             -3.102803000E-009,  4.551067000E-012, -4.368052000E-016,
              2.923080000E+004,  4.920308000E+000] )
             ),
    note = "120186"
       )

species(name = "ch3o",
    atoms = " C:1  H:3  O:1  ",
```

```
    thermo = (
       NASA( [   300.00,   1000.00], [ 2.106204000E+000,  7.216595000E-003,
               5.338472000E-006, -7.377636000E-009,  2.075611000E-012,
               9.786011000E+002,  1.315218000E+001] ),
       NASA( [  1000.00,   3000.00], [ 3.770800000E+000,  7.871497000E-003,
              -2.656384000E-006,  3.944431000E-010, -2.112616000E-014,
               1.278325000E+002,  2.929575000E+000] )
             ),
    note = "121686"
       )

species(name = "ch2o",
    atoms = " C:1  H:2  O:1 ",
    thermo = (
       NASA( [   300.00,   1000.00], [ 1.652731000E+000,  1.263144000E-002,
              -1.888168000E-005,  2.050031000E-008, -8.413237000E-012,
              -1.486540000E+004,  1.378482000E+001] ),
       NASA( [  1000.00,   5000.00], [ 2.995606000E+000,  6.681321000E-003,
              -2.628955000E-006,  4.737153000E-010, -3.212517000E-014,
              -1.532037000E+004,  6.912572000E+000] )
             ),
    note = "121286"
       )

species(name = "hco",
    atoms = " H:1  C:1  O:1 ",
    thermo = (
       NASA( [   300.00,   1000.00], [ 2.898330000E+000,  6.199147000E-003,
              -9.623084000E-006,  1.089825000E-008, -4.574885000E-012,
               4.159922000E+003,  8.983614000E+000] ),
       NASA( [  1000.00,   5000.00], [ 3.557271000E+000,  3.345573000E-003,
              -1.335006000E-006,  2.470573000E-010, -1.713851000E-014,
               3.916324000E+003,  5.552299000E+000] )
             ),
    note = "121286"
       )

species(name = "ch2",
    atoms = " C:1  H:2 ",
    thermo = (
       NASA( [   250.00,   1000.00], [ 3.762237000E+000,  1.159819000E-003,
               2.489585000E-007,  8.800836000E-010, -7.332435000E-013,
               4.536791000E+004,  1.712578000E+000] ),
       NASA( [  1000.00,   4000.00], [ 3.636408000E+000,  1.933057000E-003,
              -1.687016000E-007, -1.009899000E-010,  1.808256000E-014,
               4.534134000E+004,  2.156561000E+000] )
             ),
    note = "120186"
       )

species(name = "ch3",
    atoms = " C:1  H:3 ",
    thermo = (
       NASA( [   300.00,   1000.00], [ 2.430443000E+000,  1.112410000E-002,
              -1.680220000E-005,  1.621829000E-008, -5.864953000E-012,
               1.642378000E+004,  6.789794000E+000] ),
       NASA( [  1000.00,   5000.00], [ 2.844052000E+000,  6.137974000E-003,
              -2.230345000E-006,  3.785161000E-010, -2.452159000E-014,
               1.643781000E+004,  5.452697000E+000] )
             ),
    note = "121286"
       )

species(name = "ch4",
    atoms = " C:1  H:4 ",
    thermo = (
       NASA( [   300.00,   1000.00], [ 7.787415000E-001,  1.747668000E-002,
```

```
             -2.783409000E-005,   3.049708000E-008,  -1.223931000E-011,
             -9.825229000E+003,   1.372219000E+001] ),
      NASA( [ 1000.00,   5000.00], [ 1.683479000E+000,   1.023724000E-002,
             -3.875129000E-006,   6.785585000E-010,  -4.503423000E-014,
             -1.008079000E+004,   9.623395000E+000] )
            ),
    note = "121286"
      )

species(name = "c2h3",
    atoms = " C:2  H:3  ",
    thermo = (
      NASA( [   300.00,   1000.00], [ 2.459276000E+000,   7.371476000E-003,
              2.109873000E-006,  -1.321642000E-009,  -1.184784000E-012,
              3.335225000E+004,   1.155620000E+001] ),
      NASA( [ 1000.00,   5000.00], [ 5.933468000E+000,   4.017746000E-003,
             -3.966740000E-007,  -1.441267000E-010,   2.378644000E-014,
              3.185435000E+004,  -8.530313000E+000] )
            ),
    note = "12787"
      )

species(name = "c2h4",
    atoms = " C:2  H:4  ",
    thermo = (
      NASA( [   300.00,   1000.00], [-8.614880000E-001,   2.796163000E-002,
            -3.388677000E-005,   2.785152000E-008,  -9.737879000E-012,
             5.573046000E+003,   2.421149000E+001] ),
      NASA( [ 1000.00,   5000.00], [ 3.528419000E+000,   1.148518000E-002,
            -4.418385000E-006,   7.844601000E-010,  -5.266848000E-014,
             4.428289000E+003,   2.230389000E+000] )
            ),
    note = "121286"
      )

species(name = "c2h5",
    atoms = " C:2  H:5  ",
    thermo = (
      NASA( [   300.00,   1000.00], [ 2.690702000E+000,   8.719133000E-003,
              4.419839000E-006,   9.338703000E-010,  -3.927773000E-012,
              1.287040000E+004,   1.213820000E+001] ),
      NASA( [ 1000.00,   5000.00], [ 7.190480000E+000,   6.484077000E-003,
            -6.428065000E-007,  -2.347879000E-010,   3.880877000E-014,
             1.067455000E+004,  -1.478089000E+001] )
            ),
    note = "12387"
      )

species(name = "c3h4",
    atoms = " C:3  H:4  ",
    thermo = (
      NASA( [   200.00,   1000.00], [ 2.613074870E+000,   1.212233710E-002,
              1.854054000E-005,  -3.452584750E-008,   1.533533890E-011,
              2.154156420E+004,   1.025033190E+001] ),
      NASA( [ 1000.00,   6000.00], [ 6.316948690E+000,   1.113362620E-002,
            -3.962890180E-006,   6.356337750E-010,  -3.787498850E-014,
             2.011746170E+004,  -1.097188620E+001] )
            ),
    note = "112/92"
      )

species(name = "c3h5",
    atoms = " C:3  H:5  ",
    thermo = (
      NASA( [   200.00,   1000.00], [ 3.787946930E+000,   9.484143350E-003,
              2.423433680E-005,  -3.656040100E-008,   1.485923560E-011,
              1.862612180E+004,   7.828224990E+000] ),
```

```
        NASA( [ 1000.00,  6000.00], [ 6.547611320E+000,  1.331522460E-002,
                -4.783331000E-006,  7.719498140E-010, -4.619308080E-014,
                 1.727147070E+004, -9.274868410E+000] )
              ),
     note = "bur 92"
        )

species(name = "c3h6",
     atoms = " C:3  H:6  ",
     thermo = (
        NASA( [  300.00,  1388.00], [ 3.946154440E-001,  2.891076620E-002,
                -1.548868080E-005,  3.888142090E-009, -3.378903520E-013,
                 1.066881640E+003,  2.190037360E+001] ),
        NASA( [ 1388.00,  5000.00], [ 8.015959580E+000,  1.370236340E-002,
                -4.662497330E-006,  7.212544020E-010, -4.173701260E-014,
                -1.878212710E+003, -2.001606680E+001] )
              ),
     note = "5/27/97 therm"
        )

species(name = "c3h7",
     atoms = " C:3  H:7  ",
     thermo = (
        NASA( [  300.00,  1000.00], [ 1.051551800E+000,  2.599198000E-002,
                 2.380054000E-006, -1.960956900E-008,  9.373247000E-012,
                 1.063186300E+004,  2.112255900E+001] ),
        NASA( [ 1000.00,  5000.00], [ 7.702698700E+000,  1.604420300E-002,
                -5.283322000E-006,  7.629859000E-010, -3.939228400E-014,
                 8.298433600E+003, -1.548018000E+001] )
              ),
     note = "n-l 9/84"
        )

species(name = "c7h15-2",
     atoms = " C:7  H:15  ",
     thermo = (
        NASA( [  300.00,  1382.00], [-3.791557670E-002,  7.567265700E-002,
                -4.074736340E-005,  9.326789430E-009, -4.923607450E-013,
                -2.356053030E+003,  3.373215060E+001] ),
        NASA( [ 1382.00,  5000.00], [ 2.163688420E+001,  3.233248040E-002,
                -1.092738070E-005,  1.683570600E-009, -9.717740910E-014,
                -1.058736160E+004, -8.522096530E+001] )
              ),
     note = "2/10/95"
        )

species(name = "c7h15o2",
     atoms = " C:7  H:15  O:2  ",
     thermo = (
        NASA( [  300.00,  1390.00], [ 2.374993340E+000,  8.346519060E-002,
                -5.138973200E-005,  1.642176620E-008, -2.195052160E-012,
                -1.992379610E+004,  2.530673420E+001] ),
        NASA( [ 1390.00,  5000.00], [ 2.490236890E+001,  3.507169200E-002,
                -1.204403060E-005,  1.874648220E-009, -1.089477910E-013,
                -2.829760500E+004, -9.739235420E+001] )
              ),
     note = "7/23/98"
        )

species(name = "c7ket12",
     atoms = " C:7  H:14  O:3  ",
     thermo = (
        NASA( [  300.00,  1396.00], [ 5.824336970E-001,  1.012078690E-001,
                -7.658559960E-005,  3.007386060E-008, -4.829027920E-012,
                -4.680544190E+004,  3.333314490E+001] ),
        NASA( [ 1396.00,  5000.00], [ 2.974729060E+001,  3.066222940E-002,
                -1.055635900E-005,  1.646273430E-009, -9.581716750E-014,
```

```
             −5.668568280E+004, −1.224324900E+002] )
             ),
    note = "7/23/98"
       )

species(name = "c5h11co",
    atoms = " C:6  H:11  O:1 ",
    thermo = (
       NASA( [  300.00,   1383.00], [ 2.144790690E+000,  6.178635630E−002,
             −3.741346900E−005,  1.132837950E−008, −1.369176980E−012,
             −1.434511720E+004,  2.231280450E+001] ),
       NASA( [ 1383.00,   5000.00], [ 1.947838120E+001,  2.504660290E−002,
             −8.548613460E−006,  1.325579440E−009, −7.685032960E−014,
             −2.079239370E+004, −7.219955780E+001] )
             ),
    note = "2/29/96"
       )



#−−−−−−−−−−−−−−−−−−−−−−−−−−−−−−−−−−−−−−−−−−−−−−−−−−−−−−−−−−−−−−−−−−−−−−−−−−−−−
#  Reaction data
#−−−−−−−−−−−−−−−−−−−−−−−−−−−−−−−−−−−−−−−−−−−−−−−−−−−−−−−−−−−−−−−−−−−−−−−−−−−−−

#  Reaction 1
reaction(  "nc7h16 + h <=> c7h15−2 + h2",  [4.38000E+007, 2, 4760])

#  Reaction 2
reaction(  "nc7h16 + oh <=> c7h15−2 + h2o",  [9.70000E+009, 1.3, 1690])

#  Reaction 3
reaction(  "nc7h16 + ho2 <=> c7h15−2 + h2o2",  [1.65000E+013, 0, 16950])

#  Reaction 4
reaction(  "nc7h16 + o2 <=> c7h15−2 + ho2",  [2.00000E+015, 0, 47380])

#  Reaction 5
reaction(  "c7h15−2 + o2 <=> c7h15o2",  [1.56000E+012, 0, 0])

#  Reaction 6
reaction(  "c7h15o2 + o2 <=> c7ket12 + oh",  [4.50000E+014, 0, 18232.7])

#  Reaction 7
reaction(  "c7ket12 <=> c5h11co + ch2o + oh",  [9.53000E+014, 0, 41100])

#  Reaction 8
reaction(  "c5h11co <=> c2h4 + c3h7 + co",  [9.84000E+015, 0, 40200])

#  Reaction 9
reaction(  "c7h15−2 <=> c2h5 + c2h4 + c3h6",  [7.04500E+014, 0, 34600])

#  Reaction 10
reaction(  "c3h7 <=> c2h4 + ch3",  [9.60000E+013, 0, 30950])

#  Reaction 11
reaction(  "c3h7 <=> c3h6 + h",  [1.25000E+014, 0, 36900])

#  Reaction 12
reaction(  "c3h6 + ch3 <=> c3h5 + ch4",  [9.00000E+012, 0, 8480])

#  Reaction 13
reaction(  "c3h5 + o2 <=> c3h4 + ho2",  [6.00000E+011, 0, 10000])

#  Reaction 14
reaction(  "c3h4 + oh <=> c2h3 + ch2o",  [1.00000E+012, 0, 0])

#  Reaction 15
```

```
reaction(  "c3h4 + oh <=> c2h4 + hco",  [1.00000E+012, 0, 0])

#  Reaction 16
reaction(  "ch3 + ho2 <=> ch3o + oh",  [5.00000E+013, 0, 0])

#  Reaction 17
reaction(  "ch3 + oh <=> ch2 + h2o",  [7.50000E+006, 2, 5000])

#  Reaction 18
reaction(  "ch2 + oh <=> ch2o + h",  [2.50000E+013, 0, 0])

#  Reaction 19
reaction(  "ch2 + o2 <=> hco + oh",  [4.30000E+010, 0, −500])

#  Reaction 20
reaction(  "ch2 + o2 <=> co2 + h2",  [6.90000E+011, 0, 500])

#  Reaction 21
reaction(  "ch2 + o2 <=> co + h2o",  [2.00000E+010, 0, −1000])

#  Reaction 22
reaction(  "ch2 + o2 <=> ch2o + o",  [5.00000E+013, 0, 9000])

#  Reaction 23
reaction(  "ch2 + o2 <=> co2 + h + h",  [1.60000E+012, 0, 1000])

#  Reaction 24
reaction(  "ch2 + o2 <=> co + oh + h",  [8.60000E+010, 0, −500])

#  Reaction 25
reaction(  "ch3o + co <=> ch3 + co2",  [1.57000E+014, 0, 11800])

#  Reaction 26
reaction(  "co + oh <=> co2 + h",  [8.98700E+007, 1.38, 5232.88])

#  Reaction 27
reaction(  "o + oh <=> o2 + h",  [4.00000E+014, −0.5, 0])

#  Reaction 28
reaction(  "h + ho2 <=> oh + oh",  [1.70000E+014, 0, 875])

#  Reaction 29
reaction(  "oh + oh <=> o + h2o",  [6.00000E+008, 1.3, 0])

#  Reaction 30
three_body_reaction( "h + o2 + M <=> ho2 + M",  [3.60000E+017, −0.72, 0],
         efficiencies = " co:2  co2:5  h2:3.3  h2o:21  ")

#  Reaction 31
three_body_reaction( "h2o2 + M <=> oh + oh + M",  [1.00000E+016, 0, 45500],
         efficiencies = " co:2  co2:5  h2:3.3  h2o:21  ")

#  Reaction 32
reaction(  "h2 + oh <=> h2o + h",  [1.17000E+009, 1.3, 3626])

#  Reaction 33
reaction(  "ho2 + ho2 <=> h2o2 + o2",  [3.00000E+012, 0, 0])

#  Reaction 34
reaction(  "ch2o + oh <=> hco + h2o",  [5.56300E+010, 1.095, −76.517])

#  Reaction 35
reaction(  "ch2o + ho2 <=> hco + h2o2",  [3.00000E+012, 0, 8000])

#  Reaction 36
reaction(  "hco + o2 <=> ho2 + co",  [3.30000E+013, −0.4, 0])
```

```
#  Reaction 37
three_body_reaction( "hco + M <=> h + co + M",  [1.59100E+018, 0.95, 56712.3])

#  Reaction 38
reaction(  "ch3 + ch3o <=> ch4 + ch2o",  [4.30000E+014, 0, 0])

#  Reaction 39
reaction(  "c2h4 + oh <=> ch2o + ch3",  [6.00000E+013, 0, 960])

#  Reaction 40
reaction(  "c2h4 + oh <=> c2h3 + h2o",  [8.02000E+013, 0, 5955])

#  Reaction 41
reaction(  "c2h3 + o2 <=> ch2o + hco",  [4.00000E+012, 0, −250])

#  Reaction 42
reaction(  "c2h3 + hco <=> c2h4 + co",  [6.03400E+013, 0, 0])

#  Reaction 43
reaction(  "c2h5 + o2 <=> c2h4 + ho2",  [2.00000E+010, 0, −2200])

#  Reaction 44
reaction(  "ch4 + o2 <=> ch3 + ho2",  [7.90000E+013, 0, 56000])

#  Reaction 45
reaction(  "oh + ho2 <=> h2o + o2",  [7.50000E+012, 0, 0])

#  Reaction 46
reaction(  "ch3 + o2 <=> ch2o + oh",  [3.80000E+011, 0, 9000])

#  Reaction 47
reaction(  "ch4 + h <=> ch3 + h2",  [6.60000E+008, 1.6, 10840])

#  Reaction 48
reaction(  "ch4 + oh <=> ch3 + h2o",  [1.60000E+006, 2.1, 2460])

#  Reaction 49
reaction(  "ch4 + o <=> ch3 + oh",  [1.02000E+009, 1.5, 8604])

#  Reaction 50
reaction(  "ch4 + ho2 <=> ch3 + h2o2",  [9.00000E+011, 0, 18700])

#  Reaction 51
reaction(  "ch4 + ch2 <=> ch3 + ch3",  [4.00000E+012, 0, −570])

#  Reaction 52
reaction(  "c3h6 <=> c2h3 + ch3",  [3.15000E+015, 0, 85500])
```